The Significance of Proton Beams in the Multiscale Solar Wind

by

Benjamin L. Alterman

A dissertation submitted in partial fulfillment
of the requirements for the degree of
Doctor of Philosophy
(Applied Physics)
in the University of Michigan
2019

Doctoral Committee:

Professor Justin C. Kasper, Co-Chair
Professor Stefano Livi, Co-Chair
Professor Enrico Landi
Professor Susan Therese Lepri
Professor James Arthur Slavin
Doctor Bartholomeus van der Holst

Benjamin L. Alterman

balterma@umich.edu

ORCiD iD: 0000-0001-6673-3432

I dedicate this thesis to Christopher Kevorkian, who gave me an unlikely gift. A long time ago, you convinced me to read a Harry Potter novel. Born dyslexic, I didn't think I could. Without your gift, I may not have written this thesis. Thank you for being the best and a lifelong friend.

ACKNOWLEDGMENTS

While only one person's name is listed as a dissertation's author, this document represents the work of a great many people: those who have taught, supported, mentored, and simply been my friend. Although I will certainly overlook too many names, I would like to specifically thank several people. First, my thesis committee. Justin Kasper, Stefano Livi, Susan Lepri, Jim Slavin, Enrico Landi, and Bart van der Holst, thank you for creating a research environment where I have had the opportunity to learn, grow, and explore space physics. Kris Klein and Mike Stevens, you have both played integral roles in my research and growth as a scientist. Çagliyan Kurdak and Cynthia McNabb, your commitment have made Applied Physics the model it is. Brian Arbic, thank you for bringing me to the University of Michigan and supporting me as I found my footing in graduate school. Len Fisk, Jim Raines, Mark Moldwin, Dan Welling, Elaine Meinzer, Bryan White, Darren Britten-Bozzone, Jan Beltran, and Debbie Eddie helped make my time in CLaSP the multifaceted experience that I find most rewarding and enriching. Jens Zorn, thank you for your guidance and wisdom on this journey. Angeline, Paul, Theresa, Annika, Jeremey, Andy, and The Ross Leaders Academy helped transform my Michigan experience into a well rounded and holistic adventure. In no particular order, Geoff Gorham, Martin Gunderson, Janet Folina, Tonnis ter Veldhuis, James Doyle, James Heyman, Andrew Beveridge, and Nannette Goldman, thank you for adding new dimensions to my education and preparing me to tackle graduate school. To my friends Matt, Mark, Sarah, Abby, Emma, Will, Gianna, Sean, Sam, and Christopher: you have been incredible, supported me when the stress was difficult to bear, kept life full of fun and joy, and been incredibly gracious as I've been unavailable. Mr. Hocker, you assigned me my very first kindergarten science project. Of all places, can you believe glass bottles, paint, and a heat lamp lead me here? Uncle Howard, thank you for all the books. It might have taken me a few years to start reading them, but I think it did the trick. Sharon, Mom, and Dad, "thank you" can't cover it. Then again, I don't think words could, so "thank you" will have to do. I also want to thank you. If you're reading this, odds are you played a part and the fault is certainly mine for not including you. So please consider yourself among this list. Finally, no scientific publication is complete without acknowledging how one is funded to explore and investigate the unknown. My PhD has been funded under NASA contract SV4-84016 as well as NASA grants NNX14AR78G, 80NSSC18K0986, and NNX17AI18G. I'm grateful that you paid me to do this.

TABLE OF CONTENTS

Dedication . . . . **ii**

Acknowledgments . . . . **iii**

List of Figures . . . . **vi**

List of Tables . . . . **xiii**

List of Abbreviations . . . . **xv**

Abstract . . . . **xvii**

Chapter

1 Introduction **1**

- 1.1 History and Background 1
- 1.2 The Sun and Solar Cycle’s Impact on the Solar Wind 5
- 1.3 Coulomb Collisions 10
- 1.4 Local Regulation of Differential Flow 14
- 1.5 Recap and Path Forward 21

2 Helium Variation Across Two Solar Cycles Reveals a Speed-Dependent Phase Lag **23**

- 2.1 Abstract 23
- 2.2 Introduction 23
- 2.3 Data Sources 26
- 2.4 Solar Cycle Variation 26
- 2.5 Time-Lagged Cross Correlation 27
- 2.6 Phase Delay 29
- 2.7 Robustness of $\mathrm{A_{He}}(v)$ 30
- 2.8 Helium Filtration 31
- 2.9 Conclusion 33

3 21 Years of Proton Beams at 1 AU **36**

- 3.1 Abstract 36
- 3.2 Introduction 36
- 3.3 Measurement Technique, Fit Algorithm & Data Selection 39
- 3.4 Typical Beam Properties 42

3.5 Missing Beams 51
3.6 Summary & Conclusions 54
3.7 Appendix: A Comparison of the Single and Two Population Proton Bulk Parameters 59

4 Collisionally Young Differential Flow 66

4.1 Abstract 66
4.2 Introduction 67
4.3 Data Sources & Selection 69
4.4 Fast Wind Differential Flow 72
4.5 Uncorrelated Fluctuations 73
4.6 Trends with Collisional Age 73
4.7 Corrections to the Alfvén Speed 78
4.8 Trends in A_c 83
4.9 Discussion 85
4.10 Conclusions 87

5 Near-Sun Proton Beams 89

5.1 Abstract 89
5.2 Introduction 89
5.3 Data Sources 91
5.4 Overview of Encounter 1 95
5.5 Event Properties 101
5.6 Discussion and Conclusion 111

6 On The Limitations of Applying Reduced Free Energy Parameter Spaces to Proton Beams in the Solar Wind 116

6.1 Abstract 116
6.2 Introduction 117
6.3 Data Sources 118
6.4 Proton Beams in The Prototypical $(\beta_\parallel, R)$ Plane 120
6.5 Instabilities in the Proton Beam Reduced Free Energy Plane 122
6.6 Maximum Growth Rates 125
6.7 Discussion 130
6.8 Conclusion 133

7 Concluding Remarks 135

Appendices 142

Bibliography 148

LIST OF FIGURES

1.1 Bulk solar wind properties measured at 1 AU as a function of solar cycle. Properties presented are (A) magnetic field magnitude ($\boldsymbol{B}$), (B) helium abundance ($\mathrm{A_{He}}$) and beam abundance ($\mathrm{A_{beam}}$), (C) beam-core differential flow and drift energy fraction, and (D) total proton plasma beta and beam-to-core thermal pressure ratio. Panel (E) shows the 13 month smoothed SSN. Table 1.1 gives the cross correlation coefficient ρ between each quantity Q in Panels (A) through (D) with sunspot number (SSN). 9

1.2 Proton beam-core differential flow ($\Delta v_{p_2,p_1}/C_{A;p_1+p_2}$) as a function of Coulomb number ($N_{c;p_2,p_1}$). $N_{c;p_2,p_1}$ is an empirical, single point estimate of the number of Coulomb collisions a given plasma parcel has experienced as it propagates from the Sun to the *Wind* spacecraft. 13

1.3 An example solar wind instability analysis that assumes only parallel proton plasma beta ($\beta_{\parallel}$) and temperature anisotropy ($R_T = T_{\perp}/T_{\parallel}$) are the significant and varying sources of free energy governing instability onset. The 2D Probability Distribution Function (PDF) is given in color. Instability thresholds identified in the legend are taken from Verscharen et al. (2016) for the case that the growth rate is $\gamma/\Omega_p = 10^{-2}$. Unstable plasma measurements are those farther from the PDF's centroid than the thresholds. This figure also demonstrates a technique for identifying the border of the (β, R) distribution used in Figure 3.5. Here, the cyan line outlining the 2D PDF is a smoothed version of the accompanying red line that reduces the significance outliers at the edges that, by construction, are driven by low counting statistics. 20

2.1 Helium abundance ($\mathrm{A_{He}}$) as a function of time and solar wind speed. Solar wind speed (v_{sw}) is divided into ten quantiles. Thirteen month smoothed SIDC Sunspot Number (SSN, dashed black) is plotted on the secondary y-axis. The legend indicates the middle of a given v_{sw} quantile and the Spearman rank correlation coefficient between $\mathrm{A_{He}}$ and SSN for that quantile. In effect, this figure updates Fig. (1) of Kasper et al. (2012, 2007). The present drop in $\mathrm{A_{He}}$ reflects the onset of solar minimum 25. 24

2.2 Plots characterizing the cross correlation coefficient as a function of solar wind speed (v_{sw}) for the observed (empty markers) and delayed (filled markers) SSN using 250 day averages. The marker color and shape match the style of Figure 2.1. Dotted lines connect the markers to aid the eye. Panels are: (a) Spearman rank cross-correlation coefficient and (b) Delay (τ) of Peak Spearman rank cross correlation as a function of v_{sw}. In (b), the dashed green line indicates a robust fit and the panel's insert provides the functional form, fit parameters, and quality metrics. A positive delay indicates that changes in SSN precede changes in $\mathrm{A_{He}}$. 28

2.3 Helium abundance ($\mathrm{A_{He}}$) as a function of (a) observed and (b) delayed SSN in one example v_{sw} quantile. A line connects the points to aid the eye. Line and marker color correspond to the number of days since mission start. Marker shape matches the quantile in previous figures. This v_{sw} quantile covers the range $347\ \mathrm{km\,s^{-1}} < v_{\mathrm{sw}} \leq 363\ \mathrm{km\,s^{-1}}$. A green, dashed line presents a robust fit to each trend. The insert at top of each panel gives the function fit, fit parameters, and quality metrics. Delaying SSN by the phase offset appropriate to this v_{sw} quantile reduces the impact of the hysteresis effect, as the increase in delayed R^2 indicates. That χ^2_ν is closer to unity in (b) indicates that a linear model better describes $\mathrm{A_{He}}$ as a function of delayed SSN. 29

2.4 A summary of the zero solar activity helium abundance, $\mathrm{A_{He}}(\mathrm{SSN} = 0)$, as a function of v_{sw} for all robust fits in the fashion of Figure 2.3. Error bars indicate the standard deviation of each quantity over the range in averaging windows $225 \leq N_{\mathrm{days}} \leq 275$, each centered on the $N_{\mathrm{days}} = 250$ value. Unfilled markers show all SSN. Filled markers show identical calculations with $\mathrm{SSN} < 25$. The black dashed curve is the relationship between $\mathrm{A_{He}}$ and SSN derived by Kasper et al. (2007). That repeating our calculation with a reduced range in SSN shows better agreement with the results of Kasper et al. (2007) indicates that our results, covering the full range of solar activity in cycles 23 and 24, are consistent with their results from the two year interval surrounding minimum 23. 31

3.1 An example of four look directions (top) and the corresponding velocity distribution function (VDF) (bottom) as measured by the *Wind*/SWE Faraday Cups on April 21, 2017. (Top) Clockwise, the four look directions are the direction most parallel to $\boldsymbol{B}$, most perpendicular to $\boldsymbol{B}$, most parallel to the proton core velocity, and most radial. Each panel also indicates θ_{Bn}, the angle between Faraday cup (FC) normal direction and the magnetic field. The bi-Maxwellian is fit in red and the isotropic is fit in blue. An anisotropic fit to the alpha particles is indicated in pink. (Bottom) Contours of the VDF marked with solid lines are 0.8, 0.6, 0.4, 0.2 and dashed lines are 0.1, 0.032, 0.01, 0.0031, 0.001 of the maximum phase space density, matching those in Marsch et al. (1982b). The marks at $\sim \pm 50\ \mathrm{km\,s^{-1}}$ are the local Alfvén speed. This figure is plotted in the proton core rest frame and the bottom of the figure indicates $\boldsymbol{v}_{p_1}$ in the GSE frame. 41

3.2 Four hour averages in Carrington rotation (CR) 2177. Panels (A) through (D) mark proton cores (X_1) in dashed green and proton beams (X_2) in solid orange. All Panels mark dashed green lines with circles and solid orange lines with squares at every 50th point. When no beam is measured, a gap is present. A two day interval surrounding two sector boundaries are highlighted in blue. Table 3.1 has select cross correlation coefficients for plotted quantitites. 43

3.3 A histogram of the solar wind speed (v_{sw}) from $250\,\mathrm{km\,s^{-1}}$ to $800\,\mathrm{km\,s^{-1}}$. The solar wind speed is calculated as the magnitude of the plasma velocity center-of-mass frame. The most common solar wind speed is $376\,\mathrm{km\,s^{-1}}$. The mean solar wind speed is $437\,\mathrm{km\,s^{-1}}\ \pm 100\,\mathrm{km\,s^{-1}}$. 46

3.4 Significant quantities as a function of solar wind speed (v_{sw}) for bins with at least 5 measurements are shown. Bins are $10\ \mathrm{km\,s^{-1}}$ wide. Every 5th to 7th bin and, in all Panels but (F), its standard deviation is marked for aesthetic clarity. Note Panel (E) uses $\mathrm{stdev}/3$. As a boolean's standard deviation does not represent a typical range of values in a manner suited to this figure, Panel (F) excludes them. Tables 3.2 and 3.3 summarizes these trends in fast, intermediate, and slow wind. 48

3.5 Plasma stability in the reduced parameter $(\beta_{\parallel;s}, R_s)$ plane for both the proton core (p_1, indicated in color) and protons from a single bi-Maxwellian model (p, contours). Stability is calculated at the growth rate $\gamma/\Omega_p = 10^{-2}$ for a plasma that includes one proton population. The lowest level shown (solid cyan) is the outer edge of the proton core distribution. From lowest to highest, the other levels shown are are 0.01, 0.1, 0.3, 0.7, 0.99. All but the the 99% level are labelled. The 99% level indicates the single population distribution and is located at $(\beta_{\parallel;p}, R_p) = (0.83, 0.61)$. 50

3.6 The PDF of the relative beam fraction calculated such that the fit normalizes to 1. The PDF of the automated fits is shown in black with error bars smaller than the line. Green indicates the subset fit and is marked by plusses at every 10th bin. The orange solid line is the fit to the green curve. The manual fit PDF (labelled MF) is shown in dashed gray with uncertainties as error bars that are approximately the line width. Using the area between the empirical PDF and fit, we estimate that $974,485 \pm 65,258$ proton beams are unresolved. 53

3.7 2D Plots comparing (a) the proton core and (b) the total proton number density from the two-population fits to the proton density from the single population fit. Only bins with at least 10 counts are shown. The top in each case is the PDF and the bottom is column normalized version of the 2D histogram to emphasize the trend. The solid green line indicates unity. The dashed green line indicates the average of the two-population quantity in the column defined by the single-population fit; every 5th bin is marked with an unfilled plus. Gray regions indicate the standard deviation around the dashed green trend. A robust fit using the standard deviations as weights is given with a dash-dash-dot blue line. The text insert indicates the fit parameters and their uncertainties. The fits and trends in a given top and bottom pair of panels are identical. . . . 60

3.8 2D Plots comparing (a) the proton core and (b) the total proton center-of-mass velocity's x-component from the two-population fits to the parallel proton temperature from the single population fit. Figure style follows Figure 3.7 61
3.9 2D Plots comparing (a) the proton core and (b) the total proton center-of-mass velocity's y-component from the two-population fits to the parallel proton temperature from the single population fit. Figure style follows Figure 3.7 62
3.10 2D Plots comparing (a) the proton core and (b) the total proton center-of-mass velocity's z-component from the two-population fits to the parallel proton temperature from the single population fit. Figure style follows Figure 3.7 63
3.11 2D Plots comparing (a) the proton core and (b) the total proton parallel temperature from the two-population fits to the parallel proton temperature from the single population fit. Figure style follows Figure 3.7 64

4.1 Fits from four example look directions from the *Wind* Faraday cups using a new data processing algorithm. Three ion populations are shown: α (purple), p_1 (red), and p_2 (blue). The angle of a given look direction with respect to the average magnetic field throughout the spectrum is indicated in the top right of each panel. Errors for each Energy/charge bin are vertical dashed lines. 70
4.2 VDFs corresponding to the spectrum shown in Fig. 4.1. The joint proton VDF is shown on (top) and the α particle VDF is shown on (bottom). The proton beam can be identified by the secondary shoulder with a large $v_\parallel$ in (top) plot. Contours follow Marsch et al. (1982b). In decreasing order, solid lines are 0.8, 0.6, 0.4, 0.2 and dashed lines are 0.1, 0.032, 0.01, 0.0031, 0.001 of the maximum phase space density. 71
4.3 Normalized Alpha particle (α, p_1) and proton beam (p_2, p_1) differential flow in collisionless, fast solar wind. Both differential flows are normalized by an Alfvén speed approximation from Eq. 4.2 using both proton densities. Bins within 30% of the maximum are selected for fitting to exclude core-halo distributions. 74
4.4 A 2D histogram showing uncorrelated differential flow fluctuations $(\delta\Delta v)$ for $\Delta v_{\alpha,p_1}$ and $\Delta v_{p_2,p_1}$. That the fit is a circle centered on the origin indicates that the fluctuations are uncorrelated. 75
4.5 2D histograms of α particle and p_2 Alfvén speed normalized differential flow each as a function of its collisional age. Only bins with at least 30% of the a column maximum are shown. Measurements with a collisional age $A_c \lesssim 1.2 \times 10^{-2}$ is indicated to the left of the blue line. 77
4.6 The ratio of alpha particle to proton beam differential flow $(\Delta v_{\alpha,p_1}/\Delta v_{p_2,p_1})$ in collisionless ($10^{-2} \leq A_c \leq 10^{-1}$, dashed) and the youngest measured data ($10^{-2} \leq A_c \leq 1.2 \times 10^{-2}$, solid). 79
4.7 Examples of the Gaussian fits to 1D distributions of α and p_2 normalized differential flow along with the associated residuals. As discussed in Section 4.7, the Alvén speed normalizations shown minimize the width of these distributions. 82

4.8 Example α-particle and p_2 normalized differential flow illustrating the impacts of various Alfvén speed approximations. In both cases shown, inclusion of the proton core anisotropy (Eq. 4.3) reduces the width in comparison to the isotropic Magnetohydrodynamics (MHD) Alfén speed (Eq. 4.2), while including the anisotropy and the dynamic pressure ($p_{\tilde{v}}$) increases it. 84
4.9 Trends of 1D fits to $\Delta v_{\alpha,p_1}/C_A$ and $\Delta v_{p_2,p_1}/C_A$ as a function of A_c. Error bars are the Widths of the 1D fits. Each trend has been fit and the parameters are shown in the appropriate insert. While $\Delta v_{\alpha,p_1}$ markedly decays with increasing A_c, $\Delta v_{p_2,p_1}$ is relatively constant with A_c. To within the fit uncertainty, proton beams differentially stream at approximately the local Alfvén speed. 86

5.1 An example VDF from Solar Probe Cup (SPC). This figure averages over several SPC spectra so as to accentuate the VDF's structure. 93
5.2 An overview of SPC measurements taken during 1st encounter (E1) that include a proton beam averaged into 2 hour intervals. Each column has been normalized to its maximum value and the mode in each column (most common bin) is over plotted in green. From top to bottom, the panels plot (A) the magnetic field magnitude, (B) proton moment specific entropy, (C) proton core specific entropy, (D) proton core number density, (E) proton core speed, and (F) proton core temperature. 98
5.3 An overview of SPC proton beam measurements taken during E1 averaged into 2 hour intervals. The format follows Figure 5.2. From top to bottom, the panels plot (A) proton beam abundance A_{p_2}, (B) proton beam-core drift $\Delta v_{p_2,p_1}$, (C) Alfvén speed C_A, (D) normalized drift $\Delta v/C_A$, and (E) both the number of spectra measuring a proton beam and the probability of measuring a proton beam in the same 2 hour interval. 100
5.4 Proton core number density PDFs for events S1 to S6 (colors), the full 1st encounter (dash, dot, dot black with unfilled *X*), and low solar activity data from the *Wind* spacecraft at 1st Earth-Sun Lagrange Point (L1) (solid black, unfilled *X*). 102
5.5 Proton beam number density PDFs in the format of Figure 5.4. 103
5.6 Proton beam abundance PDFs in the format of Figure 5.4. 104
5.7 Proton core speed PDFs in the format of Figure 5.4. 104
5.8 Proton beam speed PDFs in the format of Figure 5.4. 105
5.9 Proton core temperature PDFs in the format of Figure 5.4. To facilitate comparison between the near-Sun and L1 measurements, we utilize the parallel component of the L1 temperatures. 106
5.10 Proton beam temperature PDFs in the format of Figure 5.4. For the L1 proton beams assigned the bi-Maxwellian temperature, the parallel component is used. 107
5.11 Proton beam-to-core temperature ratio PDFs in the format of Figure 5.4. To facilitate comparison between the near-Sun and L1 measurements, we utilize the parallel component of the L1 temperatures. 108
5.12 Proton beam-core differential flow PDFs in the format of Figure 5.4. 109
5.13 Alfvén speed PDFs in the format of Figure 5.4. 109

5.14 Proton beam-core Alfvén speed normalized differential flow PDFs in the format of Figure 5.4. 110
5.15 Coulomb number PDFs in the format of Figure 5.4. 111

6.1 The probability of measuring a proton beam in the $(\beta_\parallel, R)$ plane defined for (Top) p (Kasper et al., 2006) and (Bottom) p_1 (Chapter 3). The instability contours are derived by Verscharen et al. (2016) for a single bi-Maxwellian proton population. As such, they are formally only applicable to the (Top) panel and are included on the (Bottom) panel primarily for reference. The green contour indicates the alternate panel's distribution of beam-containing measurements. 121
6.2 Proton beam-core differential flow $(\Delta v_{p_2,p_1}/C_{A;p_1+p_2})$ as a function of modified proton core beta $(\tilde{\beta}_{p_1})$ from SPC. The 2D histogram indicates column normalized number of counts in each bin. The orange line with unfilled squares indicates the trend from Tu et al. (2004) derived with Helios 2 data over the range $0.1 \leq \beta \leq 1.0$ (gray band on the lower edge of the plot). The dark blue lines indicate 1D Gaussian fits to $\tilde{\beta}_{p_1}$ in each column with error bars indicating the standard deviation from each fit. The red line with unfilled plusses indicates a fit to the trend of the blue fits, both in the style of Figure 4.9. The insert gives the fit trend fit parameters and the associated fit uncertainties. The DG curves present a theoretical instability threshold (Daughton and Gary, 1998) that depends both modified plasma beta and beam density fraction $(n_{p_2}/n_{p_1+p_2})$. The light blue or cyan line marked with open diamonds (DG $\bar{n}$) uses the average of all $(n_{p_2}/n_{p_1+p_2})$ measurements to calculate the threshold. The fuchsia or pink line marked with open circles (DG $n(\tilde{\beta})$) uses the average of $(n_{p_2}/n_{p_1+p_2})$ in each $\tilde{\beta}_{p_1}$ column to calculate the threshold. 124
6.3 The PDF of measurements in the canonical $(\beta_\parallel, R)$ plane defined for the bulk or core (p_1) protons derived from automated fitting algorithms. The species identified in the 557 manual fits are plotted on top of the 2D PDF. Verscharen et al. (2016) derives the plotted instability contours accounting for a single bi-Maxwellian proton population. As such, these contours must be interpreted with caution and primarily used as reference when comparing them with a two-proton population data set. 126
6.4 (a) Maximum and (b) Median non-zero growth rates $\gamma_{\max}/\Omega_{p_1}(\vec{k}\rho_{p_1})$ along with (c) Probability $\gamma_{\max}/\Omega_{p_1} > 0$. (Top) All 557 manually fit spectra. (Others) Three of the five $(\beta_{\parallel;p_1}, R_{p_1})$ regions defined by Verscharen et al. (2016) for which there are more than 5 spectra. The top right corner of each panel identifies the region to which it belongs. 128
6.5 The maximum growth rate for each of the 557 manual fits plotted over the automated fits in the canonical $(\beta_\parallel, R)$ plane. Instability contours are identical to Figure 6.3 and the same caveats apply. 132

A.1 Two plots of beam abundance ($A_{p2/p1}$) as a function of time and solar wind speed (v_{sw}). Following the style of Alterman and Kasper (2019), v_{sw} is split into 10 quantiles and averages are taken in $250\,\mathrm{day}$ wide bins. The 13-month smoothed sunspot number (SSN) is plotted on the secondary y-axis in dashed black. The legend indicates the middle of the v_{sw} quantile and the Spearman rank cross correlation coefficient between $A_{p2/p1}$ and SSN ($\rho(A_{p2/p1}, \mathrm{SSN})$) for that quantile. The symbol separating the two is $\rho(A_{p2/p1}, \mathrm{SSN})$'s sign. Marker color and symbol identify the v_{sw} quantile. The (top) panel treats missing beams as if $n_{p_2} = 0$ in the $A_{p2/p1}$ averages. The (bottom) panel only averages spectra for which $n_{p_2} > 0$. Note that top panel uses unfilled markers to signify that $n_{p_2} = 0$ is used. The bottom panel uses partially transparent and filled markers to signify that $n_{p_2} > 0$. 143

A.2 A summary of the cross correlation coefficient between $A_{p2/p1}$ and SSN ($\rho(A_{p2/p1}, \mathrm{SSN})$) as a function of its v_{sw} quantile. The marker colors, symbol, and fill follow Figure A.1 to identify the v_{sw} quantile and manner in which the averaging treated missing beams. 145

LIST OF TABLES

1.1 Cross correlation coefficients ρ between of quantities Q plotted from Figure 1.1 Panels (A) through (D) with SSN plotted in Panel (E). In all cases except $P_{\Delta v}/P_{\mathrm{th}}$, $|\rho(Q, \mathrm{SSN})| > 0.7$ is highly significant. In the case of $P_{\Delta v}/P_{\mathrm{th}}$, the lack of anti-correlation is likely due to the peak during 2003. 10

1.2 Relative collision frequencies (ν) and times (τ) directly from Callen (2006, Table (2.1)) and normalized to the slowing down time (momentum exchange rate). 11

3.1 Select cross correlation coefficients from Fig. 3.2 Panels (A) through (F). . . . 46

3.2 Average properties for one-population (p) and two-population proton fits (core: p_1, beam: p_2), total: $p_1 + p_2$) in Slow ($v_{\mathrm{sw}} \leq 400\ \mathrm{km\,s^{-1}}$), Intermediate ($400\ \mathrm{km\,s^{-1}} < v_{\mathrm{sw}} \leq 600\ \mathrm{km\,s^{-1}}$), and Fast ($600\ \mathrm{km\,s^{-1}} < v_{\mathrm{sw}}$) solar wind. The total parallel thermal speed is calculated as the geometric mean of the two thermal speeds, in effect reporting the total proton temperature in $\mathrm{km\,s^{-1}}$. The ratio of the beam to core quantity (p_2/p_1) is also given for each solar wind speed interval. Standard deviations are used to indicate a typical range around the average value. 55

3.3 Average properties of quantities specific to two-population fits in Slow ($v_{\mathrm{sw}} \leq 400\ \mathrm{km\,s^{-1}}$), Intermediate ($400\ \mathrm{km\,s^{-1}} < v_{\mathrm{sw}} \leq 600\ \mathrm{km\,s^{-1}}$), and Fast ($600\ \mathrm{km\,s^{-1}} < v_{\mathrm{sw}}$) solar wind. Standard deviations are used to indicate a typical range around the average value. As the standards deviation of a boolean is ill-suited to defining the typical range of probability values, it is excluded from $\mathrm{Prob(Beam)}$ and $\mathrm{Prob(Bimax)}$. 56

3.4 The the total number of measurements (N_{spec}), number of proton beam measurements (N_{p_2}), and percentage of measurements in Slow ($v_{\mathrm{sw}} \leq 400\ \mathrm{km\,s^{-1}}$), Intermediate ($400\ \mathrm{km\,s^{-1}} < v_{\mathrm{sw}} \leq 600\ \mathrm{km\,s^{-1}}$), and Fast ($600\ \mathrm{km\,s^{-1}} < v_{\mathrm{sw}}$) solar wind where information for from Helios (Marsch et al., 1982b; Ďurovcová et al., 2019), $\mathrm{Ulysses}$ (Matteini et al., 2013), and *Wind* (this paper). The Helios data from Marsch et al. (1982b) is taken from their Fig. (13). The Helios data marked with a dagger (†) is from a recently reprocessed dataset (Ďurovcová et al., 2019) and only provide the percentage of spectra that report a proton beam. (Units are marked accordingly.) The $\mathrm{Ulysses}$ numbers are approximate as those are the values provided by Matteini et al. (2013). Omitted information in Helios or $\mathrm{Ulysses}$ data is not available in the cited sources. . . . 58

4.1 All fit parameters and their uncertainties in the manner calculated in Figure 4.7. The column indicates the parameter (Mean Value or Width) for a given differentially flowing species. The row indicates the wave speed normalization. The bold, colored row is the preferred normalization. Anisotropic Alfvén speeds including the dynamic pressure term from Eq. 4.3 are indicated by $(p_{\tilde{v}})$. The average fit uncertainty on the Mean is 4×10^{-3} and the average uncertainty on Width is 5×10^{-3}. Normalizations marked with an asterisk (*) are plotted in Figure 4.8. 83

5.1 The six E1 SPC events selected for study, labeled S1 to S6 according to when SPC chronologically encountered each. Each event occurred during November, 2018. The Start and End times are given as Day of Month Hour:Minute. The last column identifies the total duration of each event. Only events lasting at least 18 hours and at least 3,500 proton beam spectra were selected. 97

5.2 Means and standard deviations of significant proton beam quantities for each of the events. Averages of log-normally distributed quantities (n, T, & N_c) are taken in log space and converted back to report easily interpretable numbers. Means are only reported to the most significant digit of the standard deviation. Blank quantities are not measured in a given event. In addition to statistics reported in Figures 5.4 to 5.14, we also report the Coulomb Number (N_c), radial distance from the Sun, and location in Carrington coordinates for most measurements. In the case of *Wind*/SWE, we do not report the Carrington latitude ($\lambda_{\mathrm{Carrington}}$) and longitude ($\phi_{\mathrm{Carrington}}$) because the Solar Wind Experiment (SWE) data is collected over the course of > 20 years and the measurements cover the full set of possible longitudes and a continuous range of near-equatorial latitudes. The last two rows provide the total number of proton beam measurements and the probability of measuring a proton beam in each interval. The probability is calculated as the fraction of the measurements during the specified time interval that contain a proton beam. 112

6.1 The number of manually fit spectra in each of Figure 6.3's $(\beta_{\parallel;p_1}, R_{p_1})$ regions. 125

6.2 Statistics regarding the maximum unstable growth rate ($\gamma_{\max}/\Omega_{p_1}$) in each of the five regions of the $(\beta_{\parallel,p_1}, R_{p_1})$ plane defined by the instability contours derived by Verscharen et al. (2016) and the entire plane (Global). The median growth rate only accounts for those spectra with $\gamma_{\max}/\Omega_{p_1} > 0$. The probability is the fraction of non-zero $\gamma_{\max}/\Omega_{p_1}$ in units of percent. The count is the number of spectra with $\gamma_{\max}/\Omega_{p_1} > 0$. As there are only 5 spectra beyond the fast magnetosonic / whistler (FMW) threshold (See Table 6.1), the two corresponding regions are not independently tabulated outside of the *Global* column. 127

A.1 The cross correlation coefficient between A_{p_2/p_1} and SSN for each of ten v_{sw} quantiles plotted in Figure A.1. *All* refers to the top panel in the figure for which $n_{p_2} = 0$ missing beams are included in the averages. The $n_{p_2} > 0$ row refers to the bottom panel that excludes these spectra. 146

LIST OF ABBREVIATIONS

AC alternating current

ACE Advanced Composition Explorer

AIC Alfvén ion cyclotron

AR active region

CDAweb Coordinated Data Analysis Web

CH coronal hole

CIR corotating interaction region

CR Carrington rotation

DC direct current

DKIST Daniel K. Inouye Solar Telescope

E1 1st encounter

ESA electrostatic analyzer

FC Faraday cup

FIP first ionization potential

FMW fast magnetosonic / whistler

GSE Geocentric Solar Ecliptic

HCS Heliospheric Current Sheet

HV high voltage

ICME interplanetary coronal mass ejection

IMF interplanetary magnetic field

IMP Interplanetary Monitoring Platform

KS test Kolmogorov-Smirnov test

L1 1st Earth-Sun Lagrange Point

LTE local thermodynamic equilibrium

MEC Maxwell's Equation of Change

MFI Magnetic Field Investigation

MHD Magnetohydrodynamics

MM mirror mode

OFI oblique firehose

PDF Probability Distribution Function

PIC Particle-in-Cell

PSP Parker Solar Probe

SNR signal-to-noise ratio

SPAN Solar Probe Analyzer

SPC Solar Probe Cup

SPDF Space Physics Data Facility

SSN sunspot number

SWE Solar Wind Experiment

SWEAP Solar Wind Electrons, Alphas, and Protons

SWICS Solar Wind Ion Composition Spectrometer

SXR soft X-ray flux

SolO Solar Orbiter

VDF velocity distribution function

ABSTRACT

The solar wind is a multiscale, near-collisionless plasma. Three significant timescales are decades, days, and seconds. These timescales are associated with the solar cycle, Coulomb collisions, and instabilities, respectively.

To low order, the solar wind can be treated as a sum of perturbations on a steady state background. The solar cycle drives long term variation in this background. Coulomb collisions and instabilities are two mechanisms that can locally drive some perturbations towards equilibrium states. They can also be modified by the perturbations themselves.

In this thesis, I explore one aspect related to each of these timescales. In the process, I describe proton beams, a subset of solar wind protons that constitute a perturbation on the bulk or core protons. I then illustrate how the presence of a proton beam can impact a prototypical characterization of instabilities. I close by showing how proton beams vary with solar cycle and point to the necessity of describing the multiscale feedback mechanisms that must be disentangled to properly characterize a proton beam.

CHAPTER 1

Introduction

1.1 History and Background

Solar eclipses have been observed since at least 1223 B.C.E. (De Jong and Van Soldt, 1989). They provide evidence that the Sun is not a static, perfectly spherical body, but covers some extent beyond its visible disk. For at least 2000 years, transient and optically dark spots have been observed on the Sun's surface (Clark and Stephenson, 1978). The number of these spots has been known to follow an $\sim 11.7\,\mathrm{year}$ cyclic pattern called the solar cycle since at least 1844 (Hathaway, 2015). The Carrington event of 1859 was a markedly significant example that the Sun's transient behavior is geoeffective, or causes a magnetic event at Earth (Carrington, 1859; Hodgson, 1859). However, it is not until the 1900s or 1930s that these distinct observations began to synthesize.

In 1900, Max Planck (Planck, 1967a,b) derived the formula for blackbody radiation from which we know that the temperature at the Sun's visible surface or photosphere is $T_{\text{photo}} = 5600\,\mathrm{K}$ (Parker, 1997). From 1931 to 1949, a series of spectroscopic observations of the Sun and laboratory experiments revealed that the temperature in the solar corona is on the order of $T_{\text{corona}} \sim 10^6\,\mathrm{K}$, an increase in two orders of magnitude over $\sim 2000\,\mathrm{km}$ from the photosphere through the chromosphere and into the corona (Miyamoto, 1949; Parker, 1997; Sakurai, 2017). By 1939, we understood that nuclear fusion provided the primary source of solar energy through the conversion of hydrogen into helium (Bethe, 1939; Bethe and Critchfield, 1938; Parker, 1997).

The developments that birthed the field we now know as space physics must be treated in greater detail. In 1908, Hale discovered that sunspots contain a magnetic field (Hale, 1908). From 1931 through 1940, Chapman and Ferraro (1931a,b, 1932a,b, 1933, 1940) first proposed that the Earth is continually bathed in some form of solar "corpuscular radiation". In 1937, Forbush provided evidence tying solar transient events (flares) to cosmic ray levels at Earth, further connecting solar transients to events at Earth (Forbush, 1937).[1] In 1957, Chapman proposed that the "corpuscular radiation" formed a hydrostatic corona (Chapman, 1957). The same year, Biermann (1957) inferred from cometary tail observations that this radiation or corona was non-static and Alfvén (1957) proposed that it must be a plasma carrying an embedded magnetic field.

In 1958, Parker synthesized these observations these observations into a unified theory. He proposed that the corona is non-hydrostatic, has a temperature on the order of $T \sim 10^6\,\mathrm{K}$, and carries an embedded magnetic field that follows the now-called Parker spiral (Parker, 1958). Parker (1960) showed that this non-hydrostatic corona must consist of a plasma that radiates away from the Sun at speeds that transition from subsonic to supersonic at some critical distance from the Sun R_c. This distance is now called the Alfvén point or Alfvén surface (Kasper and Klein, 2019; Kasper et al., 2017). Neugebauer and Snyder (1962) provided the first definitive in situ observations of this plasma using the *Solar Plasma Experiment* onboard Mariner II. They showed that this plasma contains both ionized hydrogen (protons, p) and what was consistent with fully ionized helium (alpha particles α); caries a now-described-as frozen-in magnetic field; and that the plasma's speed is greater than both the sound speed and the characteristic speed of the plasma, i.e. that it is both supersonic and super-Alfvénic. Today, we refer to this plasma as the *solar wind*.

Following these observations, Parker published a series of five papers (Parker, 1964a,b,c, 1965a,b) that expand on his theory. In order, they argue that:

1. The solar wind's speed is strongly driven by the temperature at the corona's base and the temperature's radial profile out to this critical distance R_c, which is on the order of a few solar radii R_s (Parker, 1964a).
2. The solar wind's heat flux is necessarily parallel to the local magnetic field and at least some fraction of the heat flux drives solar wind expansion (Parker, 1964b).
3. A non-homogenos corona that releases solar wind in a filamentary nature is consistent with the supersonic solar wind (Parker, 1964c).
4. Discrepancies between his own predictions and near-Earth solar wind observations may imply that additional heating above the critical point R_c is required and suggests it is due to wave dissipation (Parker, 1965a).
5. Similar to a static corona, an expanding one that generates a supersonic solar wind is stable (Parker, 1965b).

---

[1] These are now called *Forbush events*.

During the Apollo 11 moon landing, Neil Armstrong and Buzz Aldrin deployed the Solar Wind Composition experiment (Buhler et al., 1969). This experiment consisted of a vertically oriented, solar facing sheet of aluminum foil that collected solar wind ions and was returned to Earth. Using these solar wind samples, Buhler et al. (1969) confirmed that the solar wind caries helium, thereby tying the solar wind to the processes that form the source of the Sun's energy.

Today, we know that the solar wind is a hot, tenuous, magnetized, nearly collisionless[2], and multi-species plasma continuously emitted by the Sun. It is made up of ions, electrons, and an embedded magnetic field that carry mass, momentum, and energy. In effect, the solar wind suffuses and defines the local region of space called the heliosphere.

Yet there are many open questions. While the overarching consensus is that the Sun's magnetic field is generated by its dynamo, "nothing resembling consensus exists regarding the detailed nature and relative importance," of the physical processes involved (Charbonneau, 2005). While much research indicates that the processes by which magnetic field convect and emerge through the Sun may heat the solar plasma (Cheung and Isobe, 2014; Stein, 2012), we do not know how the corona or solar wind are heated to their observed temperatures (Fox et al., 2015; Klimchuk, 2015). In other words, we do not know how solar plasma transported from the photosphere up to the critical point R_c. Nor do we understand how the plasma temperature at the Sun increases from $T_{\text{photo}} \sim 5600\,\text{K}$ in the photosphere through the $\sim 2000\,\text{km}$ thick chromosphere to between $T_{\text{corona}} \sim 10^6\,\text{K}$ and $T_{\text{corona}} \sim 2.5 \times 10^6\,\text{K}$ in the corona.

In situ solar wind observations may provide insight. Belcher and Davis (1971); Belcher et al. (1969) observed large amplitude, non-dispersive MHD Alfvén waves carried by the solar wind in near-Venus Mariner 5 data. Alfvén waves are also observed near-Earth (Steinberg et al., 1996) and beyond $5\,\text{AU}$ (Goldstein et al., 1995). In situ observations show that turbulence related to these waves decays as the solar wind propagates away from the Sun (Bruno and Carbone, 2013; D'Amicis et al., 2010). Yet even with this insight, how these waves dissipate along with how and where they heat and accelerate solar wind ions and electrons is still a mystery.

That the solar wind is a multi-species, nearly collisionless, and magnetized plasma implies multiple timescales must be disentangled to unravel this physical mystery. Because the solar wind is magnetized, the charged particles experience cyclotron resonances that break simple spherical symmetry and introduce magnetic timescales. Because the solar wind is nearly collisionless, kinetic and fluid or magnetohydrodynamic (MHD) scale effects are simultaneously significant–neither can be treated as negligible. On kinetic scales

---

[2] See Section 1.3.

that are of the order of several gyroradii or the plasma frequency, the solar wind must be studied in terms of the distribution of particles as a function of both position and velocity. For any given position or configuration, the variation of this distribution as a function of velocity parallel and perpendicular to the magnetic field is called the velocity distribution function (VDF). Interactions between charged particles (Coulomb collisions) along with charged particles and the magnetic field can produce highly non thermal structure in the VDF (Marsch, 2006). Yet, collisions do not independently dissipate these non-equilibrium or non-local thermodynamic equilibrium (LTE) features (Verscharen et al., 2019). Microinstabilities, which are further complicated by the solar wind's multi-species nature, contribute as well (Gary, 1993; Verscharen et al., 2019). Figure 24 in Verscharen et al. (2019) illustrates how these magnetic, collisional, and kinetic mechanism feedback onto each other. Further tangling the picture is the solar cycle: the magnetic inputs thought to heat the corona and solar wind along with the types of surface and coronal features associated with the solar winds release (solar wind sources) vary cyclically every $\sim 11.7\,\mathrm{years}$ (Hathaway, 2015).

The solar wind is composed of 95% protons and 4% alpha particles. This thesis leverages a unique feature of the solar wind that cannot be measured in any laboratory nor astrophysical plasma. The proton VDF can split in two, containing a core and beam population each of which appears Maxwellian within a few thermal widths of its peak, but with a differential flow between them that can be large (Marsch et al., 1982b).[3] This thesis utilizes these three ion populations to sensitively test how wave-particle coupling and dissipation impact the solar wind's evolution and its multi-scale nature by studying how proton beam properties change with time over a wide range of solar wind timescales, from the $11.7\,\mathrm{year}$ solar cycle through Coulomb collisions and down to kinetic and instability timescales.

The remainder of this chapter proceeds as follows. Section 1.2 defines the solar cycle and demonstrates the variation of various parameters related to the different time scales with solar activity. Section 1.3 summarizes the significance of Coulomb collisions and illustrates one non-LTE feature that they dissipate. Section 1.4 then points to the significance of local regulation of proton beams during the solar wind's evolution. Specifically, Section 1.4.1 foreshadows early indications that Coulomb collisions may only regulate proton beams after the plasma has reached a collisionality beyond a certain threshold. Section 1.4.2 reviews the theory of instabilities, identifies key results related to alpha particles, and points towards future work on kinetic processes that may regulate proton beam-core drifts.

---

[3] While alphas can exhibit a similar two-population behavior (Marsch et al., 1982a), such a study is beyond the current scope and this these treats them as a single population.

1.2 The Sun and Solar Cycle's Impact on the Solar Wind

The solar dynamo drives the solar cycle, the ~ 11.7 year (Hathaway, 2015) cycle over which the polarity of the Sun's magnetic field is known to rotate with respect to the Sun's spin axis. Sunspots are localized, optically dark regions on the surface of the Sun that appear, "where the most concentrated magnetic field bundles cross the photosphere..." (van Driel-Gesztelyi and Green, 2015). They are characterized by strong magnetic fields (Thomas and Weiss, 2008), range in size from around $3500\ \mathrm{km}$ to $60000\ \mathrm{km}$ (Thomas and Weiss, 2008), and typically persist for weeks (Rempel and Schlichenmaier, 2011).

In 1844, Schwabe observed that the number of sunspots or SSN followed an approximately $10\,\mathrm{year}$ cycle. In 1919, Hale et al. connected sunspots to the solar cycle (Hale et al., 1919). Today, the SSN provides the longest duration observations of this solar cycle (Hathaway, 2015) over which the dominant component of the Sun's dynamo field switches polarity. One cycle is defined by the time period over which SSN increases from zero to a maximum value and returns again to zero (Hathaway, 2015). While sunspots generally appear at midlatitudes, the latitude at which they emerge progressively approaches–and does not cross–the solar equator through the course of the solar cycle (Maunder, 1903, 1904).[4] As the solar dynamo drives the solar cycle, the photosphere, chromosphere, transition region, and corona respond to the cycle as well. In turn, these changes impact surface features on the Sun that have been otherwise categorized into various solar wind source regions such that in situ solar wind measurements reflect the solar cycle (Hirshberg, 1973; McComas et al., 2008) .

Broadly, there are three primary classes of source regions on the Sun: coronal holes (CHs), active regions (ARs), and the streamer belt. Remote observations of these source regions provide clear delineations between all three. In situ signatures lay on a more opaque continuum providing clear differentiation between CH and streamer belt plasma, but less a clear distinction between streamer belt and AR solar wind. Note that the following focuses exclusively on ion properties and neglects electrons.

CHs were first quantitatively observed by Waldmeier (1956, 1975) (Cranmer, 2009). They are characterized by a strong unipolar magnetic field that expands radially outwards from the Sun (Cranmer, 2009; Schwenn, 2006a). During solar minimum, there are typically two CHs confined to the solar poles; during solar maximum, CHs are also present at lower latitudes.

CHs are the source of fast solar wind (Krieger et al., 1973), nominally $v_{\mathrm{sw}} \gtrsim 600\ \mathrm{km\,s^{-1}}$. In situ observations show that CH solar wind tends to be relatively steady state; have a

---

[4] This is commonly referred to as Spöerer's Law (Maunder, 1903).

low density, high temperature, and low heavy ion charge states; carry predominantly outward flowing Alfvén waves; have a high proton and alpha particle specific entropy; contain plasma with abundances similar to those observed in the photosphere, including a high helium abundance; carry low charge state ratios; have large alpha-proton drift speeds; carry ions with velocity fluctuations that are well correlated with magnetic field fluctuations (high cross helicity, σ_c); have hotter alpha particles than protons; experience relatively few interparticle Coulomb collisions over its propagation; and tends to present VDFs with more nonthermal structure (Aellig et al., 1999; Alterman et al., 2018; Asbridge et al., 1976; Bame et al., 1977; Cranmer, 2009; D'Amicis and Bruno, 2015; Damicis et al., 2016; D'Amicis et al., 2019; Fu et al., 2018; Kasper et al., 2008; Schwenn, 2006a,b; Verscharen et al., 2019; von Steiger et al., 2000; Xu and Borovsky, 2015; Zhao et al., 2017; Zurbuchen, 2007; Zurbuchen et al., 2012). When fast solar wind of this type overruns slow solar wind, the resulting corotating interaction region (CIR) likely to induce a geomagnetic storm (Cranmer, 2009; Schwenn, 2006b).

Waldmeier (1955) provided the first observations of the streamer belt. It is characterized by a localized collection of closed loops that encircles the Sun. The prototypical source of slow solar wind, it is a well-defined structure confined to a $\sim \pm 15^o$ band in colatitude around the solar equator during solar minimum (Eselevich and Eselevich, 2006). While the streamer belt is less well-defined during solar maximum, similar closed loop regions are still present. The streamer belt contains the Heliospheric Current Sheet (HCS) across which the interplanetary magnetic field (IMF) polarity changes (Schulz, 1973) and – excluding transient events – is magnetically closed to the heliosphere (Eselevich and Eselevich, 2006).

Though the streamer belt is magnetically closed to the heliosphere, it likely releases slow solar wind in an intermittent manner through interchange reconnection (Fisk, 1996; Fisk et al., 1999) or some other intermittent mechanism. Typical streamer belt solar wind is characterized nearly opposite that of CH-associated solar wind. It has a low proton speed, a large and variable first ionization potential (FIP) bias (i.e. non-photospheric abundances), high proton density, low temperatures, low alpha-proton drift speeds, high heavy ion charge states, equal alpha and proton temperatures, small cross helicity, high charge state ratios and low helium abundance (Abbo et al., 2016; Aellig et al., 1999; Asbridge et al., 1976; D'Amicis and Bruno, 2015; Damicis et al., 2016; D'Amicis et al., 2019; Fu et al., 2018; Schwenn, 2006a,b; von Steiger et al., 2000; Xu and Borovsky, 2015; Zhao et al., 2017; Zurbuchen, 2007; Zurbuchen et al., 2012). Streamer belt solar wind is typically collisionally dominated (Alterman et al., 2018; Kasper et al., 2008; Verscharen et al., 2019).

ARs are localized areas on the solar surface known to be coincident with increases in soft x-ray flux, large solar flares, and sunspots (van Driel-Gesztelyi and Green, 2015). Van Driel-Gesztelyi and Green (2015) provides the following concise definition:

> Active regions are the totality of observable phenomena in a 3D volume represented by the extension of the magnetic field from the photosphere to the corona, revealed by emissions over a wide range of wavelengths from radio to X-rays and γ-rays (only during flares) accompanying and following the emergence of strong twisted magnetic flux ($\mathrm{kG}, \geq 10^{20}\,\mathrm{Mx}$) through the photosphere into the chromosphere and corona... The magnetic field of ARs is a defining factor of the interplanetary magnetic field, thus their influence extends well beyond the solar corona.

Hathaway (2015) succinctly connects ARs and the solar dynamo:

> In the Babcock model [of the dynamo], the polar field at minimum is representative of the poloidal field that is sheared out by differential rotation to produce the toroidal field that erupts as active regions during the following cycle. Diffusion of the erupting active-region magnetic field and transport by the meridional flow (along with the Joy's Law tilt of these active regions) then leads to the accumulation of opposite polarity fields at the poles and the ultimate reversal of the polar fields...

As such, it may be unsurprising that ARs are, "the principle source of," (van Driel-Gesztelyi and Green, 2015) phenomena driven by the solar cycle. As with sunspots, AR emergence follows Spörer's law and the canonical butterfly diagram: the colatitude at which they emerge starts around $\sim 35^o$ at the beginning of a solar cycle and progressively decreases as the cycle advances (Fan, 2004; van Driel-Gesztelyi and Green, 2015).

Although AR and streamer belt solar wind are typically classified as slow solar wind[5], AR wind caries some signatures that are more similar to typical fast or CH wind than slow streamer belt wind. Recent results attempt to differentiate between the two categories or classes of slow wind. D'Amicis and Bruno (2015); Damicis et al. (2016); D'Amicis et al. (2019) show that σ_c is higher in AR solar wind than streamer belt; caries a constant magnetic field magnitude; has intermediate proton temperatures and charge states; and is collisionally younger. D'Amicis et al. (2019) also report that Alfvénic slow wind that may originate from ARs caries a thermal speed less than the Alfvén speed[6] and larger

---

[5] Nominally $v_{\mathrm{sw}} \lesssim 500\ \mathrm{km\,s^{-1}}$.

[6] $\beta = \frac{n_{p_1} k_B T_{p_1,\parallel}}{B^2/2\mu_0} < 1$

anisotropy[7], along with differences in turbulence-related spectra. Stansby et al. (2019) suggest that AR slow wind carries a steady state mass flux that the streamer belt does not.

Perhaps these similarities between AR and CH solar wind should be expected. ARs are typically found near boundaries on the the edge of CHs. Given that ARs are driven by the solar cycle, the dominance of ARs or the streamer belt as a slow wind source may also follow this $\sim 11.7\,\mathrm{year}$ trend (Abbo et al., 2016). On faster timescales, slow wind's variability may be partially driven by treating solar wind from ARs and the streamer belt interchangeably.

Hirshberg (1973) first connected long-term solar wind variation to the solar cycle through the variation of the solar wind magnetic field's radial component B_r. Bulk solar wind measurements at $1\,\mathrm{AU}$ also show solar cycle variability. As the solar wind carries many drivers of geomagnetic activity, perhaps this relationship should be expected (Feynman, 1982).

Figure 1.1 presents the variation of several illustrative quantities as a function of solar cycle 23 and 24, the two most recent solar cycles. Panel (E) plots SSN for cycles 23 and 24, the two most recent solar cycles. Cycle 23 started on May 5th, 1996 and reached a maximum on April 1st, 2000. Cycle 24 started on December 12th, 2008 and reached a maximum on April 1st, 2014. Cycle 24 is in the declining phase, but has not yet ended. The remaining panels in Figure 1.1 presents the variation of various such quantities as a function of time, including

(A) magnetic field magnitude (B),

(B) helium and proton beam abundance[8],

(C) ratio of proton beam flux to core flux,

(D) beam-core differential flow[9] and drift energy fraction[10],

(E) and total proton plasma beta[11] and beam-to-core thermal pressure ratio.

To ensure that each curve captures its long timescale variation, it is smoothed using a 390

---

[7] Summing over species s, $R = \frac{n_s T_{s,\perp}}{n_s T_{s,\parallel}}$ is the ratio of temperature or pressure perpendicular to the magnetic field to the same quantity parallel to the local magnetic field. For a single species, pressure anisotropy and temperature anisotropy are trivially equal.

[8] Helium abundance is given by $A_{\alpha/p_1} = A_{\mathrm{He}} = 100 \times n_\alpha / n_{p_1}$. Proton beam abundance is $A_{p_2/p_1} = A_{p_2} = 100 \times n_{p_2}/n_{p_1}$.

[9] For species i and j, $\Delta \boldsymbol{v}_{i,j} = \boldsymbol{v}_i - \boldsymbol{v}_j$. See Chapter 3.

[10] The ratio of energy in the beam-core differential flow normalized to the total proton parallel pressure $P_{\Delta v}/P_{\mathrm{th}} = \frac{\mu \Delta v^2}{P_{\parallel,p_1} + P_{\parallel,p_2}}$ for reduced proton beam-core mass μ. See Chapter 3 for details.

[11] $\beta = \frac{n k_{\mathrm{B}} T}{B^2/2\mu_0}$, the ratio of thermal to magnetic pressure.

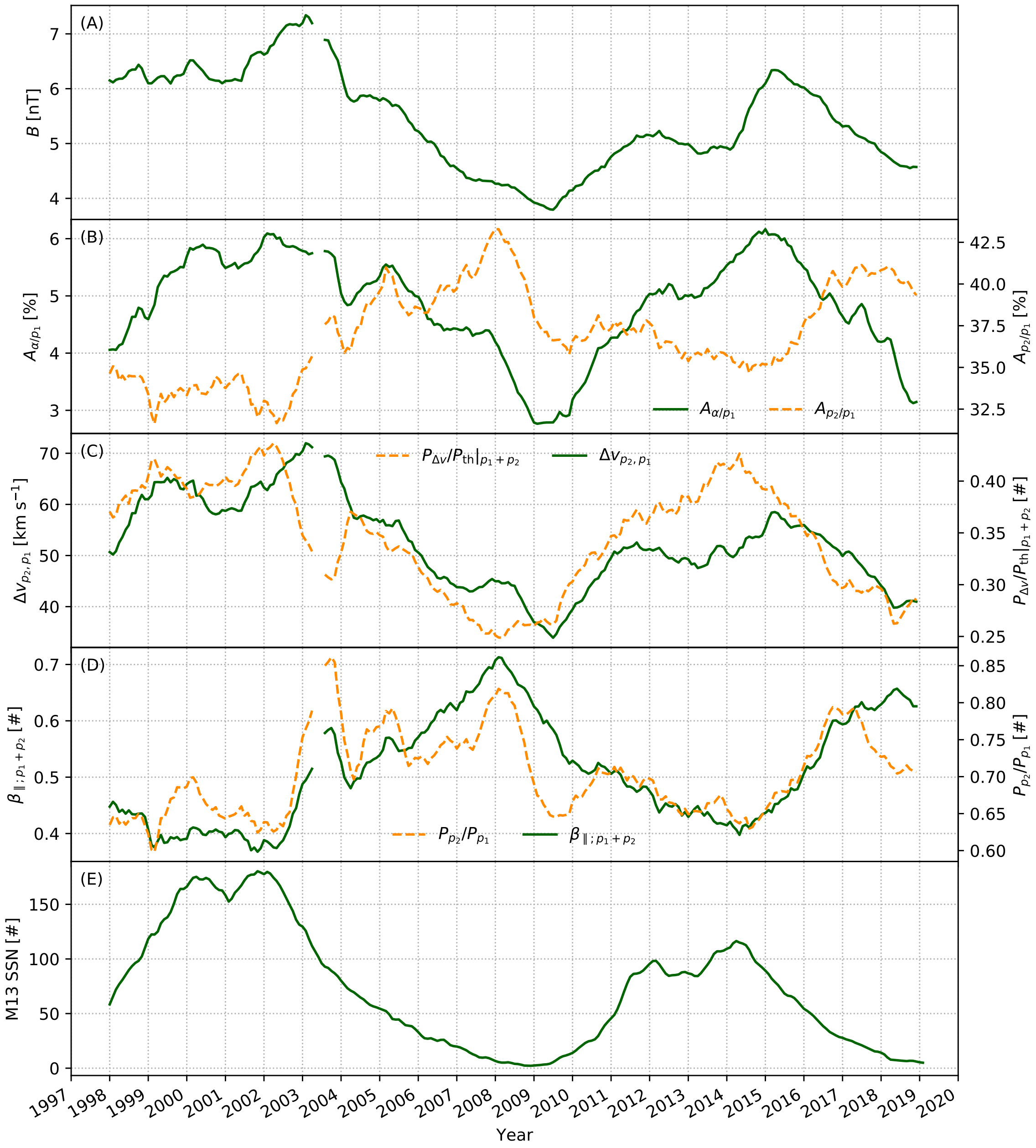

Figure 1.1: Bulk solar wind properties measured at 1 AU as a function of solar cycle. Properties presented are (A) magnetic field magnitude ($\boldsymbol{B}$), (B) helium abundance (A_{He}) and beam abundance ($\mathrm{A}_{\mathrm{beam}}$), (C) beam-core differential flow and drift energy fraction, and (D) total proton plasma beta and beam-to-core thermal pressure ratio. Panel (E) shows the 13 month smoothed SSN. Table 1.1 gives the cross correlation coefficient ρ between each quantity Q in Panels (A) through (D) with SSN.

Quantity Q	A_{α/p_1}	A_{p_2/p_1}	B	$P_{\Delta v}/P_{\text{th}}$	P_{p_2}/P_{p_1}	$\Delta v_{p_2,p_1}$	$\beta_{\parallel;p_1+p_2}$	$\frac{\text{flux}_{p_2}}{\text{flux}_{p_1}}$
$\rho(Q, \text{SSN})$	0.756	-0.855	0.772	0.886	-0.533	0.802	-0.888	-0.822

Table 1.1: Cross correlation coefficients ρ between of quantities Q plotted from Figure 1.1 Panels (A) through (D) with SSN plotted in Panel (E). In all cases except $P_{\Delta v}/P_{\text{th}}$, $|\rho(Q, \text{SSN})| > 0.7$ is highly significant. In the case of $P_{\Delta v}/P_{\text{th}}$, the lack of anti-correlation is likely due to the peak during 2003.

day rolling average.[12] To reduce scatter in the figure, only the measurement closest to each SSN measurement is plotted.

The choice of quantities in Figure 1.1 is illustrates that multiple quantities vary over the solar cycle. Table 1.1 provides the cross correlation coefficients ρ between quantities Q plotted in Panels (A) through (D) with SSN. Some quantities (e.g. magnetic field magnitude and A_{He}) vary in phase with solar activity, while others (e.g. A_{p_2/p_1}) vary out of phase with SSN. In all cases except $P_{\Delta v}/P_{\text{th}}$, $|\rho(Q, \text{SSN})| > 0.7$ is highly significant[13]. In the case of $P_{\Delta v}/P_{\text{th}}$, the lack of anti-correlation is likely due to the peak during 2003. Chapter 2 examines the variation of A_{He} in detail. Chapter 7 presents A_{p_2}.

1.3 Coulomb Collisions

Coulomb collisions are small angle electrostatic collisions between charged particles that result in the exchange of momentum and energy (Callen, 2006; Fundamenski and Garcia, 2007; Spitzer, 1962; Verscharen et al., 2019). They result in particle diffusion, dispersion, slowing down, and energy loss (Callen, 2006). While no single collision causes a 90^o deflection, a Coulomb scattering nominally refers to the cumulative effect of millions of such small angle collisions that deflect a given charged particle. As hard sphere collisions are rare, Coulomb collisions are markedly more significant in a plasma.

Spitzer (1962) is the canonical reference for Coulomb collision timescales of a single test particle t colliding with a (Maxwellian) field of background particles f. A recent review article (Verscharen et al., 2019, Section 3 and references therein) covers Coulomb collisions in tractable detail. Following the notation of Fundamenski and Garcia (2007, Eq.

---

[12] Assuming a 30 day long month, this window is 13 months or the same time period over which SSN is smoothed.

[13] See Section 2.4.

Mechanism	Rate ν [Hz]	Time τ [s]
Slowing Down	1	1
Perpendicular Diffusion	1.47	0.68
Parallel Diffusion	0.5	2.0
Energy Loss	0.03	$33.\bar{3}$

Table 1.2: Relative collision frequencies (ν) and times (τ) directly from Callen (2006, Table (2.1)) and normalized to the slowing down time (momentum exchange rate).

(35))[14], which is nearly identical to that of Callen (2006), the momentum collision rate is

$$\nu_c = \frac{q_f^2 q_t^2 \ln \Lambda}{12\pi^{3/2}\epsilon_0^2} \frac{n_f}{m_t^{1/2} T_f^{3/2}} \tag{1.1}$$

where

- q_i is the charge of particle $i = t, f$;
- n_f is the field particle number density;
- m_t is the test particle mass;
- T_f is the field particle temperature;
- ϵ_0 is the vacuum permittivity;
- and $\ln \Lambda$ is the Coulomb logarithm[15].

All units are in SI except the temperature, which is in eV (Fundamenski and Garcia, 2007). Callen (2006, Table (2.1)) explicitly compares the relative collision rates for the four characteristic processes. Table 1.2 reproduces this table, normalizing all values to the slowing down time in Equation (1.1). It also gives their relative timescales (inverse of the frequency) to facilitate comparison.

Equation (1.1) captures the collision frequencies essential scaling $\nu_c \propto n/T^{3/2}$. However, it must be noted that if the test particle t is a distribution of particles, then the collision

---

[14] To compare exactly, substitute $t = s$ and $f = s'$.

[15] The Coulomb logarithm is the result of integrating over the collision impact parameter $\int db/b$ from the effective minimum distance between two particles to the maximum separation distance over which their Coulomb interaction is still effective. The minimum distance is the minimum of the classical and quantum mechanical distances (Callen, 2006), though in practice space physics is only concerned with the classical case (Verscharen et al., 2019). The maximum distance is the Debye length (Callen, 2006; Fundamenski and Garcia, 2007; Verscharen et al., 2019). Restricted limits of integration are used because integrating over 0 to ∞ is divergent in both limits (Verscharen et al., 2019).

frequency becomes

$$\nu_c' = \nu_c \frac{\left(1 + \frac{m_f}{m_t}\right)\sqrt{\frac{m_f}{m_t}}}{2\left(1 + \frac{w_t^2}{w_f^2}\right)^{3/2}} \tag{1.2}$$

where $w_i^2 = 2k_BT_i/m_i$ is the particle's thermal speed. In addition, Equations (1.1) and (1.2) account for neither the relative drift between ion species nor the collisions of f particles with t particles, both of which are required for a fuller description of Coulomb collisional processes[16]. Nevertheless, this scaling is instructive because it illustrates that the collision rate depends on local plasma conditions and sheds light on the coronal heating problem.

Recall that plasma temperature increases by 2 orders of magnitude from the photosphere to the corona (Section 1.1). Additionally, plasma density drops and temperature increases directly above the transition region (Landi and Cranmer, 2009).[17] Therefore, Coulomb collisions are likely unimportant on the dynamical timescales of the physical processes responsible for eating the corona (Marsch, 2006).[18]

The story is different in the solar wind. By the time it reaches 1 AU, the typical collisional timescale is $\tau_\mathrm{C} = \nu_c^{-1} \sim 4$ days. In comparison, the typical expansion time is $\tau_\mathrm{exp} \sim 2$ days in fast wind and $\tau_\mathrm{exp} \sim 5$ days in slow wind. The solar wind can be considered a near, but not fully collisionless system because there is not a scale separation between τ_C and τ_exp. As such, Coulomb collisions are one of several mechanisms that dissipate non-thermal features in the solar wind and drive it towards LTE (Verscharen et al., 2019).

Differential flow is one non-LTE feature of the solar wind that Coulomb collisions can impact (Alterman et al., 2018; Kasper et al., 2017, 2008). Given by $\Delta v_{i,j} = (\boldsymbol{v}_i - \boldsymbol{v}_j) \cdot \hat{\boldsymbol{b}}$, differential flow is the velocity difference between two ion populations parallel to the local magnetic field. Indices i and j can represent two species of distinct m/q or two populations of identical m/q with distinct behavior. As any non-gyrotropic component of Δv could not persist for more than a few gyroperiods, Δv can typically be simplified to $\Delta v_{i,j} = |\boldsymbol{v}_i - \boldsymbol{v}_j|$. To paraphrase Chapter 4, non-zero Δv has been observed starting in the corona with remote observations and, with in situ measurements, out to and beyond 1 AU. Coulomb collisions are known to dissipate non-zero Δv (Alterman et al., 2018; Kasper et al., 2008; Neugebauer, 1976)

Figure 1.2 presents the collisional behavior of proton beam-core differential flow nor-

---

[16] Hernández and Marsch (1985, Eq. (18)) provides an example of how the relative drift is incorporated and Hernández and Marsch (1985, Eq. (23)) illustrates how to account for field particles f colliding with test particles t along with the t collisions with f in a single equation.

[17] See (Marsch, 2006, Table (1)) for rough values.

[18] See Klimchuk (2006, 2015) for detailed discussions of the coronal heating problem.

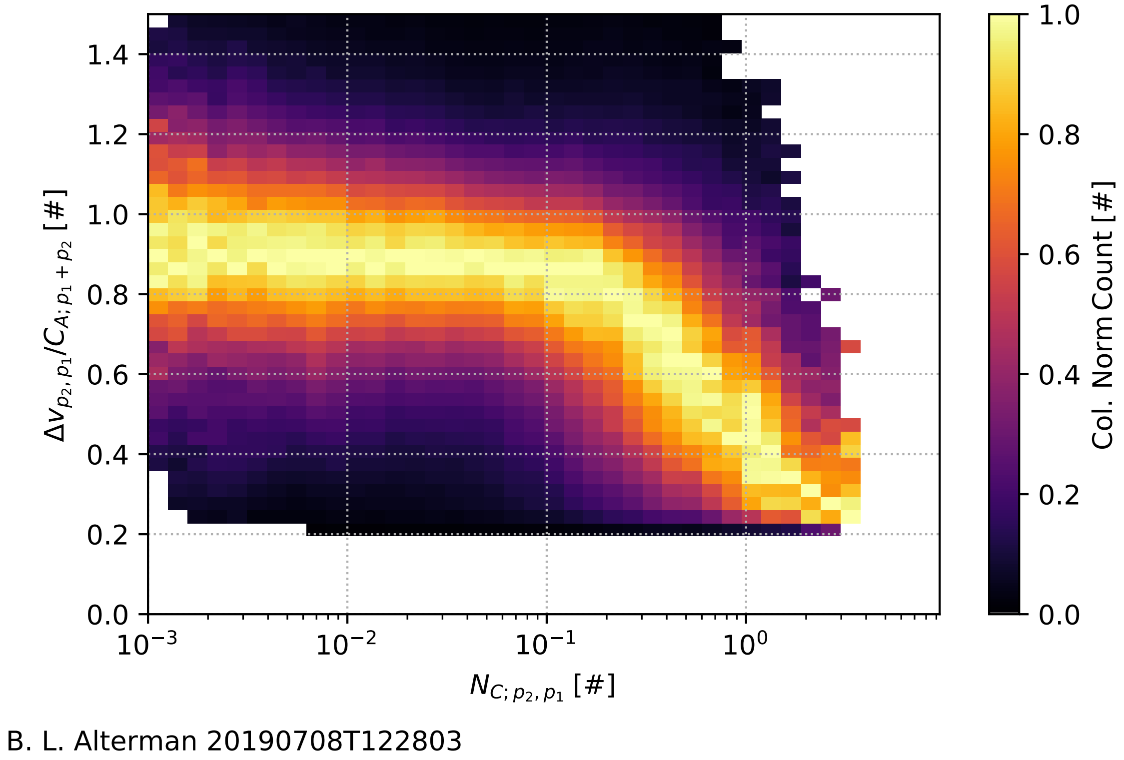

Figure 1.2: Proton beam-core differential flow ($\Delta v_{p_2,p_1}/C_{A;p_1+p_2}$) as a function of Coulomb number ($N_{c;p_2,p_1}$). $N_{c;p_2,p_1}$ is an empirical, single point estimate of the number of Coulomb collisions a given plasma parcel has experienced as it propagates from the Sun to the *Wind* spacecraft.

malized by the local Alfvén speed ($\Delta v_{p_2,p_1}/C_{A;p_1+p_2}$) as a function of Coulomb number ($N_{c;p_2,p_1}$). The Coulomb number is given by $N_c = \nu_c' \times r/v_{\mathrm{sw}}$. It is an empirical, single-point estimate of the number of Coulomb collisions a given parcel of plasma has experienced during its propagation from the Sun to the *Wind* spacecraft.[19] The Alfvén speed is the speed of a MHD wave that is known to have a high cross-correlation coefficient with both alpha-proton and proton beam-core differential flow. This high cross-correlation coefficient is taken as evidence that Δv is at least partially driven by a local wave-particle mechanism and therefore is the natural speed with which to convert Δv into a dimensionless quantity. After reviewing these quantities and their calculation in detail, Chapter 4 compares the behavior of alpha-proton differential flow ($\Delta v_{\alpha,p_1}$) with $\Delta v_{p_2,p_1}$ over the collisionally young range $10^{-2} \leq N_c \leq 10^{-1}$. Figure 1.2 simply demonstrates that proton-proton drifts are unaffected by Coulomb collisions when $N_c \leq 10^{-1}$ and, once N_c increases past this threshold, Coulomb collisions dissipate this particular non-LTE feature of the solar wind.

1.4 Local Regulation of Differential Flow

Spitzer (1962) proposed that Coulomb collisions act like dynamical friction. The associated differential equation is

$$\frac{d\Delta v}{dt} = -\nu_c \Delta v \tag{1.3}$$

for a given Δv and slowing down frequency ν_c. Assuming ν_c is constant, the solution follows an exponential decay $\Delta v(t) = \Delta v_0 \, \mathrm{e}^{-\nu_c t}$. To derive the Coulomb number, assume $t = r/v_{\mathrm{sw}}$ for propagation distance r and constant solar wind speed v_{sw}. Then $N_c = \nu_c \times r/v_{\mathrm{sw}}$, for which the simple assumption is $r = 1\,\mathrm{AU}$.

Figure 1.2 indicates that $\Delta v_{p_2,p_1}/C_A$ transitions from constant to collisionally decaying at $N_c = 0.1$. As such, the exponential term is ~ 0.9 and $\Delta v_0/C_A$ is suppressed by $\sim 10\%$, which is near the velocity uncertainty of the *Wind*/FC measurements (Kasper et al., 2006) and so likely within Δv's uncertainty. Yet the turnover is empirically clear. Therefore, this calculation suggests that the propagation distance may be shorter than $1\,\mathrm{AU}$ because Coulomb collisions only become significant at some distance from the Sun $r > \mathrm{R_S}$.

---

[19] Chapter 4, in particular the paragraph surrounding Equation (4.1) and related figures, identify this quantity as the collisional age A_c. Both collisions age (A_c) and collision number (N_c) have been used in literature (e.g. Chhiber et al. (2016); Kasper et al. (2017); Tracy et al. (2016, 2015)) to identify various method of accounting for the solar wind's collisional history during its propagation from the Sun to $1\,\mathrm{AU}$. Here, we follow Kasper et al. (2017) and use the N_c to identify the single-point estimate. Chapter 4 refers to the same quantity as the collision age A_c, while Kasper et al. (2017) use this term to account for a collisional history integrated over the solar wind's radial propagation.

1.4.1 Near-Sun Proton Beams

Parker Solar Probe (PSP) launched on August 12th, 2018. Over 6 years, PSP will have 24 solar encounters that progressively decrease in distance from the Sun starting at $35\ \mathrm{R_S}$ in August 2018 to below $10\ \mathrm{R_S}$ in December 2024 (Fox et al., 2015). E1 occurred on November 6th, 2018 and returned data from below 0.3 AU, i. e. closer to the Sun than approached by Helios. The Solar Wind Electrons, Alphas, and Protons (SWEAP) instrument suite's SPC has provided the closest yet to the Sun collected in situ plasma measurements. As preliminarily analysis in Chapter 5 shows and might be expected from Alterman et al. (2018); Hellinger et al. (2013), N_c may not govern Δv near the Sun. An alternative possibility is that one or more local wave-particle mechanisms contributes to Δv's regulation.

1.4.2 Instabilities

1.4.2.1 Theory

The VDF is a function of six-dimensional phase space and time t. Phase space is the six dimensions combining three velocity space $\mathbf{v}$ and three configuration or location space $\mathbf{r}$ dimensions. For species s with unspecified VDF $f_s(\mathbf{v}, \mathbf{r}, t)$, each species' bulk properties are constructed by taking velocity moments moments or averages over its VDF.

A moment of order i is defined by

$$M(i) \equiv \int \mathbf{v}^i f_s \, \mathrm{d}^3\mathbf{v}. \tag{1.4}$$

where the integral is taken over all of velocity space. For example, Equations (1.5) to (1.7) define species s' number density n_s, bulk velocity $\boldsymbol{u}_s$, and pressure $\overleftrightarrow{P}_s$.

$$n_s \equiv M(0) = \int f_s \, \mathrm{d}^3\mathbf{v} \tag{1.5}$$

$$\boldsymbol{u}_s \equiv M(1) = \int \mathbf{v} f_s \, \mathrm{d}^3\mathbf{v} \tag{1.6}$$

$$\overleftrightarrow{P}_s \equiv M(2) = m_s \int (\mathbf{v} - \boldsymbol{u}_s)^2 f_s \, \mathrm{d}^3\mathbf{v} \tag{1.7}$$

While we leave the VDF unspecified here, the form utilized does matter as it will impact integrals that are taken. Depending on f_s's form and/or the particular problem at hand, substituting the random velocity $\boldsymbol{c}_s \equiv \mathbf{v} - \boldsymbol{u}_s$ (Gombosi, 2004, Eq. (2.37)) into Equation (1.7) and higher order moments ($i \geq 2$) may simplify the integration.

The Boltzmann equation describes the statistical evolution of a plasma in phase space and time, irrespective of its (non-)equilibrium state (Verscharen et al., 2019). This equation is given by

$$\frac{\partial f_s}{\partial t} + \mathbf{v} \cdot \frac{\partial f_s}{\partial \mathbf{x}} + \mathbf{a} \cdot \frac{\partial f_s}{\partial \mathbf{v}} = \left(\frac{\delta f}{\delta t} \right)_c \tag{1.8}$$

with acceleration **a** describing all forces exerted on each particle and collision term $\left(\frac{\delta f}{\delta t}\right)_c$ describing inter-particle collisions.

Given that a plasma is a collection of charged particles, electromagnetic fields of the Lorentz force govern the plasma's acceleration and, assuming no other external forces, $\mathbf{a} = \frac{q_s}{m_s}\left(\mathbf{E} + \frac{\mathbf{v}}{c} \times \mathbf{B}\right)$. As such, Maxwell's equations must also be specified

$$\nabla \cdot \mathbf{E} = \frac{\rho_c}{\epsilon_0} \tag{1.9}$$

$$\nabla \cdot \mathbf{B} = 0 \tag{1.10}$$

$$\nabla \times \mathbf{E} = -\frac{\partial \mathbf{B}}{\partial t} \tag{1.11}$$

$$\nabla \times \mathbf{B} = \mu_0 \left(\mathbf{j} + \epsilon_0 \frac{\partial \mathbf{E}}{\partial t} \right) \tag{1.12}$$

for total charge density ρ_c and total current density $\mathbf{j}$. In addition, the electromagnetic nature of the system implies that the collision term $\left(\frac{\delta f}{\delta t}\right)_c$ is dominated by, if not exclusively Coulomb collisions. Note that all of Equations (1.9) to (1.12) are in SI units.

To close the system of Equations (1.8) to (1.12), note that ρ_c and $\mathbf{j}$ are functions the plasma itself and can be defined by taking moments of the VDF. As such, the total charge density in Equation (1.9) is

$$\rho_c = \sum_s q_s \int f_s \, \mathrm{d}^3\mathbf{v} \tag{1.13}$$

and the total current density in Equation (1.12) is

$$\mathbf{j} = \sum_s q_s \int \mathbf{v} f_s \, \mathrm{d}^3\mathbf{v} \tag{1.14}$$

for species s' charge q_s.

Maxwell's Equation of Change (MEC) describes the evolution of any given bulk plasma property by taking velocity moments of Equation (1.8). This introduces the moment closure problem: for a velocity moment of the Boltzmann equation at any given order i, the second term in Equation (1.8) introduces an additional power of **v** such that a bulk quantity corresponding to a moment of order $M(i+1)$ in Equation (1.4) is required. Gombosi (1994) provides a detailed derivation of the MEC, along with a discussion of how to address the closure problem. Yet even with these methods, analytic solutions to Equations (1.8) to (1.14) and the MEC do not yet exist. One option is numerical simulation, for which the physics problem dictates the choice of implementation.[20] Broadly, this choice dictates the information retained in the simulation and the cost of running it. Another option is linearizing the system.

Under linear theory, a plasma is approximated as the sum of small perturbations on a steady-state background state (Gary, 1993; Gombosi, 2004; Verscharen et al., 2019). As such, the plasma is collisionless with $\left(\frac{\delta f}{\delta t}\right)_c = 0$; Equation (1.8) becomes the Vlasov equation[21]; and the system becomes the Maxwell-Vlasov equations. In addition, any quantity[22] can be written in the form

$$X(\mathbf{v}, \mathbf{r}, t) = X_0 + \delta X(\mathbf{v}, \mathbf{r}, t) \tag{1.15}$$

for background state X_0 and small perturbation δX. Each of the perturbations o fluctuations δX is assumed to behave in a wave-like manner such that

$$\delta X(\mathbf{v}, \mathbf{r}, t) \propto e^{i(\mathbf{k}\cdot\mathbf{r} - \omega t)} \tag{1.16}$$

for real wave vector **k** and complex frequency $\omega = \omega_r + i\gamma$ (Verscharen et al., 2019). To solve for any frequency ω in terms of **k**, construct the *dispersion relation*[23] from the system of linearized Equations (1.8) to (1.14). Such solutions are called normal modes (Klein, 2013; Verscharen et al., 2019).

Instabilities are normal modes for which $\gamma > 0$, i.e. the normal mode amplitude grows instead of damps in time (Schwartz, 1980). Such modes are relevant to a system if the growth rate is an appreciable fraction of a dynamically important time scale, such as the normal mode real frequency (ω_r) or a characteristic plasma timescales like the proton gyrofrequency (Ω_p). As the background is taken as steady-sate, linear instabilities cannot formally impact bulk properties and a higher order (nonlinear) method is required to asses problems of this nature (Schwartz, 1980). Like the normal modes to which they corre-

---

[20] See Gary (2015, Page 5) for a brief comparison of Particle-in-Cell (PIC), hybrid, and gyrokinetic simulations. See Daughton et al. (2009); Gombosi et al. (2018); Hewett and Nielson (1978); Howes et al. (2006); Juno et al. (2018); Numata et al. (2010); Schekochihin et al. (2009); Stone et al. (2008); Verscharen (2019); Verscharen and Chandran (2018); Verscharen et al. (2018); Winske et al. (1985) for some examples and additional discussions of various implementations.

[21]
$$\frac{\partial f_s}{\partial t} + \mathbf{v} \cdot \frac{\partial f_s}{\partial \mathbf{x}} + \mathbf{a} \cdot \frac{\partial f_s}{\partial \mathbf{v}} = 0$$

[22] Depending the exact method implemented, this linearization assumption can be applied to any moment taken according to Equation (1.4) along with **E** and **B**, which are themselves a function of $f(\mathbf{v}, \mathbf{r}, t)$, or $f(\mathbf{v}, \mathbf{r}, t)$ itself.

[23] Some call it the dispersion matrix or tensor.

spond, instabilities can be categorized by the direction of their wave vector **k** with respect to $\hat{\boldsymbol{b}}$, the local magnetic field direction. Those for which $\boldsymbol{k} \times \hat{\boldsymbol{b}} = 0$ are commonly identified as parallel modes and those for which $\boldsymbol{k} \cdot \hat{\boldsymbol{b}} = 0$ are typically identified as oblique. Instabilities can also be categorized based on whether the mode's characteristic wavelength is short or long in comparison to "the ion thermal gyroradius or inertial length." (Gary, 2015)

Long wavelength instabilities correspond to fluid or MHD scale processes. Some call this the *inertial range* (Howes, 2015). At these wavelengths, spatial gradients in the plasma's bulk quantities are sources of free energy for which, "nonlinear multi-wave processes carry [the] fluctuating energy injected at long wavelengths through decreasing wavelengths to eventual dissipation, that is, conversion to thermal energy, at sufficiently short scale lengths." (Gary, 2015)

Short wavelength instabilities correspond to kinetic processes. They become important when the associated normal modes' characteristic wavelength is comparable to or smaller than features and gradients in the VDF (Howes, 2015). The excitation of kinetic instabilities is a multistep process in which the instability experiences linear growth and then quasilinear saturation (Gary, 2015). In magnetic turbulence spectra, the long to short wavelength transition may occur at the spectral break frequency, a frequency at which the power spectrum's slope becomes markedly more negative (Gary, 2015; Howes, 2015).

1.4.2.2 Application

Instabilities, including those in the solar wind, are a function of the available free energy sources or non-thermal features (Gary, 1993; Klein and Howes, 2015). The number of free energy sources is proportional to the number of charged populations present. As such, the dimensionality of the the associated parameter space is large.

One approach to addressing this large dimensionality is to assume that all but two free energy sources are negligible or can be treated or approximated as a fixed value (Klein et al., 2017). This method leads to a visually interpretable representation of the plasma's stability in which a threshold represents the transition from stability to instability, i.e. instability onset. Some refer to these as marginal stability contours. Any measurement farther from the PDF's centroid than a threshold is considered unstable to that instability (Verscharen et al., 2019). Remarkably, these thresholds have been rather adept at predicting the solar wind's evolution (Hellinger et al., 2006; Kasper et al., 2002; Klein et al., 2017; Maruca et al., 2012; Verscharen et al., 2016).

Two commonly encountered instabilities in kinetic plasmas are those driven by pressure anisotropy and those driven by non-zero currents. Four key pressure anisotropy-driven solar wind instabilities are the FMW or parallel firehose, oblique firehose (OFI), Alfvén ion cyclotron (AIC), and mirror mode (MM) (Gary, 2015, Section 1). A firehose instability onsets when the centripetal force of plasma flowing along a kinked magnetic field line overwhelms the magnetic tension. It requires that $R < 1$ and, typically, that $\beta > 1$ (Gary, 2015; Klein, 2013). The parallel firehose instability couples to parallel propagating fast magnetosonic or whistler modes and, as such, is also referred to as the FMW instability to differentiate it from the OFI instability (Klein, 2013; Schwartz, 1980). The OFI instability couples to non-propagating oblique Alfvén waves (Klein, 2013) and seems to describe solar wind observations more accurately (Bale et al., 2009; Hellinger et al., 2006; Kasper et al., 2002).

The AIC instability is predicted to onset when $R > 1$ (Gary, 2015; Klein, 2013). It is a parallel propagating mode (Gary, 2015) that couples to the, "short wavelength extension of the Alfvén wave branch..." (Verscharen et al., 2019, Section 4.4.3) The AIC heats cyclotron resonant particles in the perpendicular direction (Verscharen et al., 2019)

Similar to the AIC instability, the MM instability is significant when $R > 1$ (Gary, 2015; Klein, 2013). Southwood and Kivelson (1993) first showed that the MM instability, though thought to be MHD, is in fact kinetic. The MM instability grows when a plasma compression actually lowers the total pressure, as calculated by the double-adiabatic equations of state (Chew et al., 1956). More specifically, it, "arises due to the difference between the anti-phase response of the bulk plasma's thermal pressure to magnetic pressure perturbations and the in-phase response of particles... The instability generates entropy modes at oblique angles to the local mean magnetic field." (Klein, 2013)

Verscharen et al. (2016) provide thresholds for the pressure anisotropy-driven instabilities. They assume that $(\beta_{\parallel}, R)$ are the significant free energy sources for deriving marginal stability contours. Figure 1.3 plots the PDF of proton measurements in this parameter space. Unlike the previous figures that use data that include a proton beam, these proton measurements are taken from the *Wind*/SWE/FC proton-alpha dataset that only includes a single bi-Maxwellian proton population and a single bi-Maxwellian alpha particle population (Kasper et al., 2006). The red line indicates the outer most or edge bins in the PDF and the light blue or cyan line smooths this curve for visual clarity. Discussed in Section 3.4.3, the thresholds are plotted on the 2D distribution and indicated in the legend. The reason that the 2D PDF's $R_p > 1$ edge is unconstrained by either the AIC or MM instabilities is an open question in heliophysics.

Significant current-driven instabilities can arise when two ion populations differentially flow relatively to each other. Both alpha-proton (Maruca et al., 2012; Verscharen et al., 2013a) and proton beam-core differential flows (Daughton and Gary, 1998; Daughton et al., 1999; Montgomery et al., 1976, 1975) are viable sources. This thesis will focus on proton

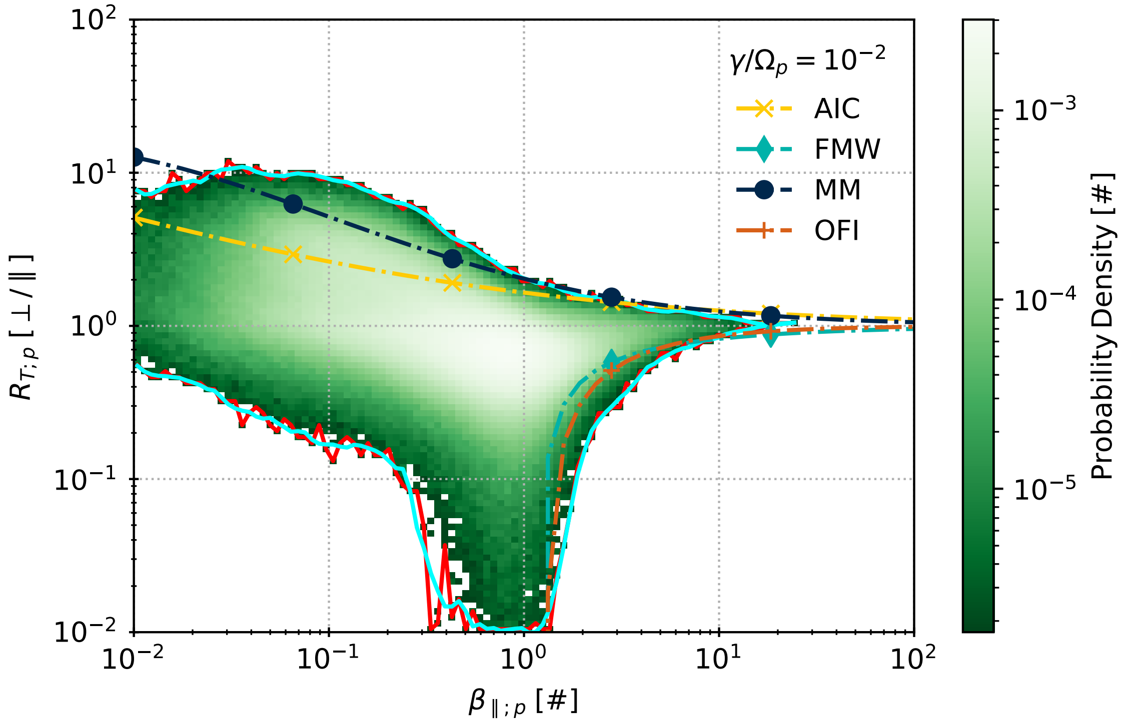

Figure 1.3: An example solar wind instability analysis that assumes only parallel proton plasma beta ($\beta_{\parallel}$) and temperature anisotropy ($R_T = T_{\perp}/T_{\parallel}$) are the significant and varying sources of free energy governing instability onset. The 2D PDF is given in color. Instability thresholds identified in the legend are taken from Verscharen et al. (2016) for the case that the growth rate is $\gamma/\Omega_p = 10^{-2}$. Unstable plasma measurements are those farther from the PDF's centroid than the thresholds. This figure also demonstrates a technique for identifying the border of the (β, R) distribution used in Figure 3.5. Here, the cyan line outlining the 2D PDF is a smoothed version of the accompanying red line that reduces the significance outliers at the edges that, by construction, are driven by low counting statistics.

beam-driven instabilities.

Schwartz (1980, Table 1) provides a general review of many solar wind instabilities, including those related to proton beams, using consistent terminology. Montgomery et al. (1976, 1975) identify three solar wind instabilities related to proton beams for large drifts $\Delta v \gtrsim C_A$. "One is closely associated with the usual Alfvén mode and the two others are associated with the 'fast' or magnetosonic mode." (Montgomery et al., 1976) Daughton and Gary (1998); Daughton et al. (1999) refine the work of Montgomery et al. (1976, 1975) to study a range in differential flows $1 \lesssim \Delta v_{p_2,p_1}/C_A \lesssim 2$, which has been empirically observed to contain an upper limit on typical solar wind proton beam measurements (Alterman et al., 2018; Marsch et al., 1982b).

In addition to the parallel and oblique magnetosonic modes of Montgomery et al. (1976, 1975), Daughton and Gary (1998); Daughton et al. (1999) also identify three Alfvén modes that they label *Alfvén I*, *Alfvén II*, and *Alfvén III*. While the *Alvén II* corresponds to the oblique Alfvén instability identified by Montgomery et al. (1976, 1975), Daughton and Gary (1998) argue that the *Alfvén I* is likely the dominant of the three proton beam-driven Alfvén instabilities. Daughton and Gary (1998) also suggest that the parallel mode is the dominant of the two magnetosonic ones. These two instabilities are strongest in complementary regions of parameter space,"The magnetosonic instability often has the larger growth rate at relatively small n_b/n_e and/or relatively large $\tilde{\beta}_{\|,c}$, whereas the Alfvén instability usually has the larger growth rate in the opposite cases." (Daughton and Gary, 1998) Note that $n_b = n_{p_2},$, $n_e = n_{p_1+p_2} = n_{p_1} + n_{p_2}$, and $\tilde{\beta}_{\|,c}$ is a modified plasma beta β_{p_1} that utilizes the total proton density and only the core temperature that Section 6.5 for defines.

Of the parallel magnetosonic and *Alfvén I* instability, Daughton and Gary (1998) suggest that the latter best describes solar wind observations and provide a marginal stability contour for it. Using Helios 2 data, Tu et al. (2004) have shown that it thresholds may not hold up for beams. Chapter 6 uses two *Wind*/SWE/FC datasets to show that proton beams are significant in the MM unstable population. The chapter then substantiates the results of Tu et al. (2004) with early SPC data. Finally, Chapter 6 uses a small, randomly chosen, manually fit, and high quality subset of *Wind*/SWE/FC data to indicate an alternative path for studying instabilities in the solar wind that does not rely on a reduced parameter space methodology.

1.5 Recap and Path Forward

This chapter reviewed the history of the solar wind. It then introduced physical processes that drive changes in the solar wind and correspond to three timescales. The solar cycle corresponds to evolution over decades. Coulomb collisions modify the solar wind on the timescale of days. Kinetic instabilities drive small scale changes in the solar wind's VDF on timescales of a second or less. This chapter also paid particular attention to the significance of proton beams in the solar wind, highlighting at least one proton beam quantity at each timescale.

The remainder of this thesis proceeds as follows. Chapter 2 examines the solar cycle variation of solar wind alpha particle abundance. Chapter 3 statistically investigates and elucidates the detailed structure of the solar wind proton VDF when it includes a proton beam. Chapter 4 studies the impact of Coulomb collisions on both alpha particle and proton beam differential flow, each taken with respect to the proton core. Chapter 5 presents an initial exploration of proton beam persistence below $0.3\,\mathrm{AU}$, illustrating that Coulomb collisions may not regulate proton beams at these near-Sun distances. Chapter 6 highlights paths of future work based on these results, including the significance of kinetic processes for proton beams. Finally, Chapter 7 summarizes these timescales and synthesizes them with the solar cycle variation of proton beams. It also suggests questions the answers to which may lead to an understanding of the solar wind that disentangles these timescales, at least as regards to proton beams.

CHAPTER 2

Helium Variation Across Two Solar Cycles Reveals a Speed-Dependent Phase Lag

This chapter studies the solar cycle variation of A_{He} as a function of v_{sw} and time. The *Astrophysical Journal Letters* published it in 2019 (Alterman and Kasper, 2019).

2.1 Abstract

We study the relationship between solar wind helium to hydrogen abundance ratio ($\mathrm{A_{He}}$), solar wind speed (v_{sw}), and SSN over solar cycles 23 and 24. This is the first full 22-year Hale cycle measured with the *Wind* spacecraft covering a full cycle of the solar dynamo with two polarity reversals. While previous studies have established a strong correlation between $\mathrm{A_{He}}$ and SSN, we show that the phase delay between $\mathrm{A_{He}}$ and SSN is a monotonic increasing function of v_{sw}. Correcting for this lag, $\mathrm{A_{He}}$ returns to the same value at a given SSN over all rising and falling phases and across solar wind speeds. We infer that this speed-dependent lag is a consequence of the mechanism that depletes slow wind $\mathrm{A_{He}}$ from its fast wind value during solar wind formation.

2.2 Introduction

Fully ionized hydrogen or protons (p) and fully ionized helium or alpha particles (He^{2+} or α) are the two most abundant solar wind ion species. The former comprises $\sim 95\%$ of the solar wind ions and the later $\sim 4\%$, both by number density. Heavier, minor ions constitute the remaining. The alpha particle abundance ($\mathrm{A_{He}} = 100 \times n_\alpha / n_p$) strongly correlates with solar activity, as indicated by the sunspot number (SSN) (Aellig et al., 2001; Kasper et al., 2012, 2007). The cross correlation and slope between $\mathrm{A_{He}}$ and SSN varies with solar wind speed (v_{sw}); is strongest in slow wind; markedly falls off above $v_{\mathrm{sw}} = 426\ \mathrm{km\,s^{-1}}$, where

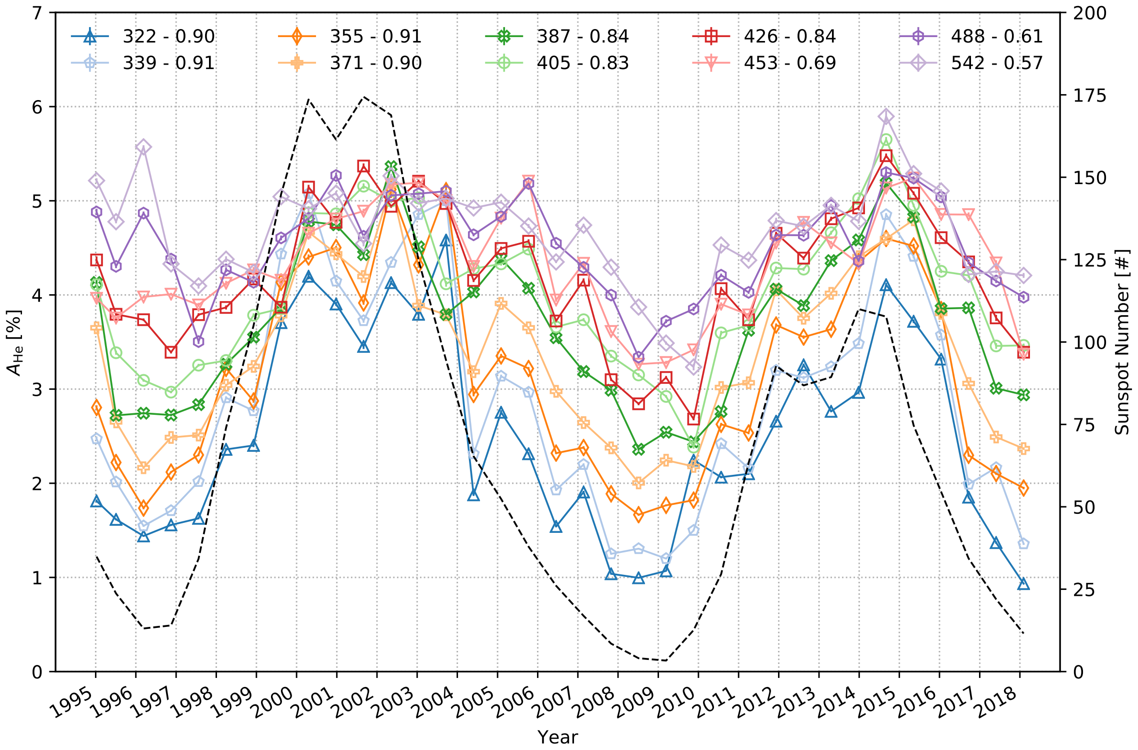

Figure 2.1: Helium abundance ($\mathrm{A_{He}}$) as a function of time and solar wind speed. Solar wind speed (v_{sw}) is divided into ten quantiles. Thirteen month smoothed SIDC Sunspot Number (SSN, dashed black) is plotted on the secondary y-axis. The legend indicates the middle of a given v_{sw} quantile and the Spearman rank correlation coefficient between $\mathrm{A_{He}}$ and SSN for that quantile. In effect, this figure updates Fig. (1) of Kasper et al. (2012, 2007). The present drop in $\mathrm{A_{He}}$ reflects the onset of solar minimum 25.

$\mathrm{A_{He}}$ takes on a stable value between 4% and 5%; and vanishes in the solar wind for speeds below $v_0 = 259\ \mathrm{km\,s^{-1}}$ (Kasper et al., 2012, 2007). This helium vanishing speed is within $1\ \sigma$ of the minimum observed solar wind speed (Kasper et al., 2007), indicating that helium may be essential to solar wind formation in the corona.

In addition to SSN, many other indicators of solar activity also follow a similar ~ 11 year cycle (Ramesh and Vasantharaju, 2014) that demonstrate a distinct phase-offset with SSN, which has been referred to as a hysteresis-like effect. These offsets range from 30 days (Bachmann and White, 1994) to 450 days (Temmer et al., 2003). Goelzer et al. (2013) have shown a similar phase lag in the interplanetary magnetic field's response to changes in SSN.

Using observations from the *Wind*/FCs, we extend the study of $\mathrm{A_{He}}$ variation with SSN and v_{sw} by Kasper et al. (2012, 2007) to include more than 23 years. This time period encompasses solar cycles 23 and 24 along with the end of solar cycle 22, thereby covering one Hale cycle. In other words, an idealized Sun with a pure dipole magnetic field would have experienced two polarity reversals and be returning to the configuration it had at the end of cycle 22.

In this work, we expand on the results of Kasper et al. (2012, 2007). We show a positive correlation between $\mathrm{A_{He}}$ and SSN across multiple solar cycles. In the slowest wind, we find a characteristic $\mathrm{A_{He}}$ that is consistent across multiple minima and maxima. Examining this relationship over one Hale cycle, we demonstrate that the phase lag between $\mathrm{A_{He}}$ and SSN found by Feldman et al. (1978) is a monotonically increasing function of v_{sw}. This delay is characteristic to a given v_{sw} and, at any one v_{sw}, a cyclic delay is sufficient to correct for this lag. Unexpectedly, $\mathrm{A_{He}}$ returns to similar values in both maximum 23 and maximum 24 even though $\mathrm{SSN_{Max,24}} < \mathrm{SSN_{Max,23}}$. Our results are consistent when using the 13-month smoothed, monthly, and daily sunspot numbers.

The remainder of this chapter is dedicated to analyzing and interpreting this speed-dependent lag. Section 2.3 describes the observations and FC specifics that are key to this study. Section 2.4 describes the variation of $\mathrm{A_{He}}$ with v_{sw} and SSN over two solar cycles. Section 2.5 analyzes the delay in response of $\mathrm{A_{He}}$ to changes in SSN as a function of v_{sw}. Section 2.6 presents the relationship between $\mathrm{A_{He}}$ and SSN in various v_{sw} quantiles, corrected for the delay of peak cross-correlation coefficient. Here, we show that correcting for the lag in $\mathrm{A_{He}}$'s response to changes in SSN reduces this hysteresis effect to a linear relationship. In Section 2.7, we use $\mathrm{A_{He}}$'s dependence on SSN to investigate the robustness of the $\mathrm{A_{He}}$, v_{sw}, SSN relationship reported by Kasper et al. (2007). In Section 2.8, we interpret our results and extend earlier hypotheses regarding two sources of slow solar wind. Finally, Section 2.9 summarizes these results and discusses future work.

2.3 Data Sources

The *Wind* spacecraft has been in continuous operation since its launch in the fall of 1994. Ogilvie et al. (1995) provide a detailed description of the SWE/FC. Kasper et al. (2006) introduce techniques for optimizing the algorithms that extract physical quantities from FC measurements. Maruca and Kasper (2013) and Alterman et al. (2018) build on these algorithms. These data have resulted high precision solar wind measurements of alpha particles (Kasper et al., 2006; Maruca and Kasper, 2013) and multiple proton populations (Alterman et al., 2018). The FC ion distributions are available on Coordinated Data Analysis Web (CDAweb)[1] and Space Physics Data Facility (SPDF)[2]. We follow Alterman et al. (2018) and reprocess the raw measurements to extract two proton populations (core and beam) along with an alpha particle population. The proton core is the population with the larger of the two proton densities. We calculate the solar wind speed as the proton center-of-mass velocity and treat the proton core as the proton density when calculating $\mathrm{A_{He}}$.

Two aspects of FCs are key to this work. First, FCs are energy-per-charge detectors. In the highly supersonic solar wind, alpha particles and protons are well separated by the instrument even when they are co-moving (Alterman et al., 2018; Kasper et al., 2017, 2008), as is commonly the case in slow solar wind. Second, the measurement quality has been stable and accurate throughout the mission (Kasper et al., 2006). These two FC characteristics enable our study of $\mathrm{A_{He}}$ variation with a single dataset from one instrument suite covering the 23 years necessary to observe one Hale cycle.

2.4 Solar Cycle Variation

Figure 2.1 presents $\mathrm{A_{He}}$ as a function of v_{sw} and time over 23 years. This time period starts at the trailing end of cycle 22 and extends through the declining phase of cycle 24. Figure 2.1 follows the format of Kasper et al. (2012, 2007, Figure (1) in each) and can be considered an update to their results. The solar wind speed measurements from the full mission have been split into 12 quantiles. The fastest and slowest quantile have been discarded due to measurement and statistical considerations. Of those quantiles retained, the lower edge of the slowest is $312\ \mathrm{km\,s^{-1}}$ and the upper edge of the fastest is $574\ \mathrm{km\,s^{-1}}$. Consequently, this study is limited to solar wind typically categorized as slow or slow and

---

[1] `https://cdaweb.sci.gsfc.nasa.gov/misc/NotesW.html#WI_SW-ION-DIST_SWE-FARADAY`

[2] `ftp://spdf.gsfc.nasa.gov/pub/data/wind/swe/swe_faraday/`

intermediate speed.[3] As in prior work, the abundance in each v_{sw} quantile is averaged into 250 day intervals. The 13-month smoothed sunspot number (SILSO World Data Center, 2018; Vanlommel et al., 2005, SSN) is interpolated to the measurement time; averaged into the same 250 day intervals as $\mathrm{A_{He}}$; and plotted on the secondary y-axis. The legend indicates the middle of the solar wind speed quantile along with its corresponding Spearman rank cross correlation coefficient between $\mathrm{A_{He}}$ and SSN. For brevity, we henceforth indicate the Spearman rank cross-correlation coefficient between $\mathrm{A_{He}}$ and SSN as $\rho(\mathrm{A_{He}}, \mathrm{SSN})$.

Figure 2.1 indicates that $\rho(\mathrm{A_{He}}, \mathrm{SSN})$ peaks at $v_{\mathrm{sw}} = 355 \ \mathrm{km\,s^{-1}}$. The present drop in $\mathrm{A_{He}}$ reflects that the Sun is entering Minimum 25. In contrast to the results of Kasper et al. (2012, 2007), $\rho(\mathrm{A_{He}}, \mathrm{SSN}) > 0.6$ indicates a meaningful cross-correlation in all but the fastest reported quantile with $v_{\mathrm{sw}} = 542 \ \mathrm{km\,s^{-1}}$ and $\rho(\mathrm{A_{He}}, \mathrm{SSN}) \geq 0.7$ is highly significant up to $v_{\mathrm{sw}} = 426 \ \mathrm{km\,s^{-1}}$. As Feldman et al. (1978) noted, there is a phase offset between $\mathrm{A_{He}}$ and $\rho(\mathrm{A_{He}}, \mathrm{SSN})$. Although the cycle 23 SSN amplitude is less than the cycle 24 amplitude, $\mathrm{A_{He}}$ unexpectedly returns to comparable values during each maximum.

2.5 Time-Lagged Cross Correlation

Visual inspection indicates a clear time lag between $\mathrm{A_{He}}$ and SSN. To quantify this lag, we calculate $\rho(\mathrm{A_{He}}, \mathrm{SSN})$ as a function of delay time applied to SSN from -200 days to $+600$ days in steps of 40 days–slightly longer than one solar rotation–for each v_{sw} quantile. We smooth these results to reduce the impact of discretization. The delay time is the time for which $\rho(\mathrm{A_{He}}, \mathrm{SSN})$ peaks as a function of delay. Panel (a) of Figure 2.2 plots the peak cross correlation coefficient as a function of v_{sw} for observed (empty marker) and delayed (filled marker) SSN. Marker colors and symbols match Figure 2.1 and are maintained throughout the Letter. Dotted lines connect the markers to aid the eye. To estimate the error in this calculation and its sensitivity to averaging timescale, we repeated it for averaging windows $N_{\mathrm{days}} = 225$ to $N_{\mathrm{days}} = 275$ in steps of 5 days. Because a trend is not apparent, we choose to quantify this variability as the standard deviation across N_{days} and represent it as error bars centered on the $N_{\mathrm{days}} = 250$ averaging window utilized in this Letter.

Several features in Panel (a) of Figure 2.2 stand out. First, it emphasizes that delayed $\rho(\mathrm{A_{He}}, \mathrm{SSN}) \geq 0.7$ is highly correlated for all v_{sw} quantiles. Second, observed and delayed $\rho(\mathrm{A_{He}}, \mathrm{SSN})$ peak at the same $v_{\mathrm{sw}} = 355 \ \mathrm{km\,s^{-1}}$. Third, the change in $\rho(\mathrm{A_{He}}, \mathrm{SSN})$ is largest and most visually striking in faster wind. However, smaller changes in slower

---

[3] To be consistent with prior work (e.g. Kasper et al. (2012, 2007)), we will use *slow* and *fast* to refer to the different extremes presented here. However, the reader should known that truly fast solar wind is excluded from our study.

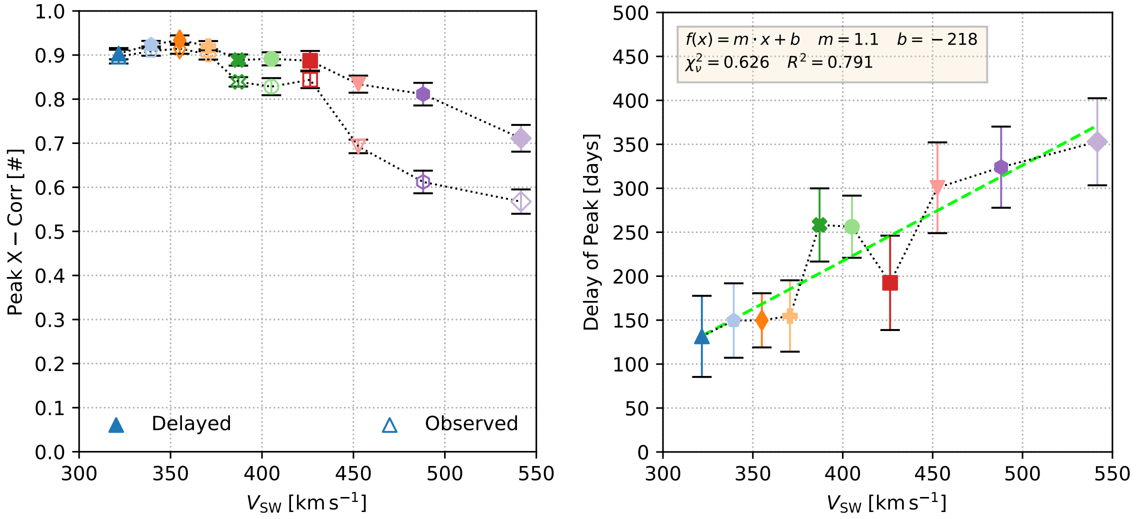

(a) (b)

Figure 2.2: Plots characterizing the cross correlation coefficient as a function of solar wind speed ($v_{\rm sw}$) for the observed (empty markers) and delayed (filled markers) SSN using 250 day averages. The marker color and shape match the style of Figure 2.1. Dotted lines connect the markers to aid the eye. Panels are: (a) Spearman rank cross-correlation coefficient and (b) Delay (τ) of Peak Spearman rank cross correlation as a function of $v_{\rm sw}$. In (b), the dashed green line indicates a robust fit and the panel's insert provides the functional form, fit parameters, and quality metrics. A positive delay indicates that changes in SSN precede changes in $\mathrm{A_{He}}$.

wind's $\rho(\mathrm{A_{He}}, \mathrm{SSN})$ are statistically more significant because they are less likely to be due to random fluctuations.

Panel (b) of Figure 2.2 examines τ, the delay of peak $\rho(\mathrm{A_{He}}, \mathrm{SSN})$, as a function of $v_{\rm sw}$. A positive delay indicates that changes in SSN precede changes in $\mathrm{A_{He}}$. The insert at the top of the figure indicates the functional form, fit parameters, and quality metrics. As with Panel (a) of Figure 2.2, the error bars indicate the variability of τ in each $v_{\rm sw}$ quantile. Solving the fit equation for $\tau = 0$, or the speed at which $\mathrm{A_{He}}$ responds immediately to changes in SSN, results in $v_{\rm i} = 200 \ \mathrm{km\,s^{-1}}$. Nevertheless, it is not unambiguously clear if delay time τ monotonically increases with $v_{\rm sw}$ or there are two distinct delay times. If it is actually the latter, then $\mathrm{A_{He}}$ in slow wind responds to changes in SSN with a delay time $\tau_{\rm slow} = 150$ days; faster wind responds after $\tau_{\rm fast} > 300$ days; and $v_{\rm i}$ represents a non-trivial conflation of these two delays. If this is not the case, it may be that $\tau_{\rm slow}$ is the shortest delay with which $\mathrm{A_{He}}$ responds to changes in SSN. As discussed below, in either case all helium released into the solar wind still lags changes in SSN.

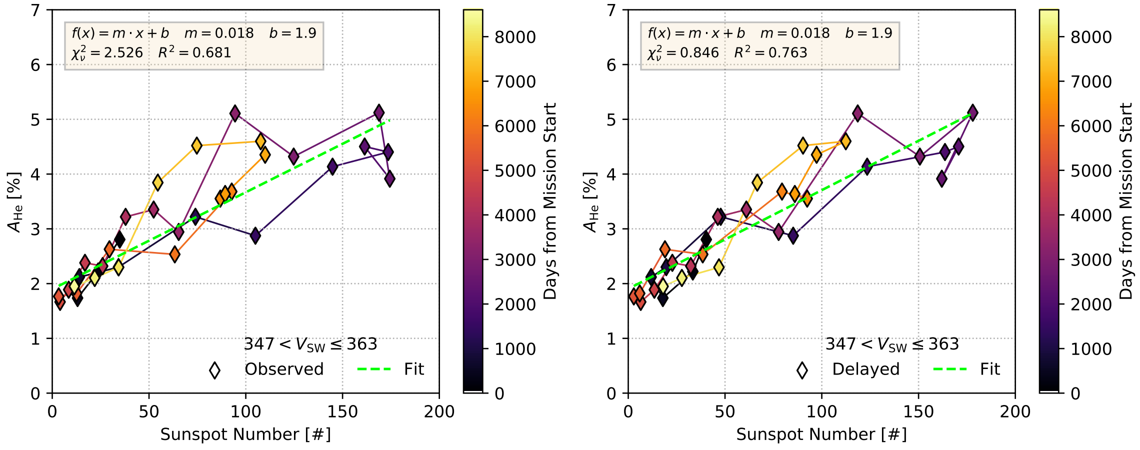

(a) (b)

Figure 2.3: Helium abundance (A_{He}) as a function of (a) observed and (b) delayed SSN in one example v_{sw} quantile. A line connects the points to aid the eye. Line and marker color correspond to the number of days since mission start. Marker shape matches the quantile in previous figures. This v_{sw} quantile covers the range $347 \text{ km s}^{-1} < v_{sw} \leq 363 \text{ km s}^{-1}$. A green, dashed line presents a robust fit to each trend. The insert at top of each panel gives the function fit, fit parameters, and quality metrics. Delaying SSN by the phase offset appropriate to this v_{sw} quantile reduces the impact of the hysteresis effect, as the increase in delayed R^2 indicates. That χ^2_ν is closer to unity in (b) indicates that a linear model better describes A_{He} as a function of delayed SSN.

2.6 Phase Delay

Figure 2.3 presents A_{He} as a function of SSN in the example quantile $v_{sw} = 355 \text{ km s}^{-1}$. This is the v_{sw} quantile for which the change in cross-correlation coefficient $\Delta\rho(A_{He}, \text{SSN})$ is smallest and the phase delay's effect is least likely to be due to random fluctuations. Panel (a) uses the observed SSN. Panel (b) uses SSN delayed by the time indicated in Panel (b) of Figure 2.2, ~ 150 days. A line connects the points to aid the eye. Both line and marker color indicate the days since mission start, given by the color bars. Marker shapes match the style of previous figures. Both panels contain a robust fit to the data, each indicating the monotonic, increasing trend. As in Panel (b) of Figure 2.2, the insert at the top of each panel describes the fit.

Panel (a) clearly shows the hysteresis pattern of A_{He} as a function of SSN. As seen with other indices (e.g. Bachmann and White (1994)), time moves counter-clockwise in this plot.[4] As noted by Bachmann and White (1994) for several solar indices, the clustering

---

[4] Not all indices present with the same handedness and the handedness of some changes across solar cycles (Özgüç and Ataç, 2001). A larger study of A_{He} variation is necessary to generalize this handedness observation.

of data at small SSN indicates that the hysteresis effect is stronger at solar maximum and weaker at solar minimum.

In panel (b), the larger R^2 indicates that this spread of $\mathrm{A_{He}}$ about the trend decreases. Note that R^2 corresponds to the square of the correlation coefficient of $\mathrm{A_{He}}$ and SSN derived from a robust fit and not directly from the measurements. *Although R is similar to $\rho(\mathrm{A_{He}}, \mathrm{SSN})$, they are not trivially equal.* That delayed χ^2_ν is markedly closer to unity indicates that a linear model better characterizes $\mathrm{A_{He}}$ as a function of delayed rather than observed SSN. Because delayed SSN only reduces the spread of $\mathrm{A_{He}}$ about the trend, it is expected that the trends and fit parameters in both cases are similar.

2.7 Robustness of $\mathrm{A_{He}}(v)$

Kasper et al. (2007) describe the relationship between $\mathrm{A_{He}}$ and v_sw in slow wind ($v_\mathrm{sw} \leq 530\ \mathrm{km\,s^{-1}}$) using data from a 2 year interval surrounding solar Minimum 23. They find that $\mathrm{A_{He}}(v) = 1.63 \times 10^{-2}\,(v - v_0)$, where $v_0 = 259 \pm 12\ \mathrm{km\,s^{-1}}$ is the speed below which helium vanishes from the solar wind. The robust fits in Figure 2.3 allow us to extract $\mathrm{A_{He}}$ at zero solar activity for all v_sw quantiles. This quantity, $\mathrm{A_{He}}(\mathrm{SSN} = 0)$, represents low solar activity conditions across this Hale cycle that are appropriate for comparison to the minimum 23 results from Kasper et al. (2007).

Figure 2.4 plots $\mathrm{A_{He}}(\mathrm{SSN} = 0)$ in all v_sw quantiles for delayed SSN with unfilled markers. As observed SSN does not deviate from delayed SSN in this figure, it is omitted for clarity. The black dashed curve is the fit of $\mathrm{A_{He}}(v)$ from Kasper et al. (2007). To better compare this analysis to the work of Kasper et al. (2007), filled markers present the results of repeating this analysis for $\mathrm{SSN} < 25$, a range in SSN representative of solar minimum 23. That $\mathrm{A_{He}}(\mathrm{SSN} = 0)$ is smaller in this re-analysis using a restricted range of SSN further substantiates that our results are consistent with those of Kasper et al. (2007) even though ours cover multiple solar cycles, a larger range in solar activity conditions, and uses a different analysis technique. Furthermore, the agreement between these two distinct analysis techniques supports the interpretation that helium release is essential to solar wind formation (Kasper et al., 2007). The discrepancy between our fastest quantile with $v_\mathrm{sw} = 542\ \mathrm{km\,s^{-1}}$ and their trend is expected because (1) it is outside of the speed range they fit and (2) they found thet $\mathrm{A_{He}}$ at this and similarly high speeds takes on a stable value between 4% and 5%.

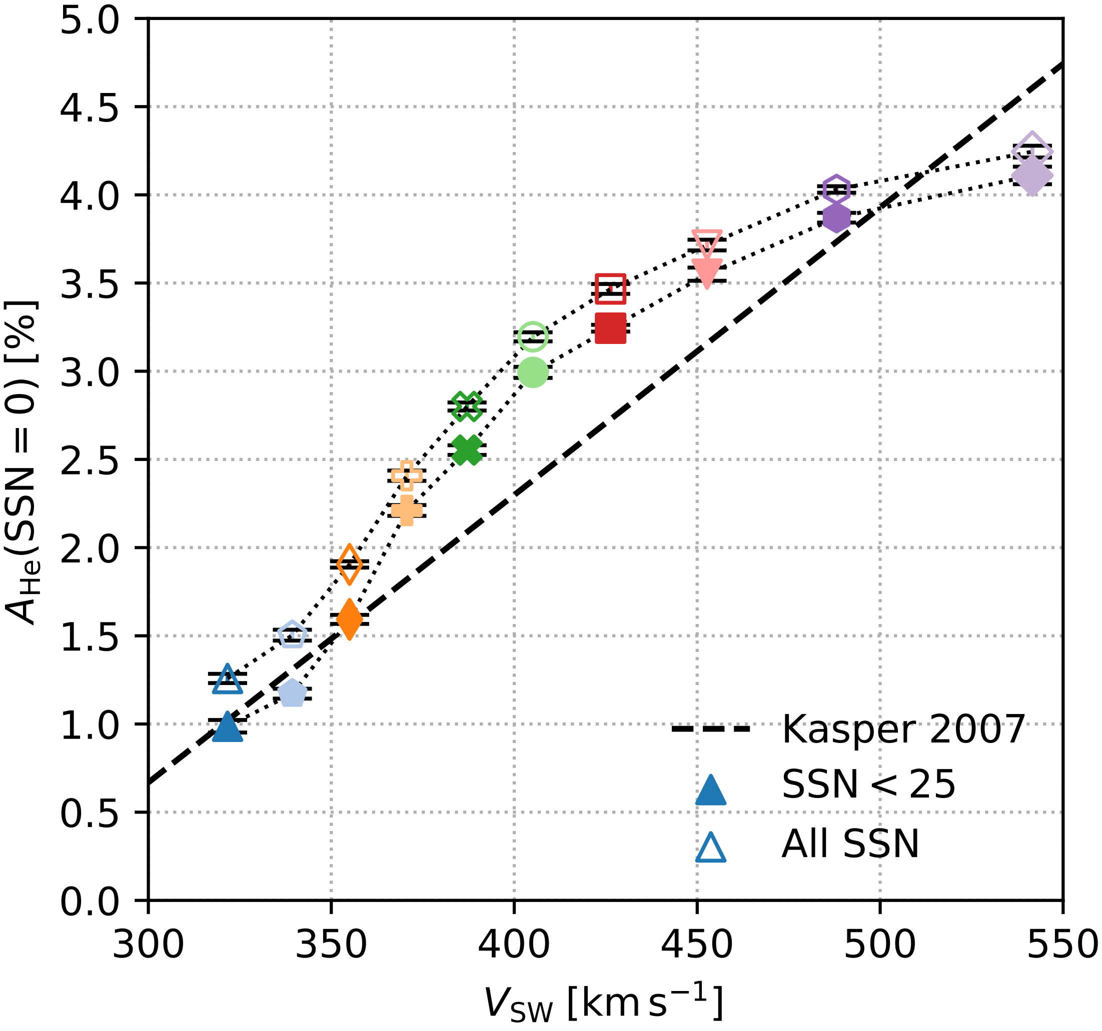

Figure 2.4: A summary of the zero solar activity helium abundance, $\mathrm{A}_{\mathrm{He}}(\mathrm{SSN}=0)$, as a function of v_{sw} for all robust fits in the fashion of Figure 2.3. Error bars indicate the standard deviation of each quantity over the range in averaging windows $225 \leq N_{\mathrm{days}} \leq 275$, each centered on the $N_{\mathrm{days}} = 250$ value. Unfilled markers show all SSN. Filled markers show identical calculations with $\mathrm{SSN} < 25$. The black dashed curve is the relationship between A_{He} and SSN derived by Kasper et al. (2007). That repeating our calculation with a reduced range in SSN shows better agreement with the results of Kasper et al. (2007) indicates that our results, covering the full range of solar activity in cycles 23 and 24, are consistent with their results from the two year interval surrounding minimum 23.

2.8 Helium Filtration

Many solar indices have a distinct phase-offset or hysteresis-like behavior with SSN (Ramesh and Vasantharaju, 2014, and references therein). Two such indicators include Lyman-α (Lα) intensity and soft x-ray flux (soft X-ray flux (SXR)). Lα measures activity in the

Sun's chromosphere & transition region (Fontenla et al., 2002, 1988) and lags SSN by 125 days (Bachmann and White, 1994). SXR is most common in ARs (van Driel-Gesztelyi and Green, 2015), and lags SSN by 300 days to 450 days (Temmer et al., 2003).

While $\mathrm{A_{He}}$ is approximately 8.5% within the Sun's convection zone and out to the photosphere (Asplund et al., 2009; Laming, 2015), it rarely exceeds 5% in the corona (Laming and Feldman, 2003; Mauas et al., 2005). It has long been assumed that $\mathrm{A_{He}}$ is initially modified in the photosphere. However, the speed-dependent lag in $\mathrm{A_{He}}$'s response to changes in SSN found here suggests additional processes at higher altitudes further modify helium's abundance. Slow solar wind's 150 day lag tracks lags in transition region and chromosphere structures, while faster wind's 300 day lag is more consistent with higher altitude structures in the corona. How could the transition region or corona modify the helium abundance?

Kasper et al. (2007) propose that two mechanisms release fully ionized helium into the slow solar wind, one each in the streamer belt and ARs. ARs have a strong magnetic field that extends from the photosphere into the corona, originate well above the equatorial region, tend to migrate towards the equator as they get older, and have loops that tend to grow with age (van Driel-Gesztelyi and Green, 2015). In contrast, the streamer belt has a weaker magnetic field, is composed of loops larger than those typical of ARs, is magnetically closed to the heliosphere, and is typically considered the source of slow solar wind (Eselevich and Eselevich, 2006). Stakhiv et al. (2016) identify signatures of these two solar sources in the Advanced Composition Explorer (ACE)/Solar Wind Ion Composition Spectrometer (SWICS) composition measurements.

If there are two sources of slow wind, solar wind originating in the streamer belt is more processed than that originating in ARs, where SXR is enhanced. Slower wind $\mathrm{A_{He}}$ ($v_{\mathrm{sw}} < 375\ \mathrm{km\,s^{-1}}$) originates from the streamer belt with a phase delay $\tau_{\text{slow}} = 150\ \mathrm{days}$. It appears more depleted than faster solar wind from ARs that has a phase delay $\tau_{\text{fast}} > 300\ \mathrm{days}$. The magnitude of $\mathrm{A_{He}}$'s reduction from its photospheric value and the speed-dependent delay then reflect the extent to which a given source region is magnetically open to the heliosphere. As the phase delay between $\mathrm{A_{He}}$ and SSN is an increasing function of v_{sw}, ARs and the streamer belt may be two extreme cases along the continuum of slow wind helium depletion mechanisms.

For illustrative purposes, one candidate mechanism that may contribute to this processing is the FIP effect. The FIP effect is the empirical observation that solar wind ions are fractionated, or their abundances differ from their photospheric value based on their first ionization potential (Laming, 2015; Meyer, 1991, 1993, and references therein). Low FIP elements (FIP $< 10\ \mathrm{eV}$) tend to increase or experience an enhancement. This low-FIP enhancement also leads to an apparent depletion in high-FIP elements, as with helium. Under the framework of Rakowski and Laming (2012), time averaged coronal Alfvén waves create a pondermotive force that accelerates ions into the corona and leads to fractionation in coronal loops. The FIP effect is strongest in the upper chromosphere and lower transition region, weakest in regions of strong magnetic field, and stronger in longer loops (Rakowski and Laming, 2012). Feldman et al. (2005) found that FIP bias in ARs increases with age.

However, this is just one of several possible mechanisms that could cause this phase lag. Other mechanisms that might impact the speed-dependent phase lag may include interchange reconnection (Fisk, 2003) and gravitational settling (Borrini et al., 1981; Hirshberg, 1973; Vauclair and Charbonnel, 1991). Moreover, these are mechanisms are not mutually exclusive. Laming (2004); Rakowski and Laming (2012); Schwadron et al. (1999) include gravitational settling in their models of the FIP effect. Schwadron et al. (1999) also relies on interchange reconnection to create the magnetic structures necessary for FIP fractionation to occur. As Rakowski and Laming (2012) show, the combination of coronal loop length, differences in gravitational scale height, and the FIP effect can lead to the apparent depletion of $\mathrm{A_{He}}$. Whatever the underlying mechanism, it should also account for the observation that $\mathrm{A_{He}}$ returns to a similar value during solar maximum, irrespective of SSN during maximum.

2.9 Conclusion

Following the methods of Kasper et al. (2012, 2007), we have analyzed the relationship between $\mathrm{A_{He}}$ and the 13-month smoothed sunspot number (SSN) by studying their cross correlation coefficient using 250 day averages. We have verified that our results are consistent when using the monthly and daily SSN. Our data covers 23 years, including cycle 23 and 24 along with the tail end of cycle 22. This time period is more than the 22 years of a Hale cycle over which the pure dipole field of an idealized Sun would experience two polarity reversals and return to an initial configuration. As shown in Figure 2.1, the present decrease in $\mathrm{A_{He}}$ clearly demonstrates that we are entering solar Minimum 25. While the significance of the cross correlation coefficient $\rho(\mathrm{A_{He}}, \mathrm{SSN})$ decreases with increasing v_{sw}, Figure 2.1 shows that $\rho(\mathrm{A_{He}}, \mathrm{SSN})$ is meaningful up to $v_{\mathrm{sw}} = 488\ \mathrm{km\,s^{-1}}$ and highly significant up to $v_{\mathrm{sw}} = 426\ \mathrm{km\,s^{-1}}$. A subject of future work is investigating why $\mathrm{A_{He}}$ returns to a similar value in Maximum 24 even though cycle 24's amplitude is markedly smaller than cycle 23's.

Feldman et al. (1978) comment on a phase offset between $\mathrm{A_{He}}$ and SSN. Panel (b) of Figure 2.2 reveals that (1) the length of this delay is an increasing function of v_{sw} and

(2) the v_{sw} quantile most correlated with SSN does not change when SSN is appropriately delayed in each quantile. We have also argued that, although changes in $\rho(\mathrm{A_{He}}, \mathrm{SSN})$ are most dramatic in faster v_{sw} quantiles, the probability of smaller changes in slower wind's larger $\rho(\mathrm{A_{He}}, \mathrm{SSN})$ is much smaller and therefore more significant.

Panel (b) of Figure 2.2 presents the delay applied to SSN necessary to maximize $\rho(\mathrm{A_{He}},$ $\mathrm{SSN})$ as a function of v_{sw}. The delay is a monotonically increasing function of v_{sw} and linear fit to this trend reveals that the speed at which $\mathrm{A_{He}}$ responds instantaneously to changes in SSN is $v_{\mathrm{i}} = 200\ \mathrm{km\,s^{-1}}$. Yet the speed of instantaneous response is less than the vanishing speed, $v_{\mathrm{i}} < v_0$. Therefore any helium released into the solar wind will necessarily respond to changes in SSN after some delay. If trend in Panel (b) of Figure 2.2 is correct, then the minimum delay in $\mathrm{A_{He}}$'s response to SSN is 68 ± 13 days, or approximately two Carrington Rotations. Here, we also note that there may be two distinct phase delays (τ_{slow} and τ_{fast}) with which $\mathrm{A_{He}}$ responds to changes in SSN and the fit quantity v_{i} may be a conflation of the physics related to each phase delay. Under either interpretation, helium released into the solar wind is a delayed response to changes in SSN.

In Section 2.6, we present robust fits to $\mathrm{A_{He}}$ as a function of observed and delayed SSN in each v_{sw} quantile. It visually illustrates that applying a time delay to SSN reduces the spread of $\mathrm{A_{He}}$ about its trend. In Section 2.7, we use helium abundance at zero solar activity derived from these fits to demonstrate that our results using 23 years of data are consistent with the trend found by Kasper et al. (2007) for a two year interval surrounding solar minimum 23.

In Section 2.8, we discuss how the demonstrated phase delay or hysteresis effect is qualitatively similar to the phase delays between SSN and many regularly observed solar indices (Ramesh and Vasantharaju, 2014, and references therein). We note that the two aforementioned phase delays (τ_{slow} and τ_{fast}) are consistent with $\mathrm{L}\alpha$ and SXR and that this consistency is indicative of two distinct source regions. Slower wind ($v_{\mathrm{sw}} < 375\ \mathrm{km\,s^{-1}}$) with a lower $\mathrm{A_{He}}$ originates in the streamer belt and responds to changes in SSN with characteristic delay time $\tau_{\mathrm{slow}} = 150$ days. Faster wind with a larger $\mathrm{A_{He}}$ originates in ARs and responds to changes in SSN with characteristic delay time $\tau_{\mathrm{fast}} > 300$ days. These different delay times indicate that $\mathrm{A_{He}}$ is processed by one or more mechanisms above the photosphere. Assuming that the results of Kasper et al. (2007) apply across the solar cycle and helium universally vanishes from the solar wind when $v_{\mathrm{sw}} < 259\ \mathrm{km\,s^{-1}}$ irrespective of solar activity, one possible interpretation is that there is a minimum $\mathrm{A_{He}}$ necessary for solar wind formation, the mechanisms that reduces $\mathrm{A_{He}}$ to a value less than its photospheric value prevents solar wind release below the vanishing speed v_0, and–using the fit from Panel (b) of Figure 2.2–any helium that enters the solar wind is released after 68 days, approximately two Carrington rotations. If this is the case, helium in the high-speed solar wind may represent the solar wind's "ground state" (Bame et al., 1977; Schwenn, 2006a) and the observed depletion of $\mathrm{A_{He}}$ is the result of source regions departing from states that release fast wind, i. e. those magnetically open to the heliosphere. A rigorous study of the relationship between $\mathrm{A_{He}}$ and solar indices other than SSN may better constrain helium variation by source region and is a subject of future work.

This work highlights the value of recent and forthcoming advances in heliophysics. PSP (Fox et al., 2015) launched in August, 2018 and completed its first perihelion in November of that year. Solar Orbiter (SolO) (Müller et al., 2013) will launch in 2020. The thermal ion instruments on board (Kasper et al., 2016) provide an unprecedented opportunity to study the solar wind, its formation, and its acceleration. For example, PSP will make measurements near and below the Alfvén critical point, i.e. at distances within which mapping the solar wind to specific sources is significantly simplified in comparison with *Wind*. McMullin et al. (2016) anticipate that the Daniel K. Inouye Solar Telescope (DKIST)will begin operations in 2020. DKIST's Cryo-NIRSP instrument will be capable of simultaneously imaging solar helium at various heights in the corona. Combining DKIST measurements with PSP and SolO measurements will enhance our ability to differentiate between the mechanisms releasing helium into the solar wind–e.g. from the streamer belt or ARs–and better constrain the delay in helium's response to changes in SSN.

CHAPTER 3

21 Years of Proton Beams at 1 AU

Proton beams are one method for characterizing the non-LTE heat flux referenced in Chapter 1. Sections Section 3.1 through Section 3.6 constitute a manuscript characterizing them at 1 AU written in preparation for the *Journal of Geophysical Research: Space Physics*. Section 3.7 serves an appendix to this work that briefly compares the results of fitting the *Wind*/SWE/FC measurements with a single proton population and two proton populations.

3.1 Abstract

We fit Solar wind proton spectra from the *Wind* spacecraft Solar Wind Experiment (SWE) Faraday cups with a model velocity distribution function consisting of two proton populations: one bi-Maxwellian and one isotropic or Maxwellian population. This analysis revealed a significant secondary population at least 71% of the time in the solar wind over 21 years of the *Wind* mission from 1998 through 2019. This secondary population or proton beam can contain significant free energy and typically drifts at approximately the local Alfvén speed faster than the core or bulk protons, which strongly indicates ongoing wave-particle interactions. The ubiquity of these two-population proton observations, particularly in the slow solar wind, constitutes a nearly 500 fold increase in statistics compared to Helios and reports proton beams 2.4 times as often as Ulysses. These measurements mark a significant advancement in our ability to measure and understand an important non-thermal feature of the solar wind.

3.2 Introduction

The solar wind is highly sensitive to the its VDF's structure (Klein et al., 2018, 2017; Schwartz, 1980), i. e. the distribution of ions parallel and perpendicular to the local magnetic field. Solar wind ions regularly exhibits many non-thermal features both within a given species and between different species. Unequal pressures parallel and perpendicular to the local magnetic field[1] along with unequal thermal and magnetic pressures[2] are characteristic signatures specific to a given species (Berger et al., 2011; Kasper et al., 2017; Tracy et al., 2016). Unequal temperatures and relative drifts[3] (Alterman et al., 2018; Kasper et al., 2008; Neugebauer, 1976) are characteristic signatures of such departures from local thermodynamic equilibrium (LTE) apparent when comparing different ion species. Within a single species, phase-space fluxes in excess of a single Maxwellian or bi-Maxwellian have been observed (Alterman et al., 2018; Asbridge et al., 1974; Chen et al., 2016; Feldman et al., 1973b, 1974b; Marsch and Goldstein, 1983; Marsch and Livi, 1987; Marsch et al., 1982b; Montgomery et al., 1976).

Broadly, two non-exclusive physical processes drive solar wind evolution in a manner different from purely collisionless adiabatic expansion: wave-particle interactions and Coulomb collisions. Wave-particle interactions describe the broad class of mechanism by which energy is exchanged between solar wind particles and electromagnetic fields (Araneda et al., 2008, 2002; Daughton and Gary, 1998; Daughton et al., 1999; Hellinger and Trávníček, 2011; Kaghashvili et al., 2004; Matteini et al., 2010a,b; Montgomery et al., 1976; Schwartz, 1980; Schwartz et al., 1981; Tu et al., 2002). Coulomb collisions are irreversible small angle collisions that have an integrative effect over the solar wind's radial evolution (Alterman et al., 2018; Kasper et al., 2008; Livi and Marsch, 1986, 1987; Marsch and Goldstein, 1983; Marsch and Livi, 1985, 1987; Neugebauer, 1976). While the timescale associated with wave-particle interactions is on the order of $1\ \mathrm{s}$ and that associated with Coulomb collisions is on the order of $4\ \mathrm{days}$, both are a strong function of the shape of the solar wind's VDF (Livi and Marsch, 1986; Marsch and Livi, 1985) – especially its deviations from (bi-)Maxwellian configurations – and therefore couple (Verscharen et al., 2019). In general, beams have a marked impact on the structure of the solar wind's VDF, but little impact on its bulk speed. This impact tends to increase with higher order moments (e.g. temperature) with correspondingly more complex uncertainties.

Datasets characterizing these excess phase-space fluxes have been previously produced with Interplanetary Monitoring Platform (IMP) 6 (Asbridge et al., 1974; Feldman et al., 1973a,b), Helios (Marsch et al., 1982b; Ďurovcová et al., 2019), and Ulysses (Goldstein et al., 2000, 2010; Matteini et al., 2013) measurements. These excess phase-space densities are typically labeled a secondary population, beam, or "double-humped" distributions. We refer to them interchangeably as secondary populations and beams.

---

[1] Pressure anisotropy, $R = P_{\mathrm{th},\perp}/P_{\mathrm{th},\parallel}$

[2] Plasma beta, $\beta = \frac{nk_BT}{B^2/2\mu_0}$

[3] Differential flow, Δv

Feldman et al. (1973a,b) first reported a proton beam in three months of IMP 6 electrostatic analyzer data covering March 18, 1971 to June 12, 1971.[4] Two methods were used to identify two-population proton distributions (Feldman et al., 1973a,b). Both rely on reducing 3D measurements to a single 1D VDF parallel to the local magnetic field. To reduce the impact of time aliasing, these authors have required that a secondary population persist for various time intervals, e. g. ranging from $\sim 7 \text{ min}$ to $\sim 30 \text{ min}$. They also required that the proton and electron heat fluxes were aligned to within 15^{o}.

The method of identifying a proton beam in *Helios* data differs from IMP 6. In Helios, Marsch et al. (1982b) derived 1D distributions by summing over angular components of the VDF. Two populations were identified by examining the persistence of two proton peaks in 1D distributions through time.(Schwenn et al., 1980) Marsch et al. (1982b) required that the ratio of the beam to core phase-space at the peak of each distribution stayed above 1%, i.e. $F(0)/F(V_D) > 0.01$. Marsch et al. (1982b) relaxed the time-persistence requirement used by Feldman et al. (1973a,b) and report a total of 5,765 beams over the course of the Helios missions. In contrast to Marsch et al. (1982b), Ďurovcová et al. (2019) follow Stansby et al. (2019) and fit both the beam and core with bi-Maxwellian distributions.

Goldstein et al. (2000) document a method for fitting two proton populations in approximately 1.5 years of Ulysses data. This method selected data based on a χ^2 goodness-of-fit statistic and returned 747 spectra. Neugebauer et al. (2001, Appendix A) document a different method of identifying proton beams to study six example magnetic hole events in Ulysses data. Goldstein et al. (2010); Matteini et al. (2013) apply this latter method to examine radial trends in Ulysses data over several years. Matteini et al. (2013) use 45,000 proton beam measurements processed in this fashion to study signatures of kinetic instabilities from 1.3 AU to 5 AU.

The *Wind*/SWE/FCs (Ogilvie et al., 1995) have provided continuous and highly stable (Kasper et al., 2006) solar wind measurements for more than 20 years. Nonlinear fitting of the FC spectra with bi-Maxwellian distributions continue to yield robust measurements of a single proton population and alpha particles. Large scale statistical studies with this data have enabled high precision and high accuracy measurements of the alpha particle abundance (Aellig et al., 2001; Alterman and Kasper, 2019; Kasper et al., 2012, 2007), the alpha to proton temperature ratios (Kasper et al., 2008; Maruca et al., 2013) both species' anisotropy (Hellinger et al., 2006; Kasper et al., 2002, 2008; Maruca and Kasper, 2013; Maruca et al., 2012), alpha-proton differential flow (Alterman et al., 2018; Kasper et al., 2008, 2006), the impact of Coulomb collisions (Alterman et al., 2018; Kasper et al., 2008),

---

[4] Asbridge et al. (1974) also detected 8 simultaneous two-population proton and two-population alpha particle distributions using the same methods as Feldman et al. (1973a,b) over a period of 10 months.

and wave-particle interactions (Klein et al., 2018), including (β, R)-dependent instabilities (Chen et al., 2016; Hellinger et al., 2006; Kasper et al., 2002; Maruca et al., 2012; Verscharen et al., 2016).

We have updated the *Wind*/SWE/FC analysis to accommodate two proton populations. They are characterized by one bi-Maxwellian population and one isotropic or Maxwellian population. Using a single model to simultaneously quantify large and small scale excess phase-space densities, our analysis enables statistical studies of smaller deviations from LTE that cover a broad range of parameter space over multiple solar cycles.

The remainder of this manuscript proceeds as follows. Section 3.3 briefly reviews the instrument used, data reduction algorithms, and data selection. Section 3.4 describes the properties of a proton beam in an example Carrington Rotation (CR), as a function of solar wind speed (v_{sw}), and in the (β, R) plane. Section 3.5 estimates the number of proton beams that are not detected by our methods. Finally, Section 3.6 summarizes the results and presents our conclusions.

3.3 Measurement Technique, Fit Algorithm & Data Selection

Previous analysis of solar wind ion spectra measured by SWE/FC report single-population proton and alpha properties. In this study, we present simultaneous fits to two proton populations within a single spectrum. Ogilvie et al. (1995) described the SWE instrument suite. In summary, the Faraday cup subsystem consists of two wide field-of-view cups that are oriented at $\pm 15^o$ relative to the spin plane. Over the spacecraft's 3s spin period, the FCs measure the solar wind ion flux in one energy-per-charge (E/q) window along 20 look directions. Over 32 consecutive spacecraft rotations, 32 logarithmically spaced E/q windows are measured. These 32×20 independent E/q measurements form one raw current spectrum. The current spectra are archived and publicly available on CDAweb.[5] Each current spectrum is reduced to the physical quantities number density (n), velocity (v), and thermal speed (w). The Faraday cup data quality has remained effectively unchanged over the duration of the mission. (Kasper et al., 2006)

The exact parameters extracted from the raw spectra or currents depend on the method by which they have been processed. Because the instrument response is not analytically invertible and the function that maps an actual ion VDF to a current spectrum is not unique, spectra are reduced to physical quantities by fitting each to an analytic, model VDF con-

---

[5] See acknowledgements for urls.

volved with the instrument response. The choice of model VDF determines the parameters into which a spectrum is reduced.

Figure 3.1 presents one example solar wind VDF from the *Wind* FCs. The strongest features of an ion spectrum can be well described by a two-species model for single population alpha particles and single population protons, each represented by a bi-Maxwellian. In Figure 3.1, these are the red and pink curves respectively centered at $\sim 0.5\,\mathrm{kV}$ and $\sim 3.25\,\mathrm{kV}$. Kasper et al. (2006) combined the FC spectra with measurements from the Wind Magnetic Field Investigation (MFI) (Koval and Szabo, 2013; Lepping et al., 1995) to derive 3D measurements of both species that include a number density, 3-component vector velocity, and thermal speeds perpendicular and parallel to the local magnetic field (i. e. a temperature anisotropy). Maruca and Kasper (2013) used higher time resolution MFI measurements to further constrain the measured temperature anisotropies.

Inspection of SWE Faraday cup spectra reveal that deviations from a bi-Maxwellian can significantly impact the fit quality. Comparison with MFI measurements reveal that these deviations are aligned with the magnetic field. We extend the model VDF of Kasper et al. (2006) to account for these deviations in solar wind protons by including a proton beam. The result is

$$f(\boldsymbol{v}) = \frac{n_{\mathrm{bi}}}{\pi^{3/2} w_\parallel w_\perp^2} \exp\left[-\frac{(\boldsymbol{v}-\boldsymbol{u}_{\mathrm{bi}})^2}{w_\perp^2 + w_\parallel^2}\right] + \frac{n_{\mathrm{iso}}}{(\pi w_{\mathrm{iso}}^2)^{3/2}} \exp\left[-\frac{\Delta v^2}{w_{\mathrm{iso}}^2}\right] \tag{3.1}$$

. Reducing a FC spectrum with Equation (3.1) returns nine proton quantities:

1. two number densities n_{bi} & n_{iso},
2. a vector velocity associated with the bi-Maxwellian $\boldsymbol{v}_{\mathrm{bi}}$,
3. a drift velocity $\Delta v = |\boldsymbol{v}_{\mathrm{iso}} - \boldsymbol{v}_{\mathrm{bi}}|$ between the bi-Maxwellian and isotropic components of the model VDF,
4. a pair of bi-Maxwellian thermal speeds parallel ($w_\parallel$) and perpendicular ($w_\perp$) to the local magnetic field ($\boldsymbol{B}$),
5. and an isotropic or Maxwellian thermal speed (w_{iso}).

Note that we define a thermal speed as $w_{s,c}^2 = 2k_B T_{s,c}/m_s$ for species s and component (perpendicular, parallel, or scalar) c. In this work, we consider the proton core (p_1) to be the population with the larger number density and the proton beam (p_2) to be other. While not universally true, the bi-Maxwellian component often corresponds to the core and the Maxwellian or isotropic component often corresponds to the beam. In the top of Figure 3.1,

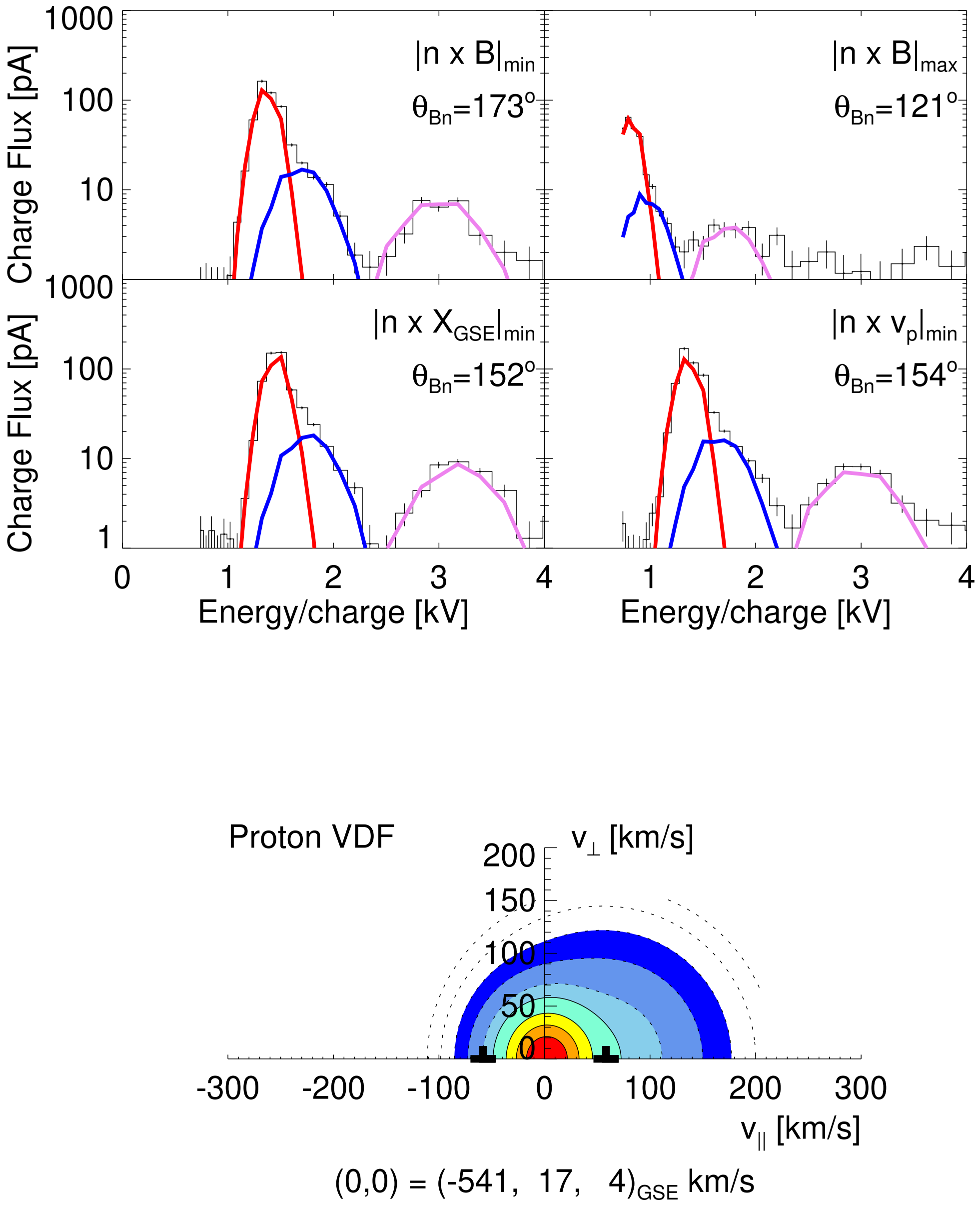

Figure 3.1: An example of four look directions (top) and the corresponding VDF (bottom) as measured by the *Wind*/SWE Faraday Cups on April 21, 2017. (Top) Clockwise, the four look directions are the direction most parallel to $\boldsymbol{B}$, most perpendicular to $\boldsymbol{B}$, most parallel to the proton core velocity, and most radial. Each panel also indicates θ_{Bn}, the angle between FC normal direction and the magnetic field. The bi-Maxwellian is fit in red and the isotropic is fit in blue. An anisotropic fit to the alpha particles is indicated in pink. (Bottom) Contours of the VDF marked with solid lines are 0.8, 0.6, 0.4, 0.2 and dashed lines are 0.1, 0.032, 0.01, 0.0031, 0.001 of the maximum phase space density, matching those in Marsch et al. (1982b). The marks at $\sim \pm 50 \ \mathrm{km\,s^{-1}}$ are the local Alfvén speed. This figure is plotted in the proton core rest frame and the bottom of the figure indicates $\boldsymbol{v}_{p_1}$ in the GSE frame.

the bi-Maxwellian (red) is the core and the isotropic population is the beam (blue, centered at $\sim 1.75\,\mathrm{kV}$). For reference, alpha particles are indicated in pink.

A two-population fit to solar wind protons can be conceived of as a measurement of the solar wind VDF resolved to higher-order. A typical spectroscopic definition for a well defined secondary peak in a single spectrum is when valley between the primary and secondary peak is 10% of the secondary peak (Wüest et al., 2007). This definition implies that the secondary peak is sufficiently well developed that the population it describes is far in excess of a non-Maxwellian perturbation on a primary Maxwellian population. This definition also systematically excludes cases in which the beam is a minor perturbation on the core or the core and beam protons are in a configuration similar to an electron core-halo distribution. As a two population configuration is a non-equilibrium solar wind configuration, any two population fit will tend to evolve towards a single bi-Maxwellian or Maxwellian population. Therefore, a constraint as stringent as those outlined by Wüest et al. (2007) would systematically exclude near-equilibrium, non-LTE measurements and introduce systematic bias. Therefore, we consider the two-population protons well resolved when $\chi^2_\nu < 5$. Based on manual inspection of the data, we also require that the correction from the drifting, isotropic population be at least 1%[6], the energy in the drift be between 1% and 10x the total parallel thermal pressure of both populations[7], the the drift speed be between 27.5% and 172.5% of the Alfvén speed, and the drift speed be less than $350\ \mathrm{km\,s^{-1}}$. Due to operational constraints on the spacecraft, data from before 1998 is ill suited to resolving proton beams. This enables us to resolve 3,220,926 proton beam measurements over more than 20 years during the *Wind* mission in a wide range of solar wind conditions across two solar cycles.

3.4 Typical Beam Properties

Here we present typical properties of proton beams. Section 3.4.1 reports on proton beams in an example Carrington rotation (CR). Section 3.4.2 reports the solar wind speed over 20+ years and the variations of quantities of interest as a function of v_{sw}. Section 3.4.3 describes the stability of the measurements in the $(\beta_{\|}, R)$ plane.

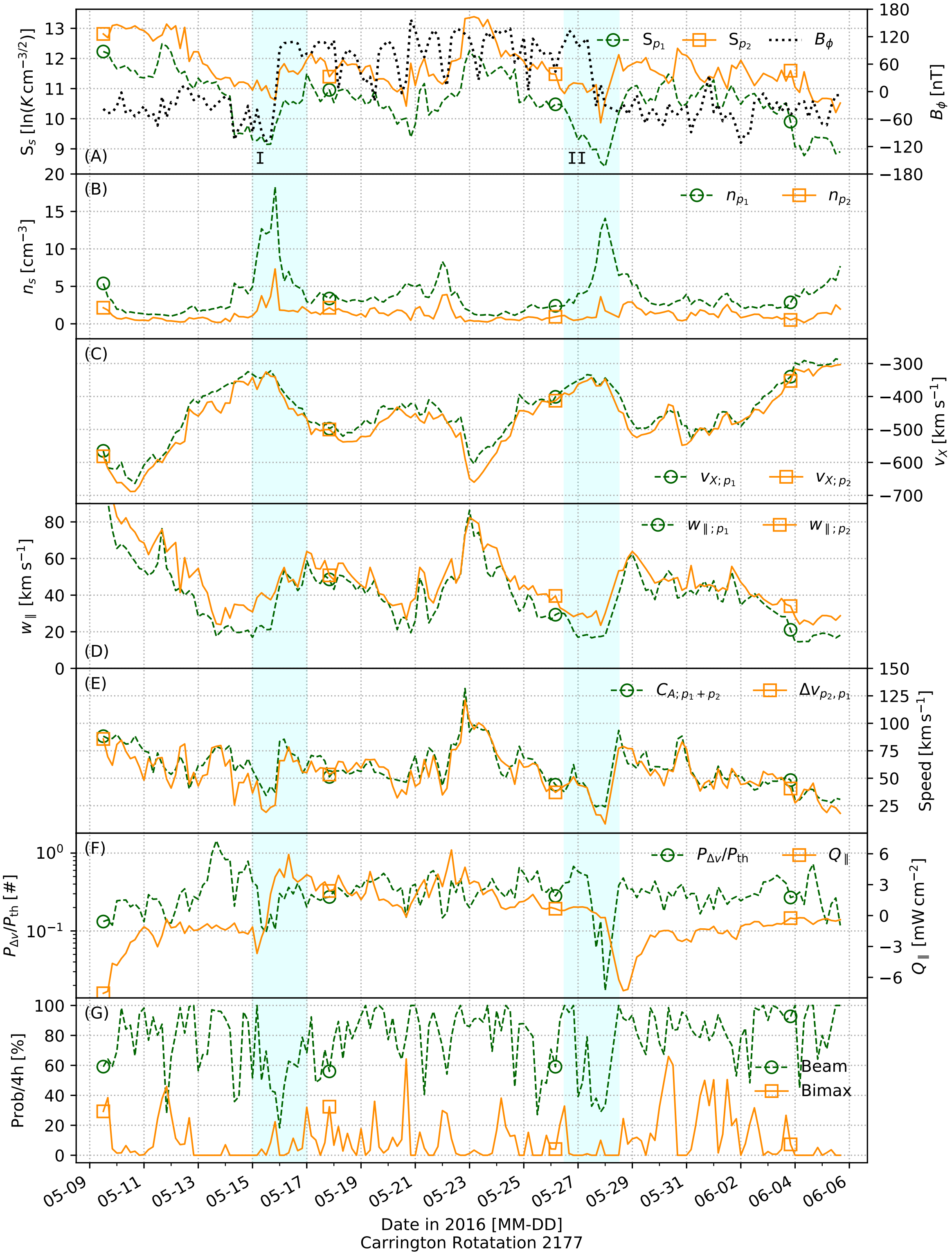

Figure 3.2: Four hour averages in CR 2177. Panels (A) through (D) mark proton cores (X_1) in dashed green and proton beams (X_2) in solid orange. All Panels mark dashed green lines with circles and solid orange lines with squares at every 50th point. When no beam is measured, a gap is present. A two day interval surrounding two sector boundaries are highlighted in blue. Table 3.1 has select cross correlation coefficients for plotted quantitites.

3.4.1 Carrington Rotation 2177

CR 2177 ran from May 10th to June 6th, 2016 during the declining phase of solar cycle 24. The daily sunspot number during CR 2177 ranged between 0 and 88, with an average value of 41 (SILSO World Data Center, 2018). Neither a shock (Stevens and Kasper, 2018) nor an interplanetary coronal mass ejection (ICME)[8] (Cane and Richardson, 2003; Richardson and Cane, 2010) has been reported during this time frame. We applied a 3-point median filter to the measurements during this CR to remove spikes. Figure 3.2 presents four hour averages of the filtered data. In Panels (B) through (D), the proton core quantity (X_1) is shown in dashed green and the proton beam quantity (X_2) is shown in solid orange. When no proton beam is measured, a gap is shown in the beam quantities. For all Panels except (A), dashed green lines are marked with circles, solid orange lines are marked with squares, every 50th point is marked. Table 3.1 gives the cross correlation coefficients for quantities in Figure 3.2 Panels (B) through (E) along with several significant coefficients for quantities across panels.

Panel (A) presents the magnetic field polar angle in dotted black. The blue highlighted regions labeled I and II indicate two sector crossings. Both are marked by large changes in the polar magnetic field field angle that ostensibly correspond to magnetic sector crossings.

Panel (A) also plots the proton specific entropy. The specific entropy can be defined as $S_i \propto \ln(T_i/n_i^{\gamma-1})$ where T_i is the i^{th} species' temperature, n_i is its number density and γ is the polytropic index (Siscoe and Intriligator, 1993; Siscoe, 1983). Marked changes in specific entropy can identify when plasma measurements transition between different solar wind streams (Burton et al., 1999; Pagel et al., 2004). We plot it here to emphasize that the times identified as (I) and (II) are transitions between different solar wind streams. That the cross correlation coefficient between the beam and core specific entropy is > 0.8 emphasizes that the transition between streams is identifiable in measurements of both proton populations, even if in compression region (II) the proton beam is not measured.

Panel (B) presents the beam (p_2) and core (p_1) number densities. The cross correlation coefficient between the densities is 0.752. Both densities increase during the sector crossings, consistent with compression regions. The primary gap in beam measurements occurs during the second crossing (II) when no reliable beams are measured.

Panel (C) presents the component of both proton speeds directed radially away form the Sun in the GSE frame, i.e. the x-component. The cross correlation coefficient between the speeds is 0.978. As the majority of the solar wind flow is anti-sunward, the Parker spiral

---

[6] $\ln f_2\left(\Delta v\right)/f_1\left(\Delta v\right) > -3\ln 10$

[7] Section 3.4.2 defines and describes this.

[8] www.srl.caltech.edu/ACE/ASC/DATA/level3/icmetable2.htm

has significant non-radial components at 1 AU, and the drifts are aligned with the magnetic field, the correlation between v_x of the two proton components is expected. Excluding transient occurrences, the beam is flows faster than the core. Consistent with compression regions, the speeds increase at both sector crossings.

Panel (D) presents the beam and core thermal speed, defined as $w^2 = 2k_bT/m$. To account for the way the "core" and "beam" are selected based on the ratio of $n_{\text{iso}}/n_{\text{bimax}}$, we label both as a parallel component here. However, only 11.2% of the non-filtered measurements correspond to bi-Maxwellian proton beams in this CR. The cross correlation coefficient between the thermal speeds is 0.931. The beam is typically hotter than the core and markedly departs from the core temperature immediately prior to the first sector crossing. Consistent with compression regions, both temperatures increase following each crossings.

Panel (E) presents the magnitude of the differential flow and the local Alfvén speed. The differential flow between species i and j is $|\Delta v_{i,j}| = |\boldsymbol{v}_i - \boldsymbol{v}_j|$. Following Alterman et al. (2018), the Alfvén speed is calculated as $C_A = B/\sqrt{\mu_0 \rho_{p_1+p_2}}$, where $\rho_{p_1+p_2}$ indicates that we are using the total proton mass density. The cross correlation coefficient between these quantities is 0.872 indicating that the magnitude of the drift tracks the local Alfvén speed well. During the sector crossings, the drift speed has large, discontinuous changes of $25\,\mathrm{km\,s^{-1}}$ or more.

Panel (F) presents the drift energy fraction and the parallel heat flux. The drift energy fraction is the fraction of parallel thermal energy in the proton VDF occupied by the drift. It is given by

$$E_{\Delta v} = \frac{\mu \Delta v^2}{P_{\parallel,1} + P_{\parallel,2}} \tag{3.2}$$

for parallel thermal pressures $P_{\parallel,s}$ and pressure due to the differential flow $\mu\Delta v^2$, for which μ is the reduced mass of the two proton populations. This quantity is significant for characterizing the prominency of a proton beam and the VDF's non-thermal structure. It peaks before the first sector crossing and decreases during both crossings, reaching its smallest value during the crossing II. We estimate the parallel heat flux as

$$q_\parallel = \sum_s \rho_s \left(\tilde{v}^3_{\parallel,s} + \frac{3}{2} \tilde{v}_{\parallel,s} w^2_{\parallel,s} \right) \tag{3.3}$$

where $\tilde{v}_{\parallel,s}$ is the component of each species' speed parallel to the local magnetic field calculated in the plasma frame $\tilde{v}_{\parallel,s} = (\boldsymbol{v}_s - \boldsymbol{v}_{\text{CoM}}) \cdot \hat{\boldsymbol{b}}$ and $w_{\parallel,s}$ is each species'f parallel thermal speed. The sum is taken over the species p_1 and p_2. Of note, the heat flux follows the sign of B_ϕ and changes signs in both sector crossings.

n_1	v_1	w_1	C_A	$\Delta v/C_A$	S_{p_1}	$q_\parallel$	$q_\parallel$	n_2/n_1
n_2	v_2	w_2	Δv	B_ϕ	S_{p_2}	B_ϕ	$\Delta v/C_A$	Prob(Bimax)
0.779	0.978	0.930	0.868	0.821	0.807	0.678	0.742	0.628

Table 3.1: Select cross correlation coefficients from Fig. 3.2 Panels (A) through (F).

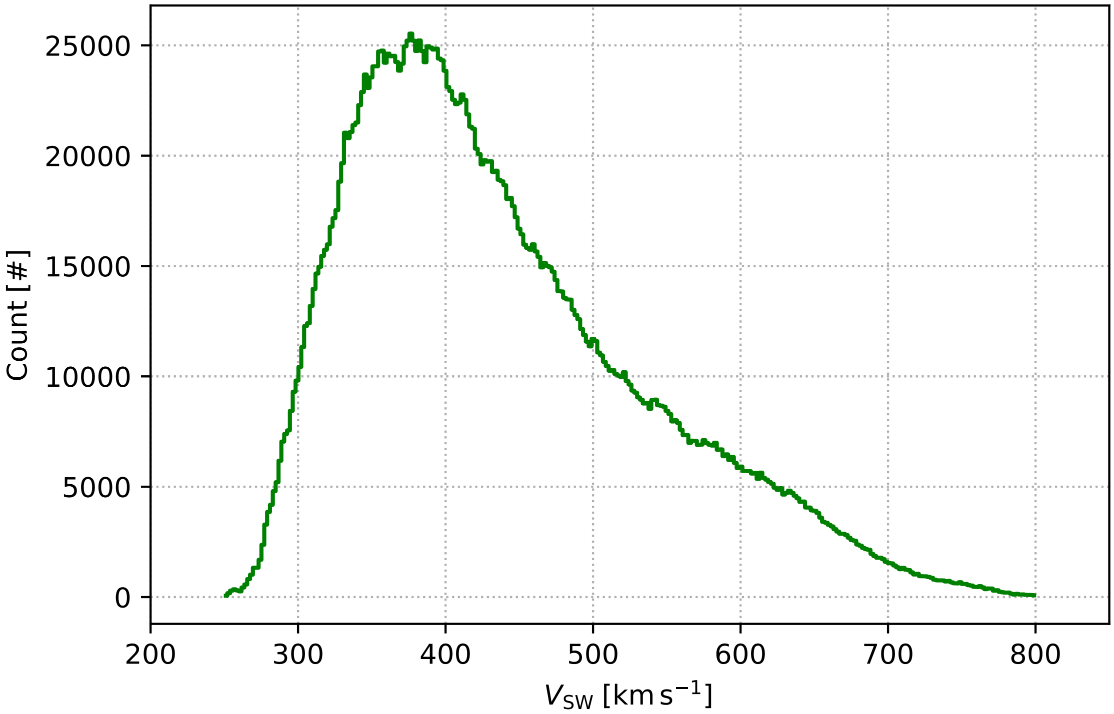

Figure 3.3: A histogram of the solar wind speed (v_{sw}) from $250\,\mathrm{km\,s^{-1}}$ to $800\,\mathrm{km\,s^{-1}}$. The solar wind speed is calculated as the magnitude of the plasma velocity center-of-mass frame. The most common solar wind speed is $376\,\mathrm{km\,s^{-1}}$. The mean solar wind speed is $437\,\mathrm{km\,s^{-1}} \pm 100\,\mathrm{km\,s^{-1}}$.

Panel (G) presents the probability of measuring a proton beam (dotted green) in each 4-hour window. During both sector crossings, the number of reported proton beams drops and then climbs immediately after. The sector crossings also correspond to the two longest decreases in the probability of measuring a beam during this CR. This panel also plots the probability that the bi-Maxwellian population in Equation (3.1) is labelled the proton beam (solid orange). While particular trend is apparent for the probability of measuring a bi-Maxwellian beam, the quantity correlates well with the number density ratio (n_2/n_1, Table 3.1, not plotted for clarity).

3.4.2 Solar Wind Speed

Figure 3.3 reports the solar wind speed v_{sw} for all spectra. The $\sim 1.98\ \mathrm{km\,s^{-1}}$ wide bins are calculated using an automated algorithm[9] that accounts for data variability and size. The most common solar wind speed is $376\ \mathrm{km\,s^{-1}}$ and the mean solar wind speed is $437\ \mathrm{km\,s^{-1}}\ \pm 100\ \mathrm{km\,s^{-1}}$. For statistical reasons and based on inspection of the data, we exclude speeds with $v_{\mathrm{sw}} \geq 800\ \mathrm{km\,s^{-1}}$.

Figure 3.4 presents the variation of significant proton quantities as a function of solar wind speed in $10\ \mathrm{km\,s^{-1}}$ wide bins. Solar wind speed is calculated as in Figure 3.3. Approximately 1 in 5 to 1 in 7 markers is shown[10] with, in all Panels but (F), its standard deviation σ. In the case of Panel (E), these are $\sigma/3$ so that the error bars fit within the plot ranges. The larger spread in these values is not unexpected as they combine low order moments (velocity and density) with pressure to characterize heat flux, a higher order moment with a correspondingly larger uncertainty. As the standard deviation of a boolean value does not represent a typical range of values in a manner suited to this figure, error bars are excluded in Panel (F). Following Figure 3.2, proton core quantities (X_1) are shown in dashed green and proton beam quantities (X_2) are shown in solid orange in Panels (B) to (D). Similarly, for all Panels except (A), dashed green lines are marked with circles and solid orange lines are marked with squares. Normalized quantities in Panels (B) to (D) are shown in dotted fuchsia, marked by plusses, and plotted against the secondary y-axis on the right side of the figure. Tables 3.2 and 3.3 summarize typical values for quantities in panels (B) to (F) in Slow ($v_{\mathrm{sw}} \leq 400\ \mathrm{km\,s^{-1}}$), Intermediate ($400\ \mathrm{km\,s^{-1}} < v_{\mathrm{sw}} \leq 600\ \mathrm{km\,s^{-1}}$), and Fast ($600\ \mathrm{km\,s^{-1}} < v_{\mathrm{sw}}$) solar wind.

Panel (A) presents the magnetic field magnitude. It is typically between $4.0\ \mathrm{nT}$ and $6.8\ \mathrm{nT}$, increasing to $> 6\ \mathrm{nT}$ for speeds $v_{\mathrm{sw}} > 720\ \mathrm{km\,s^{-1}}$. The average standard deviation is $2.4\ \mathrm{nT}$.

Panel (B) presents beam and core number densities. Both dimension-full number densities decrease with speed, however the change in beam density is markedly less than core density. The typical beam density ratio (n_2/n_1) increases with speed by a factor of > 2 from 21% at $285\ \mathrm{km\,s^{-1}}$ to $> 40\%$ at $465\ \mathrm{km\,s^{-1}}$ and - excluding the fastest bin - peaking at 47% when $v_{\mathrm{sw}} = 675\ \mathrm{km\,s^{-1}}$. The average standard deviations are $\sigma\left(n_1\right) = 2.1\ \mathrm{cm^{-3}}$, $\sigma\left(n_2\right) = 1.0\ \mathrm{cm^{-3}}$, and $\sigma\left(n_2/n_1\right) = 0.2$.

Panel (C) presents both population thermal speeds. Here we show the parallel com-

---

[9] `https://docs.scipy.org/doc/numpy/reference/generated/numpy.histogram_bin_edges.html`

[10] The marker and standard deviation frequency increase by 1 or 2 bins so that they don't overlap within a plot.

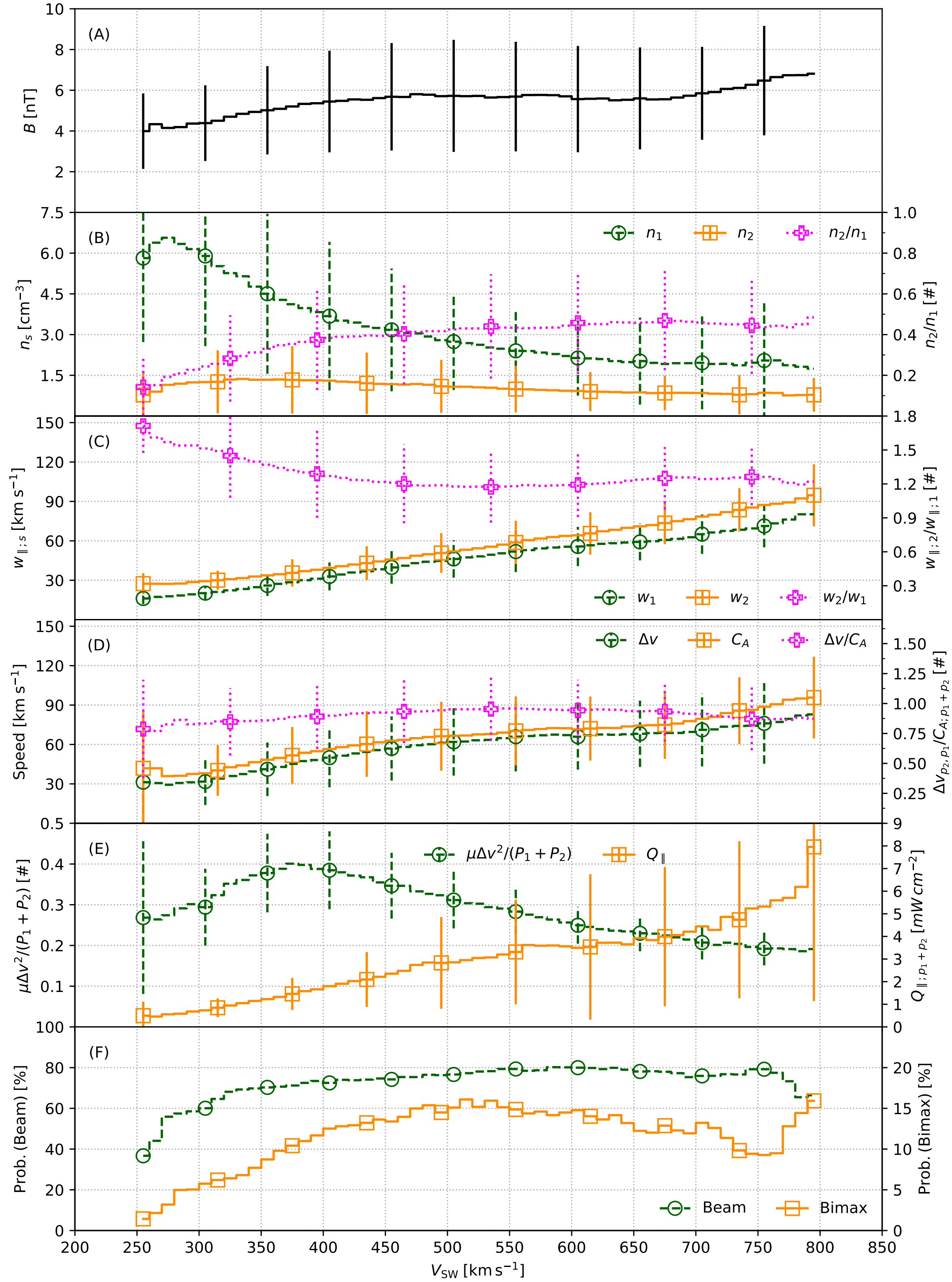

Figure 3.4: Significant quantities as a function of solar wind speed ($v_{\rm sw}$) for bins with at least 5 measurements are shown. Bins are $10\ \mathrm{km\,s^{-1}}$ wide. Every 5th to 7th bin and, in all Panels but (F), its standard deviation is marked for aesthetic clarity. Note Panel (E) uses $\mathrm{stdev}/3$. As a boolean's standard deviation does not represent a typical range of values in a manner suited to this figure, Panel (F) excludes them. Tables 3.2 and 3.3 summarizes these trends in fast, intermediate, and slow wind.

ponent to account for the way we assign the "beam" and "core" label to each population. The parallel thermal speeds increase approximately linearly with speed and the beams are typically hotter than the core. Above $\sim 500\ \mathrm{km\,s^{-1}}$, the slope of both thermal speeds drops off, in particular for the core. The thermal speed ratio $w_{\|,2}/w_{\|,1}$ reflects this change as it decreases monotonically from 1.71 at $v_{\mathrm{sw}} = 255\ \mathrm{km\,s^{-1}}$ to 1.17 at $v_{\mathrm{sw}} = 535\ \mathrm{km\,s^{-1}}$, then increases to 1.26 at $v_{\mathrm{sw}} = 745\ \mathrm{km\,s^{-1}}$, before falling off at the three fastest speeds. The average standard deviations are $\sigma\left(w_{\|,1}\right) = 12.6\ \mathrm{km\,s^{-1}}$, $\sigma\left(w_{\|,2}\right) = 14.0\ \mathrm{km\,s^{-1}}$, and $\sigma\left(w_{\|,2}/w_{\|,1}\right) = 0.3$

Panel (D) shows the Alfvén speed (C_A), differential flow (Δv), and the Alfvén speed normalized differential flow ($\Delta v/C_A$). The Alfvén speed is calculated as in Figure 3.2. After decreasing over the three slowest bins, both the differential flow and the Alfvén speed increase with solar wind speed until $v_{\mathrm{sw}} = 600\ \mathrm{km\,s^{-1}}$, at which point the Alfvén speed increases slightly faster than Δv. The typical normalized drift is $\Delta v/C_A > 0.84$ for all speeds $v_{\mathrm{sw}} \geq 310\ \mathrm{km\,s^{-1}}$, peaking at 0.96 when $v_{\mathrm{sw}} = 545\ \mathrm{km\,s^{-1}}$. The average standard deviations are $\sigma\left(\Delta v\right) = 25.1\ \mathrm{km\,s^{-1}}$, $\sigma\left(C_A\right) = 25.2\ \mathrm{km\,s^{-1}}$, and $\sigma\left(\Delta v/C_A\right) = 0.3$

Panel (E) shows the drift energy fraction (dashed green and circles) and magnitude of the parallel heat flux (solid orange and squares). The typical drift energy fraction increases from 27% in the slowest bins to 40% at $v_{\mathrm{sw}} = 375\ \mathrm{km\,s^{-1}}$, falling again to 19% at $v_{\mathrm{sw}} = 795\ \mathrm{km\,s^{-1}}$. The average drift energy fraction uncertainty is $\sigma\left(E_{\Delta v}\right) = 0.2$. The heat flux increases monotonically from $0.5\ \mathrm{mWcm^{-3}}$ in the slowest bins to $8.0\ \mathrm{mWcm^{-3}}$ at $v_{\mathrm{sw}} = 795\ \mathrm{km\,s^{-1}}$, with a slight plateau between $v_{\mathrm{sw}} = 550\ \mathrm{km\,s^{-1}}$ and $v_{\mathrm{sw}} = 650\ \mathrm{km\,s^{-1}}$. The average heat flux standard deviation is $\sigma\left(Q_{\|}\right) = 6.4\ \mathrm{mWcm^{-3}}$ and increases with v_{sw}.

Panel (F) shows the probability of measuring a beam (dashed green with circles) and the probability that the proton beam has a bi-Maxwellian temperature (solid orange with squares) as a function of v_{sw}. We define the probability of measuring a beam in a given v_{sw} interval as $100 \times N_{p_2}/N_{\mathrm{spec}}$ where N_{p_2} is the number of spectra with a non-zero beam density (3,220,926) and N_{spec} are the total number of spectra (4,606,186). From $v_{\mathrm{sw}} = 270\ \mathrm{km\,s^{-1}}$ to $585\ \mathrm{km\,s^{-1}}$, the probability of measuring a beam increases from 56% to 80% and then decreases to 65% by $v_{\mathrm{sw}} = 785\ \mathrm{km\,s^{-1}}$. The probability that the proton beam has a bi-Maxwellian temperature increases from 1.4% at $v_{\mathrm{sw}} = 255\ \mathrm{km\,s^{-1}}$ to 16.1% at $v_{\mathrm{sw}} = 515\ \mathrm{km\,s^{-1}}$, decreasing again to to 9.3% at $v_{\mathrm{sw}} = 755\ \mathrm{km\,s^{-1}}$. Above this speed, the probability of a bi-Maxwellian beam increases to a maximum of 16.3% at $v_{\mathrm{sw}} = 795\ \mathrm{km\,s^{-1}}$ with appropriately increasing uncertainty due to the decrease in the number of measurements.

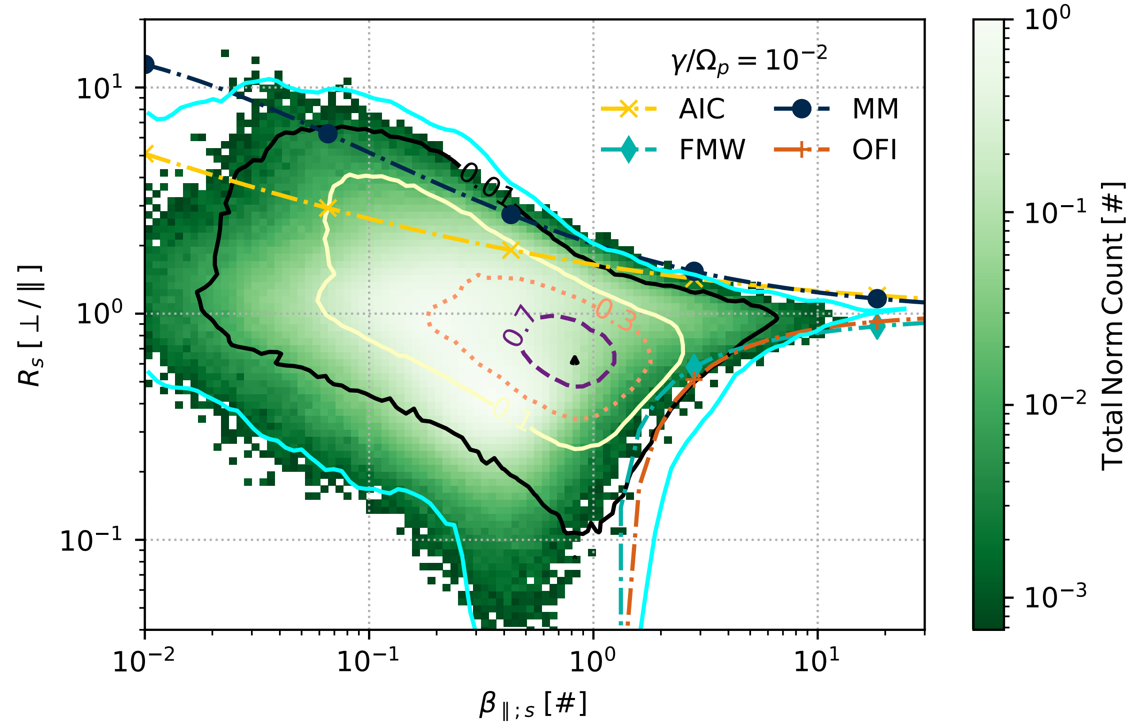

Figure 3.5: Plasma stability in the reduced parameter $(\beta_{\parallel;s}, R_s)$ plane for both the proton core (p_1, indicated in color) and protons from a single bi-Maxwellian model (p, contours). Stability is calculated at the growth rate $\gamma/\Omega_p = 10^{-2}$ for a plasma that includes one proton population. The lowest level shown (solid cyan) is the outer edge of the proton core distribution. From lowest to highest, the other levels shown are are 0.01, 0.1, 0.3, 0.7, 0.99. All but the the 99% level are labelled. The 99% level indicates the single population distribution and is located at $(\beta_{\parallel;p}, R_p) = (0.83, 0.61)$.

3.4.3 Instabilities in the $(\beta_\parallel, R)$ Plane

When a plasma is not in LTE, unstable normal modes that grow with time can be excited. Some of these instabilities transfer energy from particles to electromagnetic fields, reshaping the VDF (Klein et al., 2018; Verscharen et al., 2019). The particular class of instability excited depends on the sources of free energy, e.g. $R \neq 1$, $\Delta v \neq 0$, $\beta \neq 1$, and the presence of multiple species (Verscharen et al., 2019). Multiple authors have shown that two key parameters for identifying when a proton or proton-alpha plasma go unstable are proton (core) temperature anisotropy ($R_T = T_\perp/T_\parallel$) and proton (core) plasma β (Chen et al., 2016; Hellinger et al., 2006; Kasper et al., 2002; Maruca et al., 2012; Verscharen et al., 2013b).

Figure 3.5 presents the proton core (β, R) plane for two cases. The 2D histogram uses proton core $\beta_{\parallel,p_1} = \frac{n_{p_1} k_B T_{\parallel,p_1}}{B^2/2\mu_0}$ and anisotropy is $R_T = T_{\perp,p_1}/T_{\parallel,p_1}$. Only bins with at least 5 measurements are shown. The contours are derived from a 2D histogram generated with *Wind*/SWE observations using a single proton population (Kasper et al., 2006) such that $\beta_{\parallel,p} = \frac{n_p k_B T_{\parallel,p}}{B^2/2\mu_0}$ and the temperature anisotropy is $R_T = T_{\perp,p}/T_{\parallel,p}$, where p indicates that the model VDF used in the fitting procedures only contains a single proton population. Again, only bins with at least 5 measurements are used. The lowest level shown (solid cyan) is the outer edge of the single proton distribution.[11] From lowest to highest, the other levels shown are are 0.01, 0.1, 0.3, 0.7, 0.99. The 99% level is located at $(\beta_{\parallel;p}, R_p) = (0.83, 0.61)$ and all other contour levels are labelled. For both the 2D histogram and the contours, we have selected only spectra with a resolved proton beam. So that we can more easily compare the two data sets, we also only select the subset of cases for which the proton core is has a bi-Maxwellian temperature.

While not strictly applicable to the two population VDFs, we follow Matteini et al. (2013) and show four constant growth rate contours for $\gamma/\Omega_p = 10^{-2}$ as determined by Verscharen et al. (2016). The MM is marked in dark blue with circules. The AIC is marked in yellow with ×. The OFI is marked in orange with vertical bars. The FMW is marked in light blue with diamonds. By inspection, the 2D histogram derived from the two-component fits occupies a smaller fraction of the (β, R) plane than the single-population fits such that the two-component population appears well-constrained by both the OFI and FMW modes as well as being closer to the MM limit than the single-component fit.

3.5 Missing Beams

When the $\Delta v_{p_2,p_1}$ is sufficiently large and the two populations' temperatures are sufficiently cold, resolving the solar wind proton VDF into two distinct populations is straightforward. On the other hand, if the two populations overlap too much, they become impossible to distinguish. After all, they are all protons and the instrument cannot paint each population with a different color and tell from which population individual protons come. For a large fraction of the *Wind* dataset, especially in collisionally young data, the two populations are easy to separate. But Δv becomes progressively smaller compared to the parallel thermal speed as the collisional age increases and a proton beam becomes progressively more difficult to resolve. As such, it is difficult to tell what happens to proton beams at large N_c. Do the typical properties of beams measured at high N_c truly represent the typical beam or just a faster, cooler population we can resolve? Section 3.3 alludes to this problem. Here, we estimate both when we are unable to resolve proton beams and the number of spectra

---

[11] As the outer boundaries of a (β, R) plot are prone to outliers, we smooth the curve for visual clarity (Savitzky and Golay, 1964; Steinier et al., 1972) without loosing the essential shape of the boundary.

that have an undetected beam. We refer to this quantity as the missing beam fraction.

Let plasma N be the number of measurements, n be the subset containing a proton beam, and $x = n/N$ is the fraction split off into a beam. At $x = 0$, the probability that we will create a beam $P(0) = 1$ because no beams exit and we must create a beam. At $x = 1$, $P(1) = 0$ because we have created all possible beams. The simplest equation with such probability is $P(x) = 1 - x$, which we generalize to $P(x) = A(1-x)^b$. To account for the choice that the beam is identified as the population satisfying $\min(n_{\mathrm{iso}}, n_{\mathrm{bimax}})$, we fold the domain back on itself and define $P'(x) = P(x) + P(1-x)$ for $x = [0, 0.5]$ such that $\int_0^{0.5} P(x)\,\mathrm{d}x = 1$ and $A = b+1$. The resulting equation is $P'(x) = (b+1)((1-x)^b + x^b)$. Because this simple technique does not account for covariance between the beam and core densities, it should be considered an upper limit on the number of missing proton beams.

Figure 3.6 plots the PDF of measured beams in solid black. [12] The PDF is calculated in such a fashion as to account for the total number of measurements, including those without a resolved beam. If all proton beams were measured, we would expect the PDF to be a monotonically decreasing function of $x = \min(n_1, n_2)/n_{\mathrm{tot}}$. The portion of the PDF showing this monotonic decay $(x > 0.17)$ is plotted in green and one in 10 bins are marked with an unfilled plus. The solid orange curve is a fit to the PDF over this reduced section of the domain with decay exponent $b = 2.8397 \pm 0.0002$. The area between the PDF (green & black) and the fit represents an upper bound on the number of unresolved proton beams or missing beam fraction (MBF) $974,485 \pm 65,258$, which is equivalent to $\sim 29\%$ of the resolved proton beams and $\sim 21\%$ of all proton measurements, including those without a resolved proton beam.

Klein et al. (2018) studied a statistically meaningful sample of *Wind*/FC measurements consisting of 309 measurements that we have expanded to 557 spectra. In the case of these spectra, the fitting procedure was manually guided and so no data quality selection is applied to the measurements. The gray curve in Figure 3.6 (labelled MF) represents the same procedure applied to these 557 spectra. The bin width has been increased to account for the smaller number of measurements.[13] Repeating the above procedure for the manual fits results in a fit exponent 2.54 ± 0.07, which corresponds to an upper limit of 141 ± 3 missing beams.[14] While not identical, the trends for the two PDFs are qualitatively similar and agree.

---

[12] Bin width $\Delta x = 0.003$ is determined by the automated algorithm `https://docs.scipy.org/doc/numpy/reference/generated/numpy.histogram_bin_edges.html`.

[13] Bin width $\Delta x = 0.05$ is determined by the automated algorithm `https://docs.scipy.org/doc/numpy/reference/generated/numpy.histogram_bin_edges.html`.

[14] Repeating the missing beam calculation for the automated fitting routines in these larger bins results in $b = 2.86 \pm 0.03$, with $1,132,097 \pm 27,752$ missing beams, which is consistent with the results in Figure 3.6.

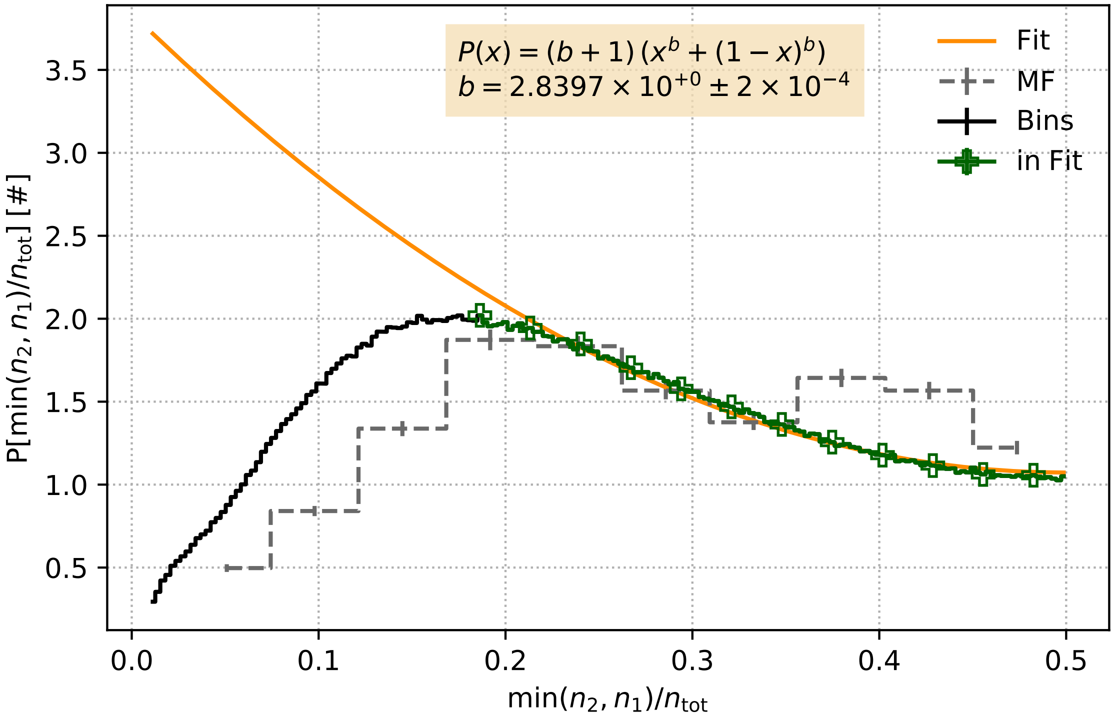

Figure 3.6: The PDF of the relative beam fraction calculated such that the fit normalizes to 1. The PDF of the automated fits is shown in black with error bars smaller than the line. Green indicates the subset fit and is marked by plusses at every 10^{th} bin. The orange solid line is the fit to the green curve. The manual fit PDF (labelled MF) is shown in dashed gray with uncertainties as error bars that are approximately the line width. Using the area between the empirical PDF and fit, we estimate that $974,485 \pm 65,258$ proton beams are unresolved.

3.6 Summary & Conclusions

The evolution of the solar wind is highly sensitive to local structure of its VDF and the associated sources of free energy. The VDF's local gradients can alter both collisional processes and wave-particle interactions (Daughton and Gary, 1998; Daughton et al., 1999; Klein et al., 2018; Liu et al., 2019; Livi and Marsch, 1987; Pezzi et al., 2016; Verscharen et al., 2019). Proton beams can provide additional sources of free energy and significantly alter gradients within the VDF.

The goal of this paper is to describe solar wind at 1 AU when proton beams are measured, thereby establishing an empirical foundation for their impact and significance. To that end, we present proton beam measurements from the *Wind*/SWE/FCs collected in the solar wind covering the years 1998 through May 5, 2019. Section 3.3 discusses our techniques for reducing currents measured by the FCs into physical parameters and the data quality criteria. Section 3.4 presents proton beam measurements in an example CR (Section 3.4.1), as a function of v_{sw} (Section 3.4.2), and in the (β, R) plane (Section 3.4.3). In Section 3.5, we then estimate the number of proton beams that are undetected by our instruments.

Section 3.3 describes the fitting algorithms used to reduce *Wind* Faraday cup measurements into physical quantities. This fitting algorithm models solar wind protons as two populations, one with an isotropic or Maxwellian temperature and the other with a bi-Maxwellian temperature. Note that in an ideal case, both proton populations would be fit with a bi-Maxwellian temperature to capture the VDF's local shape. However, doing so in an automated fashion that yields a statistically large and reliable dataset pushes up against resolution limitations of the SWE/FC system. Restricting one proton population to a Maxwellian enables resolution of the VDF's structure to higher order and with greater statistics. The potential trade off might artificially bias the differential flow away from larger (cases with $T_{\perp,2} > T_{\|,2}$) and smaller (cases with $T_{\perp,2} < T_{\|,2}$) beam anisotropies. The impacts of restricting one proton population to an isotropic temperature is an avenue of future work.

Section 3.4.1 describes the temporal variation of both proton populations in CR 2177 using 4 hour averages. As summarized in Table 3.1, the number densities, radial velocities, and thermal speeds of both populations are well correlated, as are the drift and Alfvén speed. That Δv and C_A are well correlated supports the evidence that the proton beam-core drift is regulated by the Alfén speed (Alterman et al., 2018; Marsch et al., 1982b; Montgomery et al., 1976).

This CR also highlights two sector crossings in blue. That the number densities, speeds,

Quantity	Units	v_{sw}	p_1	p_2	$p_1 + p_2$	p_2/p_1
n	$[\text{cm}^{-3}]$	Fast	2.0 ± 1.5	0.9 ± 0.7	2.9 ± 2.0	0.5 ± 0.2
		Inter.	3.0 ± 2.2	1.1 ± 1.1	4.2 ± 2.9	0.4 ± 0.3
		Slow	4.7 ± 3.0	1.3 ± 1.2	6.0 ± 3.7	0.3 ± 0.2
$w_{\parallel}$	$[\text{km s}^{-1}]$	Fast	59.8 ± 15.2	71.0 ± 17.2	93.5 ± 19.9	1.2 ± 0.3
		Inter.	42.3 ± 14.8	48.6 ± 16.1	65.1 ± 19.8	1.2 ± 0.3
		Slow	25.7 ± 8.8	33.5 ± 9.6	42.7 ± 11.3	1.4 ± 0.4

Table 3.2: Average properties for one-population (p) and two-population proton fits (core: p_1, beam: p_2), total: $p_1 + p_2$) in Slow ($v_{\text{sw}} \leq 400 \ \text{km}\,\text{s}^{-1}$), Intermediate ($400 \ \text{km}\,\text{s}^{-1} < v_{\text{sw}} \leq 600 \ \text{km}\,\text{s}^{-1}$), and Fast ($600 \ \text{km}\,\text{s}^{-1} < v_{\text{sw}}$) solar wind. The total parallel thermal speed is calculated as the geometric mean of the two thermal speeds, in effect reporting the total proton temperature in $\text{km}\,\text{s}^{-1}$. The ratio of the beam to core quantity (p_2/p_1) is also given for each solar wind speed interval. Standard deviations are used to indicate a typical range around the average value.

thermal speeds, specific entropy, and drift velocity increase during each suggests that they correspond to compression regions. Consistent with these increase, the magnitude of the parallel heat flux increases. The sign of the parallel heat flux changes at these crossings, suggesting that the proton heat flux follows the local orientation of the magnetic field $Q_{\parallel}$. Given the definition of $Q_{\parallel}$ in Equation (3.3) and that $\Delta v/C_A$ (omitted in Figure 3.2) is well correlated with B_{ϕ}, this is unsurprising.

Figure 3.2 presents three additional quantities that describe these proton beam measurements. The drift energy fraction $E_{\Delta v}$ describes the relative significance of the pressure in the differential flow as compared to the parallel thermal pressure and shows no particular trend in the sector crossings. The beam measurement probability is the fraction of all measurements within a given 4 hour window that contain a proton beam. This probability Prob(Beam) drops during both sector crossings and reaches its smallest value in this CR during the first crossing, indicating that proton beams may be more difficult to measure during solar wind compression. That Prob(Beam) and $E_{\Delta v}$ are not well correlated with any of the presented quantities indicates suggests a lack of bias towards a particular set of plasma measurements that depends on sector structure or temporal variation at this scale. Of those measurements with a beam, the probability that a proton beam is reported with a bi-Maxwellian temperature (or conversely that the proton core is reported with an isotropic temperature). This quantity is relatively well correlated with the beam density ratio (n_2/n_1, omitted for clarity), indicating that the likelihood that the proton beam is measured with a bi-Maxwellian temperature may be related to the significance of the secondary peak, irrespective of the relative distance between the two proton peaks in velocity space.

Section 3.4.2 extends our examination of these quantities to the full mission. Figure 3.3

Quantity	Units	Fast	Inter.	Slow
Δv	$[\mathrm{km\ s^{-1}}]$	68.5 ± 26.0	58.3 ± 25.3	40.7 ± 20.9
$C_{A;p_1+p_2}$	$[\mathrm{km\ s^{-1}}]$	74.9 ± 25.3	63.9 ± 25.6	47.4 ± 21.9
$\Delta v / C_{A;p_1+p_2}$	$[\#]$	0.9 ± 0.3	0.9 ± 0.3	0.9 ± 0.3
$Q_{\parallel;p_1+p_2}$	$[\mathrm{mW\ cm^{-2}}]$	3.9 ± 10.1	2.6 ± 5.4	1.2 ± 1.8
$\mu \Delta v^2/(P_1 + P_2)$	$[\#]$	0.2 ± 0.1	0.3 ± 0.2	0.4 ± 0.3
$\mathrm{Prob(Beam)}$	$[\%]$	78.6	76.0	68.5
$\mathrm{Prob(Bimax)}$	$[\%]$	13.2	14.1	8.6

Table 3.3: Average properties of quantities specific to two-population fits in Slow ($v_{\mathrm{sw}} \leq 400\ \mathrm{km\,s^{-1}}$), Intermediate ($400\ \mathrm{km\,s^{-1}} < v_{\mathrm{sw}} \leq 600\ \mathrm{km\,s^{-1}}$), and Fast ($600\ \mathrm{km\,s^{-1}} < v_{\mathrm{sw}}$) solar wind. Standard deviations are used to indicate a typical range around the average value. As the standards deviation of a boolean is ill-suited to defining the typical range of probability values, it is excluded from $\mathrm{Prob(Beam)}$ and $\mathrm{Prob(Bimax)}$.

plots a histogram of the solar wind speed. Figure 3.4 presents the same quantities in Figure 3.2 as a function of solar wind speed v_{sw}. Tables 3.2 and 3.3 summarize these quantities in three characteristic solar wind speed ranges: Fast ($v_{\mathrm{sw}} \geq 600\,\mathrm{km\,s^{-1}}$), Intermediate ($400\,\mathrm{km\,s^{-1}} < v_{\mathrm{sw}} \leq 600\,\mathrm{km\,s^{-1}}$), and Slow ($v_{\mathrm{sw}} \leq 400\ \mathrm{km\,s^{-1}}$).

Table 3.2 summarize the number densities and thermal speeds. The typical beam to core density ratio is between 0.1 and 0.7 across wind speeds, which covers the ranges reported by both Helios (Marsch et al., 1982b) and Ulysses (Goldstein et al., 2000, 2010; Matteini et al., 2013). Contrary to Marsch et al. (1982b, Fig. (14)), the density ratio increases with speed and, similar to both Goldstein et al. (2000, 2010) and Matteini et al. (2013), we do find measurements of proton beams with densities comparable to that of the core.

The proton beam temperature is typically larger than the parallel proton core temperature. Daughton and Gary (1998) studied magnetosonic and Alfvén proton beam/core instabilities in the solar wind and show that their growth rates have a strong dependence on T_2/T_1. Following their Fig. (6), magnetosonic instability's growth rates become the dominant when $T_2/T_1 > 1$. The results in Figure 3.4 and Table 3.2 suggest that, while the two instabilities may be active in intermediate and fast wind, the magnetosonic instability is likely to be the more significant of the two in slower solar wind's evolution. Such a study is a direction of future work.

Table 3.3 summarizes the other quantities in Figure 3.4 in the same intervals. Similar to Marsch et al. (1982b), the drift speed increases from slow to fast wind. The Alfvén speed also increases with v_{sw}, but the normalized drift speed is approximately constant. This is consistent with arguments that proton beam-core drift is regulated by the local Alfvén speed, e. g. Montgomery et al. (1976). The parallel heat flux ($Q_{\parallel}$) and the range of values it can take on both increase with v_{sw}. The increase in $\sigma\left(Q_{\parallel}\right)$ with v_{sw} is likely due to both the fact that only 7% of the measurements are made with speeds $v_{\mathrm{sw}} \geq 600\ \mathrm{km\,s^{-1}}$ and that higher order moments of the VDF tend to have correspondingly larger uncertainties.

While the probability of measuring a proton beam is relatively uniform with v_{sw}, the drift energy fraction and probability of measuring a bi-Maxwellian beam are not. The drift energy fraction $E_{\Delta v}$ is typically largest in slow wind and peaks in slow wind at $v_{\mathrm{sw}} = 375\ \mathrm{km\,s^{-1}}$. The probability of measuring a bi-Maxwellian proton beam $(\mathrm{Prob(Bimax)})$peaks in intermediate speed wind at $v_{\mathrm{sw}} = 585\ \mathrm{km\,s^{-1}}$. The SWE/FC measurements are logarithmically spaced in energy and have a resolution $\Delta E/E$ of either 6.5 % or 13 % (Ogilvie et al., 1995). Therefore, at higher energies, the FCs may lack the capability to resolve the small scale structure and gradients in the VDF necessary for the fitting algorithms (Section 3.3) to consistently partition the energy into the drift and parallel temperature of either population across speeds. Following the statements about $E_{\Delta v}$ with respect to Figure 3.2, we therefore cannot rule out that the peaks of these two quantities and the partitioning of parallel energy into the drift or the thermal temperature of either proton population is a function of instrument resolution and not a physical mechanism regulating proton beams.

Many instabilities that drive the solar wind's evolution are strongly dependent on proton parallel beta and anisotropy (Daughton and Gary, 1998; Daughton et al., 1999; Klein et al., 2018, 2017; Verscharen et al., 2019). Figure 3.5 presents the distribution of measurements in the $(\beta_{\parallel}, R)$ plane. The color scale presents the distribution of proton core measurements. The contours present the distribution of proton measurements as determined by fitting procedures that only extract a single proton from the FC currents (Kasper et al., 2006). The outer most contour indicates the outer edge of the single-proton distribution. Similar to the single-proton case (Bale et al., 2009; Hellinger et al., 2006; Kasper et al., 2002; Matteini et al., 2007; Verscharen et al., 2019), neither distribution is limited by the A/IC threshold. However, the proton core distribution does not extend as far past the MM threshold as the single-proton distribution. Moreover, in the case of the FMW and OFI thresholds, the proton core seems to be significantly more limited by both instabilities, rarely crossing the OFI threshold. We infer that, when instrument resolution allows it, modeling the proton VDF with two populations better characterizes its resonant structure.

In Section 3.5 we constructed a probability distribution function and fit it to the empirical PDF (Figure 3.6) to estimate the number of proton beams that go unmeasured by our instrument. We found that $974,485 \pm 65,258$ proton beams were below our instrument resolution. Equivalent to 29% of the measured proton beams and 21% of all measurements, this implies that the *Wind*/SWE/FCs are only measuring 69% of all proton beams. As a result, a significant fraction of both the parallel pressure and, more significantly, resonant structure of the VDF is undetected.

Spacecraft	N_{spec}	N_{p_2}	Fast [%]	Inter. [%]	Slow [%]
Wind	4,606,186	3,255,811	8.3	48.3	43.5
Helios[15]	—	5,765	40.7	44.6	14.7
Helios†[16]	—	56 %	—	—	—
Ulysses	$\sim 150,000$	$\sim 45,000$	—	—	—

Table 3.4: The the total number of measurements (N_{spec}), number of proton beam measurements (N_{p_2}), and percentage of measurements in Slow ($v_{\mathrm{sw}} \leq 400~\mathrm{km\,s^{-1}}$), Intermediate ($400~\mathrm{km\,s^{-1}} < v_{\mathrm{sw}} \leq 600~\mathrm{km\,s^{-1}}$), and Fast ($600~\mathrm{km\,s^{-1}} < v_{\mathrm{sw}}$) solar wind where information for from Helios (Marsch et al., 1982b; Ďurovcová et al., 2019), Ulysses (Matteini et al., 2013), and *Wind* (this paper). The Helios data from Marsch et al. (1982b) is taken from their Fig. (13). The Helios data marked with a dagger (†) is from a recently reprocessed dataset (Ďurovcová et al., 2019) and only provide the percentage of spectra that report a proton beam. (Units are marked accordingly.) The Ulysses numbers are approximate as those are the values provided by Matteini et al. (2013). Omitted information in Helios or Ulysses data is not available in the cited sources.

Figure 3.6 also plots the PDF of measured proton beams using 557 randomly chosen spectra, an expanded set of measurements from those of Klein et al. (2018). In general, the two PDFs agree for intermediate size beams. However, the manually fit spectra report a larger fraction of high density beams ($n_2/n_{\mathrm{tot}} \gtrsim 0.35$) and a smaller fraction of low density beams ($n_2/n_{\mathrm{tot}} \lesssim 0.2$). These differences are likely due in part to systematic bias: (1)the manual fits report two bi-Maxwellian proton populations (Klein et al., 2018) while this data set reports one bi-Maxwellian and one isotropic population and (2) the user-guided manual fits are more likely to report a single proton population with a larger $T_{\|}$ than two proton populations with a small beam that is not well separated from the core. Nevertheless, that the fit exponents agree to within 12% suggests that the two results are consistent.

Table 3.4 presents the number of measurements and the subset with a proton beam from two sets of combined Helios 1 and 2 data, a Ulysses beam-containing dataset, and this paper. The two Helios data sets come from Marsch et al. (1982b) and a recently reprocessed data set from Ďurovcová et al. (2019). Marsch et al. (1982b, Fig. (13)) report a combined 5,765 proton beam measurements from both Helios probes and breaks down the measurement frequency across Slow ($v_{\mathrm{sw}} \leq 400~\mathrm{km\,s^{-1}}$), Intermediate ($400~\mathrm{km\,s^{-1}} < v_{\mathrm{sw}} \leq 600~\mathrm{km\,s^{-1}}$), and Fast ($600~\mathrm{km\,s^{-1}} < v_{\mathrm{sw}}$) solar wind. We find 565 times the number of proton beams in SWE/FC data measured by *Wind*. Breaking this down by solar wind type, we find intermediate speed proton beams with relatively the same frequency to within 3.7 percentage points. However, Marsch et al. (1982b) report fast wind proton beams 4.9 times more often than we find with *Wind* and we find slow wind proton beams 3.0 times more often than Marsch et al. (1982b). Comparing with the recently reprocessed Helios dataset (Ďurovcová et al., 2019) that uses fitting techniques instead of moments, we find proton beams 1.3 times more often than Ďurovcová et al. (2019) in their reprocessed Helios dataset. Comparing to Ulysses, we report 72 times as many proton beams (Matteini et al., 2013) and identify proton beams ~ 2.4 times as frequently.

3.7 Appendix: A Comparison of the Single and Two Population Proton Bulk Parameters

Kasper et al. (2006) document non-linear fitting method for reducing currents measured by a FC into physical quantities. They use this method to extract physical quantities for a single proton population and alpha particles. This chapter extends their method to extract two proton populations from the same FCs onboard the *Wind* spacecraft. Here, we statistically compare the two-population proton fits with the equivalent single population protons from Kasper et al. (2006). We illustrate that, while the velocity of the protons changes little when the fitting algorithms are expanded to include a proton beam, the shape (both density and temperature) do.

Figures 3.7 to 3.11 compare a given quantity from the (a) proton core and (b) total proton number in the two-population fits (y-axis) to the analogous quantity from the single population algorithms (x-axis). The top panel in each figure is a 2D PDF and the bottom panel is a column normalized 2D histogram. Only bins with at least 10 counts are shown. The PDFs indicate the relative likelihood of a given result from the two-populations fits for a given value of the single-population fit. The column normalized histograms emphasize the trend of the two-population quantity as a function of the single-population quantity. The solid green line indicates unity, i. e. where the two-population value equals the single population value. The dashed green line marked with unfilled plusses (every 5th bin) indicates the mean of the two-population fit in the single-population bins. The gray bands are the standard deviation for each mean indicated by the dashed green line. The dashed blue line is robust fit to the means weighted by the standard deviations. Typically the dashed blue and dashed green lines are colocated. The fit parameters to their uncertainty is given in the insert. The trends and fits in a given top and bottom pair of panels are identical.

Figure 3.7 compares the (a) proton core and (b) total proton densities from the two population fits to the proton densities derived from the single population fits. Comparing the dashed lines, column normalized trends, and fit parameters to unity, the proton core typically reports a number density is smaller than that of the single-population protons. For higher densities ($n \gtrsim 15\ \mathrm{cm}^{-3}$), equal density between the core and single-population

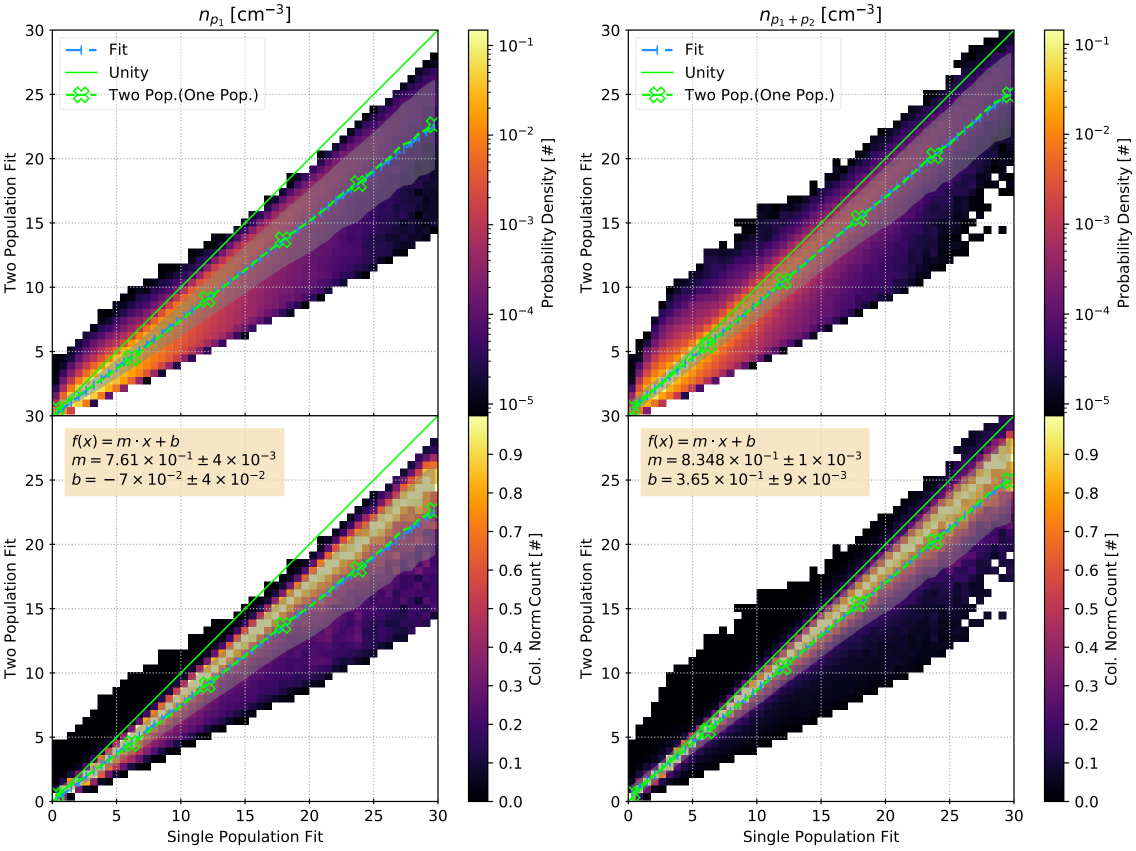

(a) (b)

Figure 3.7: 2D Plots comparing (a) the proton core and (b) the total proton number density from the two-population fits to the proton density from the single population fit. Only bins with at least 10 counts are shown. The top in each case is the PDF and the bottom is column normalized version of the 2D histogram to emphasize the trend. The solid green line indicates unity. The dashed green line indicates the average of the two-population quantity in the column defined by the single-population fit; every 5th bin is marked with an unfilled plus. Gray regions indicate the standard deviation around the dashed green trend. A robust fit using the standard deviations as weights is given with a dash-dash-dot blue line. The text insert indicates the fit parameters and their uncertainties. The fits and trends in a given top and bottom pair of panels are identical.

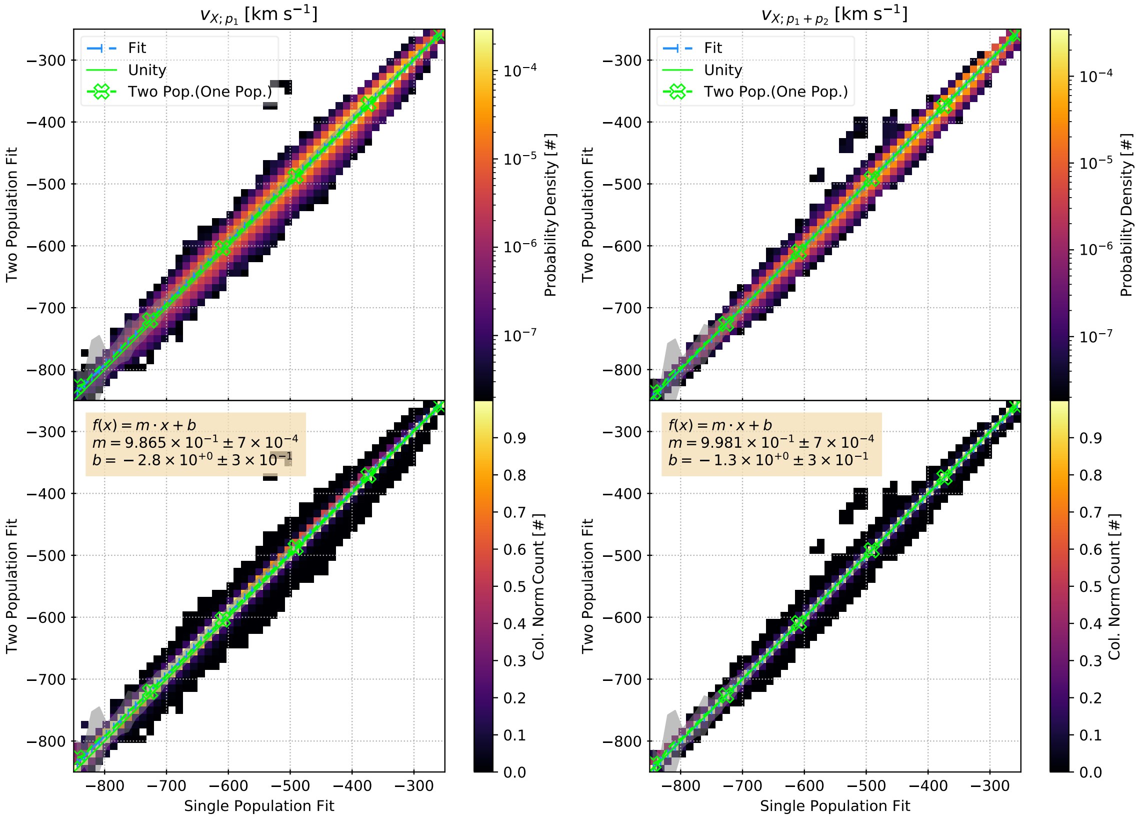

(a) (b)

Figure 3.8: 2D Plots comparing (a) the proton core and (b) the total proton center-of-mass velocity's x-component from the two-population fits to the parallel proton temperature from the single population fit. Figure style follows Figure 3.7

protons is an upper limit on the proton core and the fit indicates that $n_{p_1} = 76.1\% n_p$. While the total proton density ($n_{p_1+p_2}$) is typically only 0.8348 times that of the single-population density, this is $\sim 10\%$ larger than the proton core. That equal density with the single-population protons is not an upper bound on the total two-population density implies that the results of fitting the measured spectra with a single population and beam-core model VDF disagree when a small proton beam cannot be rejected by the single population fitting algorithms. For completeness, we note that the difference in minimum resolved proton core number density and single-population proton density (fit parameter $b = -0.07$) is vanishingly small, whereas the total $n_{p_1+p_2}$ to single proton comparison implies that the significance of small proton beams cannot be ruled out as trivial.

Figure 3.8 compares the x-component of (a) the proton core and (b) the center-of-mass velocity to the single population protons in the Geocentric Solar Ecliptic (GSE) frame. In other words, this is the radial component of the velocity. The figure's format follows

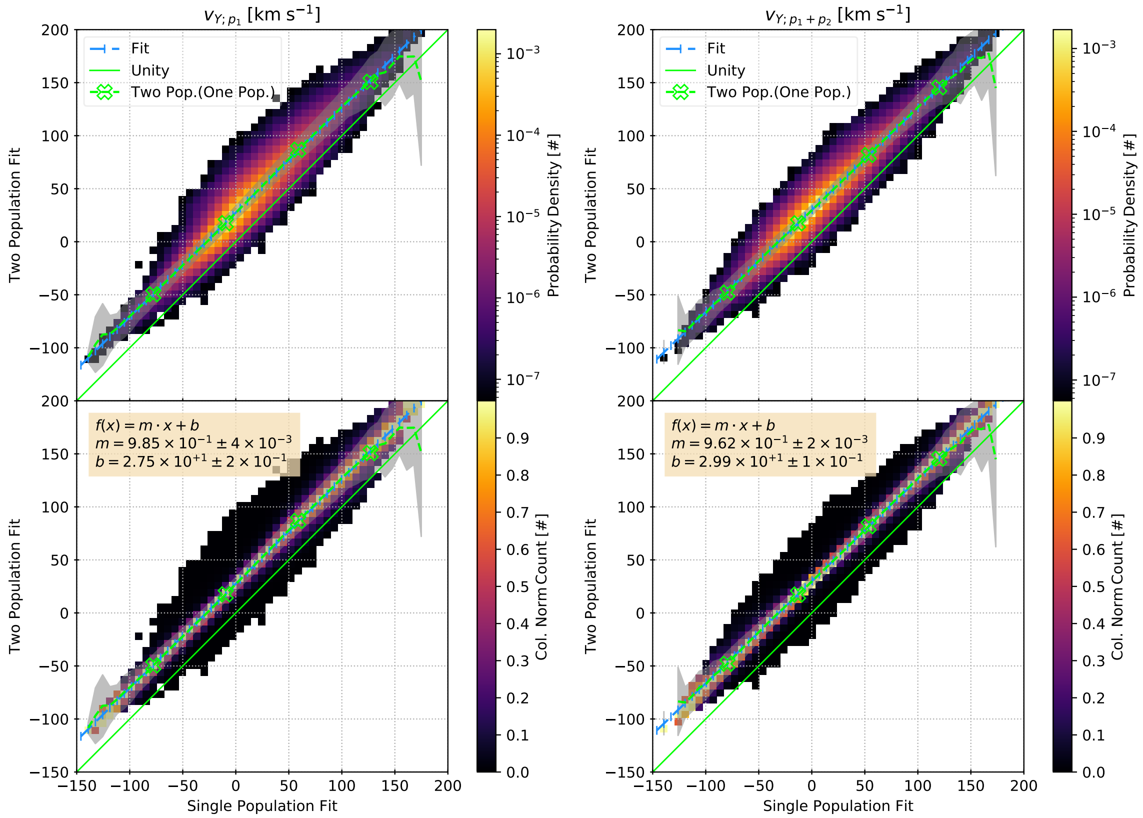

(a) (b)

Figure 3.9: 2D Plots comparing (a) the proton core and (b) the total proton center-of-mass velocity's y-component from the two-population fits to the parallel proton temperature from the single population fit. Figure style follows Figure 3.7

Figure 3.7. In both cases, the two-population fit is within 1.5% of single population's x-component and the statistical offset (fit parameter b) in both cases is on the order of a couple $\mathrm{km\,s^{-1}}$, or approximately the size of a low-velocity energy window and therefore negligible. As the majority of the solar wind's flow is anti-sunward and the radial component of the velocity is one of the higher quality FC measurements, the statistical agreement of the results from both fitting routines lends confidence to the results.

Figures 3.9 and 3.10 examine the y- and z-components of the proton velocity in the same manner as Figure 3.8. As these are in the GSE frame, the z-component is perpendicular to the plane of the Earth's orbit (nominally the out-of-ecliptic direction) and the y-component completes the triad, effectively in the direction anti-parallel to the Earth's orbital direction. As the Parker spiral is typically larger than 45^o at 1 AU and any proton beam-core drift that is not parallel to $\boldsymbol{B}$ would be washed out within a few gyroperiods, it is expected that the z-component of the velocity would show little offset ($< 1\ \mathrm{km\,s^{-1}}$)

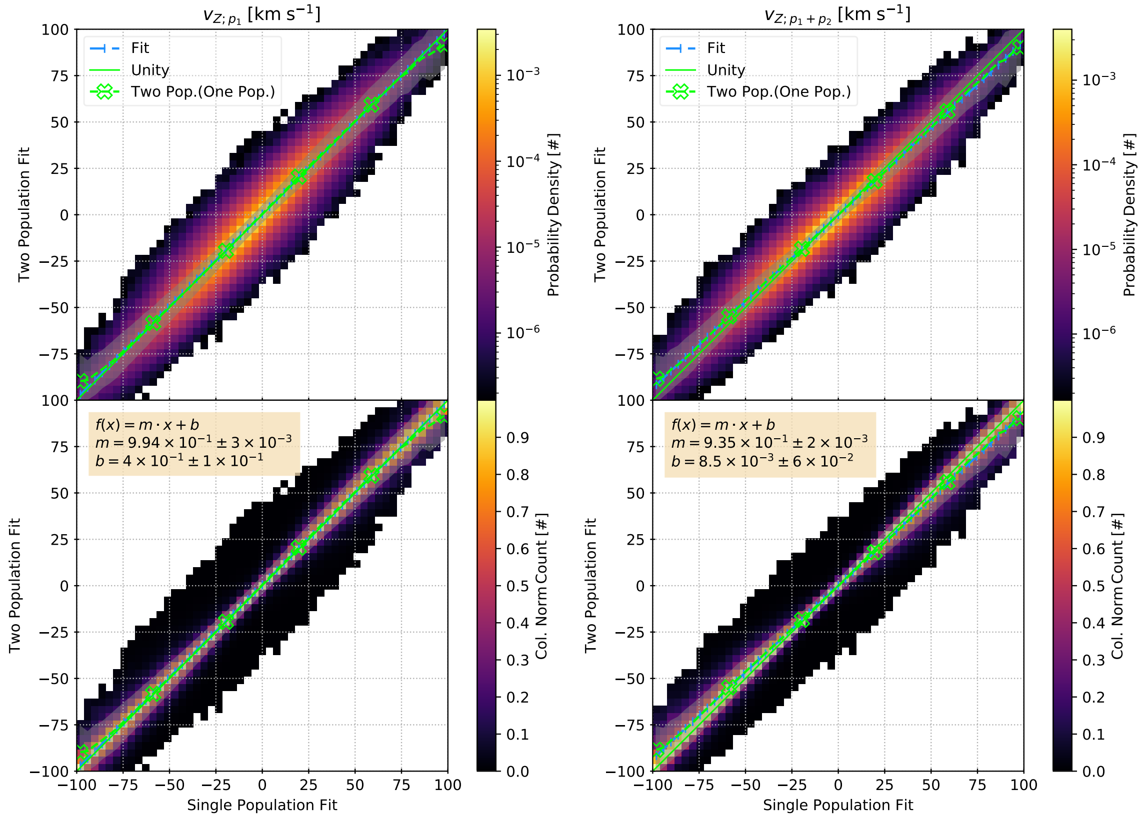

(a)

(b)

Figure 3.10: 2D Plots comparing (a) the proton core and (b) the total proton center-of-mass velocity's z-component from the two-population fits to the parallel proton temperature from the single population fit. Figure style follows Figure 3.7

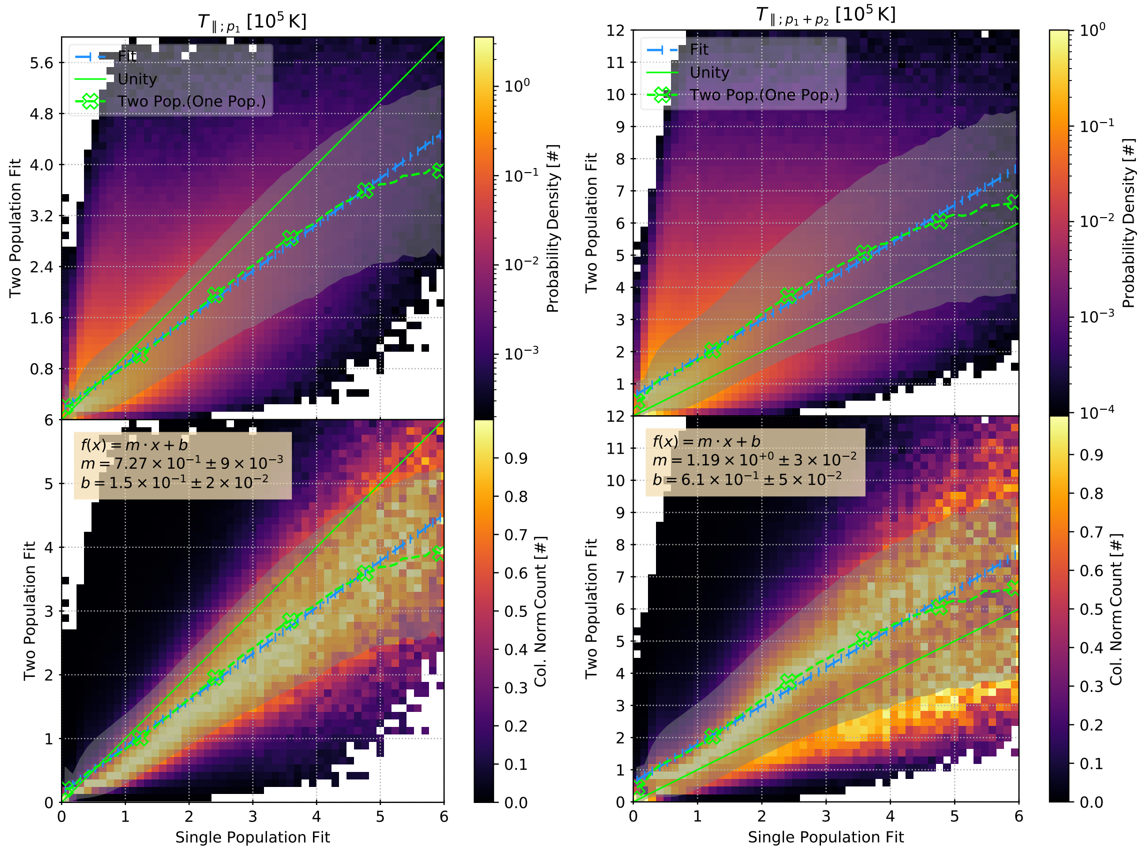

(a)

(b)

Figure 3.11: 2D Plots comparing (a) the proton core and (b) the total proton parallel temperature from the two-population fits to the parallel proton temperature from the single population fit. Figure style follows Figure 3.7

with respect to the single-population fit, but the y-component of the velocity would show a marked offset from the single-population fits ($\sim 30\ \mathrm{km\,s^{-1}}$), approximately twice earth's orbital speed around the Sun). Outside of these offsets, the agreement between the two-population and single-population velocity components is better than 5%.

Figure 3.11 compares the parallel temperatures in the style of Figure 3.7. Panel (a) compares the proton core temperature and panel (b) compares the sum of the proton core temperature and the proton beam temperature to the single-proton temperature. In the case of panel (b), the comparison does not include the energy stored in the differential flow. Note that unlike previous figures, the y-range in panel (b) of this figure is twice that in panel (a) and so the aspect ratio in (b) differs from (a) by a factor of 2.

In comparison to Figures 3.7 to 3.10, the comparison between the parallel component of the temperature shows the largest difference between the two-population and single-population fits. The offset between the two- and one-population fits (fit constant b) is on the order of 10%. The proton core temperature is typically 28% smaller than the single-population proton temperature and the sum of the beam and core temperatures is approximately 19% larger than the single population temperature. Moreover, in comparison to Figures 3.7 to 3.10, the range in typical values (gray band and scatter in column normalized panel) is markedly more significant.

Figures 3.7 to 3.11 statistically compare the number density, velocity vector components, and parallel temperature from the proton core along with the total proton beam and core with the analogous quantity derived from the single population proton fits. Figure 3.7 illustrates that, statistically, the number density of the proton beam is a non-trivial correction to the solar wind proton density. Figures 3.10 to 3.10 demonstrate that the location of the proton distribution in velocity space only markedly changes in the y-GSE component, as expected due to the addition of a secondary proton population of non-trivial density that drifts along the Parker spiral. Figure 3.11 statistically compares the parallel component of the temperature across the two fit algorithms. Only a comparison of the parallel component is present because differential flow must be along $\hat{\boldsymbol{b}}$. Noting that the comparison between these temperatures do not account for the additional energy stored in the differential flow, this supports the interoperation that proton beams capture non-trivial thermal structure int he solar wind that is unresolved by a single proton population. Given the non-trivial density and temperature of the proton beam, a description of the resonant interaction between solar wind protons and fields would be incomplete without the beam's inclusion.

CHAPTER 4

Collisionally Young Differential Flow

This chapter compares collisionally young proton beam-core and alpha-proton differential flow. The *Astrophysical Journal* published it in 2018 (Alterman et al., 2018). The authors are B. L. Alterman, Justin C. Kasper, Michael L. Stevens, and Andriy Koval.

4.1 Abstract

In fast wind or when the local Coulomb collision frequency is low, observations show that solar wind minor ions and ion sub-populations flow with different bulk velocities. Measurements indicate that the drift speed of both alpha particles and proton beams with respect to the bulk or core protons rarely exceeds the local Alfvén speed, suggesting that a magnetic instability or other wave-particle process limits their maximum drift. We compare simultaneous alpha particle, proton beam, and proton core observations from instruments on the *Wind* spacecraft spanning over 20 years. In nearly collisionless solar wind, we find that the normalized alpha particle drift speed is slower than the normalized proton beam speed; no correlation between fluctuations in both species' drifts about their means; and a strong anti-correlation between collisional age and alpha-proton differential flow, but no such correlation with proton beam-core differential flow. Controlling for the collisional dependence, both species' normalized drifts exhibit similar statistical distributions. In the asymptotic, zero Coulomb collision limit, the youngest measured differential flows most strongly correlate with an approximation of the Alfvén speed that includes proton pressure anisotropy. In this limit and with this most precise representation, alpha particles drift at 67% and proton beam drift is approximately 105% of the local Alfvén speed. We posit that one of two physical explanations is possible. Either (1) an Alfvénic process preferentially accelerates or sustains proton beams and not alphas or (2) alpha particles are more susceptible to either an instability or Coulomb drag than proton beams.

4.2 Introduction

Simple models of solar wind acceleration (e.g. Parker (1958)) are unable to explain the solar wind's acceleration to high speeds. Wave-particle interactions are likely necessary to explain these observations. Differential flow is the velocity difference between two ion species. It is a useful indicator of such interactions and related acceleration.

Ionized hydrogen (protons) are the most common ions in the solar wind, usually constituting over 95% by number density. Fully ionized helium (alpha particles, α) are the second most common species and constitute $\sim 4\%$ of the solar wind by number density. Within a few thermal widths of their mean speed, solar wind protons are well described by a single bi-Maxwellian VDF. However, an asymmetric velocity space shoulder has also been observed in the proton distribution. It can be described by a second, differentially flowing Maxwellian. We refer to the primary proton component as the proton core (p_1) and the secondary component as the proton beam (p_2). Proton beams are most easily measured in fast solar wind, when the local Coulomb collision frequency is small in comparison to the local expansion time, and the solar wind is typically cold.

Differential flow is the velocity difference between two ion species or populations. It has been measured in the solar wind plasma at many solar distances starting in the corona and, when the local collision rate is smaller than the expansion time, extending out to and beyond 1 AU (Asbridge et al., 1976; Feldman et al., 1974a; Goldstein et al., 1995; Kasper et al., 2008; Landi and Cranmer, 2009; Marsch et al., 1982a,b; Neugebauer, 1976; Steinberg et al., 1996). Kasper et al. (2006) showed that α differential flow is aligned with the magnetic field $\boldsymbol{B}$ to within several degrees as long as it is larger than $\sim 1\%$ of the measured solar wind speed, consistent with any apparent non-parallel flow being measurement error. It should not be surprising that differential flow is field aligned because any finite differential flow perpendicular to $\boldsymbol{B}$ would immediately experience a Lorentz force until the plasma was again gyrotropic on a timescale comparable to the ion gyroperiod. We denote the differential flow as $\Delta v_{b,c} = (\boldsymbol{v}_b - \boldsymbol{v}_c) \cdot \hat{\boldsymbol{b}}$, where b can c indicate distinct ion species or populations within a single species and $\hat{\boldsymbol{b}}$ is the magnetic field unit vector. Positive differential flow is parallel to local $\boldsymbol{B}$ and negative differential flow is antiparallel to it. Simultaneous measurements of α-particles and protons indicate that $\Delta v_{\alpha,p1}$ is typically $\lesssim 70\%$ of the local Alfvén speed, C_A. Asbridge et al. (1976); Feldman et al. (1974a); Kasper et al. (2017, 2008); Neugebauer (1976) While measurements of heavier ions (e.g. iron, oxygen, carbon) show similar behavior Berger et al. (2011), proton beam-core differential flow ($\Delta v_{p_2,p_1}$) has been reported at approximately the local Alfvén speed or larger Marsch et al. (1982b). Given that the local Alfvén speed in the solar wind is generally a decreasing function of distance from the Sun, this apparent Alfvén speed limit implies that there is effectively a local wave-mitigated limit on $\Delta v_{p2,p1}$, for which several instability processes have been hypothesized. Daughton and Gary (1998); Daughton et al. (1999); Goldstein et al. (2000) Simulations by Maneva et al. (2015) showed that a nonlinear streaming instability limits alpha particle drift to a maximum of $0.5\,C_A$.

Raw data from the Wind/SWE Faraday cups are now archived at the NASA Space Physics Data Facility (SPDF) and available online at CDAweb. We have developed a new fitting algorithm that returns simultaneous parameters for three solar wind ion populations (α, p_1, and p_2) and have processed over 20 years for Faraday cup solar wind measurements. For this project, we have restricted the analysis to measurements with clear differential flow signatures for both the alpha particle and proton beam components. We find that $\Delta v_{\alpha,p_1}/C_A$ and $\Delta v_{p_2,p_1}/C_A$ are indeed clustered around characteristic values that are consistent with previous results, but with considerable spreads in the respective distributions. We investigate possible contributions to the spreads; the apparent impact of Coulomb collisions in the weakly-collisional regime; and the limitations of calculating the Alfvén speed under the commonly assumed frameworks of ideal and anisotropic MHD. We report that in collisionless solar wind:

1. α particle and p_2 differential flow speeds exhibit distinctly different trends with the locally-measured Coulomb collision rate;
2. Coulomb collisions account for the dominant contribution to the spread in $\Delta v/C_A$;
3. and an accounting for the proton pressure anisotropy in the local Alfvén speed, as under anisotropic MHD, significantly reduces the spread in $\Delta v/C_A$.

For the most nearly collisionless solar wind measured at 1 AU and using the more precise, anisotropic approximation of the Alfvén speed we report that:

1. $\Delta v_{p_2,p_1}$ is $106\% \pm 15\%$ of the local Alfvén speed;
2. $\Delta v_{\alpha,p_1}$ is $62\% \pm 13\%$ of the local Alfvén speed;
3. and $\Delta v_{p_2,p_1} \approx 1.7 \times \Delta v_{\alpha,p_1}$.

Finally, we extrapolate to the perfectly collisionless limit, and estimate that:

1. $\Delta v_{p_2,p_1}$ is $\sim 105\% \pm 15\%$ of the Alfvén speed and
2. $\Delta v_{\alpha,p_1}$ is $67\% \pm 9\%$ of the Alfvén speed.

4.3 Data Sources & Selection

The *Wind* spacecraft launched in fall 1994. Its twin Faraday cup instruments have collected over 6.1 million proton and alpha particle direction-dependent energy spectra, the majority of which are in the solar wind. Ogilvie et al. (1995) Available on CDAweb, these raw spectra consist of measured charge flux as a function of angle and energy-per-charge for each cup. With these spectra, we reconstruct 3D VDFs for each ion species and extract the bulk plasma properties: number density, velocity, and thermal speed. Over more than 20 years, refinements in the data processing algorithms have yielded new information from these distributions including precise α particle abundances Aellig et al. (2001); Kasper et al. (2012, 2007), perpendicular to parallel proton temperature ratios Kasper et al. (2002, 2008), and relative alpha to proton temperature ratios Kasper et al. (2008); Maruca et al. (2013).

Ogilvie et al. (1995) provide a thorough description of the Solar Wind Experiment (SWE). In summary, the SWE Faraday cups measure a single energy window approximately every $3\mathrm{s}$ and a full spectrum combines multiple energy windows measured over $\sim 92\mathrm{s}$. Our fitting algorithm utilizes magnetic field measurements from the *Wind* Magnetic Field Investigation (MFI) Koval and Szabo (2013); Lepping et al. (1995) to determine each VDF's orientation relative to the local magnetic field and it assumes that the extracted parameters are approximately constant over the measurement time. In spectra for which this is not the case, automatically processed bulk properties can be unreliable.

This new fitting algorithm returns 15 simultaneous parameters for three solar wind ion-populations: alpha particles (α), proton cores (p_1) and proton beams (p_2). Kasper et al. (2006) describes the six parameter α fitting routines. The protons are jointly fit by a nine-parameter set: six to p_1 (number density, vector velocity, and parallel & perpendicular temperature) and three to p_2 (number density, differential flow, and isotropic thermal speed).[1]

Previous work with this data includes studies by Chen et al. (2016); Gary et al. (2016). Figure 4.1 shows example energy-per-charge measurements made in four representative look directions. These directions are identified by the angle between the magnetic field and the direction normal to the Faraday cup's aperture. Figure 4.2 provides the corresponding proton (top) and α (bottom) VDFs. The proton beam is the extension of the proton VDF to large $v_{\parallel} > 0$.

Our alpha particle and proton core quality requirements nominally follow Kasper et al. (2002, 2008, 2007). Because this study focuses on measurements with a clear differential

---

[1] This fitting algorithm used in this chapter differs from that in Chapter 3. The one in Chapter 3 is optimized to reliably resolve smaller proton beams at higher collisional ages than the one in this chapter. However, the Chapter 3 does not resolve alpha particles.

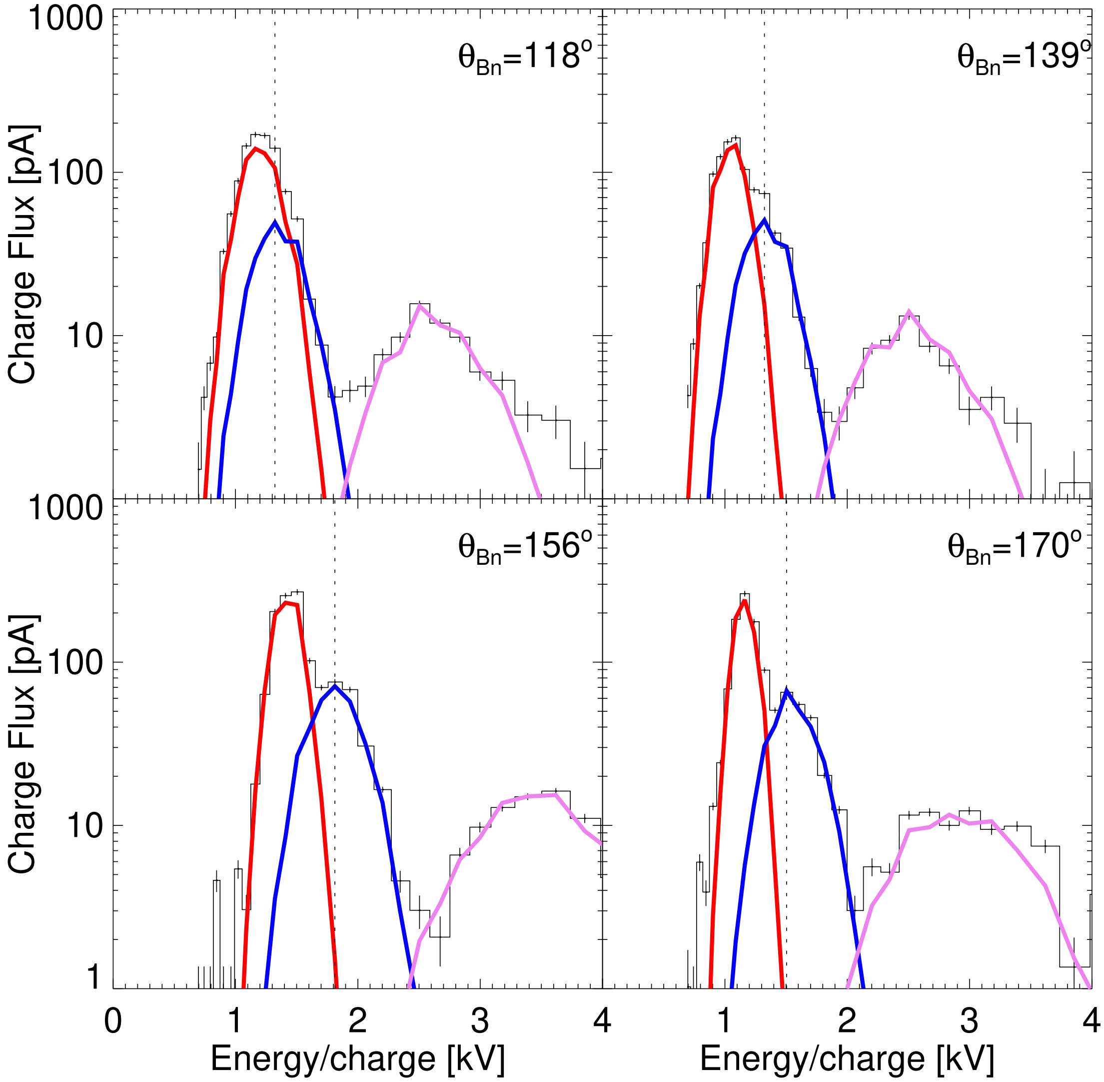

Figure 4.1: Fits from four example look directions from the *Wind* Faraday cups using a new data processing algorithm. Three ion populations are shown: α (purple), p_1 (red), and p_2 (blue). The angle of a given look direction with respect to the average magnetic field throughout the spectrum is indicated in the top right of each panel. Errors for each Energy/charge bin are vertical dashed lines.

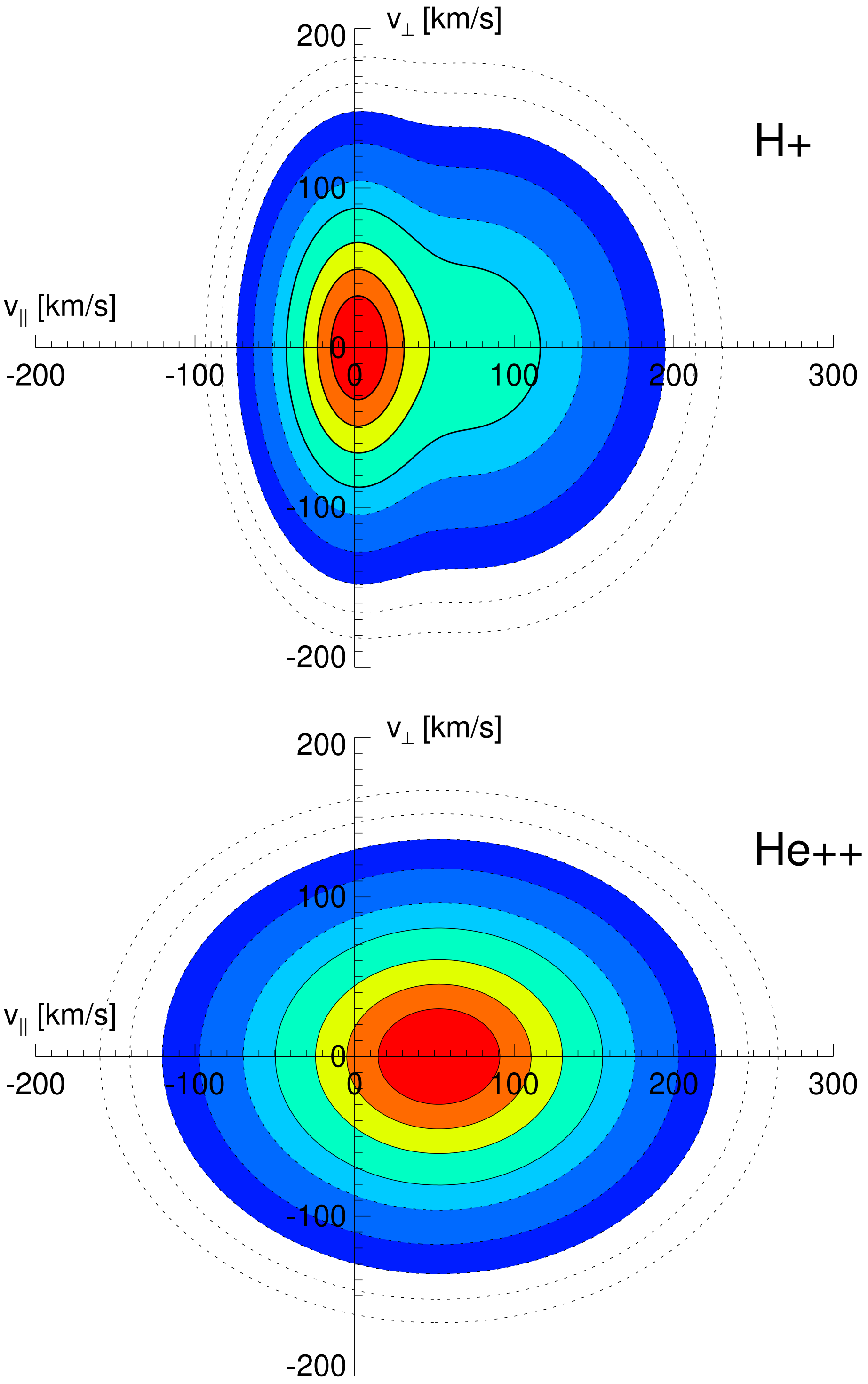

Figure 4.2: VDFs corresponding to the spectrum shown in Fig. 4.1. The joint proton VDF is shown on (top) and the α particle VDF is shown on (bottom). The proton beam can be identified by the secondary shoulder with a large $v_{||}$ in (top) plot. Contours follow Marsch et al. (1982b). In decreasing order, solid lines are 0.8, 0.6, 0.4, 0.2 and dashed lines are 0.1, 0.032, 0.01, 0.0031, 0.001 of the maximum phase space density.

flow signature, we allow an additional class of fits for which the alpha particle temperature has been fixed to the proton core temperature so long as the alphas are well separated from the proton beam. To ensure that the magnetic field is suitably constant over the measurement time, we follow Kasper et al. (2002) and we reject spectra for which the RMS fluctuation of the local magnetic field direction is larger than 20^o. In addition to the reported impact on alpha particle measurements, we find that excluding these spectra also improves the overall quality of reported proton beams. To ensure that the beam is well constrained, we only include spectra for which the beam phase space density is larger than the core phase space density at the beam's bulk velocity, i.e. $f_{p_2}/f_{p_1}\left(\boldsymbol{v}_{p_2}\right) \geq 1$. The vertical dashed lines in Figure 4.1 indicate where this ratio is evaluated in each look direction. The look directions that are most aligned with the magnetic field direction give the clearest view of the beam.

4.4 Fast Wind Differential Flow

Figure 4.3 shows the distributions of simultaneously-measured differential flows in the fast wind ($v_{\text{sw}} \geq 400~\mathrm{km\,s^{-1}}$) under conditions where the alphas and protons are both roughly collisionless ($10^{-2} \lesssim A_c \lesssim 10^{-1}$).[2] The dashed lines are alpha-proton core differential flow ($\Delta v_{\alpha,p_1}/C_A$) and the solid lines are proton beam-core differential flow ($\Delta v_{p_2,p_1}/C_A$). Here, we normalize to the ideal MHD Alfvén speed following Equation (4.2) and consider only the proton beam and core densities.[3] The gray lines are histograms of all data. In order to extract representative values and spreads thereof, we fit the green regions corresponding to 30% of the peak with a Gaussian. In selecting this portion of the histogram, we implicitly exclude an allowed class of proton VDF fits in which dominant non-Maxwellian features appear as large tails or a halo in the proton distribution instead of a secondary peak or shoulder-like fit because the uncertainty on the drift velocity is large. We leave these core-halo distributions for a later study. For the α-particle case, there is a distinct population with small drifts resulting from a combination of noise and poor quality fits. Requiring $\Delta v_{\alpha,p1}/C_A \geq 0.27$ addresses this issue. The best fit Gaussians are shown in orange. Similar to previous results (e.g. Kasper et al. (2017, 2008); Marsch et al. (1982a); Reisenfeld et al. (2001)), $\Delta v_{\alpha,p_1}/C_A = 67\% \pm 26\%$ and $\Delta v_{p_2,p_1}/C_A = 108\% \pm 16\%$, where the ranges quoted are the one-sigma widths of these fits. The widths of the Gaussians, which we will heretofore denote σ_{α,p_1} and σ_{p_2,p_1}, are attributed to a combination of (1) the range of measured solar wind conditions that support a non-zero differential flow and (2) applicable

---

[2] See Section 4.6 for a discussion of collisional age.

[3] See Section 4.7 for a discussion of the Alfvén speed.

measurement errors. In the following sections, we hypothesize and test some potential contributions to each.

4.5 Uncorrelated Fluctuations

Differential flow is strongest in solar wind with large Alfvénic fluctuations and therefore thought to be a signature of local wave-particle interactions, e.g. cyclotron-resonance-induced phase space diffusion for the case of proton beaming Tu et al. (2004). If differential flow is in general a product of local wave-particle interactions, the difference in widths observed in the histograms of Figure 4.3 may follow from a resonance condition or aspect of the wave-particle coupling that depends on ion species characteristics, such as charge-to-mass ratio. To test this, we compare the magnitudes of correlated α and p_2 streaming fluctuations about their mean.

Figure 4.4 is a 2D histogram of proton beam differential flow fluctuations ($\delta\Delta v_{p_2,p_1}$) and alpha differential flow fluctuations ($\delta\Delta v_{\alpha,p_1}$), each about their mean. Comparing fluctuations in Δv removes other sources of variation in the magnitude of Δv, such as large scale variations in the Alfvén speed or the bulk speed of the solar wind. Fluctuations are calculated by subtracting a running 14 minute mean from each Δv time series, and requiring spectra for $\sim 50\%$ of the time period. Because the fitting algorithms returns the parallel component of the beam differential flow, comparing any other component would incorporate additional information about the magnetic field. An ellipse is fit to the 2D histogram and contours of the fit are shown. The insert gives the function and fit parameters. The ellipse is a circle centered at the origin, indicating that the variations in $\Delta v_{\alpha,p_1}$ and $\Delta v_{p_2,p_1}$ are uncorrelated on these scales. We conclude that the difference in Δv distribution widths, i.e. $\sigma_{\alpha,p_1} \neq \sigma_{p_2,p_1}$, described in the previous section is not due to any species-specific difference in response to large scale, local fluctuations. We repeated this calculation for running means calculated over various time intervals ranging from 5 minutes to more than 20 minutes and multiple requirements for the minimum number of spectra per window. The result is not sensitive to either parameter.

4.6 Trends with Collisional Age

In a hot and tenuous plasma – even in the absence of classical hard collisions – the cumulative effect of small angle Coulomb collisions acts like a simple drag force that gradually slows differentially flowing particles Spitzer (1962). Tracy et al. (2016) showed that collisions with bulk protons are the dominant source of Coulomb drag on all other ions in the

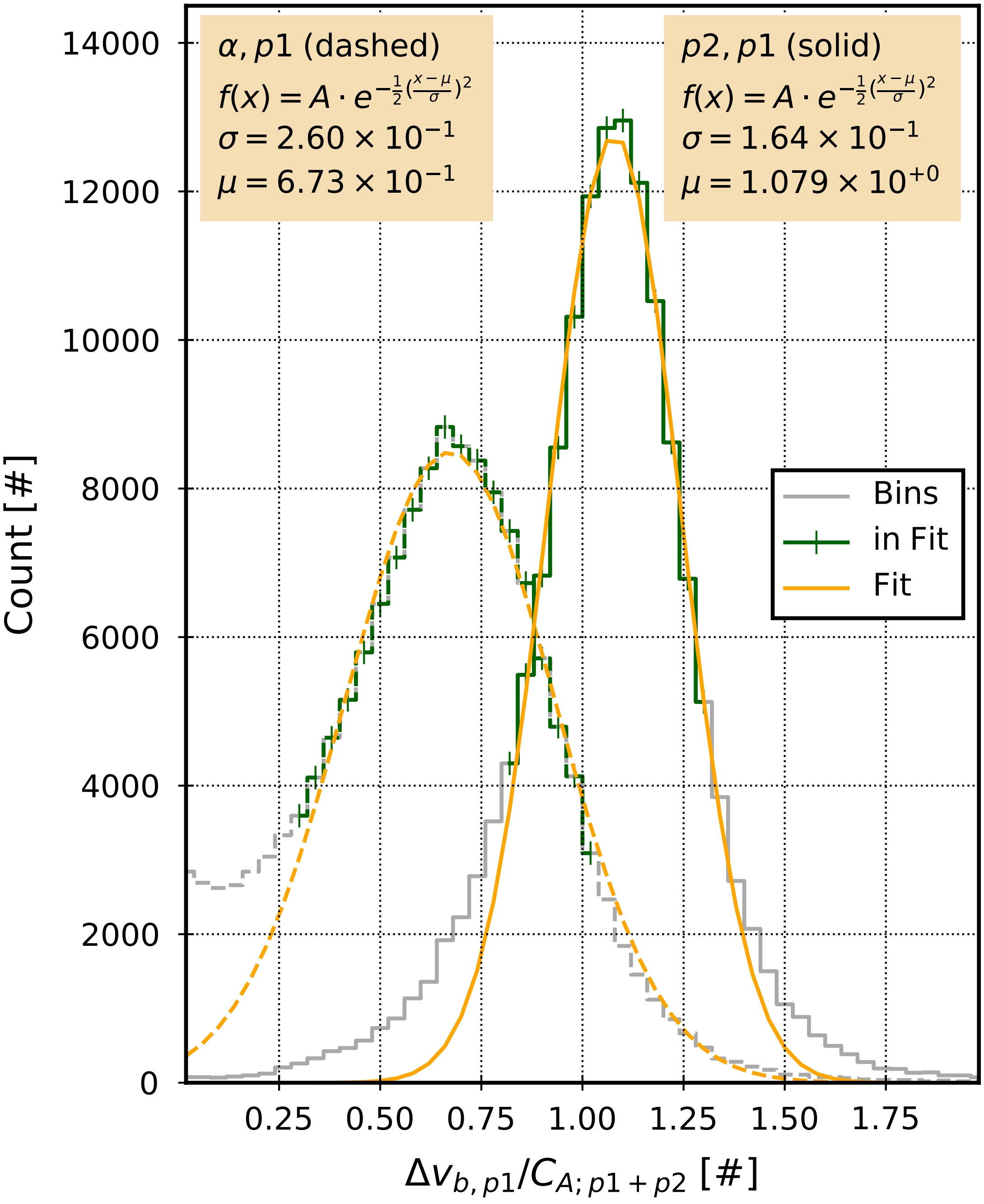

Figure 4.3: Normalized Alpha particle (α, p_1) and proton beam (p_2, p_1) differential flow in collisionless, fast solar wind. Both differential flows are normalized by an Alfvén speed approximation from Eq. 4.2 using both proton densities. Bins within 30% of the maximum are selected for fitting to exclude core-halo distributions.

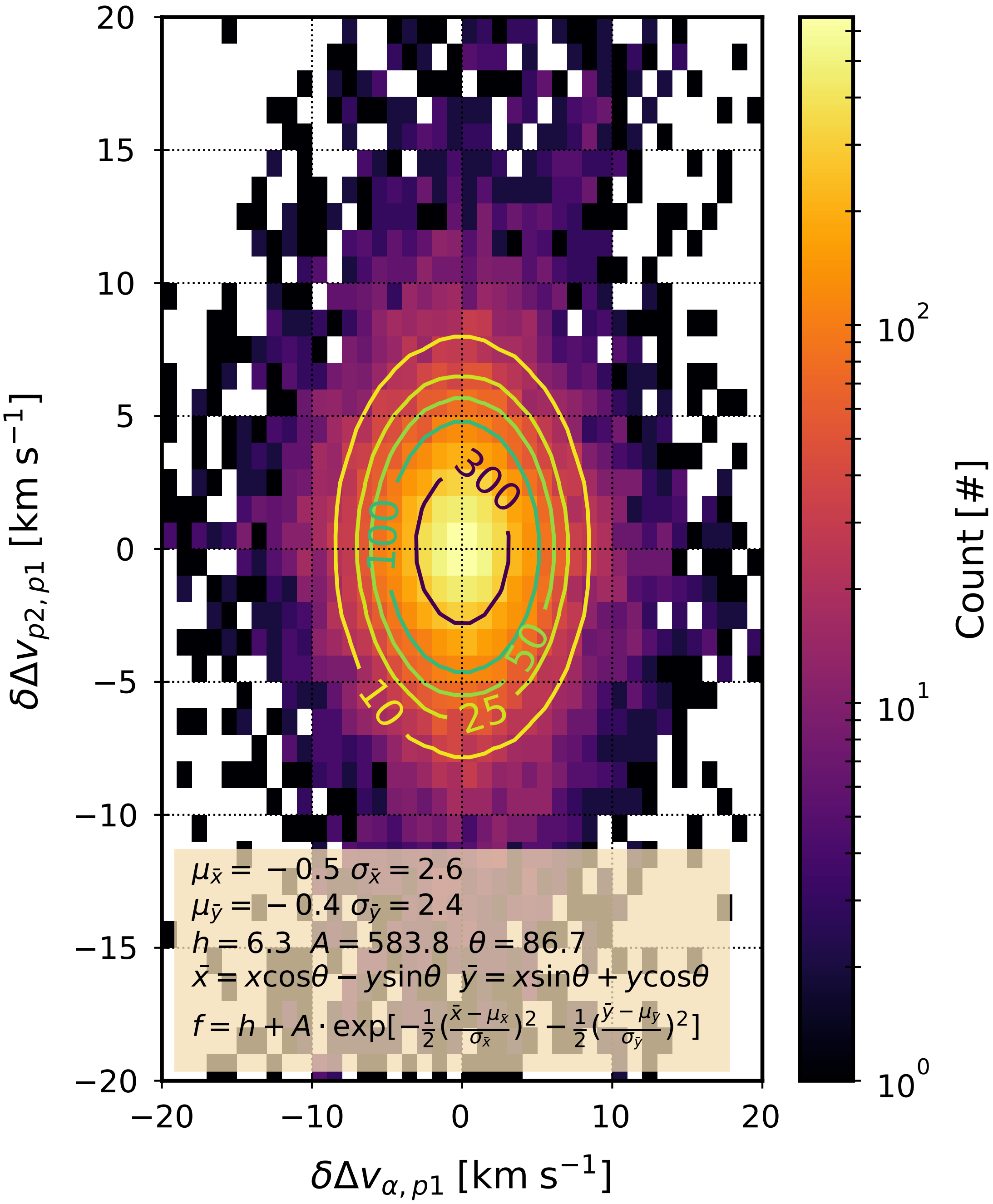

Figure 4.4: A 2D histogram showing uncorrelated differential flow fluctuations ($\delta\Delta v$) for $\Delta v_{\alpha,p_1}$ and $\Delta v_{p_2,p_1}$. That the fit is a circle centered on the origin indicates that the fluctuations are uncorrelated.

solar wind. Kasper et al. (2017, 2008) have demonstrated that $\Delta v_{\alpha,p_1}/C_A$ is a strong, exponentially decaying function of the Coulomb collisional age, the ratio of the local collision rate to the local expansion rate.

The differential equation describing Coulomb drag is $\frac{\mathrm{d}\Delta v}{\mathrm{d}t} = -\nu_c \Delta v$, where ν_c is the effective collision rate. In integral form, this becomes $\Delta v = \Delta v_0 \exp\left[- \int_0^{t_0} \nu_c \, \mathrm{d}t\right]$. Under the highly-simplified assumption that ν_c and the solar wind speed (v_{sw}) are constant over the propagation distance r, the integral is commonly estimated as $\int_0^{t_0} \nu_c \, \mathrm{d}t = \nu_c r / v_{\mathrm{sw}}$. We follow Kasper et al. (2008) and refer to this empirical proxy for the total number of collisions experienced over the expansion history as the collisional age (A_c) of the solar wind.

$$A_c = \nu_c \times \frac{r}{v_{\mathrm{sw}}} \tag{4.1}$$

Kasper et al. (2017) refer to the same quantity as the Coulomb Number (N_c). Chhiber et al. (2016) provide a detailed comparison of this empirical proxy to simulations. As we show below, the exponential decay of Δv with collisional age implies that $\Delta v / C_A$ histogram widths σ_{α,p_1} and σ_{p_2,p_1} is highly sensitive to the range of A_c in the sample.

Based on the work of Tracy et al. (2016), we neglect collisions amongst the minor populations themselves and only consider collisions of α or p_2 ions with proton core ions (p_1). Based on the work of Kasper et al. (2017, 2008), we limit our analysis of the collisional age dependence to collisionless and weakly collisional regimes that constitute the range $10^{-2} \lesssim A_c \lesssim 10^{-1}$. This is the range in which $\Delta v_{\alpha,p_1}/C_A$ is empirically non-zero.

Because the proton beam can have a non-negligible density in comparison to the proton core, we calculate the collision frequency between two species following Hernández and Marsch (1985, Eq. (23)) in a self-consistent manner by integrating over test and field particles from both components. Our treatment of the Coulomb logarithm follows (Fundamenski and Garcia, 2007, Eq. (18)). We assume that r is the distance traveled from a solar source surface to the spacecraft's radial location, ≈ 1 AU, and we take the solar wind velocity to be $v_{\mathrm{sw}} \approx v_{p_1}$.

Measurements of $\Delta v_{\alpha,p_1}/C_A$ and $\Delta v_{p_2,p_1}/C_A$ are binned by collisional age and histogrammed in Figure 4.5 across the aforementioned range. Each column has been normalized by its maximum value in order to emphasize the trends with A_c. Only bins with at least 30% of the column maximum are shown. To characterize the collisionally "youngest" solar wind spectra that have been measured, we define a sufficiently large and statistically significant subset that reflects the limiting behavior. We have chosen this "youngest" range to be ($10^{-2} \leq A_c \leq 1.2 \times 10^{-2}$). The rightmost limit of this subset is marked with a blue line on the figure.

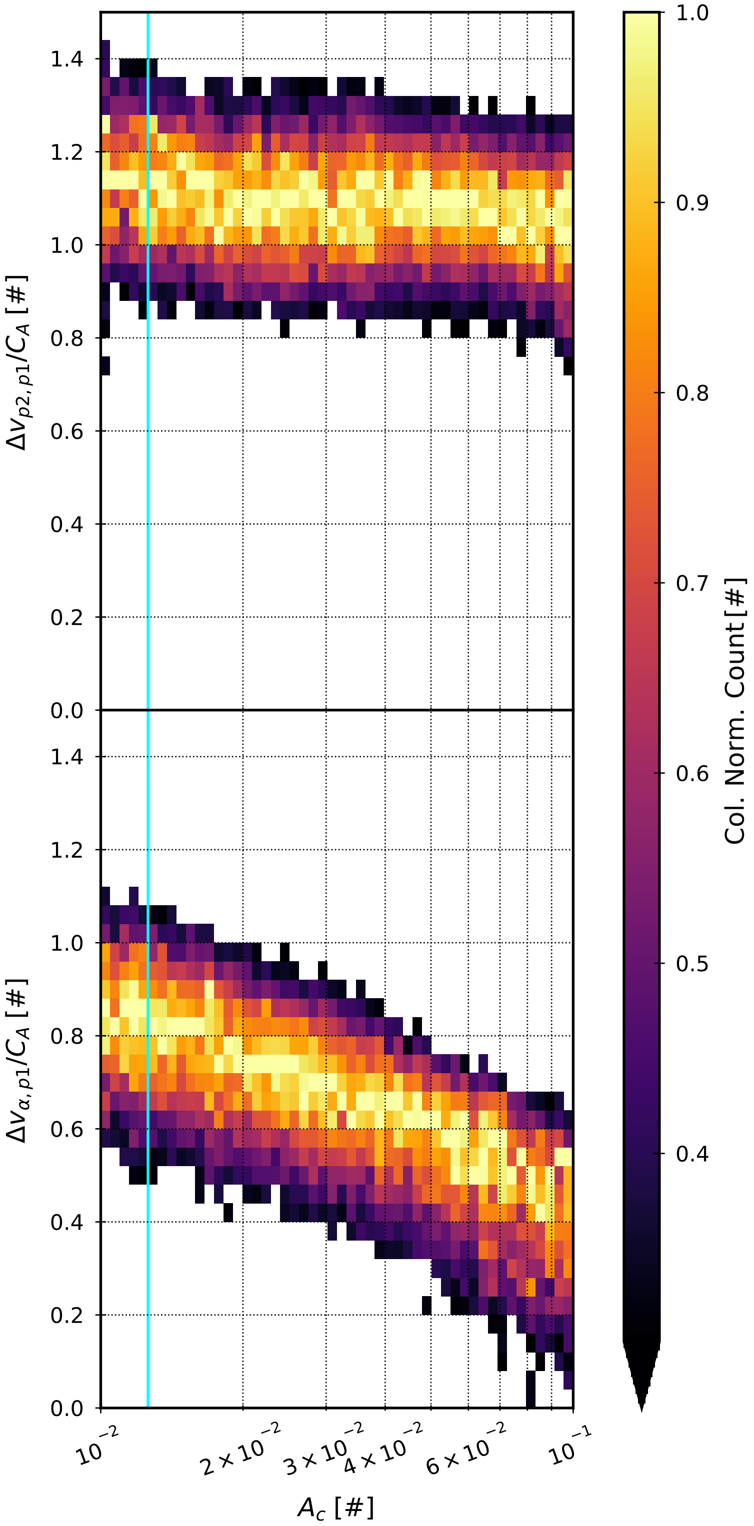

Figure 4.5: 2D histograms of α particle and p_2 Alfvén speed normalized differential flow each as a function of its collisional age. Only bins with at least 30% of the a column maximum are shown. Measurements with a collisional age $A_c \lesssim 1.2 \times 10^{-2}$ is indicated to the left of the blue line.

In the case of α particles, the decrease from the mean value in the reference or youngest region of $\Delta v_{\alpha,p_1}/C_A \sim 0.8$ down to $\Delta v_{\alpha,p_1}/C_A \sim 0.4$ over the range shown would appear to account for a significant fraction of σ_{α,p_1}, up to a $\sim$ 40% spread. In contrast, the proton analogue exhibits a far weaker apparent decay with increasing collisions,showing a decrease of at most approximately one-tenth the slope of the alpha particle trend. In other words, $\Delta v_{p_2,p_1}/C_A$ is nearly independent of the collisional age.

We would also like to derive the general and limiting cases for the differential flow speed ratios $\Delta v_{p2,p1}/\Delta v_{\alpha,p1}$ in spectra where the two are observed simultaneously. In Figure 4.6, we compare $\Delta v_{\alpha,p_1}$ to $\Delta v_{p_2,p_1}$ directly in the full low-collision regime and in the very young reference regime. The ratios $\Delta v_{\alpha,p_1}/\Delta v_{p_2,p_1}$ are histogrammed, with the dashed line indicating the full low-collision sample $10^{-2} \leq A_c \leq 10^{-1}$ and the solid line indicating the reference or youngest subsample ($10^{-2} \leq A_c \leq 1.2 \times 10^{-2}$). The selection of data that contributes to Figure 4.6 is slightly different and more restrictive than in the previous section, because here we require that both the alpha-core and proton beam-core collision rates simultaneously fall in the target range.

As before, we characterize these distributions in Figure 4.6 in a manner insensitive to the tails by fitting a Gaussian to bins with a count of at least 30% of the most populated bin. Similar to Figure 4.3, all binned data are shown in gray; the regions fit are green; and the fits are orange. The text inserts give the functional form and fit parameters up to the fit uncertainty. As there are fewer counts in the youngest A_c range, the histograms have been normalized by their maximum values in order to emphasize the difference in the respective means (μ) and widths (σ) of the distributions.

Over the low-collision range, $\Delta v_{p_2,p_1}$ is approximately $1.6\times$ faster than $\Delta v_{\alpha,p_1}$. Over the youngest range, that reduces to $1.4\times$. The width or characteristic spread in $\Delta v_{\alpha,p_1}/\Delta v_{p_2,p_1}$ is $1.37\times$ larger over the broader, low-collision range than the youngest range. Having demonstrated that $\Delta v_{\alpha,p_1}$ and $\Delta v_{p_2,p_1}$ are uncorrelated in these ranges and that the mean value of $\Delta v_{\alpha,p_1}/C_A$ changes by about 0.4 over the full range, we attribute most of the spread in the ratio $\Delta v_{\alpha,p_1}/\Delta v_{p_2,p_1}$ to the observed decay of $\Delta v_{\alpha,p_1}$ with increasing Coulomb collisions.

4.7 Corrections to the Alfvén Speed

Alfvén waves are parallel propagating, transverse, non-compressive fluctuations in MHD plasmas. Alfvén (1942) Under ideal MHD and considering only a single, simple fluid, the phase speed of these waves (the Alfvén speed) is given by the ratio of the magnetic field

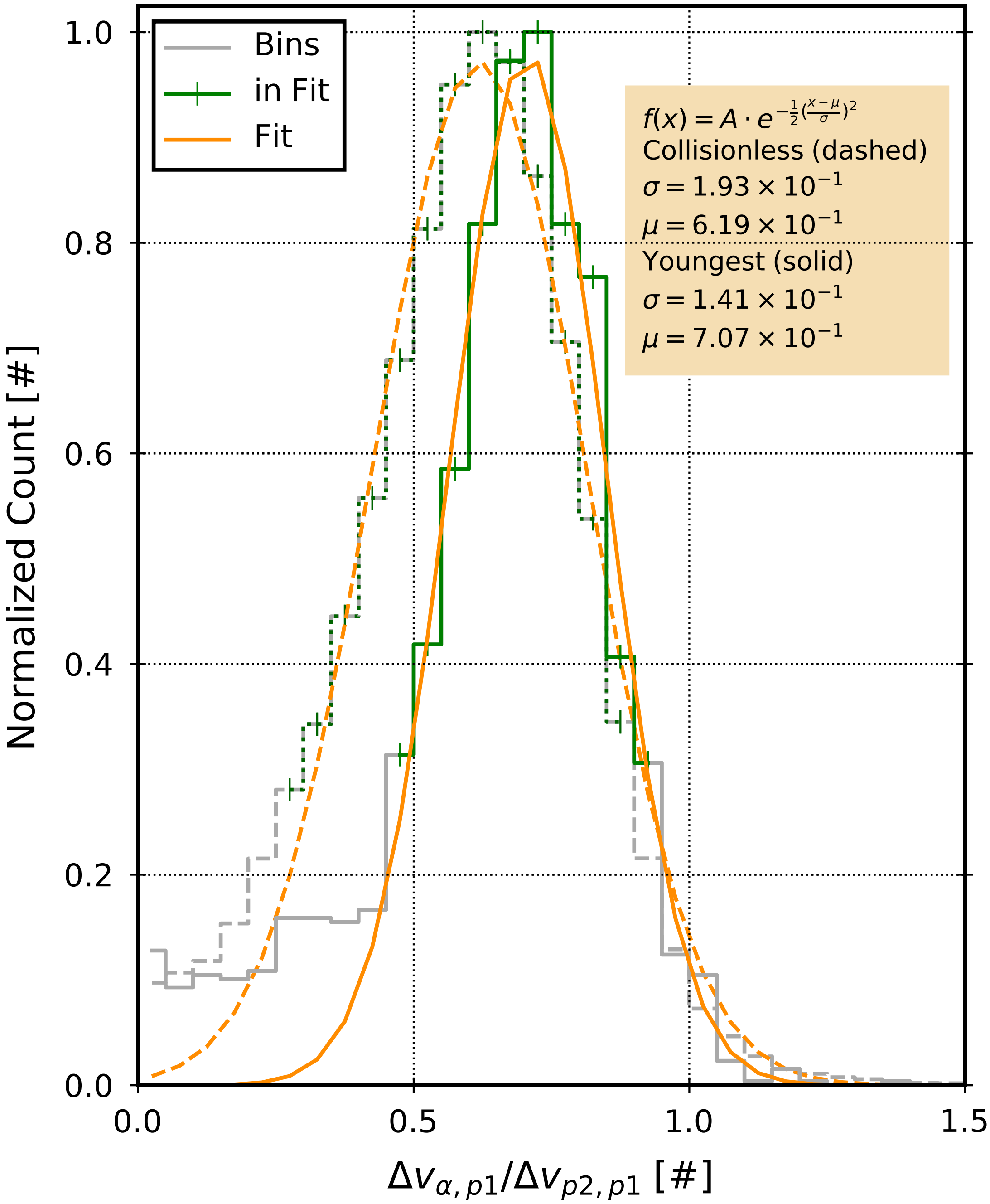

Figure 4.6: The ratio of alpha particle to proton beam differential flow ($\Delta v_{\alpha,p_1}/\Delta v_{p_2,p_1}$) in collisionless ($10^{-2} \leq A_c \leq 10^{-1}$, dashed) and the youngest measured data ($10^{-2} \leq A_c \leq 1.2 \times 10^{-2}$, solid).

magnitude (B) to the square root of the mass density (ρ):

$$C_A = \frac{B}{\sqrt{\mu_0 \rho}}. \tag{4.2}$$

Barnes and Suffolk (1971) derived an approximation to the phase speed of the Alfvén wave under anisotropic MHD that accounts for pressure anisotropy and differential flow of multiple ion species:

$$C_A^{\mathrm{Ani}} = C_A \left[1 + \frac{\mu_0}{B^2}\left(p_\perp - p_\parallel\right) - \frac{\mu_0}{B^2} p_{\tilde{v}}\right]^{1/2}. \tag{4.3}$$

.

Here, C_A is the ideal MHD Alfvén speed from Equation (4.2). The second term in the brackets gives the correction due to the thermal anisotropy of the plasma. Total thermal pressure perpendicular and parallel to the local magnetic field are $p_i = \sum_s n_s k_b T_{s,i} = \frac{\rho_{p_1}}{2} \sum_s \frac{\rho_s}{\rho_{p_1}} w_{s;i}^2$ for components $i = \perp, \parallel$. The third term in the brackets gives the correction due to the dynamic pressure from differential streaming in the plasma frame which is $p_{\tilde{v}} = \sum_s \rho_s \left(\boldsymbol{v}_s - \boldsymbol{u}\right)^2 = \rho_{p_1} \sum_s \frac{\rho_s}{\rho_{p_1}} \left(\boldsymbol{v}_s - \boldsymbol{u}\right)^2$. Here, $\boldsymbol{u}$ is the plasma's center-of-mass velocity; a given species' mass density is ρ_s; and its velocity is $\boldsymbol{v}_s$. All species s are summed over. Pressure terms have been written in terms of mass density ratios to emphasize the significance of correction factors discussed in the following paragraphs and cataloged in Table 4.1. When the plasma is isotropic and there is either vanishingly slow differential flow or a vanishingly small differentially flowing population, the term in brackets is equal to unity and Equation (4.3) reduces to Equation (4.2).

This anisotropic, multi-component formalism of Barnes and Suffolk (1971) ought to be a more appropriate and higher fidelity description of the solar wind plasma than the commonly-evoked ideal single-fluid approximation. Nevertheless, it is instructive to give a rough illustration of the magnitude of each correction term under typical conditions. We note first that the proton core in the solar wind is often anisotropic, with core pressure ratios falling primarily in the range $0.1 \lesssim p_\perp/p_\parallel \lesssim 10$. The absolute correction to the Alfvén speed, via the second bracketed term in Equation (4.3), that follows from this anisotropy alone is ~6%-7% for the median case and can be as high as ~50%. With regards to the third bracketed term, we note that a typical proton beam carrying 10% of the total protons at a speed of roughly C_A relative to the core would carry a ~5% self-consistent correction to the Alfvén speed, owing to proton beam-core dynamic pressure.

Our goal in this section is to relax the ideal MHD approximation by considering these next-order approximations for the speed of the predominant parallel-propagating wave in the solar wind. We explore whether the spreads in normalized differential flow, i.e. the widths of the 1D distributions of $\Delta v/C_A$, are further minimized when the contributions of anisotropic and dynamic pressure are considered. In order to disentangle this element from the Coulomb collision effect described in the previous section, we limit our analysis in this section to the "youngest" plasma, i.e. measurements drawn from the youngest-measured reference regime to the left of the blue line in Figure 4.5.

Figure 4.7 plots distributions and fits in the now-familiar style, together with the fit residuals, for one possible renormalization of $\Delta v_{\alpha,p_1}/C_A$ and $\Delta v_{p_2,p_1}/C_A$. The color selection for the various components in the top panel follows the convention from the previous figures and again only bins with counts at least 30% of the maximum are used in the fit. Residuals are shown for the bins in the fit, and the fit parameters are shown in the inserts. The amplitudes A are omitted because they are of no consequence. In this particular case, the α and p_2 differential flow are normalized by the Alfvén speeds with proton core pressure anisotropy taken into account. For reasons discussed below, the normalization in the proton beam-core example (Right) also accounts for the beam contribution to the proton mass density.

We consider a family of similar approximations to the Alfvén speed, each accounting for corrections associated with the measured anisotropies and multiple component terms in Equation (4.3). As these contributions rely on higher-order moments of the spectrum fit[4], they can carry relatively large uncertainties. If the uncertainties are significant in the aggregate, they are expected to contribute to broadening of the $\Delta v/C_A$ distributions. However, terms that are well-measured in the aggregate, will improve the precision of the Alfvén speed when accounted for and thus reduce the width of $\Delta v/C_A$ if the true differential flows are Alfvénic in nature. In the following, we examine all possible combinations in order to ascertain whether a well-measured high order correction exists that further minimizes the width of the normalized differential flow distributions.

Table 4.1 contains fit parameters for each 1D distribution of $\Delta v/C_A$, for both the alpha-proton and proton beam-core differential flows, using the various formulations of the Alfvén speed. Overall, we find that the widths of both $\Delta v/C_A$ distributions increase substantially when the dynamic pressure term is included, indicating that either (1) the differential flows are *less* strongly correlated with generalized Alfvén speed, or (2) that the additional measurement uncertainty introduced along with a given term is in the aggregate comparable to the correction itself.

However, when only the proton core temperature anisotropy correction is factored in, the distribution width is indeed reduced relative to the isotropic case. Because the core

---

[4] See Section 4.3.

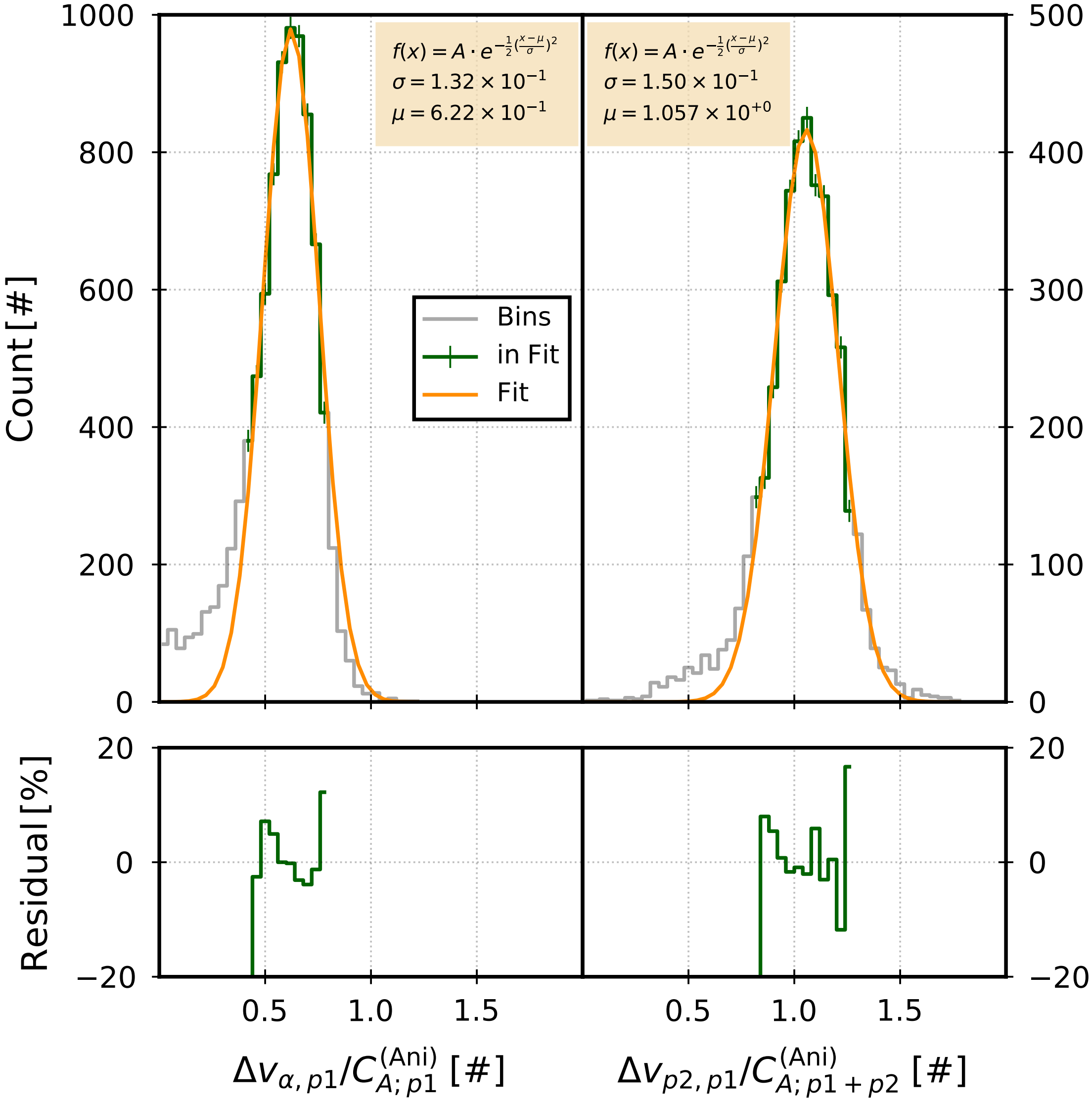

Figure 4.7: Examples of the Gaussian fits to 1D distributions of α and p_2 normalized differential flow along with the associated residuals. As discussed in Section 4.7, the Alvén speed normalizations shown minimize the width of these distributions.

Wave Speed Normalization	$\alpha-$ Particle Mean	$\alpha-$ Particle Width	Proton Beam Mean	Proton Beam Width
$C^{(\mathrm{Ani})}_{A;\alpha+p1+p2}$	0.869	0.177	1.167	0.169
$C^{(\mathrm{Ani})}_{A;\alpha+p1+p2}\ (p_{\tilde{v}})$	0.999	0.244	1.339	0.256
$C^{(\mathrm{Ani})}_{A;\alpha+p1}$	0.730	0.142	0.997	0.156
$C^{(\mathrm{Ani})}_{A;\alpha+p1}\ (p_{\tilde{v}})$	0.761	0.164	1.048	0.172
$C^{(\mathrm{Ani})}_{A;p1+p2}$*	0.784	0.160	**1.057**	**0.150**
$C^{(\mathrm{Ani})}_{A;p1+p2}\ (p_{\tilde{v}})$*	0.876	0.206	1.182	0.205
$C^{(\mathrm{Ani})}_{A;p1}$	**0.622**	**0.132**	0.874	0.164
$C_{A;\alpha+p1+p2}$	0.902	0.194	1.227	0.177
$C_{A;\alpha+p1}$	0.755	0.166	1.052	0.179
$C_{A;p1+p2}$*	0.829	0.181	1.131	0.166
$C_{A;p1}$	0.657	0.150	0.938	0.183

Table 4.1: All fit parameters and their uncertainties in the manner calculated in Figure 4.7. The column indicates the parameter (Mean Value or Width) for a given differentially flowing species. The row indicates the wave speed normalization. The bold, colored row is the preferred normalization. Anisotropic Alfvén speeds including the dynamic pressure term from Eq. 4.3 are indicated by $(p_{\tilde{v}})$. The average fit uncertainty on the Mean is 4×10^{-3} and the average uncertainty on Width is 5×10^{-3}. Normalizations marked with an asterisk (*) are plotted in Figure 4.8.

anisotropy correction term in Equation (4.3) is usually (but not always) positive, it tends to increase the Alfvén speed estimate relative to the ideal MHD approximation. Thus, the corrected mean values $\Delta v/C_A$ are generally lower. Figure 4.8 is a plot of the width vs. mean for select 1D fits that were performed in the style of Figure 4.7, illustrating these observations. In the cases shown, each Alfvén speed includes both proton densities. The cases accounting for proton core pressure anisotropy correction factor $(p_\perp - p_\parallel)$ are indicated with the square. Cases that additionally account for the proton core dynamic pressure correction factor $(p_\perp - p_\parallel - p_{\tilde{v}})$ are indicated by stars.

4.8 Trends in A_c

Using the Alfvén speed approximation that minimizes the spread in normalized differential flow for alphas and beams, we examine the behavior of $\Delta v/C_A$ as a function of A_c and in the asymptotic limit of zero collisions. We applied the same methodology used to examine 1D distributions in the youngest A_c data to binned α, p_1 and p_2, p_1 differential flow spanning the low-collision range. Figure 4.9 plots these trends. Alpha particles are shown in blue and proton beams in yellow. Mean values to 1D fits are indicated as pluses and the 1D

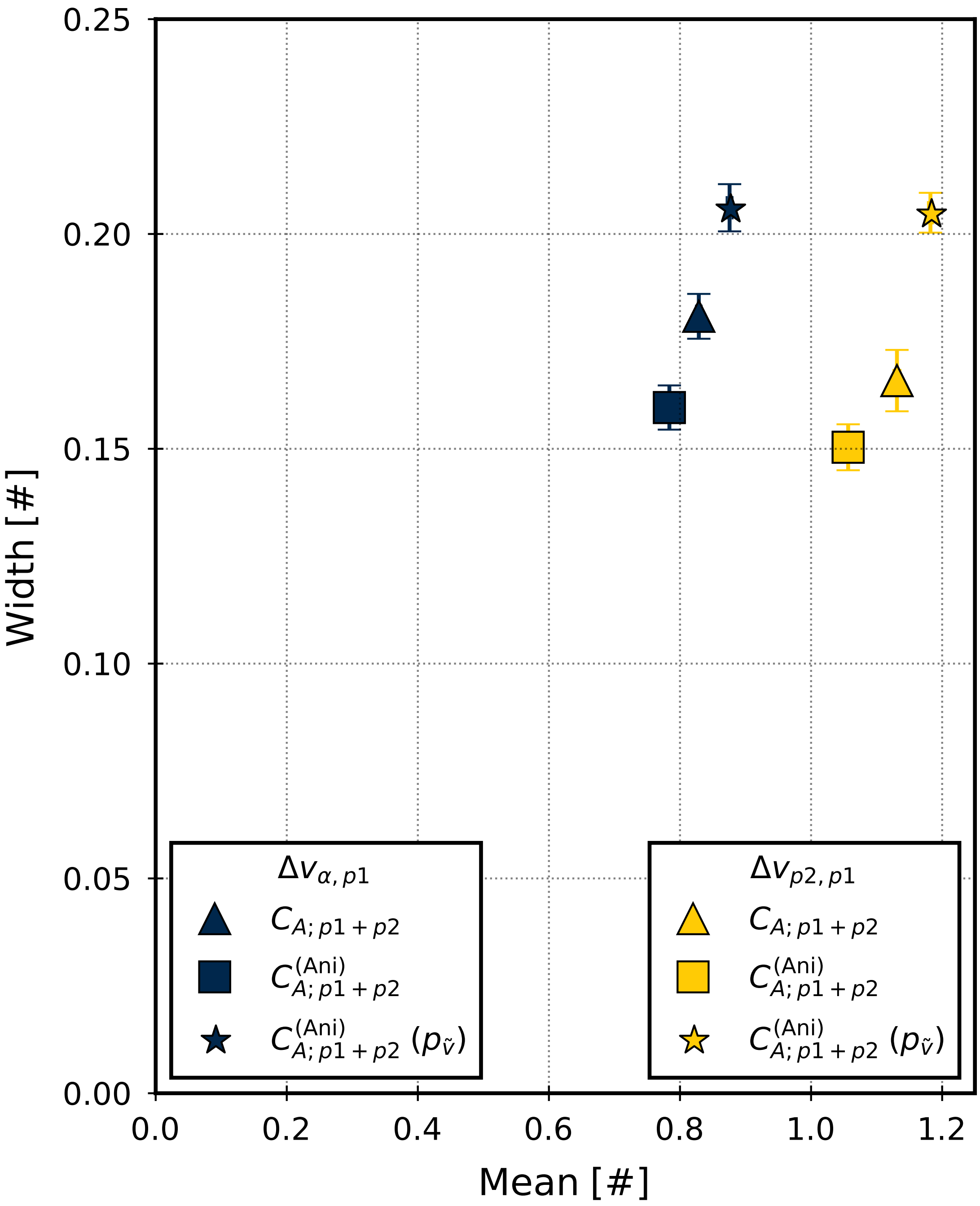

Figure 4.8: Example α-particle and p_2 normalized differential flow illustrating the impacts of various Alfvén speed approximations. In both cases shown, inclusion of the proton core anisotropy (Eq. 4.3) reduces the width in comparison to the isotropic MHD Alfén speed (Eq. 4.2), while including the anisotropy and the dynamic pressure ($p_{\tilde{v}}$) increases it.

widths are given as error bars. Fits to each trend are given as black dotted lines.

Four clear features are apparent pertaining to the mean values of both normalized differential flows and to their collisional trends. First, if we consider the asymptotic limit of zero Coulomb collisions and we account for the widths reported in Table 4.1, the alpha particles differentially stream at 67% of the local Alfvén speed and the proton beams stream at approximately the Alfvén speed. Second, that the fit constant c governing α, p_1 decay is greater than 1 indicates that our collisional age calculation over-simplifies our A_c by either under-estimating r, under-estimating ν_c, over-estimating v_{sw}, or some combination of these. Kasper et al. (2017) examined detailed scalings and more accurate versions of A_c that may correct for some of these issues and can be a subject for future study. Third, even using the formulation of the Alfvén speed that yields the highest precision, the spread in alpha particle differential flow due to the change in mean value over the collisionless range is still ~ 0.3, which is the largest single contribution to the spread in $\Delta v/C_A$. Fourth, in the asymptotic absence of collisions, the proton beams differentially flow at very nearly $(105\%$ of$)$ the Alfvén speed. Given the widths of the error bars in Figure 4.9, the difference between the youngest resolved $\Delta v_{p_2,p_1}$ and the asymptotic value could be due to the spread in our measurements.

4.9 Discussion

The evolution of solar wind velocity distribution functions is governed by an interplay between adiabatic expansion, Coulomb collisions, and wave-particle interactions. Collisional transport rates Livi and Marsch (1986); Pezzi et al. (2016) and many types of wave-particle interactions Verscharen et al. (2013a,b); Verscharen and Chandran (2013) depend on the small-scale structure of the VDF, in particular the small-scale velocity space gradients. Because measurements indicate the presence of alpha-proton differential flow starting at the corona and extending out to and beyond 1 AU, one can assume that non-zero differential flow is a coronal signature. Under this hypothesis, the decay of $\Delta v_{\alpha,p1}$ is due to dynamical friction. Kasper et al. (2017) As the proton beam-core drift and alpha-core drift are signatures of one plasma with a single expansion history, the collisional bottleneck that erodes $\Delta v_{\alpha,p1}$ could likewise be expected to erode $\Delta v_{p2,p1}$. However, the observed independence of $\Delta v_{p2,p1}/C_A$ with respect to A_c over the examined range contradicts this assumption and minimally implies either (1) an additional competing process that preferentially couples to proton beams or (2) that Eq. (4.1) underestimates the proton dynamical friction.

Several in situ mechanisms that preferentially couple to protons have been proposed. As one example, the interaction between resonant protons and kinetic Alfvén waves leads

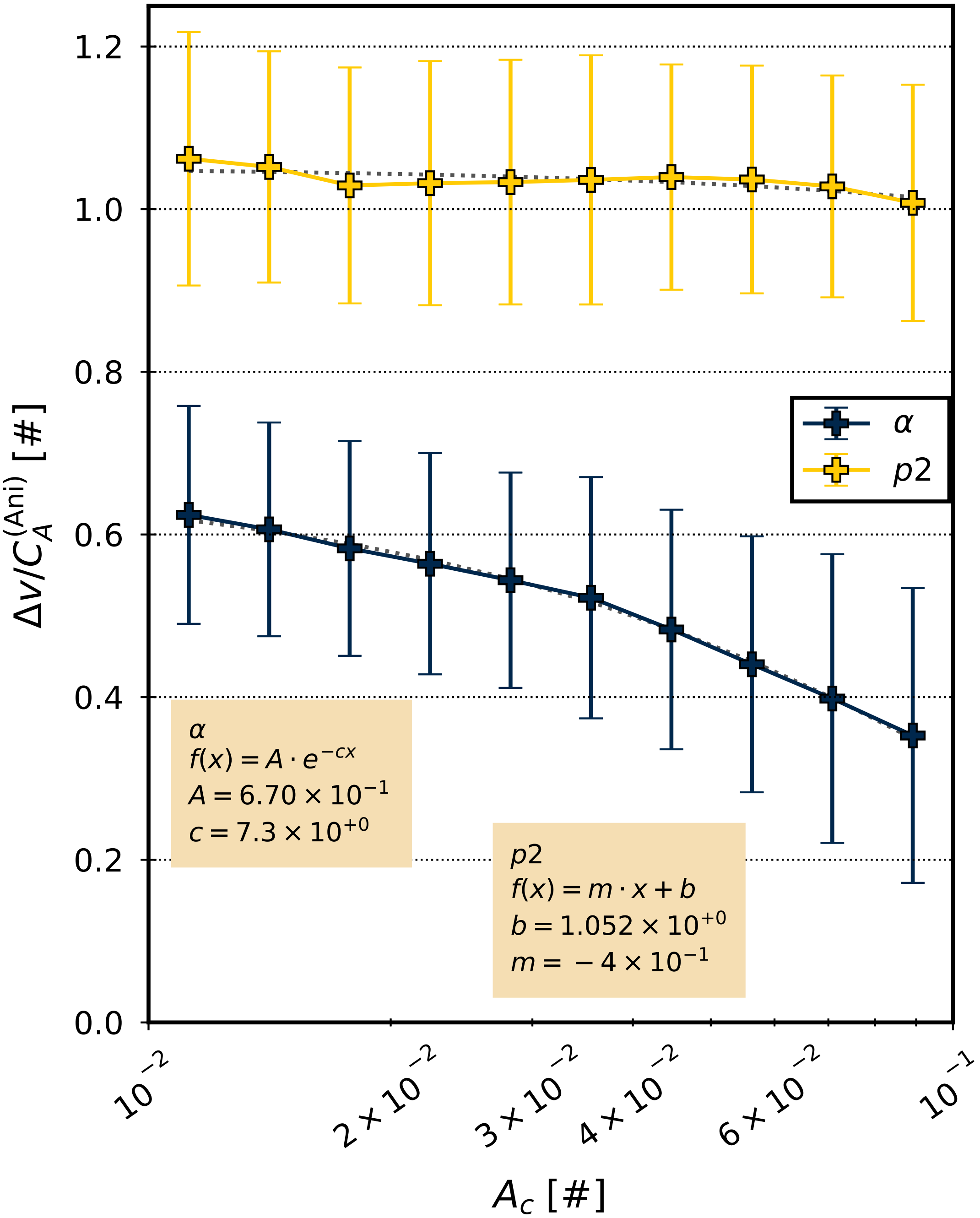

Figure 4.9: Trends of 1D fits to $\Delta v_{\alpha,p_1}/C_A$ and $\Delta v_{p_2,p_1}/C_A$ as a function of A_c. Error bars are the Widths of the 1D fits. Each trend has been fit and the parameters are shown in the appropriate insert. While $\Delta v_{\alpha,p_1}$ markedly decays with increasing A_c, $\Delta v_{p_2,p_1}$ is relatively constant with A_c. To within the fit uncertainty, proton beams differentially stream at approximately the local Alfvén speed.

to the local formation of beams Voitenko and Pierrard (2015). Such a mechanism could be responsible for the creation of proton beams throughout the solar wind's evolution or it could turn on at some distance from the Sun where plasma conditions become favorable. As another example, Livi and Marsch (1987) have argued that Coulomb scattering itself in the presence of the interplanetary magnetic field can produce skewed and beam-like distributions under certain circumstances.

The collisional age used in Eq. (4.1) assumes that the collision frequency describing proton dynamical friction does not change over the solar wind's evolution and is equal to the value measured at the spacecraft. Chhiber et al. (2016) have shown that such assumptions do not capture the full nature of proton radial evolution. Eq. (4.1) also neglects the ways in which this frequency depends on the small-scale structure of the VDF Livi and Marsch (1986); Pezzi et al. (2016). One avenue of future work is to better address collisional effects by modeling the radial dependence, building on the work of Chhiber et al. (2016) and Kasper et al. (2017). A further refinement would be to account for dependence of collision frequency on the VDF's fine structure Livi and Marsch (1986); Pezzi et al. (2016). A second avenue of future work involves modeling the force required to locally maintain differential flow. By letting this force depend on local wave amplitudes, perhaps the differential flow radial evolution could be modeled from the competition between a Coulomb frictional force and a force from resonant scattering Voitenko and Pierrard (2015).

The hypotheses of proton beams as coronal in origin or created and modified in situ are not mutually exclusive. For example, wave-resonant or frictional forcing may only be significant over a certain portion of the solar wind's radial evolution and that range may correspond to a subset of commonly measured conditions at 1 AU. Applying a holistic model to data that is differentiated by wave power or Coulomb collisions may allow us to distinguish between or unite the two origin hypotheses. The recently launched Parker Solar Probe Fox et al. (2015) and upcoming Solar Orbiter Müller et al. (2013) missions, with their closer perihelia and higher energy resolution plasma instruments Kasper et al. (2016), will also allow us to gauge the relative importance of and interplay between these effects.

4.10 Conclusions

In fast ($> 400 \text{ km s}^{-1}$) and collisionless ($A_c \leq 10^{-1}$) solar wind, $\alpha, p1$ differential flow is approximately 62% as fast as $p2, p1$ differential flow when measured by the *Wind* spacecraft's Faraday cups. The spread in $\alpha, p1$ differential flow is approximately $1.7\times$ larger than $p2, p1$ differential flow. We ruled out large-scale, in-phase wave-particle interactions by examining the correlation between fluctuations in both species parallel differential flows over multiple time scales ranging from 5 minutes to more than 20 minutes. Minimizing the spread in normalized differential flow due to the method used to approximate the Alfvén speed, we found that the difference in $\Delta v/C_A$ width for both species is predominantly due to the decay of $\Delta v_{\alpha,p1}/C_A$ with increasing Coulomb collisions. At the youngest resolved collisional age, when the impact of Coulomb collisions has been minimized, we find that proton core pressure anisotropy has the largest impact on minimizing the spread in normalized differential flow and that the increase in spread when including dynamic pressure in the anisotropic Alfvén speed is beyond what would be expected from random fluctuations. In the asymptotic absence of Coulomb collisions, α-particles differentially flow at approximately 67% of the local Alfvén speed and proton beams differentially flow at approximately 105% of it. This upper limit on $\Delta v_{\alpha,p1}/C_A$ is close to the upper limit found by Maneva et al. (2014) and worth further investigation. We also found that, unlike the known Kasper et al. (2017, 2008); Neugebauer (1976) $\alpha, p1$ decay with A_c, proton beam differential flow minimally decays and is approximately constant with collisional age.

Given the results of Tracy et al. (2016) showing that solar wind ions collisionally couple most dominantly to protons, it is unsurprising that the widths of both $\Delta v_{\alpha,p1}/C_A$ and $\Delta v_{p2,p1}/C_A$ are smallest when the Alfvén speed accounts for the proton core. That the proton core temperature anisotropy is also significant supports the conclusion of Chen et al. (2013) that solar wind helicities are closer to unity when normalzing by the anisotropic Alvén speed. That the beam differential flow width is smaller when it is normalized by an Alfvén speed including the beam density may indicate some coupling between the beams and local Alfvén waves, as predicted by Voitenko and Pierrard (2015). That the dynamic pressure term causes a larger spread in both species normalized differential flow is either a result of measurement uncertainty or some underlying physical mechanism that is beyond the scope of this paper to test.

CHAPTER 5

Near-Sun Proton Beams

This chapter studies near-Sun proton beams. It is being prepared for submission to *The Astrophysical Journal*.

5.1 Abstract

PSP has returned the first ever observations of the solar wind below $0.3\,\mathrm{AU}$. We extract proton beam measurements from these observations and compare them with *Wind*/SWE measurements made at $1\ \mathrm{AU}$. This event study suggests that proton beams may not be collisionally regulated in the near-Sun environment and a local mechanism may drive their evolution. They also illustrate that interpreting near-Sun proton beams will require more measurements across a wide variety of solar wind conditions.

5.2 Introduction

The solar wind is a near-collisionless plasma (Alterman et al., 2018; Kasper et al., 2017, 2008; Verscharen et al., 2019) that evolves as it travels away from the Sun due to a combination of and the interplay between expansion, Coulomb collisions, kinetic microinstabilities, and turbulence (Matteini et al., 2012; Verscharen et al., 2019). Within, at, and beyond $1\ \mathrm{AU}$, the solar wind departs from local thermodynamic equilibrium (LTE) and non-Maxwellian features are regularly observed. These include unequal magnetic and ion thermal pressure, unequal temperatures parallel and perpendicular to the local magnetic field, unequal temperatures between different ions, and non-zero velocity drifts between multiple ions (Alterman et al., 2018; Kasper et al., 2002; Maruca et al., 2012). These non-Maxwellian features also effect how the solar wind evolves and how the aforementioned physical processes interplay (Livi and Marsch, 1986, 1987; Livi et al., 1986; Marsch and Livi, 1987).

Protons or ionized hydrogen compose 95% of the solar wind by number density. A temperature parallel to the local magnetic field that exceeds that which can be modeled by a single bi-Maxwellian is one non-LTE feature regularly observed in solar wind protons. Commonly referred to as a proton beam and first observed by Feldman et al. (1973b) using instruments on IMP 6, proton beams have also been observed using instruments on Helios, Ulysses, and Wind (Alterman et al., 2018; Asbridge et al., 1974; Chen et al., 2016; Feldman et al., 1973a, 1974b; Goldstein et al., 2000, 2010; Hellinger et al., 2011, 2013; Marsch and Goldstein, 1983; Marsch and Livi, 1987; Marsch et al., 1982b; Matteini et al., 2013; Montgomery et al., 1976; Ďurovcová et al., 2019).

The mechanism generating proton beams is as yet undetermined. However, it is known that the closer to LTE the solar wind becomes, the smaller beams become and the more difficult they are to measure. Given that expansion, Coulomb collisions, kinetic microinstabilities, and turbulence drive solar wind ions closer to LTE as it evolves (Alterman et al., 2018; Kasper et al., 2017; Matteini et al., 2012; Verscharen et al., 2019), proton beam-core distributions in which the proton beam is small may be under reported in near-Earth measurements. In contrast, proton beam measurements near the Sun environment should not suffer from this limitation as the impact of these mechanisms is cumulative over the solar wind's proration.

PSP (Fox et al., 2015) launched on August 12th, 2018 and made its first perihelion pass through the Sun's corona (E1) 86 days later on November 6th, 2018 at 03:27 UT (Kasper and SWEAP, 2019). PSP caries the SWEAP (Kasper et al., 2016) thermal ion instrument suite, of which the SPC instrument (Case et al., 2013) is a component. SPC measured solar wind protons between 54 $\mathrm{R_S}$ and 35 $\mathrm{R_S}$ during E1 (Kasper and SWEAP, 2019), i. e. below Helios's perihelion of $0.3\,\mathrm{AU}$. This instrument provides high cadence and high resolution measurements of the solar wind's reduced VDF in the spacecraft's ram direction. During E1, the background magnetic field was predominantly radial. Therefore, outside of transients, SPC's reduced VDF measurements are preferentially weighted towards the component of the VDF along $\hat{\boldsymbol{b}}$. As such, E1 measurements provide a unique event to study near-Sun proton beams when the parallel structure of the VDF is likely to be resolved. While these are only from the 1st of 24 planned solar encounters that will approach the Sun at progressively smaller distances (Fox et al., 2015), they are the closest in situ measurements ever made and, if proton beams are generated near the Sun, measurements least likely to be modified from that initial state. As such, this paper studies SPC proton beam measurements during E1 and compare them to measurements taken at 1 AU with the *Wind*/SWE Faraday cups. We substantiate the prediction of Alterman et al. (2018) that Coulomb collisions may not regulate proton beams in the near-Sun environment. We also infer that one or more local mecahisms may be responsible for their generation.

The remainder of the paper proceeds as follows. Section 5.3 describes our data sources and selection. Section 5.4 provides an overview of key bulk solar wind and proton beam measurements during E1. This section also identifies six time periods for which the background solar wind is roughly steady. Section 5.5 compares these six time periods with the distribution of measurements over all of E1 and compares these measurements with low solar activity, slow solar wind proton beam measurements from L1. Finally, Section 5.6 interprets our observations and concludes.

5.3 Data Sources

5.3.1 Faraday Cup Ion Measurements

In a reductive sense, FCs measure the current of ions incident on the instrument. A single FC spectrum consists of multiple current measurements in sequential energy-per-charge (E/q) ranges or windows. Energy-per-charge windows are selected by modulating a high voltage (HV) alternating current (AC) waveform on top of a large direct current (DC) offset. These E/q measurements can be converted into physical quantities[1] by means of either moments or non-linear fitting. As the FC's response is not analytically invertible, non-linear fitting utilizes a model VDF to reduce the currents to physical quantities. The exact quantities returned and the number of ion species resolved depend on the details of the model VDF. Both SPC and the SWE/FCs rely on this principle.

Equation (5.1) gives the VDF's general form for ion species s.

$$f_s(\boldsymbol{v}) = \frac{n_s}{\pi \overset{\leftrightarrow}{w}_s^3} \exp\left[-\left(\frac{\boldsymbol{v} - \boldsymbol{u}_s}{\overset{\leftrightarrow}{w}_s} \right)^2 \right] \tag{5.1}$$

Here, n_s is the species' number density; $\overset{\leftrightarrow}{w}_s^2 = 2k_B \overset{\leftrightarrow}{T}_s / m_s$ is the thermal speed; and $\boldsymbol{u}_s$ is the species' bulk speed. Formally, the thermal speed is a nine-element tensor. However, it is usually reported as a two-component tensor (perpendicular and parallel to local $\boldsymbol{B}$) or a scalar in practice. Summing over protons and alpha particles accounts for nearly 99% of the solar wind.

---

[1] E.g. number density (n), velocity $(\vec{v})$, and temperature $(\overset{\leftrightarrow}{T})$.

5.3.1.1 The Solar Probe Cup

SWEAP (Kasper et al., 2016) is a a suite of charged particle detectors consisting of SPC (Case and SWEAP, 2019) and the Solar Probe Analyzers (SPANs). $\mathrm{SPAN-A}$ consists of an ion ($\mathrm{SPAN-Ai}$) and electron ($\mathrm{SPAN-Ae}$) electrostatic analyzer (ESA). $\mathrm{SPAN-B}$ is an electron ESA (Livi and SWEAP, 2019; Whittlesey and SWEAP, 2019). Both of the ESAs sit in the shadow of PSP's heat shield. SPC is a Faraday cup that looks over the heat shield in the spacecraft ram direction. Depending on the choice of HV polarity, SPC can measure a one-dimensional radial projection of solar wind ion or electron VDFs. As the flux into the FC is one parameter that impacts the signal-to-noise ratio (SNR), the accumulation time for any given measurement is typically a function of the radial distance of the spacecraft from the Sun. In this paper, we use the ion data from the encounter phase of E1.

Figure 5.1 presents an example SPC ion distribution from E1. This figure has converted the measured currents in each E/q window to measured counts in each velocity window. The uncertainty in each window is given by vertical error bars. Unlike the implication of Equation (5.1) in which each species is fit with a vector velocity, the model equation used to reduce measured currents to physical quantities in SPC follows the suggestion of Kasper et al. (2006), leverages their gyrotropic nature, and fits the alpha particles and proton beam populations with a differential flow taken with respect to the bulk/core proton distribution $\Delta v_{s,p_1}$.

In essence, the colored curves represent the mapping of the measured currents to each ion's density, velocity, and thermal speed to the height, location, and width of its curve. The blue, red, and green curves respectively are the bulk or core protons, proton beam, and alpha particles. However, there are three caveats. The first caveat is related to SPC's single, fixed field-of-view. As SPC is mounted adjacent to PSP's heat shield and looks only in the spacecraft RAM direction, it only measures the radial projection of the VDF, i. e. the reduced distribution function (Kasper et al., 2016). As such, each VDF is a function of $v*$, the velocity projection of the VDF into SPC. Similarly, each thermal speed is a radial projection.

The second caveat is related to the combination of SPC's SNR during early encounters and alpha particles' mass-to-charge (m/q) ratio. Typically, a FC's E/q windows are uniformly spaced in $\Delta E/E$. As such, higher E/q windows cover a larger absolute energy range, the solar wind's VDF is sampled in a more coarse fashion at these energies, and our ability to extract physical quantities from these E/q windows typically more limited by the instrument's SNR than at lower energies. Because alpha particles have twice the m/q as protons, a FC measures them at $\sqrt{2}$ higher velocities than their flow speeds. At

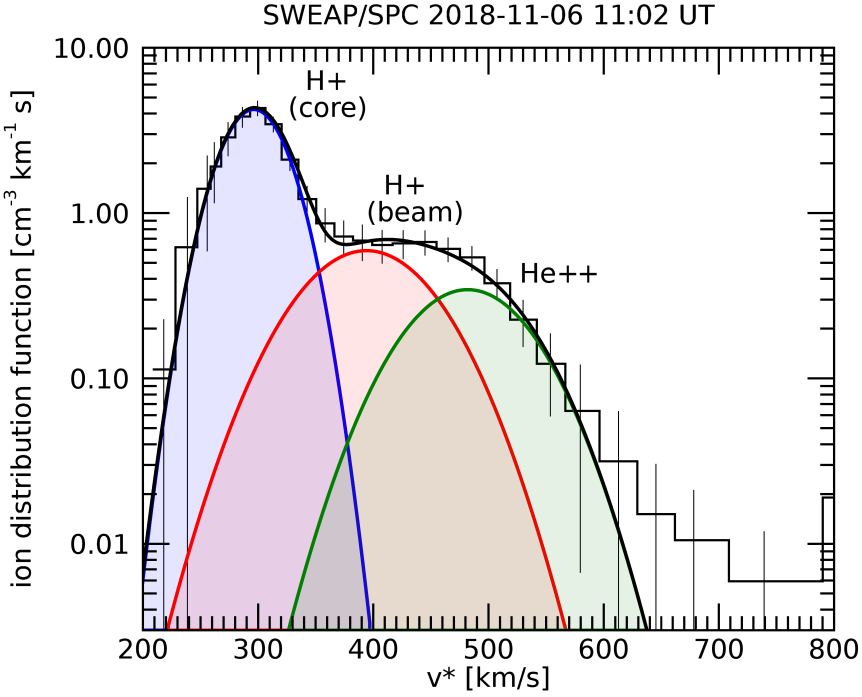

Figure 5.1: An example VDF from SPC. This figure averages over several SPC spectra so as to accentuate the VDF's structure.

L1 and larger radial distances, this implies that a FC can routinely distinguish between alpha particles and protons even when the two are co-moving at L1 (Alterman et al., 2018; Kasper et al., 2006; Maruca and Kasper, 2013). However, because SPC is optimized for measurements of the bulk or core protons during each encounter (Case et al., 2013), the combination of a proton beam with a large differential flow and larger abundance[2] along with the limitations associated with higher E/q windows most significantly limit our ability to extract physically justifiable alpha particles. As such, the alpha particles are highly constrained we utilize the alpha particles as a tool to constrain parameter space as a means of improving our ability to resolve and extract physical quantities from the proton beams.

The third caveat is the result of the proton beam and core's identical m/q. Unlike alpha particles[3] that can be measured even when they are co-moving with the proton core (Alterman et al., 2018; Kasper et al., 2006; Maruca et al., 2013), proton beams cannot because the ions constituting the proton beam and core populations have identical mass and charge. Tautologically, there is only one proton population when they are co-moving. As such, the closer to LTE the solar wind becomes, the more difficult a proton beam is to measure.

---

[2] See Figures 5.6, 5.12 and 5.14.

[3] Fully ionized helium.

5.3.1.2 SWE Faraday Cups

Wind is an in-ecliptic spacecraft that spins with a rotation axis pointed out of the ecliptic. The SWE/FC subsystem (Ogilvie et al., 1995) consists of two cups, one each mounted on the zenith and nadir decks pointing 15^o out of the ecliptic and 180^o out of phase with each other along the spin axis. The FCs measure the solar wind's VDF approximately every 92 seconds. The combination of multiple look directions from two FCs enable the *Wind*/SWE/FC subsystem to resolve an anisotropic temperatures within a single solar wind measurement. The data quality has been robust and stable over the course of the mission (Kasper et al., 2006), enabling studies that span multiple solar cycles (Alterman and Kasper, 2019). The measured currents are available on CDAweb[4]. Following Alterman et al. (2018) and Chapter 3, we have reprocessed these currents to return a proton beam and proton core population. Figure 3.1 presents an example spectrum from this instrument. (Top) The four panels are four distinct look directions from different points along the spacecraft spin during the collection of a single spectrum. The red, blue, and pink curves correspond to the proton core, proton beam, and α-particles that are extracted from these quantities. (Bottom) A 3D VDF interpolated from these measurements. As stated above, because SWE collects 1D projections of the solar wind's VDF along multiple look directions within a single spectrum, a 3D VDF can be more easily extracted using automated fitting algorithms with at least an anisotropic proton core. Additionally, note the separation between the alpha particles and proton beam: as typical and L1, the two ions do not overlap in measurement space. As such, three ion populations–proton core, proton beam, and alpha particles–are more easily resolved than with SPC.

5.3.2 Magnetic Fields

As this paper focuses on the characteristics of the proton beam, the Alfvén speed is a significant quantity to consider. As such, we utilize magnetic field measurements from PSP/FIELDS (Bale et al., 2016) and *Wind*/Magnetic Field Investigation (MFI) (Koval and Szabo, 2013; Lepping et al., 1995). In both cases, we average the magnetic field vector measurements on each spacecraft to the ion measurement time on its respective spacecraft.

---

[4] `https://cdaweb.sci.gsfc.nasa.gov`

5.3.3 Data Selection

5.3.3.1 SPC Data Selection

Proton beams are derived from FC measurements by modeling excess temperature parallel to the local magnetic field as a second, drifting population. In this study, we only select spectra with a proton beam. To ensure that the proton beam (p_2) is well separated from the core or bulk protons (p_1), we require that the ratio of the beam-to-core VDFs evaluated at the beam drift speed is > 1. We apply a similar criteria to the proton beam's overlap with the highly constrained alpha particle distribution to ensure that the beam VDF is uncontaminated. Because alpha particles are measured at a $\sqrt{2}$ larger velocity than they are traveling, the ratio of beam-to-alpha VDFs projects the alpha particles to their E/q measurement bin. During E1, a profusion of spikes were present (Horbury et al., 2019; Kasper and SWEAP, 2019). However, the non-spike magnetic field is primarily radial and pointing towards the Sun (Bale and Fields, 2019). As we are interested in the steady state behavior of proton beams, we require that $B_R/B < -0.75$ to remove the spikes. A side effect of selecting a primarily radial field is that the radial proton temperatures reported by SPC are biased towards the parallel component. Finally, we exclude cases when the Alfvén speed is aberrantly large ($C_A > 1000 \text{ km s}^{-1}$).

5.3.4 SWE Data Selection

The *Wind*/SWE/FCs have been in continuous operation since 1995. The data collected covers more than two solar cycles. After selecting for reliable proton beams (Stevens and Alterman, 2019), we account for both the current phase of the solar cycle and the maximum speed measured by SPC. As we are currently entering solar minimum 25, we restrict *Wind*/SWE data to $\mathrm{SSN} < 15$. Given that v_{sw} is approximately constant with radial distance and the maximum solar wind speed we measure with SPC (given the restrictions placed on it), we also select SWE data for which $v_{p_1} < 550 \text{ km s}^{-1}$. Table 5.2 notes the number of spectra remaining after data quality selection. Note that we have repeated our analysis additionally selecting for SWE data with a high cross helicity (Woodham et al., 2018) ($|\sigma_c| > 0.75$) on a 15 minute time scale and found no change in our results.

5.4 Overview of Encounter 1

Proton beam measurements in a FC are likely strongly dependent on local conditions in that the proton beam must be sufficiently large that it can be well resolved by the instrument.

Concurrently, the distribution of proton beams over all of E1 are a unique set of near-Sun proton beam measurements. Because E1 proton beam measurements are at the edge of SPC's optimized operational range, we choose to proceed on two parallel tracks. (1) We compare the distribution of SPC proton beam measurements throughout E1 with the L1 proton beams. (2) We select six time periods during which SPC measurements are qualitatively stable so that we can substantiate our interpretations over all of E1 against a subset of times for which conditions are roughly steady state.

Specific entropy is one is situ measurement for differentiating between solar wind streams (Borovsky, 2016; Borovsky and Denton, 2010). Neglecting the mass of a given ion species, specific entropy is typically defined as $S \propto \ln T/n^{\gamma-1}$ where T is the ion temperature, n is the number density, and γ is the polytropic index. Siscoe and Intriligator (1993) demonstrate that it captures the change in density and temperature at stream interaction regions. Burton et al. (1999) use changes in proton specific entropy to identify transitions between different solar wind streams. Pagel et al. (2004) extend the results of Zurbuchen et al. (2002) and show that–outside of ICMEs and, "except at the peak of solar maximum," (Pagel et al., 2004)–proton specific entropy can identify solar wind stream structure and serve as a proxy for the O^{7+}/O^{6+} ratio, especially when composition measurements are unavailable and/or higher time resolution measurements than typical of composition instruments are needed. Kilpua et al. (2016) further demonstrate that specific entropy changes with source region in solar Minimum 24. While S_p is not a constant along a given flow (Pagel et al., 2004; Perrone et al., 2019), changes in S_p can serve to indicate when the solar wind stream in situ measurements sample changes. In addition to S_p, its constituent quantities (T & n), as well as solar wind speed v_{sw} can serve as secondary indicators. We use these steady state conditions to approximate those that belong in the same stream. To further contextualize our measurements and event selection, we further utilize the specific entropy calculated from the proton moments (S_{p_m}) and the specific entropy calculated from the bulk or core proton fits (S_{p_1}). As the moment algorithm does not robustly reject proton beams and the fitting algorithms separate beam and core distributions, discrepancies between S_{p_m} and S_{p_1} may point to non-Maxwellian features in the VDF that merit consideration.

Figures 5.2 and 5.3 are 2D histograms summarizing E1 SPC measurements that include a proton beam as a function of time from 12:00 UTC on October 31, 2018 to 06:00 UTC on November 11, 2018. Only bins with at least 3 points are shown. Each column represents 2 hours and has been normalized to its maximum value so that the variation of data collection rates with time do not obscure the trends. A green line indicating the mode (i. e. maximum) in each column is over plotted to guide the eye. The x-axis is marked every 6 hours and the

	Start [DD HH:MM]	End [DD HH:MM]	Δt [Hours]
S1	01 08:00:00	02 08:00:00	24
S2	02 21:00:00	03 17:00:00	20
S3	03 23:00:00	04 19:00:00	20
S4	05 15:27:00	06 15:27:00	24
S5	08 00:00:00	08 18:00:00	18
S6	09 12:00:00	10 08:00:00	20

Table 5.1: The six E1 SPC events selected for study, labeled S1 to S6 according to when SPC chronologically encountered each. Each event occurred during November, 2018. The Start and End times are given as Day of Month Hour:Minute. The last column identifies the total duration of each event. Only events lasting at least 18 hours and at least 3,500 proton beam spectra were selected.

tick marks are labeled at the start of each day. In descending order, x-axis tick labels also indicate radial distance from the spacecraft to the Sun ($\mathrm{R_S}$), Carrington Longitude (λ^o), and Carrington Latitude (ϕ^o). The vertical blue line across panels indicates the November 6th, 2018 03:27 UT perihelion. As described below, each panel indicates six events labeled S1 to S6, where the number increases chronologically in time. The duration in days (rounded to 1%) of each event is noted in parentheses. All events are at least 18 hours, no more than 24 hours, and must contain at least 3,500 spectra with a proton beam. Indicator bars each have a unique color that matches probability distribution functions (PDFs) in Figures 5.4 to 5.15. The start time, end time, and duration of each event is listed in Table 5.1.

5.4.1 Overview of Bulk Properties Outside of Spikes

Figure 5.2 presents an overview of bulk solar wind parameters when a proton beam is measured. Panel (A) shows the magnetic field magnitude B. B is largest at $100\,\mathrm{nT}$ in perihelion and decreases on either side of it. By eye, each of the events S1 to S6 demonstrate a relatively stable B. Event S1 has the weakest field at $40\,\mathrm{nT}$. In comparison with Kasper and SWEAP (2019), the narrow distribution of B at each time interval reflects our rejection of spikes.

Panel (B) plots the proton moment's specific entropy S_{p_m}. By eye, S_{p_m} increases through E1 and the specific entropy in each event is relatively constant. S5 is the exception as it shows a clear, monotonic increase in S_{p_m} through the event. In addition, other than S3 and S4, each event shows a marked change in S_{p_m} before and after the event.

Panel (C) plots the proton core specific entropy S_{p_1}. In general, the core specific entropy is similar to the moment specific entropy. Over E1, the trends are quite similar and in

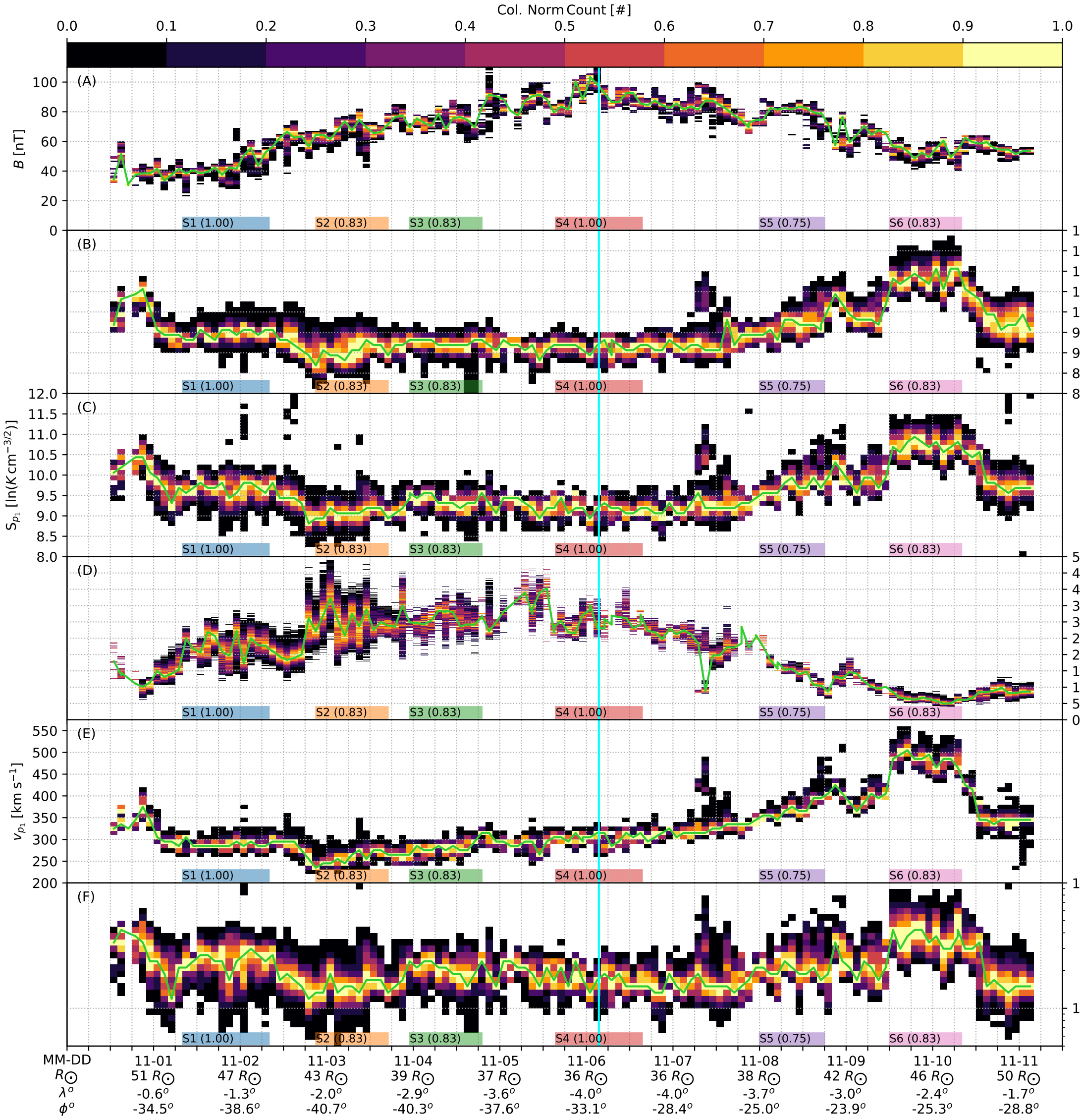

Figure 5.2: An overview of SPC measurements taken during E1 that include a proton beam averaged into 2 hour intervals. Each column has been normalized to its maximum value and the mode in each column (most common bin) is over plotted in green. From top to bottom, the panels plot (A) the magnetic field magnitude, (B) proton moment specific entropy, (C) proton core specific entropy, (D) proton core number density, (E) proton core speed, and (F) proton core temperature.

each event, S_{p_1} tends to follow S_{p_m}. Given that S_{p_m} likely includes only portions of the VDF where one may find a proton beam, the qualitative consistency between S_{p_m} and S_{p_1} substantiates our event selection. The most notable differences between S_{p_m} and S_{p_1} occur immediately before S2 and S3, which serves as further evidence for treating them separately.

Panel (D) presents the proton core number density n_{p_1}. Similar to the magnetic field, n_{p_1} increases monotonically towards perihelion and then decreases out of it. However, unlike B, the number density shows a sharp, discontinuous change around 18:00 UT on November 2nd. In comparison to Kasper and SWEAP (2019), the small standard deviation over E1 is likely due to our spike rejection. As with S_{p_m} and S_{p_1}, n_{p_1} is roughly steady through each event other than S5.

Panel (E) presents the proton core velocity. Through the Inbound leg of E1, v_{p_1} is relatively constant between $250 \ \mathrm{km\,s^{-1}}$ and $325 \ \mathrm{km\,s^{-1}}$. During the Outbound leg, it climbs monotonically until November 9th at 12:00 UT, reaching a maximum during S6, after which is markedly drops by $\sim \ 150 \ \mathrm{km\,s^{-1}}$. Similar to n_{p_1}, v_{p_1} covers a markedly smaller range than that presented by Kasper and SWEAP (2019) while still following the same general trend in speed because we preferentially select data without spikes. As with n_{p_1} and S_p v_{p_1} is approximately constant through each event except S5 during which it shows a monotonic trend.

Panel (F) plots the core temperature T_{p_1}. Unlike the other panels in Figure 5.2 that tend to display marked trends in the mode, the most notable change in T_{p_1} is that the spread in values decreases towards perihelion. The exception is S6, for which the temperature stands out as markedly enhanced. As expected, the sharp changes present before S2 and S3 in S_{p_m} and S_{p_1} are also present in T_{p_1}. Because temperature has the largest uncertainty of the first three quantities derived from a VDF (n, v, & T), we cannot rule out that the change in standard deviation is due to a combination of the SNR changing one E1's orbit, SPC's single look direction, and the variable solar wind conditions.

5.4.2 Overview of Proton Beams

Figure 5.3 presents a summary of proton beam measurements over E1 in the same format as Figure 5.2. Figures 5.4 to 5.15 present 1D PDFs of the quantities in Figure 5.3 for all of E1, each of the events, and the selected data from the *Wind*/SWE/FC subsystem. Table 5.2 summarizes the these 1D PDFs.

Panel (A) plots the proton beam abundance. The beam abundance is $A_{p_2/p_1} = A_{p_2} = 100 \times n_{p_2}/n_{p_1}$, i. e. the beam-to-core number density ratio in units of percent. The large

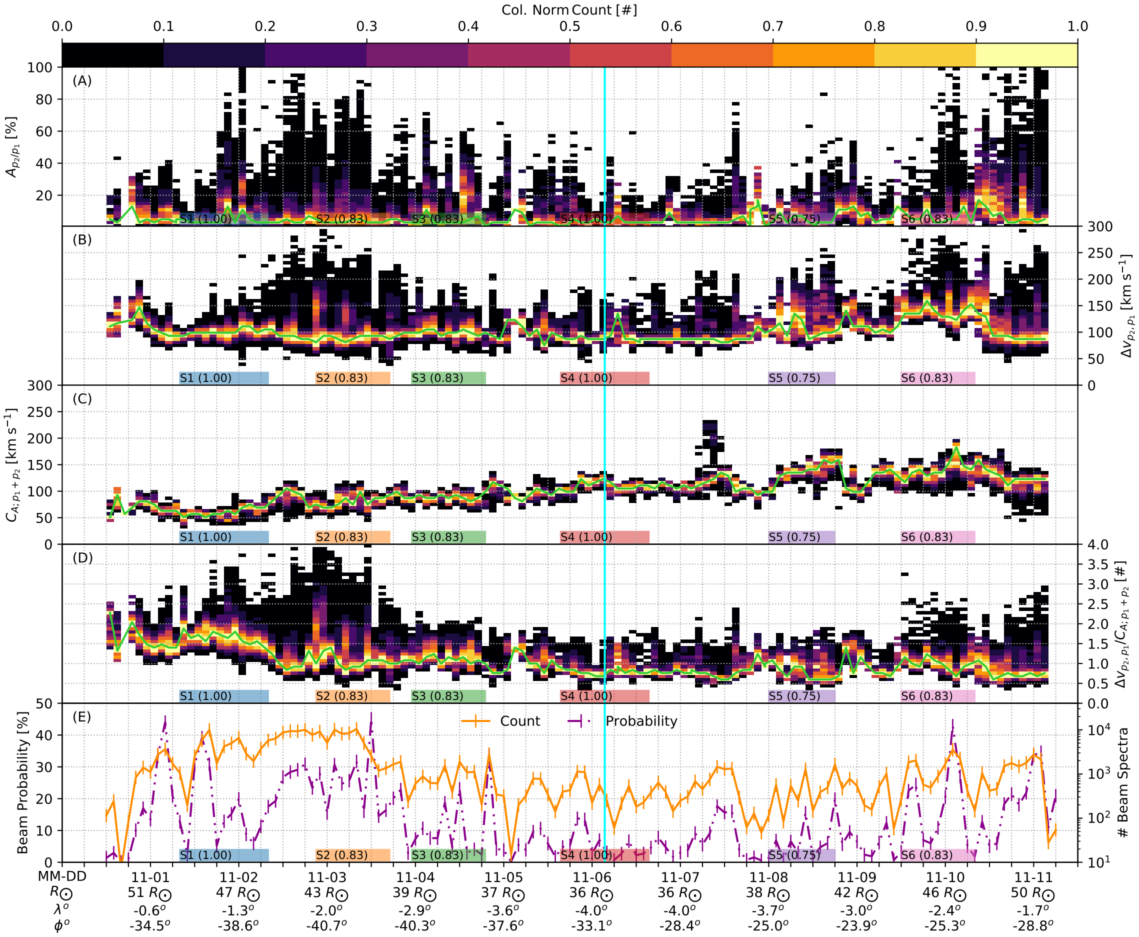

Figure 5.3: An overview of SPC proton beam measurements taken during E1 averaged into 2 hour intervals. The format follows Figure 5.2. From top to bottom, the panels plot (A) proton beam abundance A_{p_2}, (B) proton beam-core drift $\Delta v_{p_2,p_1}$, (C) Alfvén speed C_A, (D) normalized drift $\Delta v/C_A$, and (E) both the number of spectra measuring a proton beam and the probability of measuring a proton beam in the same 2 hour interval.

scatter in this figure will likely be addressed as proton beam data validation continues.

Panel (B) plots the proton beam-core differential flow. Differential flow is the difference in speeds between two ion species. As any non-gyrotropic motion would wash out within several gyroperiods, it is parallel to the local magnetic field such that $\Delta v_{i,j} = |\boldsymbol{v}_i - \boldsymbol{v}_j|$. Note that, although SPC is limited to measuring the solar wind VDF's radial projection and Panel (B) is formally the radial component of Δv, because we have selected data for which $B_r/B < -0.75$, Δv's radial projection is primarily along $\hat{\boldsymbol{b}}$. Outside of several intervals during S6, the most common value of the differential flow stays within the $100\ \mathrm{km\,s^{-1}}$ range between $50\ \mathrm{km\,s^{-1}}$ and $150\ \mathrm{km\,s^{-1}}$.

Panel (C) plots the Alfvén speed $C_A = B/\sqrt{\mu_0 \rho_{p_1+p_2}}$, where $\rho_{p_1+p_2} = \rho_{p_1} + \rho_{p_2}$ is the total mass density. During the majority of E1, C_A monotonically increases until the start of S5, at which point it levels out. The notable exceptions are the time periods before S2 and surrounding S5.

Panel (D) plots the ratio of the quantities in Panels (B) and (C): the beam-core Alfvén normalized drift $\Delta v/C_A$. Over E1, the most common $\Delta v/C_A$ varies between 0.5 and 1.5. However, the high velocity tail unexpectedly (Daughton and Gary, 1998) surpasses $\Delta v/C_A = 2$ from 12:00 UT on November 1st to 18:00 on the 3rd.

Panel (E) plots the probability of measuring a proton beam (dashdotdot purple, primary y-axis) and the number of measurements containing a proton beam (solid orange, secondary y-axis). The count rate is largest from 12:00 UT on November 1st to approximately 9:00 UT on 3rd because of instrument operational modes and then–with a few exceptions–varies between roughly 100 and 1000 in a 2 hour period for the remainder of the encounter. We calculate the probability of measuring a proton beam as the ratio between the number of proton beam measurements and the total number of measurements with a proton core–irrespective of whether or not a beam is measured–within the 2 hour time window. Coincidentally, the likelihood of measuring a beam is largest ($\sim 30\%$) when the count rate is largest.

5.5 Event Properties

Figures 5.4 to 5.15 present PDFs of the proton beams quantities summarized in Figure 5.3. Each colored curve covers one event and matches the color of the event marker in Figures 5.2 and 5.3. Each curve is also marked with a unique, unfilled marker. The black curves marked with an unfilled plus plot all the data from one instrument. The black line with a dash and two dots presents all SPC data from E1. The solid black line indicates low solar activity data from L1 as measured by the *Wind*/SWE/FCs. Only a subset of mark-

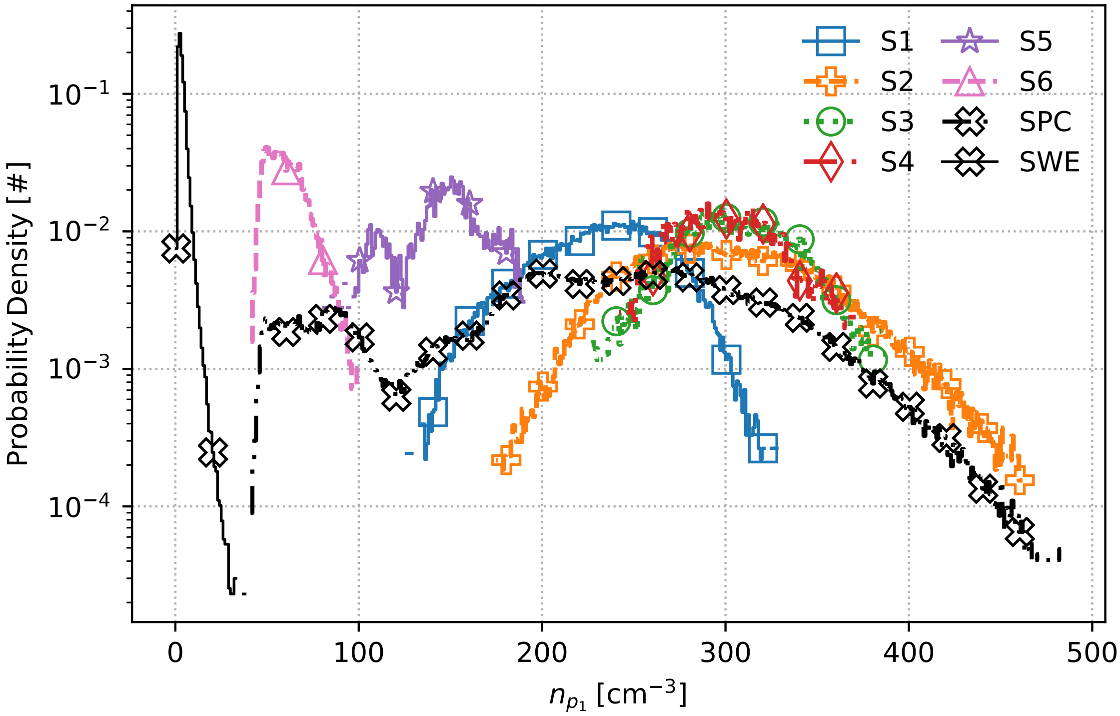

Figure 5.4: Proton core number density PDFs for events S1 to S6 (colors), the full 1st encounter (dash, dot, dot black with unfilled *X*), and low solar activity data from the *Wind* spacecraft at L1 (solid black, unfilled *X*).

ers on each curve are drawn so as to not overcrowd the plot. Presenting PDFs instead of histograms controls for the different number of measurements present in the SWE data, all of E1's SPC data, and each of SPC's events. Table 5.2 summarizes the mean and standard deviation of the measurements constituting each plotted in PDF, where the standard deviation is intended to indicate a typical range of values. It also gives the total number of measurements present in the events S1 to S6, all of E1, and all of the L1 measurements.

Figure 5.4 plots PDFs of the dimension-full proton core number density n_{p_1} for events. Over the course of E1, the core number density typically falls between 140 cm^{-3} and 320 cm^{-3}. Event S6 is the notable outlier with an average number density not surpassing 70 cm^{-3}. As expected for an expanding solar wind, the typical core density more than a order of magnitude larger during E1 than at L1.

Figure 5.5 plots PDFs of the dimension-full proton beam number density n_{p_2}. Over the course of E1, the beam number density typically falls between 2 cm^{-3} and 6 cm^{-3}. Events S3 and S6 present the largest and smallest number densities, respectively. In comparison, the typical beam density at L1 is $1.1 \text{ cm}^{-3} \pm 0.3 \text{ cm}^{-3}$. While the density of an expanding solar wind decreases with distance from the Sun, a change of $4\times$ is only 7% of the change

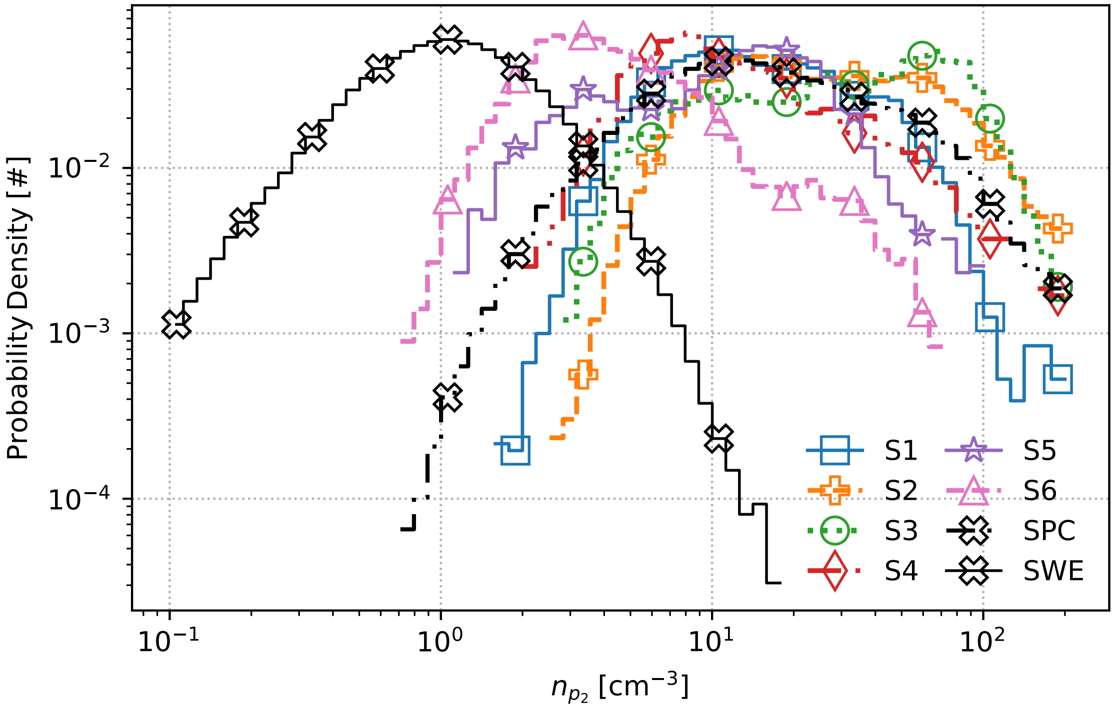

Figure 5.5: Proton beam number density PDFs in the format of Figure 5.4.

observed in the core density. Comparing the individual events to each other and to the full encounter, most events show bimodal distributions with a clear separation between the peaks that are evident neither in the L1 data nor in the full E1 PDF.

Figure 5.6 plots PDFs of the beam abundance. The beam abundance is $A_{p_2/p_1} = A_{p_2} = 100 \times n_{p_2}/n_{p_1}$, i. e. the beam-to-core number density ratio in units of percent. Over E1, A_{p_2} is strongly peaked near 0% and falls between 0% and 20%. In contrast, the low solar activity L1 data demonstrate a significant, high A_{p_2} tail with larger abundances of 20% to 40%.

Figure 5.7 plots PDFs of the core speed v_{p_1}. The typical core speed measured by SPC is $v_{p_1} = 300 \ \mathrm{km\,s^{-1}} \pm 60 \ \mathrm{km\,s^{-1}}$. Considering the multi-peaked nature of the SPC E1 distribution and the long, high velocity tail of the L1 distribution it is difficult to rule out that the long term averages collected by *Wind* are the primary reason for the discrepancies between the E1 and L1 measurements. Even though S5 and S6 have a typical core speed much larger than the other 4 events, both overlap with the high-speed SWE tail of the $v_{p_1} = 400 \ \mathrm{km\,s^{-1}} \pm 70 \ \mathrm{km\,s^{-1}}$ distribution measured at L1.

Figure 5.8 plots PDFs of the beam speed v_{p_2}. The typical beam speed v_{p_2} measured by SPC is between $300 \ \mathrm{km\,s^{-1}}$ and $460 \ \mathrm{km\,s^{-1}}$. The continuous trend from $250 \ \mathrm{km\,s^{-1}}$ to $650 \ \mathrm{km\,s^{-1}}$ in *Wind*/SWE data is expected given that SWE's many years of measurements

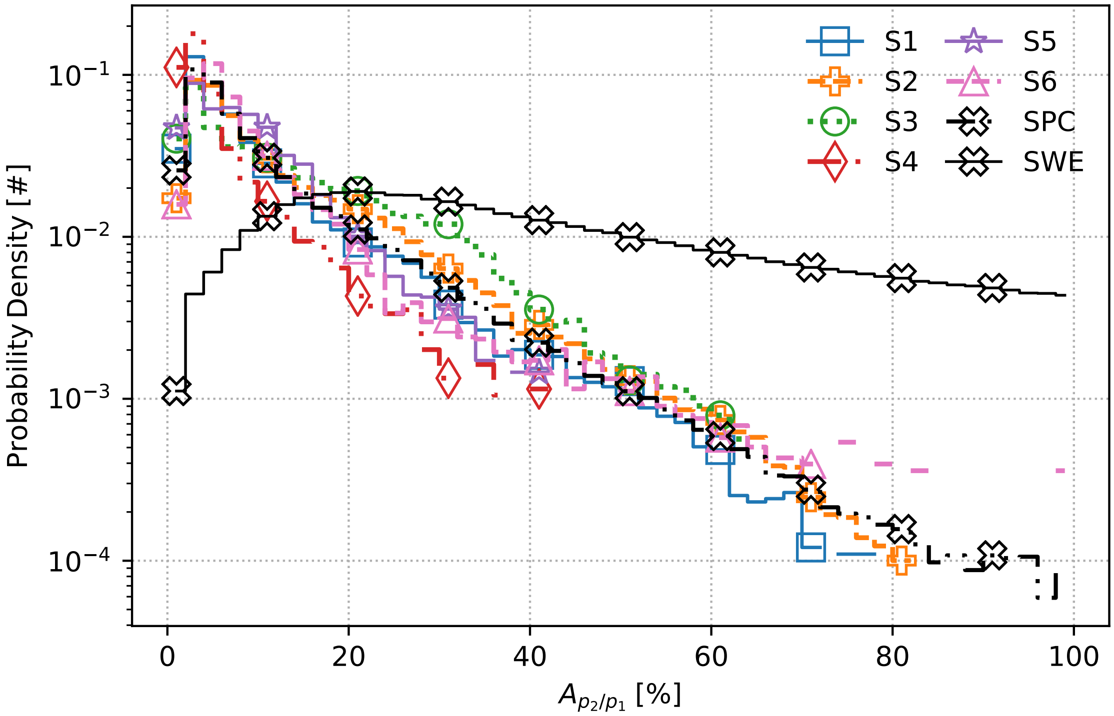

Figure 5.6: Proton beam abundance PDFs in the format of Figure 5.4.

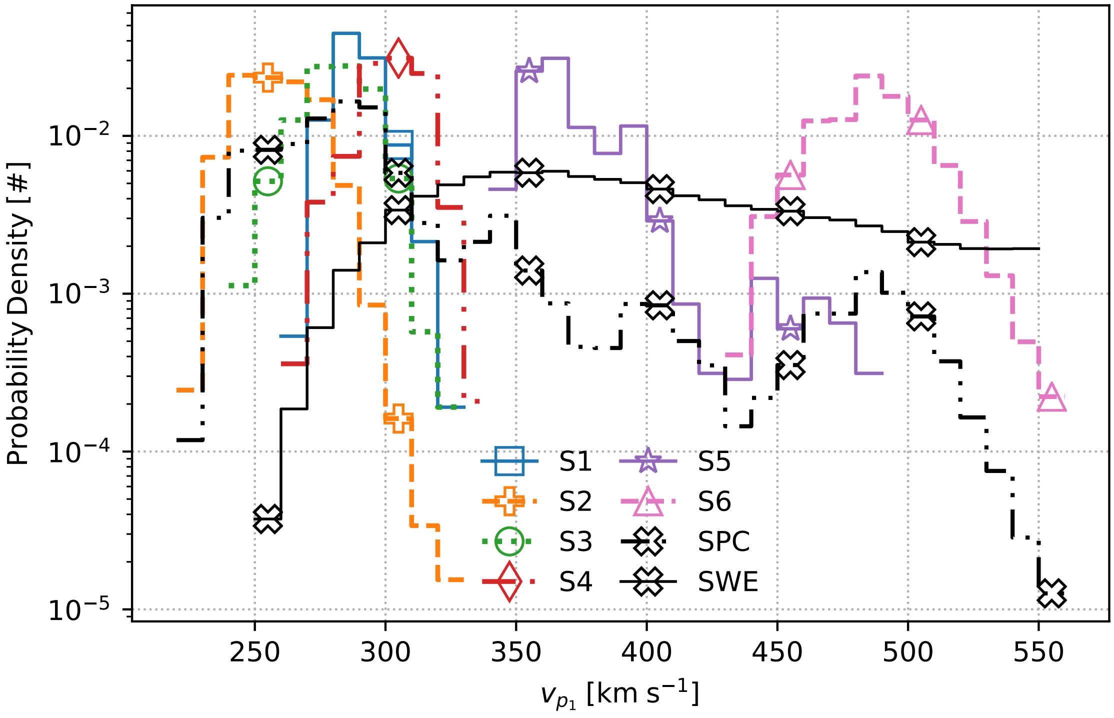

Figure 5.7: Proton core speed PDFs in the format of Figure 5.4.

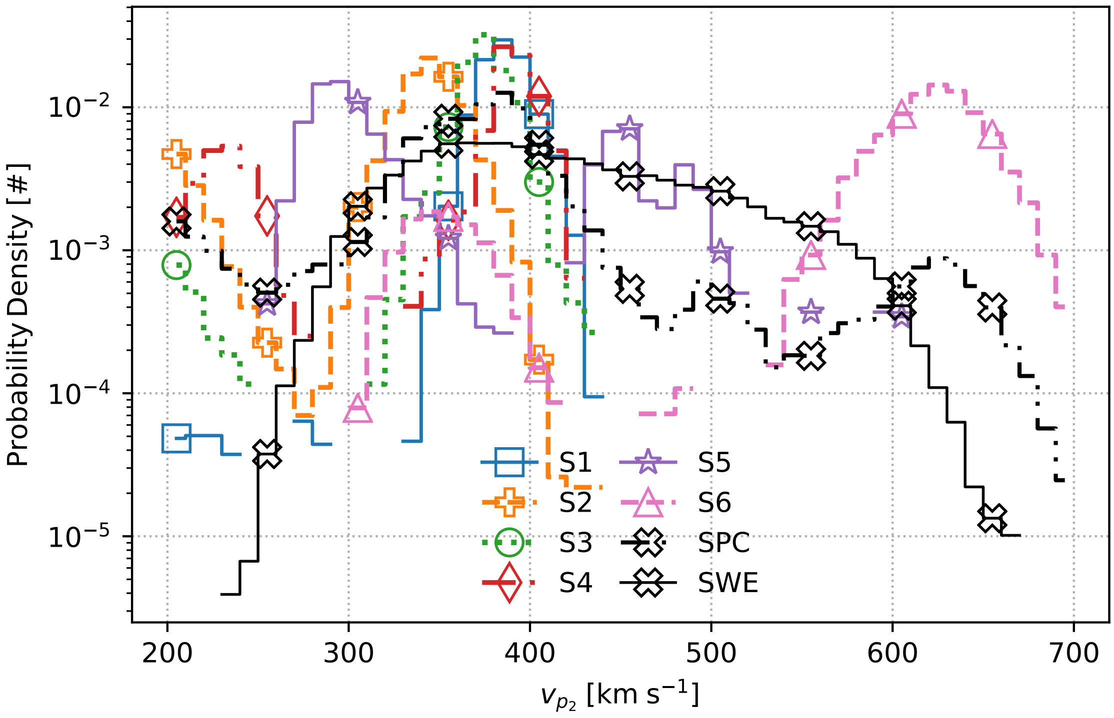

Figure 5.8: Proton beam speed PDFs in the format of Figure 5.4.

are accumulated across many different solar wind events that occur through a range of solar activity and wind conditions. As with the core speed measurements, it is difficult to rule out that the long term averages collected by *Wind* are the primary reason for the discrepancies between the E1 and L1 measurements.

Figure 5.9 plots PDFs of the core temperature. Over E1, the typical proton core temperature is between 1.1×10^5 K and 1.5×10^5 K. In comparison, 1.0×10^5 K is an upper bound on the core temperature at L1, which ranges between 0.6×10^5 K and 1.0×10^5 K. Note that because of SPC's bias towards measuring $T_\parallel$ during E1, we report the parallel proton velocity from L1.

Figure 5.10 plots PDFs of the beam temperature. Of the investigated parameters, the distribution of proton beam temperatures is in greatest agreement between SPC and SWE. Over all of E1, the typical temperatures measured by SPC are $0.9 \times 10^5 \text{ K} \pm 0.4 \times 10^5$ K. *Wind*/SWE reports a temperature $T_{p_2} = 0.9 \times 10^5 \text{ K} \pm 0.3 \times 10^5$ K at L1. Again, given SPC's bias towards parallel temperatures during E1, we also again report $T_\parallel$ from SWE.

Figure 5.11 plots PDFs of the beam-to-core temperature ratio T_{p_2}/T_{p_1}. Over all of E1, the range in temperature ratios is 0.4 to 1.0. The majority of events show a long, high T_{p_2}/T_{p_1} tail or two clear peaks in temperature ratio. Unlike the other events, the higher S3 T_{p_2}/T_{p_1} tail is the larger of the two peaks. Similar to S3, the distribution at SWE is

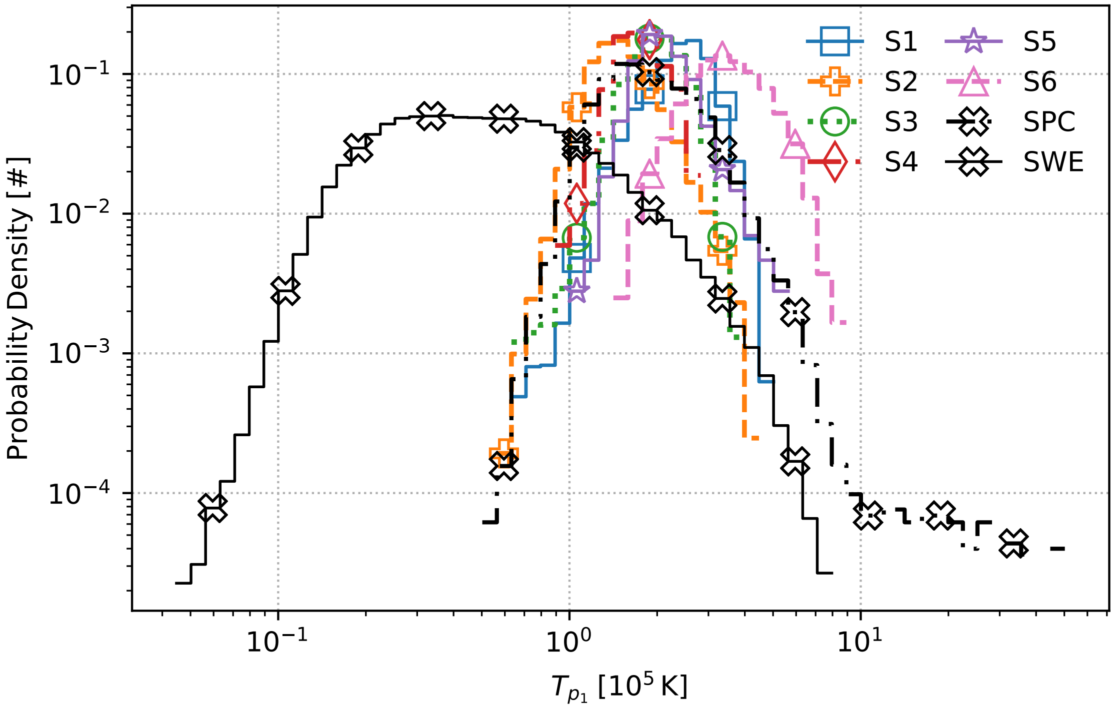

Figure 5.9: Proton core temperature PDFs in the format of Figure 5.4. To facilitate comparison between the near-Sun and L1 measurements, we utilize the parallel component of the L1 temperatures.

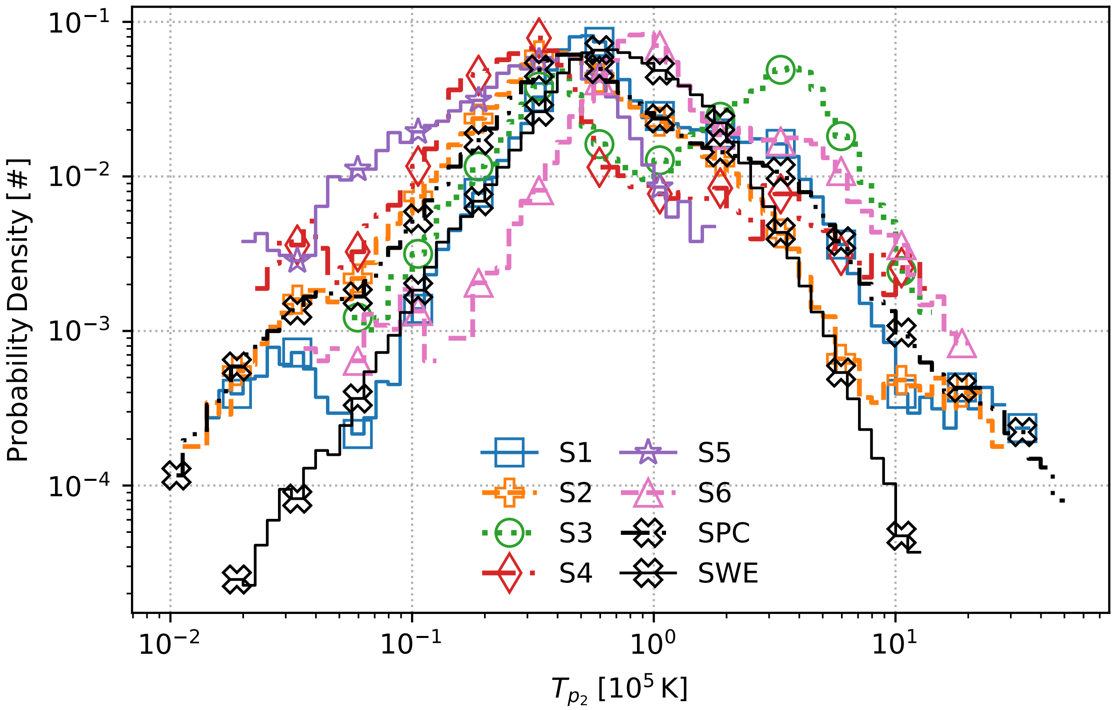

Figure 5.10: Proton beam temperature PDFs in the format of Figure 5.4. For the L1 proton beams assigned the bi-Maxwellian temperature, the parallel component is used.

also double peaked with the higher peak at larger temperatures and the higher T_{p_2}/T_{p_1} peak is the larger of the two at L1. The typical value ranges between 0.9 and 1.5. Unlike the SWE measurements, all of the SPC E1 events and the full E1 distribution show a long, low T_{p_2}/T_{p_1} tail. Again we emphasize that because proton beams primarily impact the component of the VDF parallel to the local magnetic field and SPC's temperature measurements are biased towards $T_\parallel$ due to the radial nature of $\hat{\boldsymbol{b}}$, we compare SPC temperatures with the parallel component of the SWE temperature ratio.

Figure 5.12 plots PDFs of the proton beam-core differential flow $\Delta v_{p_2,p_1}$ from both instruments. The typical drift speed measured by SPC range between $80 \ \mathrm{km\,s^{-1}}$ and $140 \ \mathrm{km\,s^{-1}}$. These speeds are markedly faster than the $40 \ \mathrm{km\,s^{-1}} \pm 20 \ \mathrm{km\,s^{-1}}$ drift speed at L1. That being said, the shapes of the PDFs measured by SPC and SWE are similar: each shows a high velocity tail and a sharp fall off at lower drift speeds. The low-speed fall off in SWE data is more dramatic.

Figure 5.13 plots PDFs of the Alfvén speed measured by SPC and SWE. We emphasize that calculating the Alfvén speed as $C_A = B/\sqrt{\mu_0 \rho}$ is an MHD estimate of an Alfvén wave, not necessarily its actual speed as determined directly from *FIELDS* measurements. The typical SPC Alfvén speed estimate is $90 \ \mathrm{km\,s^{-1}} \pm 30 \ \mathrm{km\,s^{-1}}$. The lower

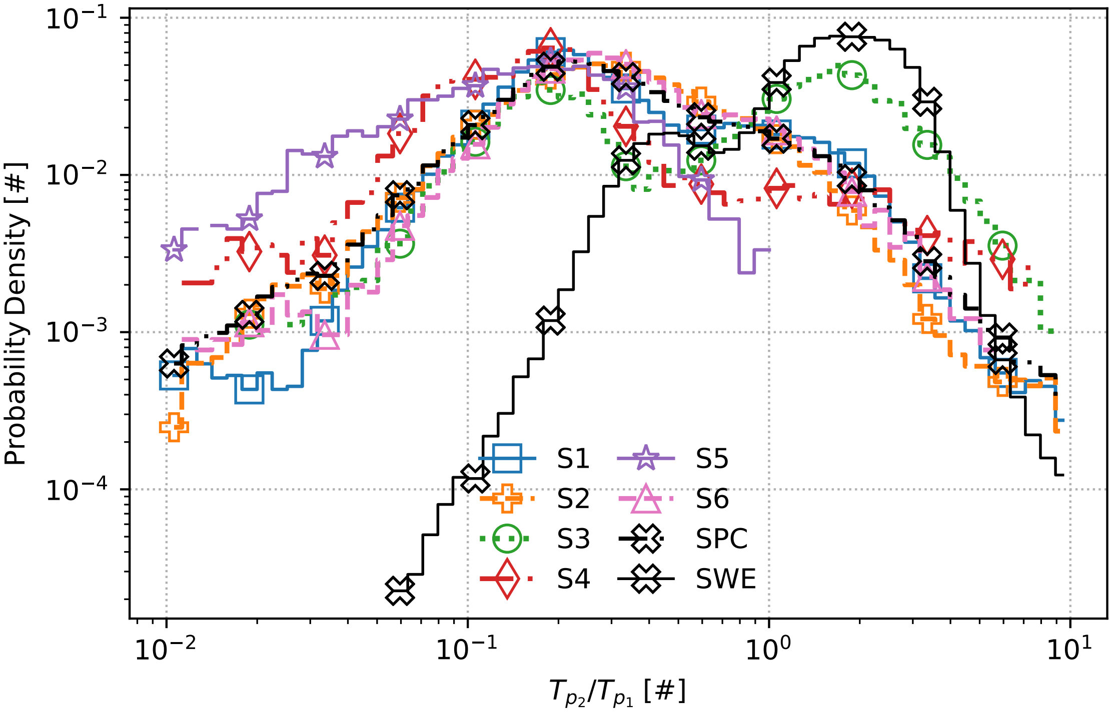

Figure 5.11: Proton beam-to-core temperature ratio PDFs in the format of Figure 5.4. To facilitate comparison between the near-Sun and L1 measurements, we utilize the parallel component of the L1 temperatures.

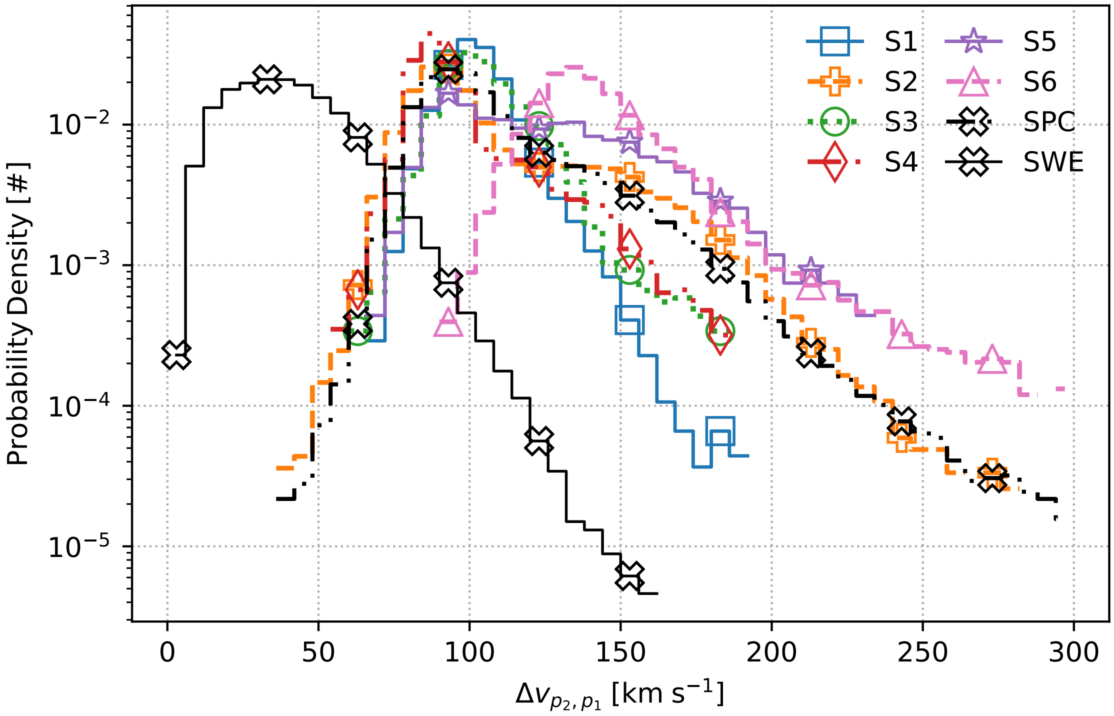

Figure 5.12: Proton beam-core differential flow PDFs in the format of Figure 5.4.

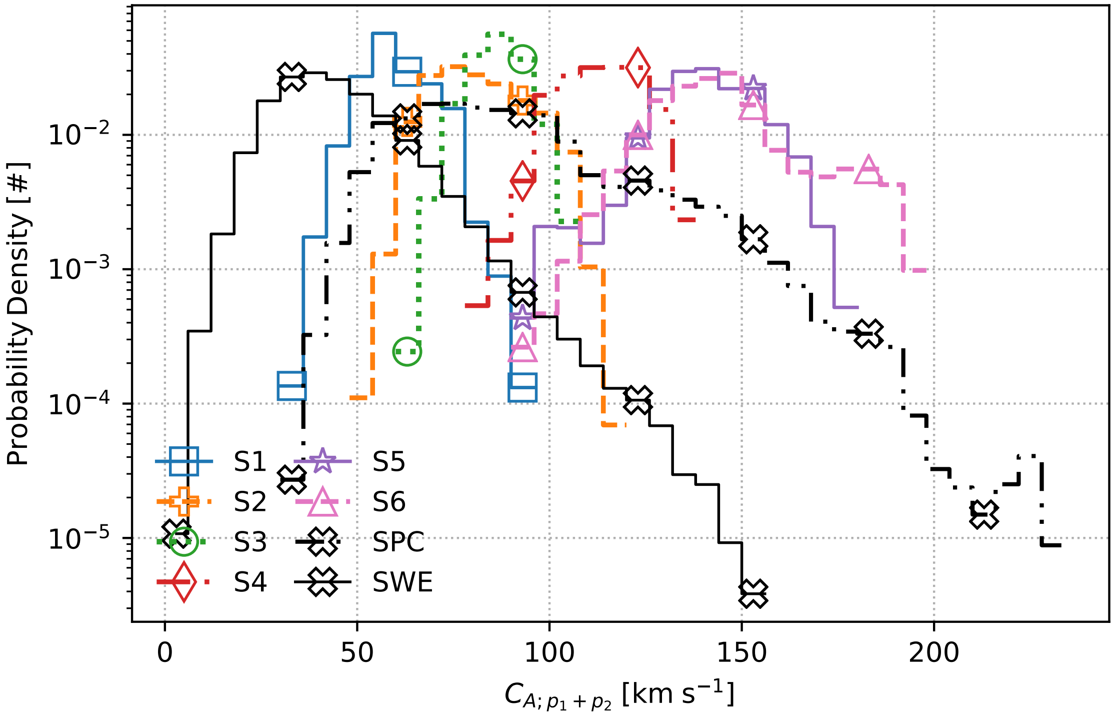

Figure 5.13: Alfvén speed PDFs in the format of Figure 5.4.

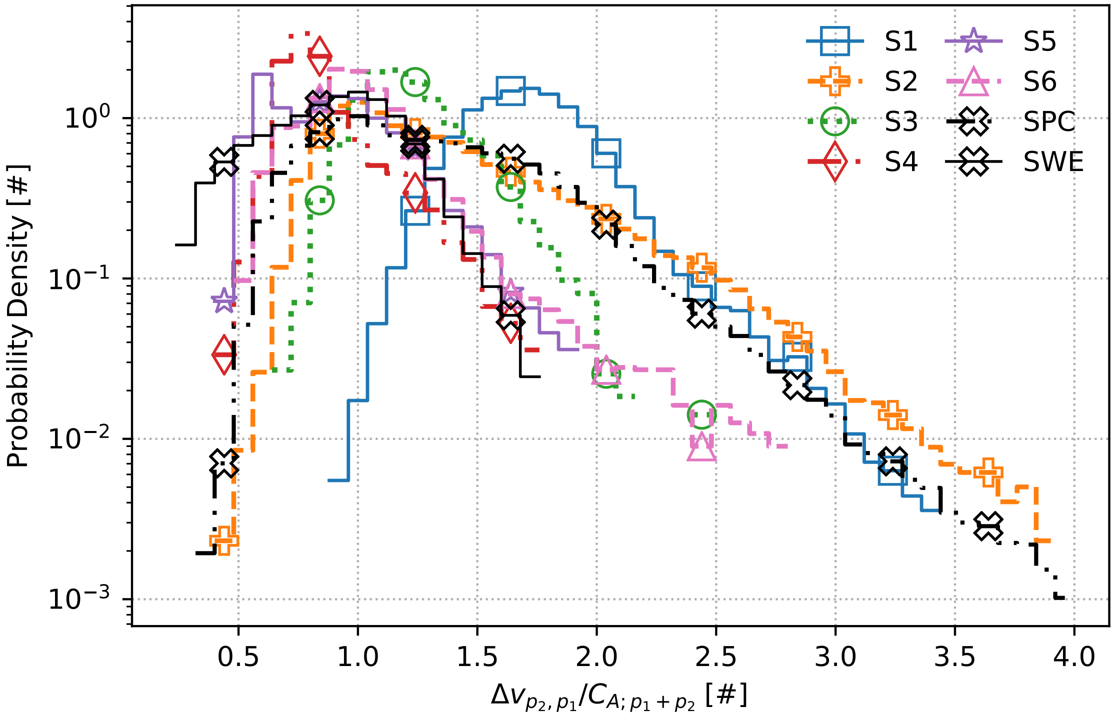

Figure 5.14: Proton beam-core Alfvén speed normalized differential flow PDFs in the format of Figure 5.4.

end of the SPC range is approximately the upper bound on the typical SWE measurements $40 \text{ km s}^{-1} \pm 20 \text{ km s}^{-1}$. As with the other figures, the smooth and continuous SWE PDF is at least partially due to the wide variety of solar wind conditions sampled over multiple solar cycles.

Figure 5.14 reports PDFs of the Alfvén speed normalized drift ($\Delta v/C_A$) measured by SPC and SWE. The typical normalized drift during E1 is 1.3 ± 0.5. The typical normalized drift measured by SWE at L1 is 0.9 ± 0.3. While only the typical values for events S4 to S6 are in rough agreement with the SWE measurements, all PDFs except S1 show roughly the same distribution as the L1 measurements. The major differences are that (1) the SPC events may have a larger high drift tail and (2) the SWE distribution does not fall off at smaller drifts in the matter that the SPC distributions do.

Figure 5.15 reports PDFs of the Coulomb number (N_c) measured by SPC and SWE. The dimensionless Coulomb number is a single-point approximation for the number of Coulomb collisions a given solar wind measurement has experienced over its radial propagation (Alterman et al., 2018; Chhiber et al., 2016; Kasper et al., 2017). As Coulomb collisions are small angle collisions and have an integrative effect over the solar wind's propagation, N_c serves as a proxy for the extent to which Coulomb collisions have isotropized

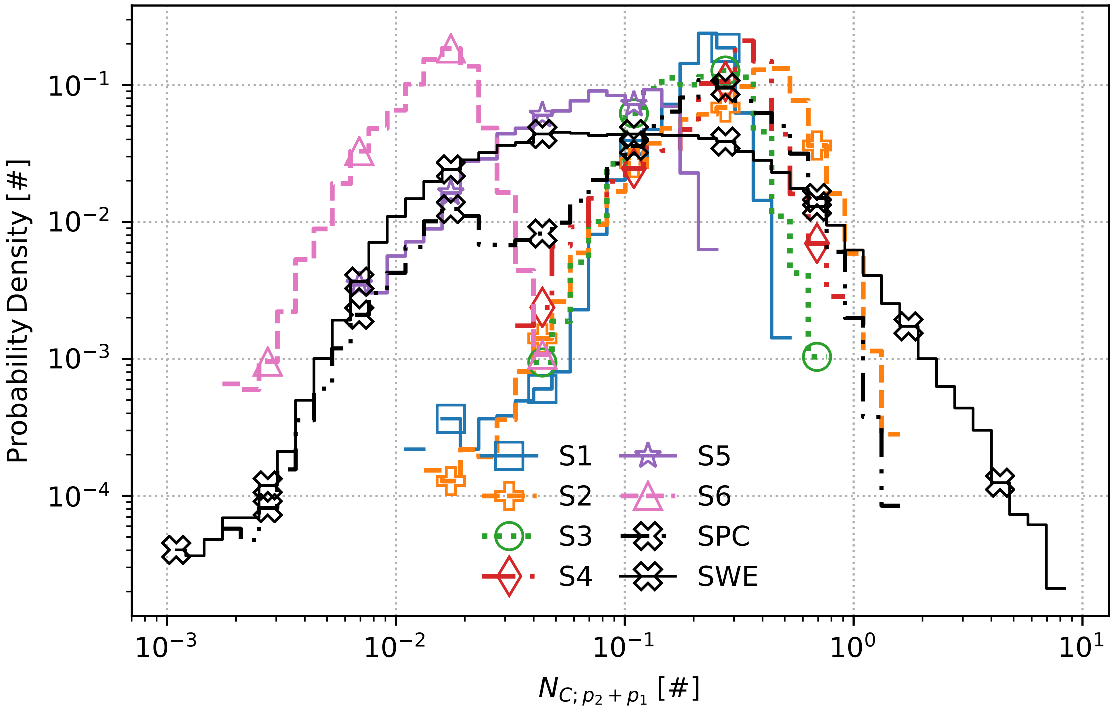

Figure 5.15: Coulomb number PDFs in the format of Figure 5.4.

a given non-thermal feature in a solar wind measurement. The Coulomb number is derived by integrating the collision frequency from $t = 0$ to some time t_1 in the argument of the exponential that describes the decay of non-LTE features. While the exact form of N_c changes based on the non-thermal feature and type of collisions considered, the quantity generally scales like $N_c \propto n/T^{3/2}$. Over all of E1, $N_c = 0.5 \pm 0.2$. As expected from the larger proton core speed during S5 and S6, N_c is lowest during these two events and S6 is the extreme outlier with $N_c = 0.16 \pm 0.03$. Unexpectedly, N_c measured at L1 is $N_c = 0.4 \pm 0.2$, which overlaps with events S1 trough S5.

5.6 Discussion and Conclusion

PSP's SPC and *Wind*/SWE's FC subsystem both provide proton beam measurements in the solar wind. PSP E1 occurred occurred from October 31st to November 12th, 2018 with perihelion occurred at 03:27 UT on November 6th, 2018 (Kasper and SWEAP, 2019). SPC provides measurements at a cadence not previously achieved at distances near the Sun never before explored with in situ instruments. *Wind* was launched in 1994 and the SWE/FCs provide long duration measurements of the solar wind at L1 across multiple solar cycles and a range of solar wind conditions. We have extracted proton beams from these

Quantity	Units	S1	S2	S3	S4	S5	S6	SPC	SWE
n_{p_1}	cm^{-3}	230 ± 40	300 ± 50	310 ± 30	300 ± 30	140 ± 20	60 ± 10	230 ± 90	4 ± 2
n_{p_2}	cm^{-3}	3 ± 1	4 ± 2	5 ± 2	3 ± 1	3 ± 1	2 ± 0.7	4 ± 2	1.1 ± 0.3
A_{p_2/p_1}	%	9.8 ± 10	10 ± 10	10 ± 10	6 ± 6	9 ± 7	10 ± 10	10 ± 10	40 ± 20
v_{p_1}	$\mathrm{km\ s}^{-1}$	289 ± 9	260 ± 10	280 ± 10	300 ± 10	370 ± 20	490 ± 20	300 ± 60	400 ± 70
v_{p_2}	$\mathrm{km\ s}^{-1}$	390 ± 20	330 ± 40	370 ± 30	360 ± 70	350 ± 80	590 ± 90	380 ± 80	420 ± 80
Δv	$\mathrm{km\ s}^{-1}$	100 ± 10	110 ± 30	110 ± 20	100 ± 20	130 ± 30	140 ± 30	110 ± 30	40 ± 20
C_A	$\mathrm{km\ s}^{-1}$	60 ± 9	80 ± 10	86 ± 7	110 ± 10	140 ± 10	140 ± 20	90 ± 30	40 ± 20
$\Delta v/C_A$	#	1.7 ± 0.3	1.4 ± 0.5	1.2 ± 0.2	0.9 ± 0.2	0.9 ± 0.3	1 ± 0.3	1.3 ± 0.5	0.9 ± 0.3
T_{p_1}	$10^5\,\mathrm{K}$	1.5 ± 0.2	1.2 ± 0.1	1.3 ± 0.1	1.3 ± 0.1	1.4 ± 0.1	1.7 ± 0.2	1.3 ± 0.2	0.8 ± 0.2
T_{p_2}	$10^5\,\mathrm{K}$	0.9 ± 0.4	0.8 ± 0.3	1.3 ± 0.7	0.7 ± 0.3	0.6 ± 0.2	1.1 ± 0.4	0.9 ± 0.4	0.9 ± 0.3
T_{p_2}/T_{p_1}	#	0.7 ± 0.3	0.6 ± 0.3	0.9 ± 0.5	0.6 ± 0.3	0.4 ± 0.2	0.7 ± 0.3	0.7 ± 0.3	1.2 ± 0.3
N_C	#	0.51 ± 0.08	0.6 ± 0.2	0.51 ± 0.1	0.6 ± 0.1	0.32 ± 0.1	0.16 ± 0.03	0.5 ± 0.2	0.4 ± 0.2
Distance	$R_\odot$	47 ± 1	41.8 ± 0.7	38 ± 0.5	35.74 ± 0.05	39.6 ± 0.6	45.4 ± 1	44 ± 4	240 ± 20
$\lambda_{\mathrm{Carrington}}$	deg.	-1.2 ± 0.2	-2.2 ± 0.2	-3.2 ± 0.2	-4.01 ± 0.05	-3.4 ± 0.1	-2.4 ± 0.2	-2 ± 0.8	—
$\phi_{\mathrm{Carrington}}$	deg.	-38.1 ± 0.8	-40.76 ± 0.08	-39.4 ± 0.5	-33 ± 1	-24.3 ± 0.3	-25.3 ± 0.5	-37 ± 5	—
Count	#	45,579	64,900	8,896	5,293	3,857	13,967	246,833	433,535
Prob.	%	15.1	24.7	6.8	5.4	5.2	17	14.7	52.2

Table 5.2: Means and standard deviations of significant proton beam quantities for each of the events. Averages of log-normally distributed quantities (n, T, & N_c) are taken in log space and converted back to report easily interpretable numbers. Means are only reported to the most significant digit of the standard deviation. Blank quantities are not measured in a given event. In addition to statistics reported in Figures 5.4 to 5.14, we also report the Coulomb Number (N_c), radial distance from the Sun, and location in Carrington coordinates for most measurements. In the case of *Wind*/SWE, we do not report the Carrington latitude ($\lambda_{\mathrm{Carrington}}$) and longitude ($\phi_{\mathrm{Carrington}}$) because the SWE data is collected over the course of > 20 years and the measurements cover the full set of possible longitudes and a continuous range of near-equatorial latitudes. The last two rows provide the total number of proton beam measurements and the probability of measuring a proton beam in each interval. The probability is calculated as the fraction of the measurements during the specified time interval that contain a proton beam.

measurements from both PSP/SWEAP/SPC in the near-Sun environment below 0.3 AU and the twin *Wind*/SWE/FCs at L1 in slow wind during low solar activity. As specific entropy is a meaningful proxy for charge states and E1 does not occur during solar maximum (Pagel et al., 2004), we used specific entropy to identify six intervals with qualitatively steady state proton beam measurements to also compare with L1 measurements. Table 5.2 summarizes the typical values for key measurements for interpreting proton beams. Those above the first line are plotted in Figures 5.4 to 5.15. The others are included for context. This is the first comparison of proton beams from below 0.3 AU with 1 AU measurements.

Broadly, it is clear from examining the six events and the full distributions from E1 that the structure in the E1 PDFs is the result of SPC over sampling a restricted set of solar wind conditions. In effect, the E1 measurements amount to several high resolution snap shots of the solar wind. In contrast, the L1 PDFs are smooth due to the long term nature of the *Wind*/SWE/FC measurements, in particular the variety of solar wind sources sampled. This difference is expected as E1 only covers approximately 12 days during the fall of 2018, where as the *Wind*/SWE measurements cover 1,418 days across two solar cycles, a collecting time that is more than two orders of magnitude longer. Therefore, we do not apply the Kolmogorov-Smirnov test (KS test) to compare the SPC and SWE measurements because the SWE measurements involve an average over solar wind conditions that are much broader than those SPC samples. That being said, at least a qualitative interpretation is warranted to contextualize the first perihelion measurements.

Figures 5.4 to 5.6 plot the dimension-full number densities and their ratio. From these figures and their typical values, we draw several observations. First, both the E1 and L1 beam abundances (Figure 5.6) peak at low abundances and show pronounced, high abundance tails. Second, the lower range of the E1 beam abundances (Figure 5.6) overlap with the upper range of the L1 abundance. Third, there is no overlap between the E1 and L1 core densities (Figure 5.4), while the lower range of the E1 beam densities overlap with the L1 beam density (Figure 5.5). While the rarefaction of n_{p_1} is expected from Helios results, the constancy of the beam density is not (Ďurovcová et al., 2019). Combined with the marked decreases in n_{p_1} between E1 and L1, this lends itself to the interpretation that A_{p_2} is systematically increased during the solar wind's propagation, which, likely, is primarily a consequence of the expansion of the solar wind impacting the proton core, but peculiarly, a different and as-yet-to-be-identified process impacting proton beam density.

Figures 5.7 to 5.8 plot the dimensionful proton beam and core speeds. These measurements highlight two observations. First, the slowest speeds measured by SPC are below the minimum solar wind speed measured at L1 by *Wind*/SWE (Kasper et al., 2007). Second, they highlight that the near-Sun measurements in SPC are a set of focused snapshots while the L1 measurements are long duration averages. We note that the tendency towards higher core speeds and constant beam speeds is consistent with prior Helios results (Ďurovcová et al., 2019). As such, more observations are needed to statistically determine if the low speed tail in SPC measurements may be accelerated to the minimum speed observed at L1.

Figures 5.9 to 5.11 plot the dimensionful temperatures and their ratio. In contrast to the velocity measurements, the temperature measurements are similar to the number density measurements in that they imply intriguing questions about the evolution of proton beams. Both the L1 and E1 core temperature measurements are unimodal. That the L1 distribution of T_{p_1} is broader than the E1 distributions is likely due to the variety of conditions sampled by SWE in comparison to SPC. That being said, the E1 distributions are peaked at higher temperatures–irrespective of solar wind speed–than the L1 distribution, implying that the proton core cools as expected (Ďurovcová et al., 2019) during solar wind evolution. In comparison, the proton beam measurements are notably bimodal in many of the SPC events and the full E1 distribution while the SWE measurements are unimodal. While the bimodal nature of the SPC T_{p_2} measurements is likely due to the snapshot nature of the SPC measurements, that the SWE and SPC PDFs overlap to this extent unexpectedly (Ďurovcová et al., 2019) implies that T_{p_2} may be consistent across radial distances, at least for Alfénic slow wind. Combined with the observations of dimensionful temperature, the temperature ratio T_{p_2}/T_{p_1} suggests that the low T_{p_2}/T_{p_1} tail in SPC measurements is likely due to SPC measuring a higher T_{p_1} than SWE, at least in this Alfvénic slow wind.

Figures 5.12 to 5.14 present PDFs of the differential flow, Alfvén speed, and Alfvén speed normalized drift. The comparison between near-Sun and L1 Δv measurements provide a less direct interpretation. As expected, near-Sun Δv, C_A, and $\Delta v/C_A$ are larger than at L1: SPC reports high velocity tails in which $\Delta v/C_A > 2$. This is larger than typically observed by Helios (Marsch et al., 1982b; Ďurovcová et al., 2019), *Wind* (Alterman et al., 2018), or Ulysses (Matteini et al., 2013). Further inferences requires additional context.

Figure 5.15 presents PDFs of the Coulomb number (N_c). Coulomb collisions are known to organize non-thermal features in the solar wind (Alterman et al., 2018; Kasper and Klein, 2019; Kasper et al., 2017, 2008; Livi et al., 1986; Marsch and Livi, 1987; Neugebauer, 1976). That SPC's N_c measurements overlap with SWE measurements is interesting because the observation runs counter to the expectation that Coulomb collisions have an integrative effect over the solar wind's propagation, for which large N_c corresponds to more collisionally processed plasma, and therefore, perhaps not expectedly (Alterman et al., 2018; Hellinger et al., 2013), does not provide clear insight into the evolution of this particular non-LTE feature.

Combining our observations from these near-Sun and L1 measurements leads to possible and conflicting interpretations of proton beams. First, the rarefaction of the proton core and relative constancy of the proton beam number densities implies that solar wind expansion does not effect proton beams. As the magnetic field and proton core density are known to follow $1/r^2$ laws, this points towards a local mechanism generating proton beams, at least in the Alfvénic slow wind primarily sampled during E1. Second, the comparison between Figures 5.9 to 5.11 point to proton core cooling that does not impact the proton beam. As the parallel temperature is constant under double adiabatic or CGL expansion (Chew et al., 1956; Matteini et al., 2013), these temperature observations imply that either there is a preferential temperature at which proton beams are locally generated or beam temperatures follow CGL expansion (which would require $n_{p_2} \propto r^{-2}$ and is therefore unlikely). Third, that Δv and $\Delta v/C_A$ decrease from their near-Sun environments to L1 lends itself to the interpretation that the differential flow is systematically slowed down during the solar wind's propagation or the local mechanism that generates it becomes less efficient at creating large drifts as the solar wind propagates towards L1.

There are two, not necessarily exclusive ways to square these seemingly contradictory observations. One is to invoke flux conservations. That the beam abundance A_{p_2} increases while both Δv and $\Delta v/C_A$ decrease from the near-Sun environment to L1 could be interpreted as simply the consequence of flux conservation: as Δv decreases, the density increases. Another, proposed by Tu et al. (2003, 2002) is quasilinear diffusion. Under their framework, the proton beam is locally generated, both Δv and C_A decrease with increasing distance from the Sun, and the beam density increases with distance. However, in either case, a more detailed study with a larger set of near-Sun measurements is required so that either theory can be tested across a variety of solar wind conditions in a large, statistically meaningful manner. Such a study will be possible as PSP continues its orbits and towards its descent below $10\ \mathrm{R_S}$ during its 23rd perihelion.

CHAPTER 6

On The Limitations of Applying Reduced Free Energy Parameter Spaces to Proton Beams in the Solar Wind

Section 3.7 closes by noting that descriptions of resonant interactions between solar wind ions and fields are incomplete without proton beams. A similar caveat applies to instabilities. Here, I begin that analysis.

6.1 Abstract

The solar wind is a near, but not fully collisionless plasma. As such, Coulomb collisions are unable to independently drive a plasma towards LTE. One class of mechanisms that may also drive a plasma towards LTE are instabilities, which are normal modes that grow with time. The types of instabilities that can arise in the solar wind depend on the available free energy sources. The number of these sources is proportional to the number of ion populations present. To make the associated free energy parameter space tractable, one can assume that only a reduced set of free energy sources are significant and derive thresholds across which instabilities are predicted to excite.

Proton beams are one type of charged particle distribution that has a marked impact on the thermal structure of solar wind protons. In this work, we demonstrate that neglecting the contribution of proton beams impedes the threshold methodology's ability to adequately characterize instabilities in the solar wind. Furthermore, selecting a reduced set of free energy sources specifically tailored to capture the proton beam's free energy contributions is similarly deficient in its ability to predict the distribution of solar wind measurements. We therefore use an alternative method for characterizing instabilities in the solar wind to demonstrate that proton beams may lead to a profusion of small growth rate instabilities at angles oblique to the magnetic field ($\theta_{\boldsymbol{k}} \sim 45^o$).

6.2 Introduction

Under the assumptions of linear theory, a plasma can be treated as the sum of a background component and small amplitude perturbations (Stix, 1992; Verscharen et al., 2019). As such, the plasma's behavior is decomposed into normal modes. Solutions whose frequency includes an imaginary amplitude that grows with time are unstable and referred to as instabilities (Gary, 1993; Marsch, 2006; Verscharen et al., 2019).

The class of instability depends on the available sources of free energy (Klein et al., 2017). Assuming the ion populations can be described by bi-Maxwellian distributions, the number of parameters that impact the class of instabilities present scales as $3+4(N_{\mathrm{ion}}-1)$, where N_{ion} is the number of ion populations present in the system (Klein et al., 2017). The majority–but not all–of these parameters correspond to free energy sources. One method for addressing this high dimensionality is to assume that all but two of the parameters are negligible and can be approximated as fixed values. This method leads to a visually interpretable representation of the plasma's stability in which a threshold represents the transition from stability to instability (Daughton and Gary, 1998; Daughton et al., 1999; Hellinger et al., 2006; Kasper et al., 2003; Klein et al., 2018, 2017; Marsch and Livi, 1987; Maruca et al., 2012; Verscharen et al., 2016, 2019; Woodham et al., 2019).

When considering a proton-electron or proton-alpha-electron plasma, two prototypically examined free energy sources are parallel plasma beta[1] and temperature anisotropy[2] (Maruca et al., 2012; Verscharen et al., 2016, 2019). In the case of a plasma for which the protons are treated as a single population, the thresholds derived for these free energy sources do not bound the full distribution of measurements.

Proton beams provide up to four additional sources of free energy[3] that add to the high dimensionality of the (in)stability parameter space. As is customary, Daughton and Gary (1998); Daughton et al. (1999) have derived instability thresholds tailored to proton beam-core distributions by assuming that the significant free energy sources are the beam density fraction ($n_{p_2}/(n_{p_1+p_2})$), a modified core parallel plasma beta ($\tilde{\beta}_{\|,p_1}$), and the normalized beam-core differential flow ($\Delta v_{p_2,p_1}/C_A$). Tu et al. (2004) study the applicability of this threshold in fast wind ($v_{\mathrm{sw}} > 600\ \mathrm{km\,s^{-1}}$) Helios 2 data and demonstrate that these instabilities may not be active in regulating the solar wind.

This work studies the impact of proton beams on solar wind stability. It starts by illustrating that they may account for the MM's inability to predict the distribution of solar wind

---

[1] $\beta_{\|,s} = \frac{n_s k_{\mathrm{B}} T_{\|,s}}{B^2/2\mu_0}$ for species s.

[2] $R_{T,s} = T_\perp/T_\|$ for species s.

[3] The presence of an additional species (n_{p_2}), the beam-core drift ($\Delta v_{p_2,p_1}$), the beam temperature anisotropy (R_{p_2}), and the beam-to-core temperature ratio (T_{p_2}/T_{p_1}).

measurements in the $(\beta_\parallel, R)$ plane. Then, using thermal ion data measured by SPC during PSP's first solar perihelion below $0.3\,\mathrm{AU}$, we study the proton beam instability thresholds in intermediate and slow solar wind ($v_{\mathrm{sw}} \leq 550\ \mathrm{km\,s^{-1}}$) . We substantiate the results of Tu et al. (2004) showing that the instabilities derived by Daughton and Gary (1998); Daughton et al. (1999) may not regulate solar wind proton beams. We then combine the data from Chapter 3 and Klein et al. (2018) to illustrate that quantifying local regulation of proton beams may require a method that accounts for more free energy sources than available in this reduced parameter space methodology.

The remainder of this chapter proceeds as follows. Section 6.3 describes the data sources and selection criteria. Section 6.4 reviews the distribution of *Wind*/SWE/FC solar wind measurements in the prototypical $(\beta_\parallel, R)$ plane; compares the two data sources from these L1 instruments; and illustrates that neglecting the proton beam may disregard non-trivial free energy sources. Section 6.5 utilizes data from SPC below $0.3\,\mathrm{AU}$ to study the instability thresholds derived by Daughton and Gary (1998); Daughton et al. (1999) specifically for the proton beam and substantiates the results from Tu et al. (2004) that these instabilities may not regulate the solar wind. Section 6.6 studies the distribution of maximum instability growth rates in in the $(\beta_\parallel, R)$ plane and illustrates that the presence of proton beams leads to instabilities that these two reduced free energy parameter spaces do not account for. Section 6.7 discusses these results. Finally, 6.8 concludes.

6.3 Data Sources

FCs are energy-per-charge (E/q) detectors from which a measured current can be converted into physical quantities. They have been a work horse of space plasma instrumentation since the dawn of the space age (Neugebauer, 2003; Neugebauer and Snyder, 1962) making long duration solar wind measurements at L1 (Alterman and Kasper, 2019; Kasper et al., 2006; Ogilvie et al., 1995), just recently entering the interstellar medium on Voyager 2 (Bridge et al., 1977, 1960), and as of August 2018 measuring the near-Sun environment below $0.3\,\mathrm{AU}$ (Fox et al., 2015; Kasper et al., 2016; Kasper and SWEAP, 2019). In this paper, we will utilize FC measurements from two spacecraft: *Wind* at L1 and PSP below $0.3\,\mathrm{AU}$.

6.3.1 *Wind*/SWE Faraday Cup Data

The *Wind*/SWE/FCs have been in continuous operation since the spacecraft's launch in 1994. The majority of this time has been spent in the solar wind. Ogilvie et al. (1995)

describes the spacecraft's instruments in detail. For the purposed of this study, we remind the reader that they are thermal ion instruments that measure a reduced projection of the solar wind's VDF every $\sim 92\,\mathrm{s}$. From these measurements, the full 3D VDF can be extracted. The instrument resolution in energy space is $\Delta E/E = 6.5\%$ (peak tracking mode) or 13% (full scan mode). The operational range of the instrument in terms of energy-per-charge (E/q) is $150\,\mathrm{V}$ to $8\,\mathrm{kV}$. A single spectrum or measurement of the VDF is made by combining approximately 32 logarithmically spaced measurements at a specific E/q, each made in 20 different look directions (Kasper et al., 2006; Ogilvie et al., 1995; Stevens and Alterman, 2019). As FCs are E/q detectors, alpha particles are measured in an energy window that is $2\times$ higher than their actual energy because they have a mass-to-charge ratio (m/q) twice that of protons. Consequently, they can always be measured in a FC, even when they are co-moving with protons (Alterman et al., 2018; Kasper et al., 2008, 2006; Maruca and Kasper, 2013). However, the constant $\Delta E/E$ resolution also implies that alpha particles are measured more coarsely than protons. Because of the resolution in the instrument's operation range where protons are measured, a secondary proton population – also known as a beam – that drifts with respect to the core can be resolved when their drift is sufficiently large (Alterman et al., 2018; Stevens and Alterman, 2019). The tradeoff between the protons and alpha particles is that the constant $\Delta E/E$ sampling windows in a FC retain the resolution in the (lower) portion of their E/q range necessary to regularly resolve a proton beam (Chapter 3), but not an alpha beam. This is limitation is in measuring alpha particles present in ESAs on Helios (Marsch et al., 1982a) as well.

Kasper et al. (2006) developed algorithms for extracting one bi-Maxwellian proton and one bi-Maxwellian alpha particle population from *Wind*/SWE/FC spectra. Chapter 3 has reprocessed these spectra in an automated fashion to extract two-population proton fits that contain a beam and a core over a wide range of solar wind conditions, including collision numbers (N_c) larger than those studied by Alterman et al. (2018). These measurements will soon be available on CDAweb. As with Chapters 3 and 5, these measurements do not include alpha particles. Additionally, the two-population proton fits treat one population as a bi-Maxwellian and the other population as a drifting Maxwellian or isotropic distribution. This choice improves fit convergence and allows them to identify smaller proton beams in an automated fashion. The larger density population is considered the core and the smaller the beam. Typically, the former reports the bi-Maxwellian temperature and the latter the isotropic. Note that in a dataset that only includes a single proton population, the proton core of a two-population fit is regularly synonymous with – but not numerically identical to – the single-population proton population. Our data selection follows Chapter 3 with the addition that we only select cases for which the larger density (and therefore the core) is associated with the bi-Maxwellian temperature.

In contrast to the automated fitting routine choice, Klein et al. (2018) manually fit 309 of the *Wind*/SWE/FC spectra chosen in a random fashion. By including a scientist in-the-loop, they can relax the Maxwellian constraint on the drifting proton population and treat both the proton beam and core as bi-Maxwellians. The scientist in-the-loop also enables Klein et al. (2018) to simultaneously extract a reliable bi-Maxwellian alpha particle measurement. In this work, we have expanded the 309 manual fits from Klein et al. (2018) to 557 manually fit spectra. These data now sample the years 2013 through 2018. We then use these 557 manual fits in combination with the automated two-population proton fits derived in Chapter 3 to study the impact of proton beams on solar wind stability.

6.3.2 PSP/SWEAP Faraday Cup Data

PSP launched in August, 2018 (Fox et al., 2015) and made it's first visit perihelion on November 6th, 2018 (Kasper and SWEAP, 2019). We refer to the period during which this perihelion took place as E1. The SWEAP instrument suite carries with it a single FC mounted adjacent to the heat shield that directly observes the solar wind in the ram direction. As explained in Chapter 5, SPC measures a radial projection of the solar wind. We follow the data selection described in that chapter. As such, the temperatures measured are biased towards $T_{\|}$ and, given the instrument's constraints, the data is well suited to studying solar wind stability.

6.4 Proton Beams in The Prototypical $(\beta_{\|}, R)$ Plane

Because proton beams are more difficult to measure than alpha particles, the *Wind*/SWE/FCs have been reporting a combined dataset with a single proton population and single alpha population (Kasper et al., 2006) for longer than a proton beam-core distribution (Chapter 3). As such, the reduced $(\beta_{\|;p}, R_p)$ parameter space is more widely studied (Hellinger et al., 2006; Kasper et al., 2003; Maruca et al., 2011, 2012; Matteini et al., 2013; Verscharen et al., 2016) and has become the prototypical reduced set of free energy sources. Verscharen et al. (2016) define four instabilities in this plane accounting for for a single proton population. These are the MM, AIC FMW, and OFI mode. That there are markedly few measurements beyond the OFI threshold is taken as evidence that this instability constrains the solar wind's evolution (Hellinger et al., 2006; Kasper et al., 2003). In contrast, it is an outstanding problem as to why there are measurements present beyond the AIC and MM thresholds.

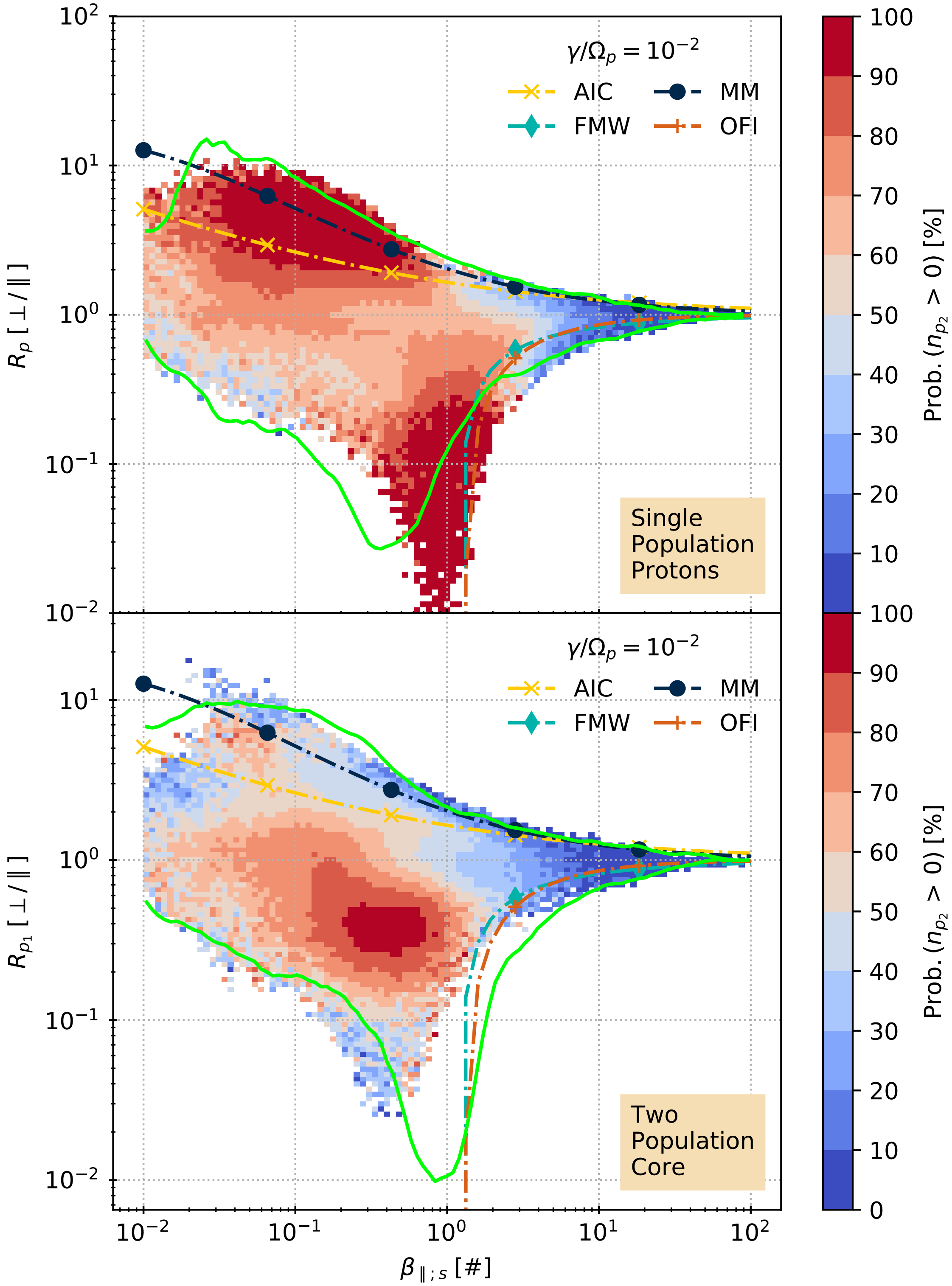

Figure 6.1: The probability of measuring a proton beam in the $(\beta_{\parallel}, R)$ plane defined for (Top) p (Kasper et al., 2006) and (Bottom) p_1 (Chapter 3). The instability contours are derived by Verscharen et al. (2016) for a single bi-Maxwellian proton population. As such, they are formally only applicable to the (Top) panel and are included on the (Bottom) panel primarily for reference. The green contour indicates the alternate panel's distribution of beam-containing measurements.

Figure 6.1 plots the probability of measuring a proton beam in (Top) the $(\beta_{\parallel;p}, R_p)$ plane defined by the single population protons (Kasper et al., 2006) and (Bottom) the two-population proton core (Chapter 3) when the core is associated with the bi-Maxwellian temperature. In the Bottom panel, the probability of measuring a beam component is the fraction of the spectra containing a beam in units of percent. In the Top panel, we select the single population spectra for which the two-population fit returns at least one proton distribution. The probability of measuring a beam in this panel is the fraction of those spectra that contain a beam. Only bins with at least 10 measurements are shown. In both panels, we plot the thresholds derived by Verscharen et al. (2016) for $\gamma/\Omega_p = 10^{-2}$. These thresholds are derived for a single, bi-Maxwellian proton population and, as such, only formally applicable to the (Top) panel. Because it is instructive and provides a useful visual reference (Matteini et al., 2013), they are also present on the (Bottom) panel plotting $(\beta_{\parallel;pc}, R_{pc})$. In the single-population case (Top), the probability of measuring a proton beam is large at the extreme anisotropies, especially above the AIC threshold. In the proton core plane (Bottom), the probability of measuring a beam is smallest at the extreme anisotropies and, instead, is largest near $(\beta_{\parallel;p_1}, R_{p_1}) = (0.4, 0.4)$. The solid green curve in each panel is the outline of the proton beam-containing measurements in the other panel as illustrated in Figure 1.3.

6.5 Instabilities in the Proton Beam Reduced Free Energy Plane

Daughton and Gary (1998); Daughton et al. (1999) suggest that a modified plasma beta $(\tilde{\beta}_{\parallel,s})$, the beam density fraction (n_{p2}/n_{p1+p2}), and the Alfvén speed normalized beam-core drift $(\Delta v_{p2,p1}/C_A)$ are three key sources of free energy associated with plasma stability when a proton beam is present. As an alternative to $(\beta_\parallel, R)$ instabilities, Daughton and Gary (1998) define an instability threshold for the growth rate $\gamma/\Omega_p = 10^{-2}$ given by Equation (6.1)

$$\Delta v/C_A = \Delta_1 + \Delta_2 \left(0.5 - \frac{n_{p2}}{n_{p2+p1}}\right)^3 \tag{6.1}$$

for which

- $\Delta_1 = 1.65\tilde{\beta}_{\parallel,p_1}^{0.06}$,
- $\Delta_2 = 5.1 + 1.9\tilde{\beta}_{\parallel,p_1}$,
- $n_{p2+p1} = n_{p2} + n_{p1}$,

- and the modified plasma beta is $\tilde{\beta}_{\parallel,p_1} = \frac{n_{p_1+p_2} k_\mathrm{B} T_{\parallel,p_1}}{B^2/2\mu_0}$.

Daughton and Gary (1998) name this the *Alfvén Type I* or *Alfvén I* instability.

Tu et al. (2004) studied the applicability of the *Alfvén I* threshold to $\Delta v_{p_2,p_1}/C_A$ using 616 proton beam containing spectra from Helios 2 data in high speed solar wind ($v_\mathrm{sw} > 600\ \mathrm{km\,s^{-1}}$) over the range $0.1 \leq \beta \leq 1.0$. They derived the empirical relationship that $\Delta v/C_A = (2.16 \pm 0.03)\beta_{\parallel,p_1}^{0.281\pm0.008}$. While they found that the stability threshold (Daughton and Gary, 1998) is robust, they suggest that this instability may not regulate the solar wind:

> By inspection of our data shown in Figures 2–4, we can only find a few unstable data points, at the upper right edges of the data distributions. Therefore the beam instability seems to be seldom at work. The theoretical instability threshold may still be considered a relevant upper bound to the observed data. However, since most data points are far from the unstable regime, they may not even be associated with and thus not considered as being regulated by a beam instability.

Figure 6.2 presents $\Delta v(\tilde{\beta}_{p_1})$ in SPC data. The gray band initiates the range in $\tilde{\beta}_{p_1}$ studied by Tu et al. (2004). As explained in Section 5.3, SPC only contains the radial projection of the proton VDF. Consequently, the T in this β is formally its radial projection. However, during E1, the local magnetic field was primarily radial and, as such, SPC measures a temperature biased towards $T_\parallel$. Therefore, $\tilde{\beta}_{p_1}$ is a close approximation of $\tilde{\beta}_{\parallel,p_1}$, but not identically the same quantity. The orange line with open squares is the trend derived by Tu et al. (2004) for high speed wind. The dark blue line is a series of 1D Gaussian fits to $\tilde{\beta}_{p_1}$ (for which the error bars are the standard deviation derived from these fits) and the red line is a robust fit to the trend of these 1D fits parameters in the style of Figure 4.9.

As a 2D parameter space is most applicable to the relationship between two free energy sources in the solar wind when considering an instability threshold (see Section 1.4.2) and this threshold depends on three, the *Alfvén I* thresholds are calculated in two ways such that the significance of the third quantity (number density, not plotted) can be interrogated. The fuchsia or pink dash-dot line marked with open diamonds (DG $\bar{n}$) uses the average of all $(n_{p_2}/n_{p_1+p_2})$ measurements to calculate the threshold. The light blue or cyan dash-dot-dot line marked with open circles (DG $n(\tilde{\beta})$) uses the average of $(n_{p_2}/n_{p_1+p_2})$ in each β column to calculate the threshold. As such, the latter threshold is not be expected to be smooth in the manner of the former. Clearly, in the range $0.1 \leq \tilde{\beta}_{p_1} \leq 1$, the difference is negligible. Note that Figure 6.2 uses the same growth rate $\gamma/\Omega_p = 10^{-2}$ as Figure 6.1. Several observations stand out in this figure.

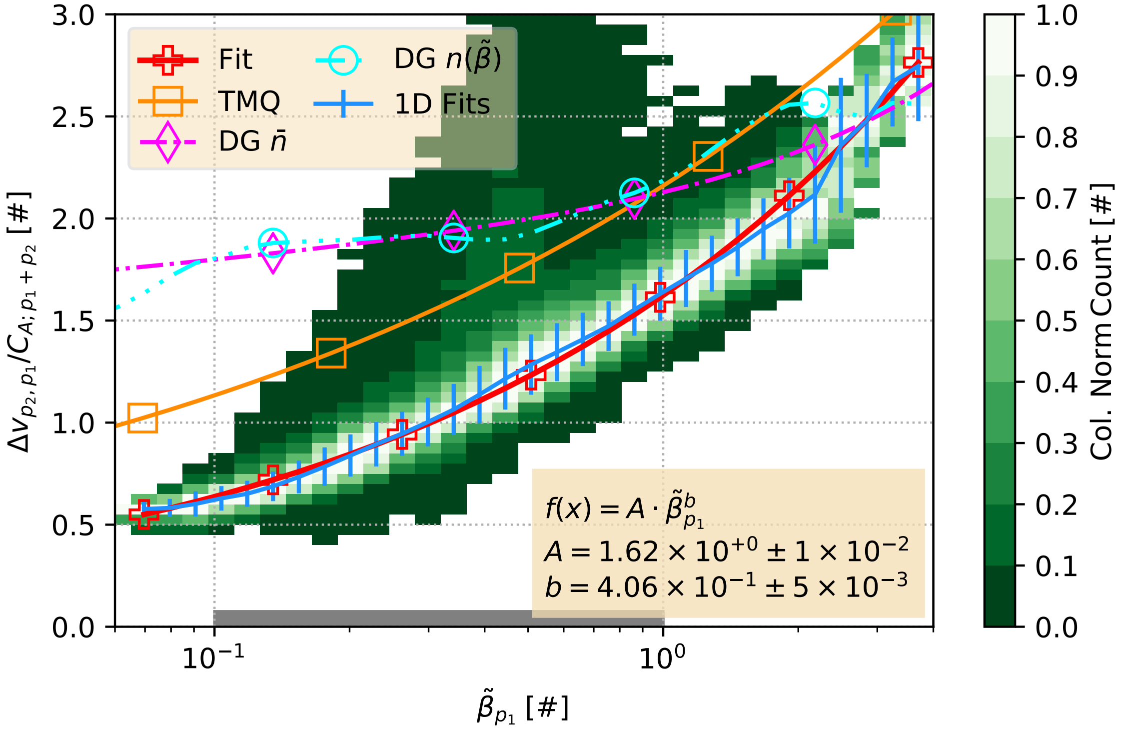

Figure 6.2: Proton beam-core differential flow ($\Delta v_{p_2,p_1}/C_{A;p_1+p_2}$) as a function of modified proton core beta ($\tilde{\beta}_{p_1}$) from SPC. The 2D histogram indicates column normalized number of counts in each bin. The orange line with unfilled squares indicates the trend from Tu et al. (2004) derived with Helios 2 data over the range $0.1 \leq \beta \leq 1.0$ (gray band on the lower edge of the plot). The dark blue lines indicate 1D Gaussian fits to $\tilde{\beta}_{p_1}$ in each column with error bars indicating the standard deviation from each fit. The red line with unfilled plusses indicates a fit to the trend of the blue fits, both in the style of Figure 4.9. The insert gives the fit trend fit parameters and the associated fit uncertainties. The DG curves present a theoretical instability threshold (Daughton and Gary, 1998) that depends both modified plasma beta and beam density fraction ($n_{p_2}/n_{p_1+p_2}$). The light blue or cyan line marked with open diamonds (DG $\bar{n}$) uses the average of all ($n_{p_2}/n_{p_1+p_2}$) measurements to calculate the threshold. The fuchsia or pink line marked with open circles (DG $n(\tilde{\beta})$) uses the average of ($n_{p_2}/n_{p_1+p_2}$) in each $\tilde{\beta}_{p_1}$ column to calculate the threshold.

	p_1	α, p_1	p_1, p_2	α, p_1, p_2	Total
MM	0	1	0	19	20
AIC & MM	0	2	0	94	96
Stable	1	188	8	239	436
FMW & OFI	0	2	0	0	2
OFI	0	3	0	0	3
Total	1	196	8	352	557

Table 6.1: The number of manually fit spectra in each of Figure 6.3's $(\beta_{\parallel;p_1}, R_{p_1})$ regions.

1. The empirical relationship derived by Tu et al. (2004) is systematically higher than the trend derived in the red fit.
2. The fit exponent b derived in the red curve is 30% larger than that derived by Tu et al. (2004).
3. The trend derived by Tu et al. (2004) is not an upper bound.
4. The threshold derived by Daughton and Gary (1998) does not limit the data distribution in this plane.

Together, these observations suggest that even a reduced free energy parameter space specifically derived to account for the proton beam may not effectively characterize solar wind stability.

6.6 Maximum Growth Rates

Instead of assuming that a subset of the solar wind's free energy sources are the primary instability drivers, Nyquist (1932) derives an alternative method that is agnostic to the free energy sources and instead identifies if a growing mode is present. Klein et al. (2017) have implemented this method in a manner applicable to solar wind measurements that counts the number of modes with a non-zero growth rate. Klein et al. (2018) have applied it to the 307 manually fit *Wind*/SWE/FC spectra in a manner that leads to a determination of the maximum growth rate ($\gamma_{\max}$) supported by a given measurement. They found that unstable spectra are more likely to have a large alpha particle drift $\Delta v_{\alpha,p_1}$, a proton core temperature anisotropy R_{p_1}, "further from isotropy," (Klein et al., 2018), and contain a proton beam. We have expanded that 307 measurement dataset by 82% to 557 measurements.

Figure 6.3 plots the distribution of these manual fits in the $(\beta_{\parallel;p_1}, R_{p_1})$ plane. The marker color and symbol indicate the species resolved in each manually fit spectrum. For

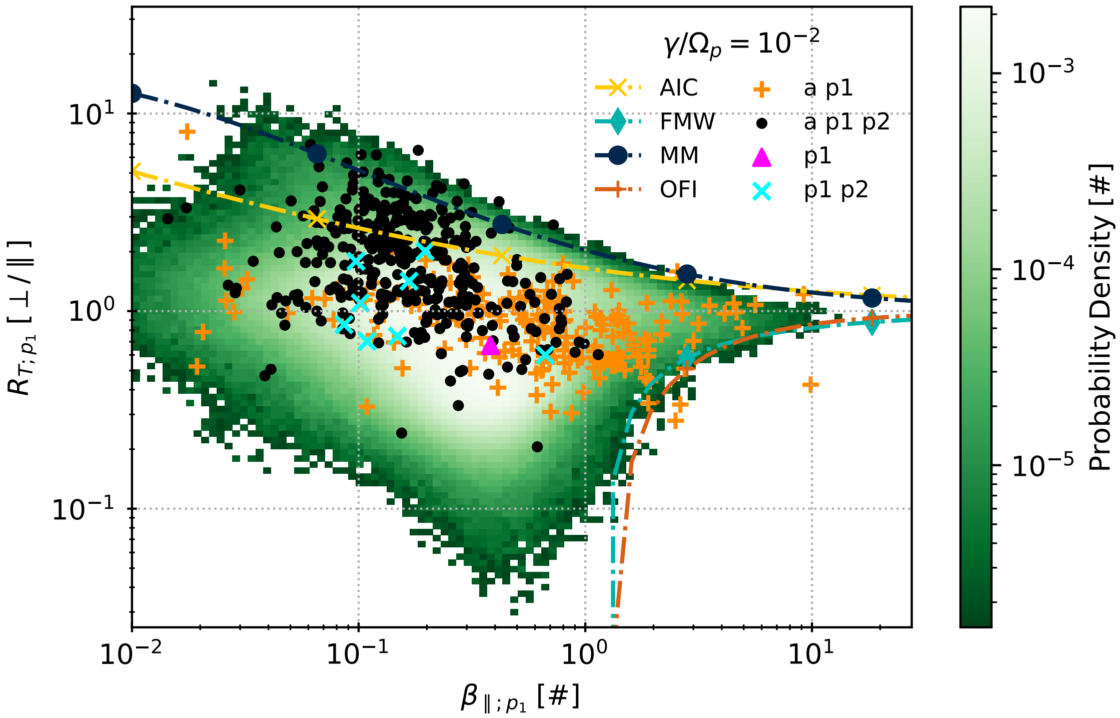

Figure 6.3: The PDF of measurements in the canonical $(\beta_{\parallel}, R)$ plane defined for the bulk or core (p_1) protons derived from automated fitting algorithms. The species identified in the 557 manual fits are plotted on top of the 2D PDF. Verscharen et al. (2016) derives the plotted instability contours accounting for a single bi-Maxwellian proton population. As such, these contours must be interpreted with caution and primarily used as reference when comparing them with a two-proton population data set.

		MM	Between AIC & MM	Stable	Global
Max	[#]	0.205	0.100	0.115	0.205
Median	[#]	0.108	0.027	0.001	0.004
Count(>0)	[#]	20	93	220	338
Prob.(>0)	[%]	3.591	17.235	78.276	60.682

Table 6.2: Statistics regarding the maximum unstable growth rate ($\gamma_{\max}/\Omega_{p_1}$) in each of the five regions of the $(\beta_{\|,p_1}, R_{p_1})$ plane defined by the instability contours derived by Verscharen et al. (2016) and the entire plane (Global). The median growth rate only accounts for those spectra with $\gamma_{\max}/\Omega_{p_1} > 0$. The probability is the fraction of non-zero $\gamma_{\max}/\Omega_{p_1}$ in units of percent. The count is the number of spectra with $\gamma_{\max}/\Omega_{p_1} > 0$. As there are only 5 spectra beyond the FMW threshold (See Table 6.1), the two corresponding regions are not independently tabulated outside of the *Global* column.

context, these manual fits are over plotted on a 2D PDF of the proton core $(\beta_{\|;p_1}, R_{p_1})$ plane. We choose the p_1 plane (Top panel of Figure 6.1) because not every manual fit is also resolved by the single population algorithms. As such, we cannot align all of the $\gamma_{\max}/\Omega_{p_1}$ with the corresponding $(\beta_{\|;p}, R_p)$ values. However, as we have down selected the two-population fits only for cases with a bi-Maxwellian core, over plotting the manual fits at their $(\beta_{\|;p_1}, R_{p_1})$ does not suffer the same limitations as plotting a beam-core derived quantity on a proton-alpha quantity would. Again, for reference, we have over plotted the instability contours derived by (Verscharen et al., 2016).[4] Table 6.1 summarizes the number of spectra with a given number of ion species in each of the five $(\beta_\|, R)$ regions defined by these instability thresholds.

We have applied the algorithm of Klein et al. (2018) and extracted $\gamma_{\max}/\Omega_{p_1}$ for each of these 557 manual spectra. Figure 6.4 plots contours of the (a) maximum, (b) median non-zero, and (c) probability of non-zero growth rate as a function of $\vec{k}\rho_{p_1}$ over all 557 measurements. The dashed cyan line indicates an angle $\theta_{\boldsymbol{k}} = \arctan(k_\perp/k_\|) = 45^o$ with respect to $\hat{\boldsymbol{b}}$. The top row covers all 557 manually fit spectra. The other three rows cover the data in the MM, between the AIC & MM, and Stable regions defined by Verscharen et al. (2016), as indicated in the top right corner of each panel. As there are only 5 spectra beyond the FMW threshold, the two corresponding regions are not independently tabulated outside of the first or *Global* row. Table 6.2 summarizes these plots.

The maximum of the growth rates identifies the region of k-space with the strongest instability. Table 6.2 indicates that the maximum $\gamma_{\max}/\Omega_{p_1}$ is 0.205 over all of $\vec{k}\rho_{p_1}$ space. The top row of Figure 6.4 also indicates that the strongest instabilities occur at large $k_\|\rho_{p_1}$

---

[4] Plotting the manual fit distribution at their $(\beta_{\|;p_1}, R_{p_1})$ on top of the single population proton $(\beta_{\|;p}, R_p)$ plane produces similar results that did not impact the interpretation of this figure.

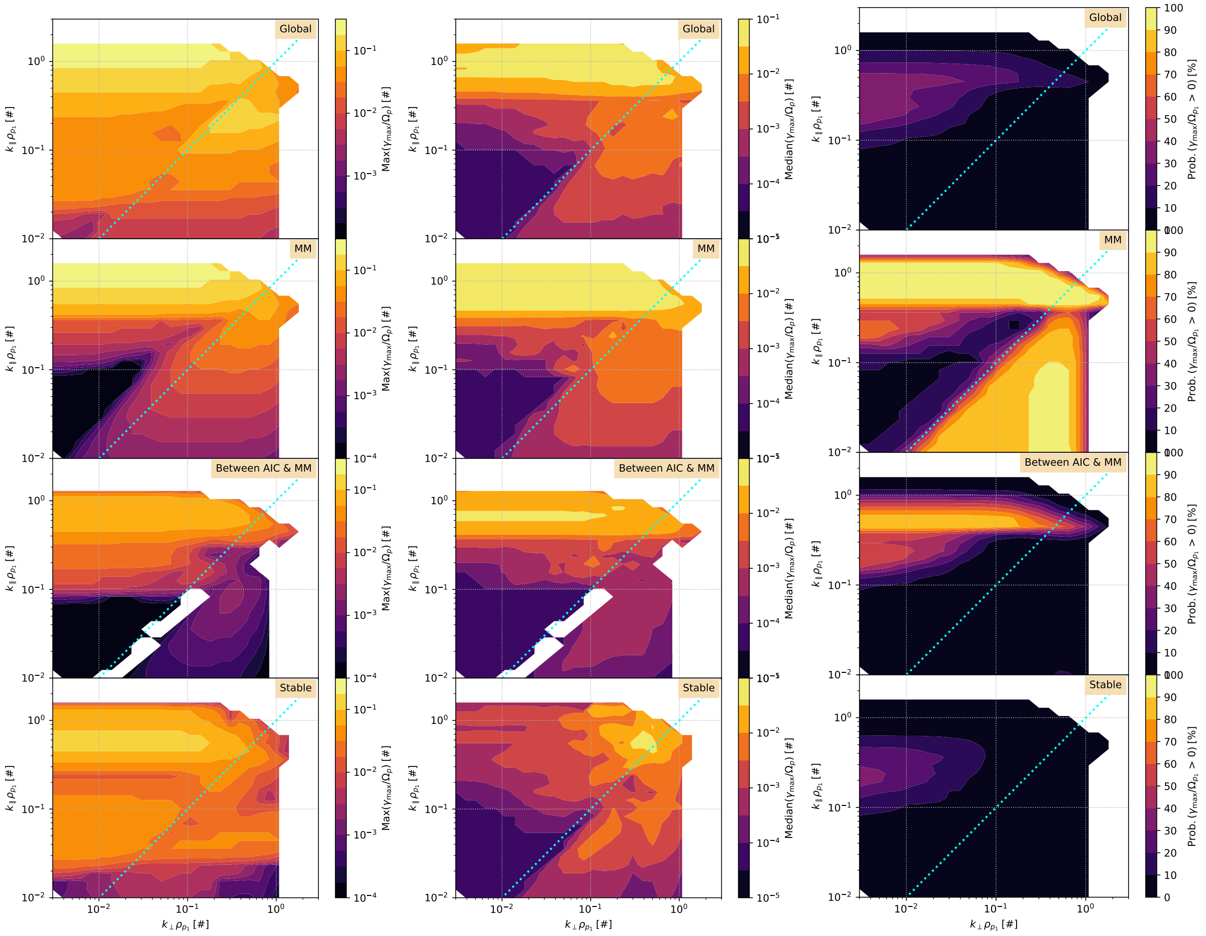

(a)

(b)

(c)

Figure 6.4: (a) Maximum and (b) Median non-zero growth rates $\gamma_{\max}/\Omega_{p_1}(\vec{k}\rho_{p_1})$ along with (c) Probability $\gamma_{\max}/\Omega_{p_1} > 0$. (Top) All 557 manually fit spectra. (Others) Three of the five $(\beta_{\parallel;p_1}, R_{p_1})$ regions defined by Verscharen et al. (2016) for which there are more than 5 spectra. The top right corner of each panel identifies the region to which it belongs.

across $k_\perp \rho_{p_1}$.

The median non-zero growth rate illustrates the typical strength of an instability in k-space. Following Table 6.2, the median of all $\gamma_{\max}/\Omega_{p_1}$s is 0.004, indicating that there is a larger number of smaller $\gamma_{\max}/\Omega_{p_1}$. The general structure of $\gamma_{\max}/\Omega_{p_1}$ in the $\vec{k}\rho_{p_1}$ plane follows the maximum of $\gamma_{\max}/\Omega_{p_1}$. However, the range of median $\gamma_{\max}/\Omega_{p_1}$ covers a range more than a decade larger than the maximum of $\gamma_{\max}/\Omega_{p_1}$ with the smallest $\gamma_{\max}/\Omega_{p_1}$ at small $\vec{k}\rho_{p_1}$ and $\theta_{\boldsymbol{k}} < 45^o$. In addition, parallel modes tend to only become strong ($\gamma_{\max}/\Omega_{p_1} > 10^{-3}$) when $k_\parallel \rho_{p_1} \gtrsim 3 \times 10^{-1}$. In contrast, perpendicular modes[5] tend to be strong ($\gamma_{\max}/\Omega_{p_1} > 10^{-3}$) over all $k_\parallel \rho_{p_1} > 2 \times 10^{-2}$.

The probability of a non-zero growth rate indicates the likelihood that an instability is supported in k-space. Over all of k-space, one will find an instability in 60.682% of spectra. Within k-space, instabilities with the largest likelihood to be measured are parallel propagating ($10^{-1} \lesssim k_\parallel \rho_{p_1} \lesssim 10^0$, $k_\perp \rho_{p_1} \lesssim 5 \times 10^{-2}$) .

The 2nd row across each of Figure 6.4's columns present spectra "unstable" to the single-proton derived mirror mode. Across all $\vec{k}\rho_{p_1}$, Table 6.2 indicates that the maximum growth rate is $\gamma_{\max}/\Omega_{p_1} = 0.205$, the largest observed over the $(\beta_{\parallel;p_1}, R_{p_1})$ plane. The median non-zero growth rate is $\mathrm{Median}(\gamma_{\max}/\Omega_{p_1}) = 0.108$. The probability that a spectrum unstable to the single-proton derived mirror mode carries a growing mode is 3.59%. The probability that a spectra carries an instability if it is beyond this threshold is large at both across perpendicular and at large parallel $\vec{k}\rho_{p_1}$.

Figure 6.4's 3nd row corresponds to the region of $(\beta_{\parallel;p_1}, R_{p_1})$ between the AIC and MM thresholds. Across all $\vec{k}\rho_{p_1}$, the maximum growth rate is $\gamma_{\max}/\Omega_{p_1} = 0.100$. The median growth rate is $\mathrm{Median}(\gamma_{\max}/\Omega_{p_1}) = 0.027$. The probability that a spectrum unstable to the single-proton derived mirror mode carries a growing mode is 17.2%. As expected (Verscharen et al., 2016), the probability that a spectrum carries an instability is largest for large $\vec{k}\rho_{p_1}$ and several orders of magnitude smaller for small $k_\perp \rho_{p_1}$.

Figure 6.4's 4th row corresponds to the region of $(\beta_{\parallel;p_1}, R_{p_1})$ considered stable. Across all $\vec{k}\rho_{p_1}$, Table 6.2 indicates that the maximum growth rate is $\gamma_{\max}/\Omega_{p_1} = 0.115$, larger than spectra both between the AIC and MM thresholds. In contrast, the median growth rate is $\mathrm{Median}(\gamma_{\max}/\Omega_{p_1}) = 0.001$, which is the smallest of all typical $\gamma_{\max}/\Omega_{p_1}$ across the $(\beta_{\parallel;p_1}, R_{p_1})$ plane. The probability that a stable spectrum carries an instability is 78.276%, the largest across the $(\beta_{\parallel;p_1}, R_{p_1})$ plane and larger than the probability that a spectrum in unstable for all manual spectra, irrespective of the instability thresholds derived by (Verscharen et al., 2016).

---

[5] Those for which $\arctan(k_\perp / k_\parallel) > 45^o$.

6.7 Discussion

The normal modes of a plasma depend on the available sources of free energy. The dimensionality of the parameter space associated with the free energy sources scales with the number of ions measured. One method to address this space's high dimensionality is to assume only a few sources of free energy are significant and derive thresholds beyond which the plasma is predicted to be unstable (Daughton and Gary, 1998; Marsch, 2006; Verscharen et al., 2019). The two prototypical parameters used are $(\beta_\parallel, R)$ (Marsch, 2006; Verscharen et al., 2016). Using *Wind*/SWE/FC data collected at L1, Section 6.4 illustrates that the proton beam may be a significant free energy source in the region of the $(\beta_\parallel, R)$ plane for which the typical instability criteria (especially AIC and MM) are violated for the single-population protons. As such, the proton beam associated free energy sources should be treated neither as a fixed quantity nor negligible.

Daughton and Gary (1998); Daughton et al. (1999) propose that instead of the typical $(\beta_\parallel, R)$ free energy sources, the beam density fraction $(n_{p_2}/n_{p_1+p_2})$, a modified plasma beta $(\tilde{\beta}_{\parallel,p_1})$, and the beam-core drift $(\Delta v_{p_2,p_1}/C_A)$ are the relevant free energy sources in regards to proton beams. Of the derived instabilities, Daughton and Gary (1998) provide a least-squares fit to their *Alfvén I* instability for $\gamma/\Omega_{p_1} = 10^{-2}$ (Equation (6.1)). Tu et al. (2004) derive an empirical relationship between $\Delta v_{p_2,p_1}/C_A$ and $\beta_{\parallel,p_1}$ using fast wind *Helios* 2 observations. They show that, while the *Alfvén I* instability is a robust limit on their , the distance between the threshold and their data is sufficient that it is questionable whether the *Alfvén I* instability plays a role in regulating the solar wind.

Because Tu et al. (2004) use *Helios* data that approaches to with $0.3\,\mathrm{AU}$ of the Sun, Section 6.5 studies the distribution of proton beam measurements in the parameter space defined by Daughton and Gary (1998) using near-Sun PSP/SWEAP/SPC data from below $0.3\,\mathrm{AU}$ during E1. Figure 6.2 shows that the asymptotic value of $\Delta v/C_A$ at small $\tilde{\beta}$ is smaller than that derived by Tu et al. (2004). This is expected because $\Delta v/C_A$ roughly scales with v_{sw} and E1 SPC data is from speeds below those used by Tu et al. (2004). Figure 6.2 also studies the *Alfvén I* threshold (Daughton and Gary, 1998) and shows that the distribution of data in the $(\tilde{\beta}_{p_1}, \Delta v/C_A)$ plane may not be limited by this threshold. Even though this may not be surprising[6], we draw the same inference as Tu et al. (2004) that the *Alfvén I* instability does not limit or regulate the solar wind. However, we draw it from the opposite vantage point: where as Tu et al. (2004) infer that the instability is inactive because the data distribution does not run into the threshold, we infer that it is not active because the proton beam distribution in our data surpasses the threshold for $\beta_\parallel > 1$. We also note that,

---

[6] Daughton and Gary (1998) derive their threshold for $\Delta v/C_A \leq 2$.

because of differences in data selection criteria[7] and measurement conditions, we cannot reject the possibility that the discrepancy between our result and the results of Tu et al. (2004) is due to data selection. Nevertheless, should the the high drift tail reported here stand up to further scrutiny and data validation, it would substantiate the conclusion of Tu et al. (2004) that solar wind proton beams are not regulated by the *Alfvén I* instability. As such, we infer that a parameter space defined by a reduced set of free energy sources may be ill-suited to studying solar wind stability when proton beams are measured.

Klein et al. (2017) implement a method developed by Nyquist (1932) for studying stability in a manner that includes all of the available free energy sources resolved by bi-Maxwellian distributions. Klein et al. (2018) utilize this tool to calculate the maximum growth rate ($\gamma_{\max}$) supported in a given solar wind plasma measurement for 309 randomly chosen and manually fit SWE/FC spectra. We have expanded this data set to 557 spectra. Section 6.6 studies $\gamma_{\max}$ in the prototypical reduced free energy $(\beta_{\|}, R)$ plane.

Figure 6.4 examines the maximum, median non-zero, and probability of a non-zero growth rate in wave vector space $\gamma_{\max}/\Omega_{p_1}(\vec{k}\rho_{p_1})$. The 1st row examines all the manually fit spectra and the remaining rows examine the spectra separated into the regions of the $(\beta_{\|;p_1}, R_{p_1})$ plane defined by four instability thresholds (Verscharen et al., 2016) for which here are more than 5 spectra. Table 6.2 statically summarizes these figures.

Figure 6.5 visually compresses the information from Figure 6.4 in the $(\beta_{\|;p_1}, R_{p_1})$ plane by replacing the species present resolved in each spectrum (Figure 6.3) with the spectrum's $\gamma_{\max}/\Omega_{p_1}$. Here, gray *X*s indicate spectra for which $\gamma_{\max}/\Omega_{p_1} = 0$. Colored circle plot $\gamma_{\max}/\Omega_{p_1} > 0$, as indicated on the top color bar. As only 2% of the measured maximum growth rates have $\gamma_{\max}/\Omega_{p_1} > 10^{-1}$ and the maximum is 0.20535, we clip the secondary color bar's $\gamma_{\max}/\Omega_{p_1}$ color scale to 10^{-1} to ease visual interpretation without jeopardizing the figure's integrity or conclusions drawn from it. Qualitatively, a substantial fraction of the data considered to be stable in the reduced parameter space defined by $(\beta_{\|}, R)$ carry an instability and $\gamma_{\max}/\Omega_{p_1}$ increases towards both large R_{p_1} and, to a lesser extent, large β_{p_1}. Quantitatively, we find that 60.682% of the randomly selected manual fits carry a non-zero growth rate $\gamma_{\max}/\Omega_{p_1} > 0$. This is approximately 6.4 percentage points higher than found by Klein et al. (2018). The maximum of these maximum growth rates is $\gamma_{\max}/\Omega_{p_1} = 0.205$ and the median non-zero maximum growth rate is $\gamma_{\max}/\Omega_{p_1} = 0.004$. Together, these two quantities suggest that there is a profusion of small $\gamma_{\max}/\Omega_{p_1}$ instabilities in the solar wind.

The 2nd row of Figure 6.4 selects the subset of data above the MM threshold. Following

---

[7] Tu et al. (2004) systematically exclude spectra with small proton beam densities, small drifts, and intermediate or slow solar wind with speeds $v_{\text{sw}} < 600\ \text{km}\,\text{s}^{-1}$ that are more stringent those used for SPC data (Chapter 5).

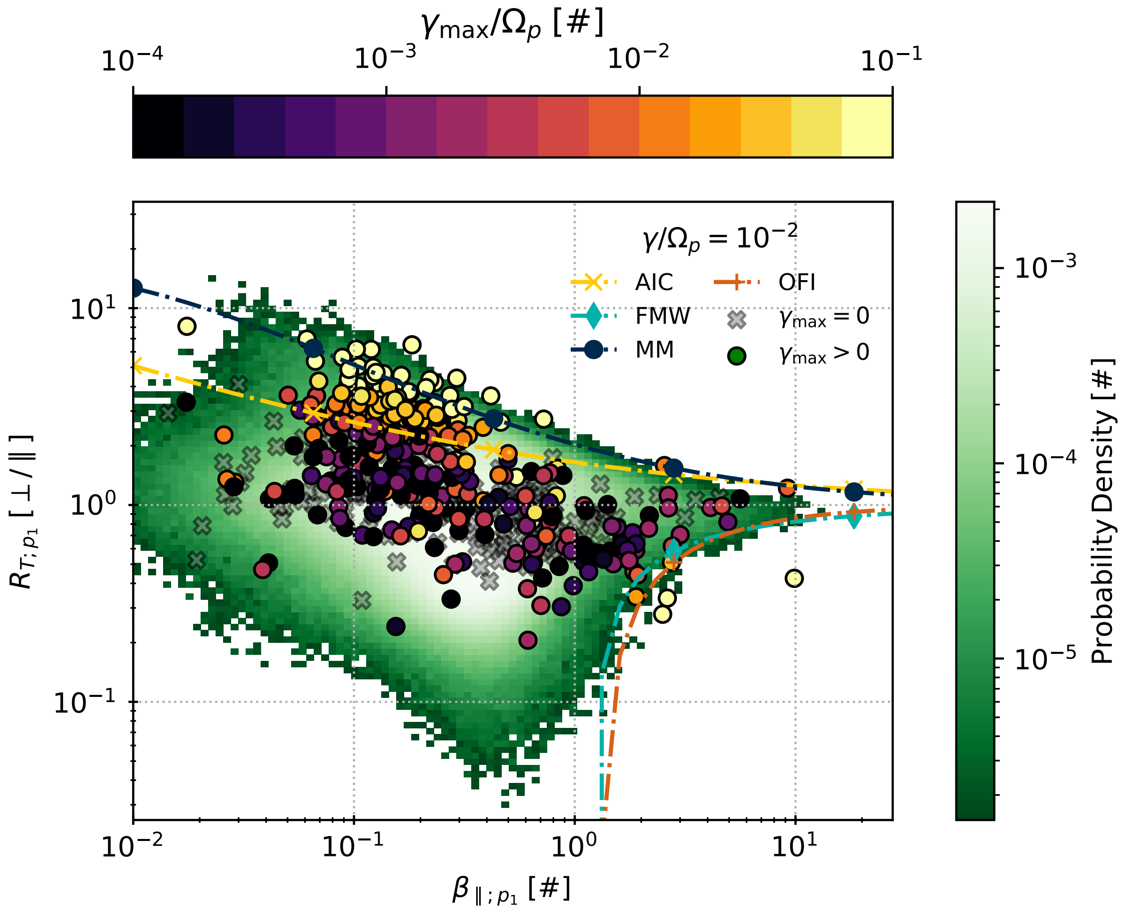

Figure 6.5: The maximum growth rate for each of the 557 manual fits plotted over the automated fits in the canonical $(\beta_\parallel, R)$ plane. Instability contours are identical to Figure 6.3 and the same caveats apply.

the example cases of Klein et al. (2017), the non-zero $\gamma_{\max}/\Omega_{p_1}$ at large $k_\parallel \rho_{p_1}$ and across $k_\perp \rho_{p_1}$ at oblique angles are expected for spectra beyond the MM threshold. This region also carries the largest $\gamma_{\max}/\Omega_{p_1} = 0.205$. The 3rd row selects spectra between the AIC and MM thresholds. Here, the presence of non-zero $\gamma_{\max}/\Omega_{p_1}$ at $k_\perp \rho_{p_1} \sim 1$ is unexpected because the AIC is a parallel mode and this is the region of $(\beta_\parallel, R)$ space where we don't expect the MM–an oblique mode–to arise (Verscharen et al., 2016). The 4th row selects the data stable to the derived thresholds (Verscharen et al., 2016). As illustrated by Klein et al. (2017), spectra typically considered stable are not expected to carry $\gamma_{\max}/\Omega_{p_1} > 0$. However, this region of the $(\beta_{\parallel;p_1}, R_{p_1})$ plane has the largest probability of carrying a non-zero $\gamma_{\max}/\Omega_{p_1}$. In the $\vec{k}\rho_{p_1}$ plane, $\gamma_{\max}/\Omega_{p_1}$ is largest at parallel $\vec{k}\rho_{p_1}$ and the largest median $\gamma_{\max}/\Omega_{p_1}$ occurs at oblique angles and large $\vec{k}\rho_{p_1}$. This likely indicates that the preponderance of growing modes are present at oblique angles ($\theta_{\boldsymbol{k}} \sim 45^o$) in this region of the $(\beta_{\parallel;p_1}, R_{p_1})$ plane.

6.8 Conclusion

The solar wind is a nearly, but not fully collisionless plasma. As such, additional physical mechanisms are necessary to extract free energy from solar wind ions. Growing normal modes or instabilities are one such class of physical processes.

The parameter space characterizing instabilities is large because the number of free energy sources scales with the number of ions present. As such, it is common to assume that most sources are either negligible or take on a fixed value in a manner that results in a reduced parameter space in which stability can be easily identified (Daughton and Gary, 1998; Daughton et al., 1999; Hellinger et al., 2006; Kasper et al., 2003; Marsch and Livi, 1987; Maruca et al., 2011, 2012; Verscharen et al., 2016, 2019). Klein et al. (2018) have shown that the presence of a proton beam makes the validity of this methodology suspect in a random sample of 309 manually validated *Wind*/SWE/FC measurements.

Reprocessing more than 21 years of SWE/FC measurements to resolve a proton beam, we have shown that it is likely the proton beam contributes to the threshold methodology's inability to predict the high anisotropy limit (AIC or MM) on plasma stability (Hellinger et al., 2006; Kasper et al., 2003). Following Tu et al. (2004), we find that these challenges persist even when considering a different reduced set of free energy sources specifically chosen to account for the free energy introduced by a proton beam (Daughton and Gary, 1998; Daughton et al., 1999).

We have expanded the 309 randomly chosen and manually fit spectra from Klein et al. (2018) to 557 spectra. Using their methods, we extracted the maximum growth rate supported by each of these 557 spectra. Our results suggest that there is a profusion of small $\gamma_{\max}/\Omega_{p_1}$ instabilities in the solar wind, in particular at large $\vec{k}\rho_{p_1}$ and angles $\theta_{\boldsymbol{k}} \sim 45^o$ for the $(\beta_{\parallel;p_1}, R_{p_1})$ region naively considered stable. Furthermore, as the results presented in this chapter span 4 more years than the results of Klein et al. (2018) and now cover both solar maximum 24 and a non-trivial fraction of its declining phase, the discrepancies between our results and theirs suggest that variations in solar activity may impact the kinetic properties of the solar wind. A detailed study of this solar cycle variation is forthcoming.

One possible reason that the threshold methodology fails to predict all solar wind stability is that the sources of free energy assumed fixed or negligible in this threshold methodology cannot be treated as such. However, the results presented in this chapter are limited to a small sample of solar wind measurements that amount to less than 0.02% of the proton beam spectra resolved by Chapter 3 over a timespan that is 26% of that covered by Chapter 3's measurements. As such, further work is clearly necessary to quantify the significance of proton beams on solar wind stability. One path forward is simply identifying an alternative set of reduced free energy sources better suited to proton beams than those derived by Daughton and Gary (1998). Leveraging the *Wind*/SWE data in Chapter 3, we can also study $\gamma_{\max}/\Omega_{p_1}$ in a large and statistical fashion to determine key free energy sources in the solar wind and the variation of these quantities with solar cycle. Leveraging PSP/SWEAP/SPC data, we can further study the variation of these quantities with distance from the Sun to better discern how differential flow is regulated during solar wind propagation and disentangle the kinetic processes from the expansion ones. Combining the *Wind* and PSP data, we may be able to identify the key generation mechanism(s) that create solar wind proton beams.

CHAPTER 7

Concluding Remarks

This thesis has shown that the solar wind evolves across multiple timescales including seconds, days, and decades. The solar cycle is the ~ 11.7 year cyclic rotation of the orientation of the Sun's magnetic field's with respect to the solar rotation axis. Coulomb collisions are small angle electrostatic interactions between charged particles that cumulatively convert non-thermal structure in the VDF into thermal energy on a ~ 4 day timescale at $1\,\mathrm{AU}$. Instabilities are, "mechanisms that transfer energy from free-energy sources, such as non-equilibrium particle distributions..." (Verscharen et al., 2019) on timescales near or less than seconds, reshaping how energy is partitioned between solar wind ions, electrons, and magnetic fields.

The solar wind's multi-scale evolution is possible because it is not in LTE. LTE is the state in which a system's local properties do not change within its characteristic scale size. In the case of temperature, LTE implies that the heat flux is zero.

The solar wind has multiple sources of free energy that change within their respective scale sizes and is therefore a non-LTE system. The presence of an ion beyond the proton core – i. e. its abundance – is a prerequisite for a given ion carrying free energy. Chapter 2 studied the variation of solar wind helium abundance (A_He) at L1 as a function of v_sw and time. This chapter expanded on the results of Aellig et al. (2001); Feldman et al. (1978); Kasper et al. (2012, 2007). It showed that A_He's variation with v_sw and SSN has a speed-dependent phase lag, which it inferred is a difference in response of multiple slow wind source regions to the solar cycle.

Given that different the physical processes dominate each source regions, Chapter 2 shows that faster solar wind is shaped by forces in the corona and slower wind is driven by forces in the photosphere. This result caries multiple implications that should be studied.

- The ionization state of solar wind ions correspond to and freeze in at different heights in the corona. These heights are reflected in minor ion charge states. As such, the presence of a charge state phase lag with respect to SSN or absence thereof would provide a sensitive test of how coronal and photospheric forces vary with solar cycle.

- Because the solar wind's background state depends on source region, Chapter 2 also suggests that solar cycle may be important in determining solar wind temperature and speed.

- Kasper et al. (2007) establish that helium vanishes in the solar wind at the vanishing speed $v_0 = 259\ \mathrm{km\,s^{-1}}$. The authors also show that $\mathrm{A_{He}}$ approaches a constant value of 4% to 5% for speeds $v_{\mathrm{sw}} \gtrsim 550\ \mathrm{km\,s^{-1}}$, which may indicate the transition from fast to slow solar wind. Given Chapter 2 shows that the results of Kasper et al. (2007) are robust over two solar cycles, but present some variation when non-low solar activity data is included, the chapter raises two questions.

    1. Does the helium vanishing speed vary with solar cycle?
    2. Does the slow-to-fast wind transition vary with solar cycle?

Answering the these two may provide further insight into solar wind formation and how formation varies with solar source region.

Proton beams provide multiple free energy sources in the solar wind. Chapter 3 established their significance using 21+ years of two population proton measurements collected by the twin *Wind*/SWE/FC instruments at L1. Note that these measurements treat one of these two populations as isotropic and therefore give up information which, in the majority of the cases, corresponds to R_{p_2}. Section 3.4.1 characterizes them in an example CR. Section 3.4.2 studies the variation of p_2-related quantities as a function of v_{sw} and contextualizes them with p_1 measurements. Section 3.4.3 infers that resolving a proton beam sufficiently alters the distribution of measurements in the reduced free energy $(\beta_{\parallel}, R)$ plane that resolving p_2 changes the plausible interpretations regarding the impact of instabilities (especially the MM) in the solar wind. Section 3.5 determines that the *Wind*/SWE/FCs are only resolving 71% of all proton beams.

There are several topics Chapter 3 leaves for future work.

- Section 3.4.1 notes that proton beams track the core in compression regions. Future work should explicitly study proton beams in CIRs to determine, at the least, if and how solar wind compression heats proton beams.

- The size of $\Delta v_{p_2,p_1}$ increases with v_{sw}. As such, proton beams are more easily measured when v_{sw} is larger. Given that a non-trivial fraction of proton beams are unresolved by the *Wind*/SWE/FCs and the beam detectability threshold is likely a strong function of the instrument itself, a study of the missing beam fraction as a function of v_{sw} may serve to constrain how the instrument impacts proton beam measurements.

- Chapter 2 focuses on long term averages in a manner that identifies the impact of solar source region on in situ plasma properties. In other words, this chapter characterizes a component of the solar wind's slowly varying background. Given that Parker (1964a,b, 1965b) tie solar wind speed directly to the solar wind's heat flux, studying $A_{p_2/p_1}(v_{\mathrm{sw}}, t)$ in a similar manner to A_{He} may tie proton beams to source regions; further characterize the background state of the solar wind; and constrain solar wind formation.

- Recent work (D'Amicis and Bruno, 2015; Damicis et al., 2016; D'Amicis et al., 2019; Fu et al., 2018) ties helium abundance to solar wind cross helicity σ_c as an indication of solar source. Given that v_{sw} is tied to solar source and beams are more likely to be detected as v_{sw} increases, σ_c may serve as an additional test for the impacts of solar sources on proton beams.

- ICMEs are a unique, transient state in the solar wind that rapidly cary relatively unprocessed solar plasma out into the heliosphere. Marsch et al. (2009) has conducted the first event study of proton beams in an ICMEs, specifically that observed by *Helios 2* on April 3rd, 1979 at $0.68\,\mathrm{AU}$. A catalogue of 336 ICMEs that have intersected *Wind* is available online[1]. Statistically examining proton beams in ICMEs using this thesis' dataset may provide insight regarding the primordial state of proton beams should they be generated in the corona.

Coulomb collisions are small angle electrostatic interactions between charged particles that can have the integrated effect of washing out non-LTE features in the solar wind, including ion drifts (Alterman et al., 2018; Kasper et al., 2017, 2008; Klein et al., 1985; Livi et al., 1986; Maruca et al., 2013; Neugebauer, 1976). These collisions impact the solar wind's VDF in a manner that depends on its small scale structure, i.e. its gradient (Livi and Marsch, 1986; Pezzi et al., 2016). Livi and Marsch (1987) demonstrate that Coulomb collisions may contribute to the generation of proton beams. Based on the work of Livi et al. (1986), Marsch and Livi (1987) suggest that the transition between non- and collisional domains in *Helios* solar wind proton beams occurs at approximately $N_c \sim 0.3$. Figure 1.2 illustrates that this threshold may occur at $N_{c;p_2,p_1} \sim 0.2$ in *Wind*/SWE/FC data and, for $N_c \gtrsim 0.2$, Coulomb collisions may dissipate $\Delta v_{p_2,p_1}/C_A$ as they do $\Delta v_{\alpha,p_1}/C_A$ (Kasper et al., 2017, 2008; Neugebauer, 1976).

---

[1] `https://wind.nasa.gov/fullcatalogue.php`

Chapter 4 quantifiably compares collisionally young ($N_c < 0.1$) $\Delta v_{p_2,p_1}/C_A$ with $\Delta v_{\alpha,p_1}/C_A$ and determines that, in the asymptotic limit of zero collisions, $\Delta v_{p_2,p_1}/C_A = 105\%$ and $\Delta v_{\alpha,p_1}/C_A = 67\%$. Chapter 4 also demonstrates that distinct physical mechanisms may govern α particle and p_2 Collisional evolution. On the one hand, α particles collisionally relax from some large Δv generated near the Sun. On the other, some yet-to-be-identified mechanism locally sustains $\Delta v_{p_2,p_1} \sim C_A$. This comparison raises at least two questions.

- Do p_2 properties like the temperature ratio with respect to the core T_{p_2}/T_{p_1} demonstrate behavior distinct from that of alpha particles as shown by Kasper et al. (2017, 2008)? Such differences may establish ranges in N_c for studying specific kinetic processes so as to isolate specific physical mechanisms governing the evolution of each population.

- While Figures 1.2, 4.5 and 4.9 demonstrate that this difference breaks down at sufficiently large N_c, the difference also implies the existence of waves in the solar corona that act on and accelerate protons. These waves are an ideal subject of future work and Chapter 4 concludes by suggesting that, if they are stronger in the near-Sun environment, then PSP and SolO will provide measurements that may reconcile the multiple, non-exclusive proton beam generation mechanisms that have been proposed (Livi and Marsch, 1987; Tu et al., 2002; Voitenko and Pierrard, 2015).

PSP E1 measurements provide a unique and favorable opportunity to study the reduced solar wind VDF with SPC when SPC's measurements are likely to be preferentially weighted towards the VDF's component along $\hat{\boldsymbol{b}}$. Chapter 5 compares, in detail, all of E1 measurements along with six approximately steady state intervals during E1 with slow wind, low solar activity measurements collected by *Wind*/SWE at L1. As SPC's sampling time amounts to 12 days and *Wind*/SWE's amounts to 1,418 days over multiple solar cycles, Chapter 5 treats E1 as an event study during a specific set of solar wind conditions and at a specific phase of the solar cycle. Hence the selection of slow wind, low solar activity SWE data.

Chapter 5's primary finding is that near-Sun A_{p_2/p_1} is unexpectedly smaller than typical 1 AU values. Following the work in Chapter 4, Chapter 5 also shows that the Coulomb collisions may not regulate $\Delta v_{p_2,p_1}/C_A$ in the near-Sun environment, but rather some other local mechanism may locally regulate proton beams. The raises one specific and one markedly broad avenue of research.

- Flux conservation as a local p_2 regulation mechanism is a particularly focused research topic. The proton heat flux decreases with increasing distance from the Sun

(Hellinger et al., 2011, 2013). Does radial expansion impact A_{p_2/p_1} enough to account for its evolution from the near-Sun environment to L1?

- Because SPC measurements are taken in the near-Sun environment, these proton beams are likely less impacted by Coulomb collisions than a naive N_c calculation would imply. As such, these observations do not rule out the significance of Coulomb collisions over the solar wind's transit to L1. Therefore, studying the impact of Coulomb collisions and kinetic instabilities with PSP data–especially given its markedly higher time resolution that *Wind*–in the manner of Chapter 6 and through detailed event studies that compare with magnetic field measurements should also be a fruitful avenue of future work.

Instabilities are a different class of local mechanism that may regulate proton beams. The parameter space describing instabilities has a dimensionality that scales with the number of resolved ions. As this space is large, a common method for characterizing instabilities is assuming that a specific or reduced set of parameters governs the instabilities significant on the dynamical timescales of the VDF's evolutiion–or at least those of interest–and deriving a threshold that indicates instability onset or marginal stability (Daughton and Gary, 1998; Daughton et al., 1999; Klein et al., 2017; Marsch and Livi, 1987; Maruca et al., 2012; Verscharen et al., 2016, 2019).

Chapter 6 studies the significance of proton beams in two such reduced free energy planes. The more widely studied of the two planes is defined for the free energy sources $(\beta_\parallel, R)$ (Marsch and Livi, 1987; Maruca et al., 2012; Verscharen et al., 2016, 2019), typically calculated for a single bi-Maxwellian population of solar wind protons. By combining two data sets derived from *Wind*/SWE/FC measurements, Section 6.4 substantiates the inference drawn from Figure 3.5 and demonstrates that the distribution of single population proton measurements may exceed the MM instability's predicted threshold (for $\gamma/\Omega_p = 10^{-2}$) because of the presence of an unresolved p_2 population. Using SPC data from Chapter 5, Section 6.5 confirms results from Tu et al. (2004) that an alternative reduced parameter space specifically accounting for the p_2 free energy sources does not characterize an instability (Daughton and Gary, 1998; Daughton et al., 1999) that regulates $\Delta v_{p_2,p_1}/C_A$ in the near-Sun environment.

Section 6.6 applies an alternative method for studying solar wind instabilities. First developed by (Nyquist, 1932) and implemented for in situ plasma measurements by Klein et al. (2018, 2017), this method calculates the maximum growth rate ($\gamma_{\max}$) of the unstable modes in a subset of *Wind*/SWE/FC measurements. Because the reduction techniques for this subset of data utilize a scientist-in-the-loop to ensure data quality, the resulting plasma measurements contain information about the A_{s/p_1}, $\Delta v_{s,p_1}$, $R_{T,s}$, and T_s/T_{p_1} parameters contained in both the proton beam ($s = p_2$) and alpha particles ($s = \alpha$). This section finds growing modes in the subset of spectra considered stable in the prototypical $(\beta_\parallel, R)$ reduced free energy plane. Unexpectedly, a non-trivial subset of these growing modes are present at angles between the wave vector $\mathbf{k}$ and the magnetic field $\theta_\mathbf{k} \sim 45^o$, especially in the stable region of the prototypical $(\beta_\parallel, R)$ plane. Section 6.7 takes these observations as preliminary evidence that the presence of proton beams leads to a profusion of small $\gamma_\mathrm{max}/\Omega_{p_1}$, but non-negligible instabilities.

Given that N_c decreases towards the $(\beta_\parallel, R)$ instability thresholds (Bale et al., 2009) and the probability of resolving a proton beam increases towards the centroid of Figure 6.1's $(\beta_{\parallel;p_1}, R_{p_1})$ plane, the profusion of small $\gamma_\mathrm{max}/\Omega_{p_1}$ instabilities observed with the 557 manually fit spectra suggests that the gradients upon which the collision frequency (ν_c) depends (Livi and Marsch, 1986) and, consequently, the collision frequency itself are simultaneously modified by these growing modes as the solar wind evolves. Therefore, proton beams are a significant free energy source in the solar wind for which that $(\beta_\parallel, R)$ and similar marginal stability analysis must account for. Otherwise, hidden variables related to the VDF's shape and local structure will likely alter the shape of growth rate contours. Broadly, applying Nyquist's instability criteria to a large scale dataset like that documented in this thesis may further elucidate the significance of proton beams for solar wind stability.

Parker (1964a,b, 1965b) tie the solar wind's heat flux directly to the solar wind's expansion and show that it at least partially governs the solar wind's speed at its source. The Alfvén surface is the boundary at which the solar wind transitions from sub- to super-Alfvénic, i.e. its speed exceeds C_A, and the solar wind is born. As such, the solar wind's heat flux at this critical radius R_c is likely essential to solar wind formation. At the same time, Feldman et al. (1973b) have shown that the proton heat flux surpasses Parker's limit, implying significant proton heating above the Alfvén critical point.

Kasper and Klein (2019) use *Wind*/SWE/FC measurements to demonstrate that the height of the critical boundary below which preferential ion heating occurs (Kasper et al., 2017) follows the solar cycle variation of the Alfvén critical surface. Unlike Chapter 4's simple assumption that the distance utilized to calculate N_c is the distance from the Sun to the observation point, the combined work of Kasper and Klein (2019); Kasper et al. (2017) suggest that the true distance that is appropriate for measuring solar collisionality starts at the Alfvén surface. Because the solar wind's heat flux is tied to this critical boundary, the results of Kasper and Klein (2019); Kasper et al. (2017) may suggest that the solar cycle variation of R_c is reflected in proton beams. Studying the variation of proton beams with solar cycle may establish a slowly varying background against which to reference local proton beam heating. Given a non-zero abundance is a prerequisite for an ion to carry free energy, studying proton beam abundance A_{p_2/p_1} may establish that at least one of p_2's free energy sources varies with the time steady background on a decade timescale. Combining this solar cycle baseline with the variation of the maximum growth rate $\gamma_{\max}$ may disentangle the effects of the physics that occurs at these different timescales. As Parker (1964a,b,c, 1965a,b) implies by the paper titles, answering these questions should unlock our understanding of not just the Sun but astrophysical and stellar environments throughout the Universe and improve numerical models of the Sun, possibly leading to predictive space weather.

APPENDIX A

Tying Proton Beams to the Solar Cycle

Starting with Figure 1.1, this thesis has demonstrated the solar wind's multi scale evolution. Each chapter establishes a different aspect of the solar wind's evolution. Broadly, the path forward involves unravelling the multiple timescales involved. Coulomb collisions (Livi and Marsch, 1986; Pezzi et al., 2016) and instabilities (Klein et al., 2018, 2017; Verscharen et al., 2019), both of which modify and are themselves altered by local gradients in the solar wind's VDF must, be disentangled. Doing so requires a thorough understanding of the background variation of the thermal ions involved. As Coulomb collisionality is a function of distance travelled (Section 1.3 and chapter 4):, that the distance varies with solar activity (Kasper and Klein, 2019; Kasper et al., 2017), and multiple other free energy sources also show a solar cycle dependence (Figure 1.1), the solar cycle variation of proton beams must be quantified.

To lowest order, the solar wind can be described as the sum of a perturbations on a slowly varying background. These perturbations depend on the available sources of free energy and constitute departures from LTE, which themselves are a function of the number of ions present. The solar wind's free energy sources govern the instabilities that it carries (Gary, 1993; Klein et al., 2018, 2017). These free energy sources also impact the VDF's local gradients in a manner that can alter the collision frequency ν_c. Given both the available free energy sources and the distance over which Coulomb collisions can impact the solar wind, this thesis raises a specific question:

Do proton beams vary with solar cycle?

Figure A.1 plots the variation of A_{p_2/p_1} as a function of v_{sw} and time in the same manner as Figure 2.1. The solar wind speed is split into 12 quantiles over the entire *Wind* mission, of which the slowest and fastest are rejected (Section 2.4). The data in each quantile is then averaged into 250 day intervals. As with Section 2.4, the legend indicates the middle v_{sw} in each quantile and its cross correlation coefficient with the 13-month smoothed SSN

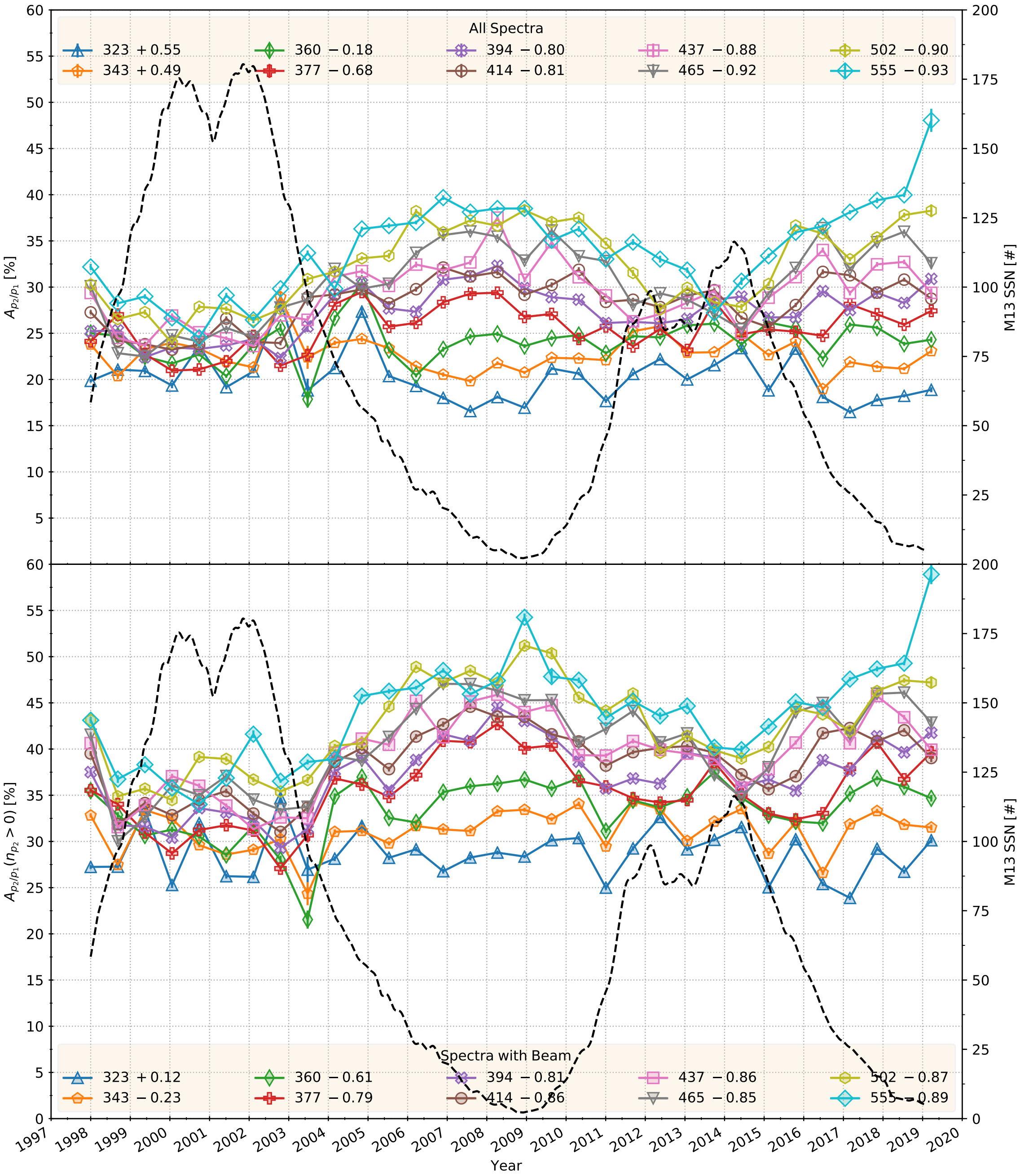

Figure A.1: Two plots of beam abundance (A_{p_2/p_1}) as a function of time and solar wind speed (v_{sw}). Following the style of Alterman and Kasper (2019), v_{sw} is split into 10 quantiles and averages are taken in $250\,\mathrm{day}$ wide bins. The 13-month smoothed sunspot number (SSN) is plotted on the secondary y-axis in dashed black. The legend indicates the middle of the v_{sw} quantile and the Spearman rank cross correlation coefficient between A_{p_2/p_1} and SSN ($\rho(A_{p_2/p_1}, \mathrm{SSN})$) for that quantile. The symbol separating the two is $\rho(A_{p_2/p_1}, \mathrm{SSN})$'s sign. Marker color and symbol identify the v_{sw} quantile. The (top) panel treats missing beams as if $n_{p_2} = 0$ in the A_{p_2/p_1} averages. The (bottom) panel only averages spectra for which $n_{p_2} > 0$. Note that top panel uses unfilled markers to signify that $n_{p_2} = 0$ is used. The bottom panel uses partially transparent and filled markers to signify that $n_{p_2} > 0$.

$\rho(A_{p2/p_1}, \mathrm{SSN})$. The symbol separating the two quantities is $\rho(A_{p2/p_1}, \mathrm{SSN})$'s sign. Due to the operational constraints, this analysis is limited to the years 1998 and following (Section 3.3). As proton beams can not be measured in all solar wind conditions (Section 3.5), the A_{p2/p_1} averages are calculated in two ways. The (top) panel accounts for missing proton beams in the average by filling them with zero. The (bottom) panel only utilizes spectra for which $n_{p_2} > 0$. The marker color and shape indicates the v_{sw} quantiles and is consistent across both panels. In the case of the (top) panel, the markers are unfilled. In the (bottom) panel, they are partially opaque so as to differentiate them from the other panel but not obscure colocated data points.

Several observations are immediately apparent from Figure A.1.

1. A_{p2/p_1} and SSN are anti-correlated with $\rho(A_{p2/p_1}, \mathrm{SSN}) < 0$ for $v_{\mathrm{sw}} \geq 360\ \mathrm{km\,s^{-1}}$ and the anti-correlation's strength increases with v_{sw}. This markedly contrasts with Figure 2.1 and Figure 2.2 Panel (a), which show a positive correlation between A_{He} and SSN.

2. Along with the solar cycle variation within a given v_{sw} quantile, the spread in A_{p2/p_1} across v_{sw} quantiles appears cyclic. It is smallest at solar maximum and largest at solar minimum.

3. Filling missing beams (Section 3.5) as zero systematically shifts A_{p_1/p_1} to smaller values and increases the range of values $\rho(A_{p2/p_1}, \mathrm{SSN})$ takes on.

4. It appears that A_{p_1/p_1} may return to similar values at solar maximum, irrespective of cycle amplitude. This is especially true in the (top) panel, for which missing beams are filled with zero.

Table A.1 summarizes $\rho(A_{p2/p_1}, \mathrm{SSN})$ for both panels and Figure A.2 plots these as $\rho(v_{\mathrm{sw}})$. The marker color and style in Figure A.2 match the appropriate panel in Figure A.1. Figure A.2 emphasizes several observations from Figure A.1. Following the arguments in Section 2.5, the impact of treating missing beams as zero has the most significant impact at larger v_{sw} where the anti-correlation is strongest. For either treatment of the missing beams and $v_{\mathrm{sw}} > 394\ \mathrm{km\,s^{-1}}$, the anti-correlation nearly meets or exceeds the highly significant threshold $\rho < -0.7$ used in Section 2.4. In addition, at the fastest speeds $v_{\mathrm{sw}} \geq 437\ \mathrm{km\,s^{-1}}$, treating the missing beams as if $n_{p_2} = 0$ were measured systematically increases ρ, which implies that at these high speeds the missing beams are driven by the same mechanism as the measured proton beams.

In contrast to the high speed behavior, A_{p_2} shows little significant correlation with SSN for speeds $v_{\mathrm{sw}} \leq 343\ \mathrm{km\,s^{-1}}$ or $360\ \mathrm{km\,s^{-1}}$, depending on the treatment of n_{p_2}. The lack

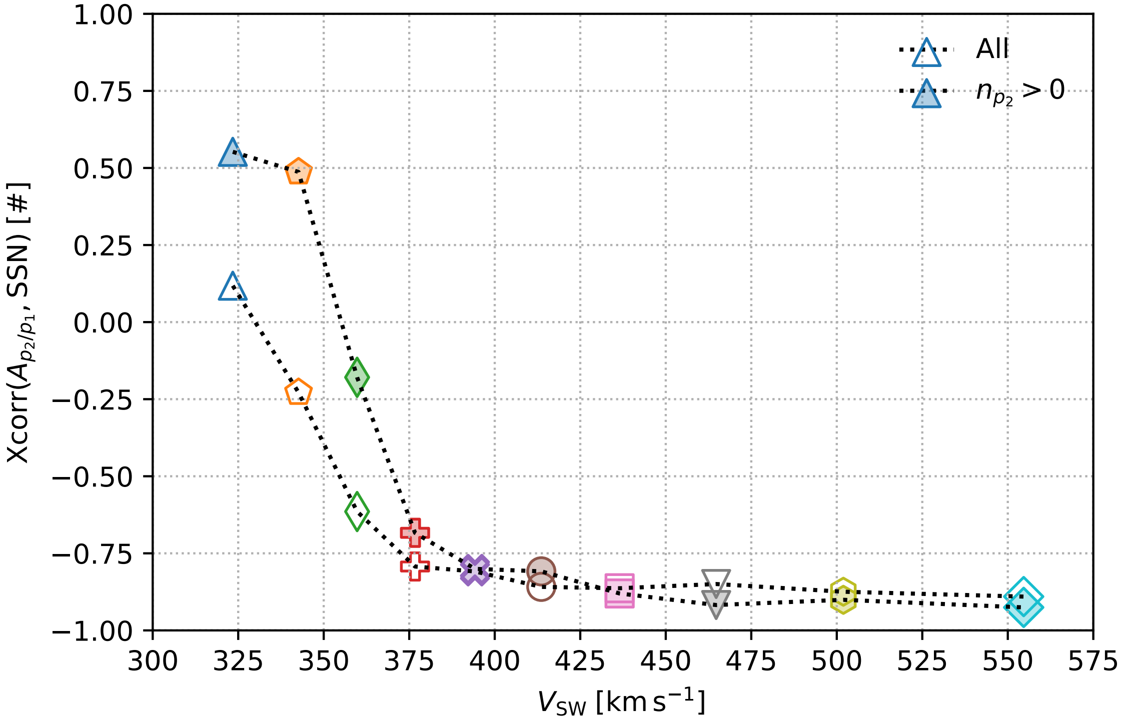

Figure A.2: A summary of the cross correlation coefficient between A_{p_2/p_1} and SSN ($\rho(A_{p_2/p_1}, \mathrm{SSN})$) as a function of its v_{sw} quantile. The marker colors, symbol, and fill follow Figure A.1 to identify the v_{sw} quantile and manner in which the averaging treated missing beams.

v_{sw} [km s^{-1}]	323	343	360	377	394	414	437	465	502	555
All	0.55	0.49	-0.18	-0.68	-0.80	-0.81	-0.88	-0.92	-0.90	-0.93
$n_{p_2} > 0$	0.12	-0.23	-0.61	-0.79	-0.81	-0.86	-0.86	-0.85	-0.87	-0.89

Table A.1: The cross correlation coefficient between A_{p_2/p_1} and SSN for each of ten v_{sw} quantiles plotted in Figure A.1. *All* refers to the top panel in the figure for which $n_{p_2} = 0$ missing beams are included in the averages. The $n_{p_2} > 0$ row refers to the bottom panel that excludes these spectra.

of correlation is not unexpected. Unlike α-particles that the *Wind*/SWE/FC can detect even when $\Delta v_{\alpha,p_1} = 0$, p_2 can only be detected when its differential flow is sufficiently large. The corresponding threshold is determined based on manual inspection of the data and, as such, likely reflects not only the physical mechanisms generating proton beams, but also a convolution of the instrument response and the detection threshold.

In the context of results presented in previous chapters, Figures A.1 and A.2 raise many questions.

- Why does A_{p_2/p_1} negatively correlate with SSN, while A_{He} shows a positive correlation coefficient? Why does $\rho(A_{p_2/p_1}, \text{SSN})$'s strength increase with v_{sw} while A_{He} decreases with it?

- Is the return to a common value at solar maximum, irrespective of cycle amplitude, common to A_{p_2/p_1} and A_{He}? How robust is each abundance's common value across solar cycles?

- As with A_{He}, is there a speed-dependent phase offset between A_{p_2/p_1} and SSN?

- What is the phase offset between A_{He} and A_{p_2/p_1}? How does it vary with v_{sw}?

- Why does the spread in A_{p_2/p_1} across v_{sw} change with time? Is this variation a function of solar cycle?

- How does A_{p_2/p_1}'s variation compare with charge state's solar cycle variation (Kasper et al., 2012) and other conserved, in situ quantities that are direct probes of solar wind sources?

- Can we recover enough information by examining missing beams across v_{sw} quantiles to determine if they are also driven by solar cycle?

- Does applying Nyqvist's instability criteria (Chapter 6) to proton beams reveal a solar cycle dependence?

- Can we utilize the solar cycle variation of proton beams and solar wind heat flux's connection to solar wind acceleration (Parker, 1964a,b, 1965b) reveal about the solar wind's acceleration?

Trying the results from this thesis' chapters Goethe and answering these may help establish the steady state behavior proton beams as this work continues to disentangle the multi scale solar wind.

BIBLIOGRAPHY

Abbo, L., Ofman, L., Antiochos, S. K., Hansteen, V. H., Harra, L., Ko, Y. K., Lapenta, G., Li, B., Riley, P., Strachan, L., von Steiger, R., and Wang, Y. M. (2016). Slow Solar Wind: Observations and Modeling. *Space Science Reviews*, 201(1-4):55–108. 6, 8

Aellig, M. R., Hefti, S., Grünwaldt, H., Bochsler, P., Wurz, P., Ipavich, F. M., and Hovestadt, D. (1999). The Fe/O elemental abundance ratio in the solar wind as observed with SOHO CELIAS CTOF. *Journal of Geophysical Research: Space Physics*, 104(A11):24769–24780. 6

Aellig, M. R., Lazarus, A. J., and Steinberg, J. T. (2001). The solar wind helium abundance: Variation with wind speed and the solar cycle. *Geophysical Research Letters*, 28(14):2767–2770. 23, 38, 69, 135

Alfvén, H. (1942). Existence of Electromagnetic-Hydrodynamic Waves. 78

Alfvén, H. (1957). On the Theory of Comet Tails. *Tellus*, 9(1):92–96. 2

Alterman, B. L. and Kasper, J. C. (2019). Helium Variation across Two Solar Cycles Reveals a Speed-dependent Phase Lag. *The Astrophysical Journal*, 879(1):L6. xii, 23, 38, 94, 118, 143

Alterman, B. L., Kasper, J. C., Stevens, M. L., and Koval, A. (2018). A Comparison of Alpha Particle and Proton Beam Differential Flows in Collisionally Young Solar Wind. *The Astrophysical Journal*, 864(2):112. 6, 12, 15, 21, 26, 37, 38, 45, 54, 66, 89, 90, 93, 94, 110, 114, 119, 137

Araneda, J. A., Marsch, E., and F.-Viñas, A. (2008). Proton core heating and beam formation via parametrically unstable alfvén-cyclotron waves. *Physical Review Letters*, 100(12):1–4. 37

Araneda, J. A., Viñas, A. F., and Astudillo, H. F. (2002). Proton core temperature effects on the relative drift and anisotropy evolution of the ion beam instability in the fast solar wind. *Journal of Geophysical Research: Space Physics*, 107(A12):1–10. 37

Asbridge, J. R., Bame, S. J., and Feldman, W. C. (1974). Abundance differences in solar wind double streams. *Solar Physics*, 37(2):451–467. 37, 38, 90

Asbridge, J. R., Bame, S. J., Feldman, W. C., and Montgomery, M. D. (1976). Helium and hydrogen velocity differences in the solar wind. *Journal of Geophysical Research*, 81(16):2719. 6, 67

Asplund, M., Grevesse, N., Sauval, A. J., and Scott, P. (2009). The Chemical Composition of the Sun. *Annual Review of Astronomy and Astrophysics*, 47(1):481–522. 32

Bachmann, K. T. and White, O. R. (1994). Observations of hysteresis in solar cycle variations among seven solar activity indicators. *Solar Physics*, 150(1-2):347–357. 25, 29, 32

Bale, S. and Fields (2019). The Magnetic Structure and Electrodynamics of the Emerging Solar Wind. *submitted.* 95

Bale, S. D., Goetz, K., Harvey, P. R., Turin, P., Bonnell, J. W., Dudok de Wit, T., Ergun, R. E., MacDowall, R. J., Pulupa, M., Andre, M., Bolton, M., Bougeret, J. L., Bowen, T. A., Burgess, D., Cattell, C. A., Chandran, B. D., Chaston, C. C., Chen, C. H., Choi, M. K., Connerney, J. E., Cranmer, S. R., Diaz-Aguado, M., Donakowski, W., Drake, J. F., Farrell, W. M., Fergeau, P., Fermin, J., Fischer, J., Fox, N. J., Glaser, D., Goldstein, M., Gordon, D., Hanson, E., Harris, S. E., Hayes, L. M., Hinze, J. J., Hollweg, J. V., Horbury, T. S., Howard, R. A., Hoxie, V., Jannet, G., Karlsson, M., Kasper, J. C., Kellogg, P. J., Kien, M., Klimchuk, J. A., Krasnoselskikh, V. V., Krucker, S., Lynch, J. J., Maksimovic, M., Malaspina, D. M., Marker, S., Martin, P., Martinez-Oliveros, J., McCauley, J., McComas, D. J., McDonald, T., Meyer-Vernet, N., Moncuquet, M., Monson, S. J., Mozer, F. S., Murphy, S. D., Odom, J., Oliverson, R., Olson, J., Parker, E. N., Pankow, D., Phan, T., Quataert, E., Quinn, T., Ruplin, S. W., Salem, C., Seitz, D., Sheppard, D. A., Siy, A., Stevens, K., Summers, D., Szabo, A., Timofeeva, M., Vaivads, A., Velli, M., Yehle, A., Werthimer, D., and Wygant, J. R. (2016). The FIELDS Instrument Suite for Solar Probe Plus: Measuring the Coronal Plasma and Magnetic Field, Plasma Waves and Turbulence, and Radio Signatures of Solar Transients. *Space Science Reviews*, 204(1-4):49–82. 94

Bale, S. D., Kasper, J. C., Howes, G. G., Quataert, E., Salem, C. S., and Sundkvist, D. (2009). Magnetic Fluctuation Power Near Proton Temperature Anisotropy Instability Thresholds in the Solar Wind. *Physical Review Letters*, 103(21):1–4. 19, 57, 140

Bame, S. J., Asbridge, J. R., Feldman, W. C., and Gosling, J. T. (1977). Evidence for a structure-free state at high solar wind speeds. *Journal of Geophysical Research*, 82(10):1487–1492. 6, 35

Barnes, A. and Suffolk, G. C. J. (1971). Relativistic kinetic theory of the large-amplitude transverse Alfvén wave. *Journal of Plasma Physics*, 5(03):315. 80

Belcher, J. W. and Davis, L. (1971). Large-amplitude Alfven waves in the interplanetary medium. II. *Journal of Geophysical Research*, 76(16). 3

Belcher, J. W., Davis, L., and Smith, E. J. (1969). Large-amplitude Alfvén waves in the interplanetary medium: Mariner 5. *Journal of Geophysical Research*, 74(16):2302–2308. 3

Berger, L., Wimmer-Schweingruber, R. F., and Gloeckler, G. (2011). Systematic Measurements of Ion-Proton Differential Streaming in the Solar Wind. *Physical Review Letters*, 106(15):151103. 37, 67

Bethe, H. A. (1939). Energy Procution in Stars. *Physical Review*, 55(1):434–456. 1

Bethe, H. A. and Critchfield, C. L. (1938). The formation of deuterons by proton combination. *Physical Review*, 54(4):248–254. 1

Biermann, L. (1957). Solar corpuscular radiation and the interplanetary gas. *The Observatory*, 77:109–110. 2

Borovsky, J. (2016). The plasma structure of coronal hole solar wind: Origins and evolution. *Journal of Geophysical Research A: Space Physics*, 121(6):5055–5087. 96

Borovsky, J. and Denton, M. H. (2010). Solar wind turbulence and shear: A superposed-epoch analysis of corotating interaction regions at 1 AU. *Journal of Geophysical Research: Space Physics*, 115(10):1–30. 96

Borrini, G., Gosling, J. T., Bame, S. J., Feldman, W. C., and Wilcox, J. M. (1981). Solar wind helium and hydrogen structure near the heliospheric current sheet: A signal of coronal streamers at 1 AU. *Journal of Geophysical Research: Space Physics*, 86(A6):4565–4573. 33

Bridge, H. S., Belcher, J. W., Butler, R. J., Lazarus, A. J., Mavretic, A. M., Sullivan, J. D., Siscoe, G. L., and Vasyliunas, V. M. (1977). The plasma experiment on the 1977 Voyager Mission. *Space Science Reviews*, 21(3):259–287. 118

Bridge, H. S., Dilworth, C., Rossi, B., Scherb, F., and Lyon, E. F. (1960). An instrument for the investigation of interplanetary plasma. *Journal of Geophysical Research*, 65(10):3053–3055. 118

Bruno, R. and Carbone, V. (2013). The solar wind as a turbulence laboratory. *Living Reviews in Solar Physics*, 10(1):1–208. 3

Buhler, F., Eberhardt, P., Geiss, J., Meister, J., and Signer, P. (1969). Apollo 11 Solar Wind Composition Experiment: First Results. *Science*, 166(3912):1502–1503. 3

Burton, M. E., Neugebauer, M., Crooker, N. U., von Steiger, R., and Smith, E. J. (1999). Identification of trailing edge solar wind stream interfaces: A comparison of Ulysses plasma and composition measurements. *Journal of Geophysical Research: Space Physics*, 104(A5):9925–9932. 44, 96

Callen, J. D. (2006). Coulomb Collisions. In *Fundamentals of Plasma Physics*, pages 1–57. self. xiii, 10, 11

Cane, H. V. and Richardson, I. G. (2003). Interplanetary coronal mass ejections in the near-Earth solar wind during 1996-2002. *Journal of Geophysical Research: Space Physics*, 108(A4). 44

Carrington, R. C. (1859). Description of a Singular Appearance seen in the Sun on September 1, 1859. *Monthly Notices of the Royal Astronomical Society*, 20(1):13–15. 1

Case, A. C. and SWEAP (2019). The Solar Probe Cup on Parker Solar Probe. *in prep.* 92

Case, A. W., Kasper, J. C., Daigneau, P. S., Caldwell, D., Freeman, M., Gauron, T., Maruca, B. A., Bookbinder, J., Korreck, K. E., Cirtain, J. W., Effinger, M. E., Halekas, J. S., Larson, D. E., Lazarus, A. J., Stevens, M. L., Taylor, E. R., Wright, K. H., and Wright Jr., K. H. (2013). Designing a sun-pointing Faraday cup for solar probe plus. *AIP Conference Proceedings*, 1539(1):458–461. 90, 93

Chapman, S. (1957). Notes on the Solar Corona and the Terrestrial Ionosphere. *Smithsonian Contributions to Astrophysics*, 2:1. 2

Chapman, S. and Ferraro, V. C. A. (1931a). A new theory of magnetic storms. *Journal of Geophysical Research*, 36(2):77. 1

Chapman, S. and Ferraro, V. C. A. (1931b). A new theory of magnetic storms. *Journal of Geophysical Research*, 36(3):171. 1

Chapman, S. and Ferraro, V. C. A. (1932a). A new theory of magnetic storms. *Journal of Geophysical Research*, 37(4):421. 1

Chapman, S. and Ferraro, V. C. A. (1932b). A new theory of magnetic storms. *Journal of Geophysical Research*, 37(2):147. 1

Chapman, S. and Ferraro, V. C. A. (1933). A new theory of magnetic storms. *Journal of Geophysical Research*, 38(2):79. 1

Chapman, S. and Ferraro, V. C. A. (1940). The theory of the first phase of a geomagnetic storm. *Journal of Geophysical Research*, 45(3):245. 1

Charbonneau, P. (2005). Dynamo Models of the Solar Cycle. *Living Reviews in Solar Physics*, 2(1):1–83. 3

Chen, C. H. K., Bale, S. D., Salem, C. S., and Maruca, B. A. (2013). Residual Energy Spectrum of Solar Wind Turbulence. *The Astrophysical Journal*, 770(2):125. 88

Chen, C. H. K., Matteini, L., Schekochihin, A. A., Stevens, M. L., Salem, C. S., Maruca, B. A., Kunz, M. W., and Bale, S. D. (2016). Multi-Species Measurements of the Firehose and Mirror Instability Thresholds in the Solar Wind. *The Astrophysical Journal*, 825(2):L26. 37, 39, 50, 69, 90

Cheung, M. C. and Isobe, H. (2014). Flux emergence (Theory). *Living Reviews in Solar Physics*, 11(1). 3

Chew, G. F., Goldberger, M. L., and Low, F. E. (1956). The Boltzmann equation and the one-fluid hydromagnetic equations in the absence of particle collisions. *Proceedings of the Royals Society of London. Series A, Mathematical and Physical Sceinces*, 236(1204):112–118. 19, 115

Chhiber, R., Usmanov, A. V., Matthaeus, W. H., and Goldstein, M. L. (2016). Solar Wind Collisional Age From a Global Magnetohydrodynamics Simulation. *The Astrophysical Journal*, 821(1):0. 14, 76, 87, 110

Clark, D. H. and Stephenson, F. R. (1978). An Interpretation of the Pre-Telescopic Sunspot Records from the Orient. *Quarterly Journal of the Royal Astronomical Society*, 19:387. 1

Cranmer, S. R. (2009). Coronal Holes. *Living Reviews in Solar Physics*, 6. 5, 6

D'Amicis, R. and Bruno, R. (2015). on the Origin of Highly Alfvénic Slow Solar Wind. *Astrophysical Journal*, 805(1):1–9. 6, 7, 137

Damicis, R., Bruno, R., and Matteini, L. (2016). Characterizing the Alfvénic slow wind: A case study. *AIP Conference Proceedings*, 1720(2016). 6, 7, 137

D'Amicis, R., Bruno, R., Pallocchia, G., Bavassano, B., Telloni, D., Carbone, V., and Balogh, A. (2010). RADIAL EVOLUTION OF SOLAR WIND TURBULENCE DURING EARTH AND ULYSSES ALIGNMENT OF 2007 AUGUST. *The Astrophysical Journal*, 717(1):474–480. 3

D'Amicis, R., Matteini, L., and Bruno, R. (2019). On the slow solar wind with high Alfvénicity: From composition and microphysics to spectral properties. *Monthly Notices of the Royal Astronomical Society*, 483(4):4665–4677. 6, 7, 137

Daughton, W. and Gary, S. P. (1998). Electromagnetic proton/proton instabilities in the solar wind. *Journal of Geophysical Research*, 103(9):20613. xi, 19, 21, 37, 54, 56, 57, 68, 101, 117, 118, 122, 123, 124, 125, 130, 133, 134, 139

Daughton, W., Gary, S. P., and Winske, D. (1999). Electromagnetic proton/proton instabilities in the solar wind: Simulations. *Journal of Geophysical Research*, 104(A3):4657–4667. 19, 21, 37, 54, 57, 68, 117, 118, 122, 130, 133, 139

Daughton, W., Roytershteyn, V., Albright, B. J., Karimabadi, H., Yin, L., and Bowers, K. J. (2009). Influence of Coulomb collisions on the structure of reconnection layers. *Physics of Plasmas*, 16(7). 17

De Jong, T. and Van Soldt, W. H. (1989). The earliest known solar eclipse record redated. *Nature*, 338(6212):238–240. 1

Eselevich, M. V. and Eselevich, V. G. (2006). Some features of the streamer belt in the solar corona and at the Earth's orbit. *Astronomy Reports*, 50(9):748–761. 6, 32

Fan, Y. (2004). Magnetic fields in the solar convection zone. *Living Reviews in Solar Physics*, 1(1):1–74. 7

Feldman, U., Landi, E., and Schwadron, N. A. (2005). On the sources of fast and slow solar wind. *Journal of Geophysical Research: Space Physics*, 110(A7):1–12. 33

Feldman, W. C., Asbridge, J. R., and Bame, S. J. (1974a). The solar wind He 2+ to H + temperature ratio. *Journal of Geophysical Research*, 79(16):2319–2323. 67

Feldman, W. C., Asbridge, J. R., Bame, S. J., and Gosling, J. T. (1978). Long-Term Variations of Selected Solar Wind Properties. *Journal of Geophysical Research*, 83(8):2177–2189. 25, 27, 33, 135

Feldman, W. C., Asbridge, J. R., Bame, S. J., and Montgomery, M. D. (1973a). Double ion streams in the solar wind. *Journal of Geophysical Research*, 78(13):2017–2027. 37, 38, 90

Feldman, W. C., Asbridge, J. R., Bame, S. J., and Montgomery, M. D. (1973b). On the origin of solar wind proton thermal anisotropy. *Journal of Geophysical Research*, 78(28):6451–6468. 37, 38, 90, 140

Feldman, W. C., Asbridge, J. R., Bame, S. J., and Montgomery, M. D. (1974b). Interpenetrating solar wind streams. *Reviews of Geophysics*, 12(4):715. 37, 90

Feynman, J. (1982). Geomagnetic and solar wind cycles, 1900–1975. *Journal of Geophysical Research*, 87(A8):6153. 8

Fisk, L. A. (1996). Motion of the footpoints of heliospheric magnetic field lines at the Sun: Implications for recurrent energetic particle events at high heliographic latitudes. *Journal of Geophysical Research: Space Physics*, 101(A7):15547–15553. 6

Fisk, L. A. (2003). Acceleration of the solar wind as a result of the reconnection of open magnetic flux with coronal loops. *Journal of Geophysical Research*, 108(A4):1157. 33

Fisk, L. A., Zurbuchen, T. H., and Schwadron, N. A. (1999). On the Coronal Magnetic Field: Consequences of Large-Scale Motions. *The Astrophysical Journal*, 521(2):868–877. 6

Fontenla, J. M., Avrett, E. H., and Loeser, R. (2002). Energy Balance in the Solar Transition Region. IV. Hydrogen and Helium Mass Flows with Diffusion. *The Astrophysical Journal*, 572(1):636–662. 32

Fontenla, J. M., Reichmann, E. J., and Tandberg-Hanssen, E. (1988). The Lyman-alpha line in various solar features. I - Observations. *The Astrophysical Journal*, 329(2):464. 32

Forbush, S. E. (1937). On the Effects in Cosmic-Ray Intensity Observed During the Recent Magnetic Storm. *Physical Review*, 51(12):1108–1109. 1, 2

Fox, N. J., Velli, M. C., Bale, S. D., Decker, R., Driesman, A., Howard, R. A., Kasper, J. C., Kinnison, J., Kusterer, M., Lario, D., Lockwood, M. K., McComas, D. J., Raouafi, N. E., and Szabo, A. (2015). The Solar Probe Plus Mission: Humanity's First Visit to Our Star. *Space Science Reviews*, 204(1-4):7–48. 3, 15, 35, 87, 90, 118, 120

Fu, H., Madjarska, M. S., Li, B., Xia, L., and Huang, Z. (2018). Helium abundance and speed difference between helium ions and protons in the solar wind from coronal holes, active regions, and quiet Sun. *Monthly Notices of the Royal Astronomical Society*, 478(2):1884–1892. 6, 137

Fundamenski, W. and Garcia, O. E. (2007). Comparison of Coulomb Collision Rates in the Plasma Physics and Magnetically Confined Fusion Literature. Technical Report 07, EFDA–JET–R(07)01. 10, 11, 76

Gary, S. P. (1993). *Theory of space plasma microinstabilities*. Cambridge University Press, Cambridge. 4, 17, 18, 117, 142

Gary, S. P. (2015). Short-wavelength plasma turbulence and temperature anisotropy instabilities: Recent computational progress. *Philosophical Transactions of the Royal Society A: Mathematical, Physical and Engineering Sciences*, 373(2041). 17, 18, 19

Gary, S. P., Jian, L. K., Broiles, T. W., Stevens, M. L., Podesta, J. J., and Kasper, J. C. (2016). Ion-driven instabilities in the solar wind: Wind observations of 19 March 2005. *Journal of Geophysical Research: Space Physics*, 121(1):30–41. 69

Goelzer, M. L., Smith, C. W., Schwadron, N. A., and McCracken, K. G. (2013). An analysis of heliospheric magnetic field flux based on sunspot number from 1749 to today and prediction for the coming solar minimum. *Journal of Geophysical Research: Space Physics*, 118(12):7525–7531. 25

Goldstein, B. E., Neugebauer, M., and Smith, E. J. (1995). Alfven waves, alpha particles, and pickup ions in the solar wind. *Geophysical Research Letters*, 105(A3):5113. 3, 67

Goldstein, B. E., Neugebauer, M., Zhang, L. D., and Gary, S. P. (2000). Observed constraint on proton-proton relative velocities in the solar wind. *Geophysical Research Letters*, 27(1):53–56. 37, 38, 56, 68, 90

Goldstein, B. E., Neugebauer, M., and Zhou, X. (2010). Ulysses Observations of the Properties of Multiple Ion Beams in the Solar Wind. *Twelfth International Solar Wind Conference*, 1216. 37, 38, 56, 90

Gombosi, T. I. (1994). *Gaskinetic Theory*. Cambridge University Press, Cambridge. 16

Gombosi, T. I. (2004). *Physics of the Space Environment*. Cambridge University Press. 15, 17

Gombosi, T. I., van der Holst, B., Manchester, W. B., and Sokolov, I. V. (2018). Extended MHD modeling of the steady solar corona and the solar wind. *Living Reviews in Solar Physics*, 15(1):1–57. 17

Hale, G. E. (1908). On the Probable Existence of a Magnetic Field in Sun-Spots. *The Astrophysical Journal*, 28(26):315. 1

Hale, G. E., Ellerman, F., Nicholson, S. B., and Joy, A. H. (1919). The Magnetic Polarity of Sun-Spots. *The Astrophysical Journal*, 49:153. 5

Hathaway, D. H. (2015). The solar cycle. *Living Reviews in Solar Physics*, 12(1). 1, 4, 5, 7

Hellinger, P., Matteini, L., Stverak, S., Trávníček, P. M., and Marsch, E. (2011). Heating and cooling of protons in the fast solar wind between 0.3 and 1 AU: Helios revisited. *Journal of Geophysical Research*, 116(A9):A09105. 90, 139

Hellinger, P. and Trávníček, P. M. (2011). Proton core-beam system in the expanding solar wind: Hybrid simulations. *Journal of Geophysical Research: Space Physics*, 116(11):1–13. 37

Hellinger, P., Trávníček, P. M., Kasper, J. C., and Lazarus, A. J. (2006). Solar wind proton temperature anisotropy: Linear theory and WIND/SWE observations. *Geophysical Research Letters*, 33(9):L09101. 18, 19, 38, 39, 50, 57, 117, 120, 133

Hellinger, P., Trávníček, P. M., Stverak, S., Matteini, L., and Velli, M. (2013). Proton thermal energetics in the solar wind: Helios reloaded. *Journal of Geophysical Research: Space Physics*, 118(4). 15, 90, 114, 139

Hernández, R. and Marsch, E. (1985). Collisional time scales for temperature and velocity exchange between drifting Maxwellians. *Journal of Geophysical Research*, 90(A11):11062. 12, 76

Hewett, D. and Nielson, C. (1978). A multidimensional quasineutral plasma simulation model. *Journal of Computational Physics*, 29(2):219–236. 17

Hirshberg, J. (1973). The solar wind cycle, the sunspot cycle, and the corona. *Astrophysics and Space Science*, 20(2):473–481. 5, 8, 33

Hodgson, R. (1859). On the Visibility of Donati's Comet. *Monthly Notices of the Royal Astronomical Society*, 19(3):86–86. 1

Horbury, T. S., FIELDS, and SWEAP (2019). Spikes in the near-Sun solar wind. *in prep.* 95

Howes, G. G. (2015). A dynamical model of plasma turbulence in the solar wind. *Philosophical Transactions of the Royal Society A: Mathematical, Physical and Engineering Sciences*, 373(2041). 18

Howes, G. G., Cowley, S. C., Dorland, W., Hammett, G. W., Quataert, E., and Schekochihin, A. A. (2006). Astrophysical Gyrokinetics: Basic Equations and Linear Theory. *The Astrophysical Journal*, 651(1):590–614. 17

Juno, J., Hakim, A., TenBarge, J., Shi, E., and Dorland, W. (2018). Discontinuous Galerkin algorithms for fully kinetic plasmas. *Journal of Computational Physics*, 353:110–147. 17

Kaghashvili, E. K., Vasquez, B. J., Zank, G. P., and Hollweg, J. V. (2004). Deceleration of relative streaming between proton components among nonlinear low-frequency Alfvén waves. *Journal of Geophysical Research: Space Physics*, 109:1–11. 37

Kasper, J. C., Abiad, R., Austin, G., Balat-Pichelin, M., Bale, S. D., Belcher, J. W., Berg, P., Bergner, H., Berthomier, M., Bookbinder, J., Brodu, E., Caldwell, D., Case, A. W., Chandran, B. D. G., Cheimets, P., Cirtain, J. W., Cranmer, S. R., Curtis, D. W., Daigneau, P., Dalton, G., Dasgupta, B., DeTomaso, D., Diaz-Aguado, M., Djordjevic, B., Donaskowski, B., Effinger, M., Florinski, V., Fox, N. J., Freeman, M., Gallagher, D., Gary, S. P., Gauron, T., Gates, R., Goldstein, M. L., Golub, L., Gordon, D. A., Gurnee, R., Guth, G., Halekas, J., Hatch, K., Heerikuisen, J., Ho, G., Hu, Q., Johnson, G., Jordan, S. P., Korreck, K. E., Larson, D., Lazarus, A. J., Li, G., Livi, R., Ludlam, M., Maksimovic, M., McFadden, J. P., Marchant, W., Maruca, B. A., McComas, D. J., Messina, L., Mercer, T., Park, S., Peddie, A. M., Pogorelov, N., Reinhart, M. J., Richardson, J. D., Robinson, M., Rosen, I., Skoug, R. M., Slagle, A., Steinberg, J. T., Stevens, M. L., Szabo, A., Taylor, E. R., Tiu, C., Turin, P., Velli, M., Webb, G., Whittlesey, P., Wright, K., Wu, S. T., and Zank, G. (2016). Solar Wind Electrons Alphas and Protons (SWEAP) Investigation: Design of the Solar Wind and Coronal Plasma Instrument Suite for Solar Probe Plus. *Space Science Reviews*, 204(1-4):131–186. 35, 87, 90, 92, 118

Kasper, J. C. and Klein, K. G. (2019). Strong Preferential Ion Heating is Limited to within the Solar Alfvén Surface. *The Astrophysical Journal*, 877(2):L35. 2, 114, 140, 142

Kasper, J. C., Klein, K. G., Weber, T., Maksimovic, M., Zaslavsky, A., Bale, S. D., Maruca, B. A., Stevens, M. L., and Case, A. W. (2017). A ZONE OF PREFERENTIAL ION HEATING EXTENDS TENS OF SOLAR RADII FROM SUN (Submitted). *ApJ*, 849(2):126. 2, 12, 14, 26, 37, 67, 72, 76, 85, 87, 88, 89, 90, 110, 114, 137, 138, 140, 142

Kasper, J. C., Lazarus, A. J., and Gary, S. P. (2002). Wind/SWE observations of firehose constraint on solar wind proton temperature anisotropy. *Geophysical Research Letters*, 29(17):1839. 18, 19, 38, 39, 50, 57, 69, 72, 89

Kasper, J. C., Lazarus, A. J., and Gary, S. P. (2008). Hot Solar-Wind Helium: Direct Evidence for Local Heating by Alfvén-Cyclotron Dissipation. *Physical Review Letters*, 101(26):261103. 6, 12, 26, 37, 38, 67, 69, 72, 76, 88, 89, 114, 119, 137, 138

Kasper, J. C., Lazarus, A. J., Gary, S. P., and Szabo, A. (2003). Solar Wind Temperature Anisotropies. *AIP Conference Proceedings*, 679(September 2003):538–541. 117, 120, 133

Kasper, J. C., Lazarus, A. J., Steinberg, J. T., Ogilvie, K. W., and Szabo, A. (2006). Physics-based tests to identify the accuracy of solar wind ion measurements: A case study with the Wind Faraday Cups. *Journal of Geophysical Research*, 111(A3):A03105. xi, 14, 19, 26, 38, 39, 40, 51, 57, 59, 67, 69, 92, 93, 94, 118, 119, 120, 121, 122

Kasper, J. C., Stevens, M. L., Korreck, K. E., Maruca, B. A., Kiefer, K. K., Schwadron, N. a., and Lepri, S. T. (2012). EVOLUTION OF THE RELATIONSHIPS BETWEEN

HELIUM ABUNDANCE, MINOR ION CHARGE STATE, AND SOLAR WIND SPEED OVER THE SOLAR CYCLE. *The Astrophysical Journal*, 745(2):162. vi, 23, 24, 25, 26, 27, 33, 38, 69, 135, 146

Kasper, J. C., Stevens, M. L., Lazarus, A. J., Steinberg, J. T., and Ogilvie, K. W. (2007). Solar Wind Helium Abundance as a Function of Speed and Heliographic Latitude: Variation through a Solar Cycle. *The Astrophysical Journal*, 660(1):901–910. vi, vii, 23, 24, 25, 26, 27, 30, 31, 32, 33, 34, 38, 69, 113, 135, 136

Kasper, J. C. and SWEAP (2019). Young Solar Wind in the Grip of the Sun's Corona. *submitted.* 90, 95, 97, 99, 111, 118, 120

Kilpua, E. K., Madjarska, M. S., Karna, N., Wiegelmann, T., Farrugia, C., Yu, W., and Andreeova, K. (2016). Sources of the Slow Solar Wind During the Solar Cycle 23/24 Minimum. *Solar Physics*, 291(8):2441–2456. 96

Klein, K. G. (2013). *The kinetic plasma physics of solar wind turbulence*. PhD thesis, University of Iowa. 17, 19

Klein, K. G., Alterman, B. L., Stevens, M. L., Vech, D., and Kasper, J. C. (2018). Majority of Solar Wind Intervals Support Ion-Driven Instabilities. *Physical Review Letters*, 120(20):205102. 36, 39, 50, 52, 54, 57, 58, 117, 118, 120, 125, 127, 131, 133, 134, 139, 142

Klein, K. G. and Howes, G. G. (2015). Predicted impacts of proton temperature anisotropy on solar wind turbulence. *Physics of Plasmas*, 22(3). 18

Klein, K. G., Kasper, J. C., Korreck, K. E., and Stevens, M. L. (2017). Applying Nyquist's method for stability determination to solar wind observations. *Journal of Geophysical Research: Space Physics*, pages 1–9. 18, 36, 57, 117, 125, 131, 133, 139, 142

Klein, L. W., Ogilvie, K. W., and Burlaga, L. F. (1985). Coulomb collisions in the solar wind. *Journal of Geophysical Research: Space Physics*, 90(A8):7389–7395. 137

Klimchuk, J. A. (2006). On solving the coronal heating problem. 12

Klimchuk, J. A. (2015). Key aspects of coronal heating. *Philosophical Transactions of the Royal Society A: Mathematical, Physical and Engineering Sciences*, 373(2042). 3, 12

Koval, A. and Szabo, A. (2013). Magnetic field turbulence spectra observed by the wind spacecraft. *AIP Conference Proceedings*, 1539(May 2014):211–214. 40, 69, 94

Krieger, A. S., Timothy, A. F., and Roelof, E. C. (1973). A coronal hole and its identification as the source of a high velocity solar wind stream. *Solar Physics*, 29(2):505–525. 5

Laming, J. M. (2004). A Unified Picture of the First Ionization Potential and Inverse First Ionization Potential Effects. *The Astrophysical Journal*, 614(2):1063–1072. 33

Laming, J. M. (2015). The FIP and inverse FIP effects in solar and stellar coronae. *Living Reviews in Solar Physics*, 12(1). 32

Laming, J. M. and Feldman, U. (2003). The Variability of the Solar Coronal Helium Abundance: Polar Coronal Holes Compared to the Quiet Sun. *The Astrophysical Journal*, 591(2):1257–1266. 32

Landi, E. and Cranmer, S. R. (2009). Ion Temperatres in the Low Solar Corona: Polar Coronal Holes at Solar Minimum. *The Astrophysical Journal*, 691(1):794–805. 12, 67

Lepping, R. P., Acũna, M. H., Burlaga, L. F., Farrell, W. M., Slavin, J. A., Schatten, K. H., Mariani, F., Ness, N. F., Neubauer, F. M., Whang, Y. C., Byrnes, J. B., Kennon, R. S., Panetta, P. V., Scheifele, J., and Worley, E. M. (1995). The Wind magnetic field investigation. *Space Science Reviews*, 71(1):207–229. 40, 69, 94

Liu, Z., Zhao, J., Sun, H., Xiang, L., Liu, W., Lu, J., and Zhou, W. (2019). Parallel-propagating Waves and Instabilities in Plasmas with Streaming Proton and Alpha Particles. *The Astrophysical Journal*, 874(2):128. 54

Livi, R. and SWEAP (2019). The Solar Probe Ion Analyzer on Parker Solar Probe. *in prep.* 92

Livi, S. and Marsch, E. (1986). On the collisional relaxation of solar wind velocity distributions. *Annales Geophysicae*, 4(1):333–340. 37, 85, 87, 89, 137, 140, 142

Livi, S. and Marsch, E. (1987). Generation of solar wind proton tails and double beams by Coulomb collisions. *Journal of Geophysical Research*, 92(6):7255–7261. 37, 54, 87, 89, 137, 138

Livi, S., Marsch, E., and Rosenbauer, H. (1986). Coulomb collisional domains in the solar wind. *Journal of Geophysical Research*, 91(A7):8045. 89, 114, 137

Maneva, Y. G., Araneda, J. A., and Marsch, E. (2014). Regulation of Ion Drifts and Anisotropies By Parametrically Unstable Finite-Amplitude Alfvén-Cyclotron Waves in the Fast Solar Wind. *The Astrophysical Journal*, 783(2):139. 88

Maneva, Y. G., Ofman, L., and Viñas, A. (2015). Relative drifts and temperature anisotropies of protons and α particles in the expanding solar wind: 2.5D hybrid simulations. *Astronomy & Astrophysics*, 578(2005):A85. 68

Marsch, E. (2006). Kinetic Physics of the Solar Corona and Solar Wind. *Living Reviews in Solar Physics*, 3. 4, 12, 117, 130

Marsch, E. and Goldstein, H. (1983). The effects of Coulomb collisions on solar wind ion velocity distributions. *Journal of Geophysical Research*, 88(A12):9933. 37, 90

Marsch, E. and Livi, S. (1985). Coulomb self-collision frequencies for non-thermal velocity distributions in the solar wind. *Annales Geophysicae*, 3(5):545–555. 37

Marsch, E. and Livi, S. (1987). Observational evidence for marginal stability of solar wind ion beams. *Journal of Geophysical Research*, 92(A7):7263. 37, 89, 90, 114, 117, 133, 137, 139

Marsch, E., Mühlhäuser, K.-H., Rosenbauer, H., Schwenn, R., and Neubauer, F. M. (1982a). Solar wind helium ions: Observations of the Helios solar probes between 0.3 and 1 AU. *Journal of Geophysical Research*, 87(A1):35. 4, 67, 72, 119

Marsch, E., Mühlhäuser, K.-H., Schwenn, R., Rosenbauer, H., Pilipp, W., and Neubauer, F. M. (1982b). Solar wind protons: Three-dimensional velocity distributions and derived plasma parameters measured between 0.3 and 1 AU. *Journal of Geophysical Research*, 87(A1):52. vii, ix, xiii, 4, 21, 37, 38, 41, 54, 56, 58, 67, 71, 90, 114

Marsch, E., Yao, S., and Tu, C. Y. (2009). Proton beam velocity distributions in an interplanetary coronal mass ejection. *Annales Geophysicae*, 27(2):869–875. 137

Maruca, B. A., Bale, S. D., Sorriso-Valvo, L., Kasper, J. C., and Stevens, M. L. (2013). Collisional thermalization of hydrogen and helium in solar-wind plasma. *Physical Review Letters*, 111(24):1–5. 38, 69, 93, 137

Maruca, B. A. and Kasper, J. C. (2013). Improved interpretation of solar wind ion measurements via high-resolution magnetic field data. *Advances in Space Research*, 52(4):723–731. 26, 38, 40, 93, 119

Maruca, B. A., Kasper, J. C., and Bale, S. D. (2011). What Are the Relative Roles of Heating and Cooling in Generating Solar Wind Temperature Anisotropies? *Physical Review Letters*, 107(20):201101. 120, 133

Maruca, B. A., Kasper, J. C., and Gary, S. P. (2012). INSTABILITY-DRIVEN LIMITS ON HELIUM TEMPERATURE ANISOTROPY IN THE SOLAR WIND: OBSERVATIONS AND LINEAR VLASOV ANALYSIS. *The Astrophysical Journal*, 748(2):137. 18, 19, 38, 39, 50, 89, 117, 120, 133, 139

Matteini, L., Hellinger, P., Goldstein, B. E., Landi, S., Velli, M., and Neugebauer, M. (2013). Signatures of kinetic instabilities in the solar wind. *Journal of Geophysical Research: Space Physics*, 118(6):2771–2782. xiii, 37, 38, 51, 56, 58, 59, 90, 114, 115, 120, 122

Matteini, L., Hellinger, P., Landi, S., Trávníček, P. M., and Velli, M. (2012). Ion Kinetics in the Solar Wind: Coupling Global Expansion to Local Microphysics. *Space Science Reviews*, 172(1-4):373–396. 89, 90

Matteini, L., Landi, S., Del Zanna, L., Velli, M., and Hellinger, P. (2010a). Parametric decay of linearly polarized shear Alfvn waves in oblique propagation: One and two-dimensional hybrid simulations. *Geophysical Research Letters*, 37(20):2–6. 37

Matteini, L., Landi, S., Hellinger, P., Pantellini, F., Maksimovic, M., Velli, M., Goldstein, B. E., and Marsch, E. (2007). Evolution of the solar wind proton temperature anisotropy from 0.3 to 2.5 AU. *Geophysical Research Letters*, 34(20):1–5. 57

Matteini, L., Landi, S., Velli, M., and Hellinger, P. (2010b). Kinetics of parametric instabilities of Alfvén waves: Evolution of ion distribution functions. *Journal of Geophysical Research: Space Physics*, 115(9):1–12. 37

Mauas, P. J. D., Andretta, V., Falchi, A., Falciani, R., Teriaca, L., and Cauzzi, G. (2005). Helium Line Formation and Abundance in a Solar Active Region. *The Astrophysical Journal*, 619(1):604–612. 32

Maunder, E. W. (1903). Spoerer's law of zones. *The Observatory*, 26:329–330. 5

Maunder, E. W. (1904). Note on the Distribution of Sun-spots in Heliographic Latitude, 1874 to 1902. *Monthly Notices of the Royal Astronomical Society*, 64(8):747–761. 5

McComas, D. J., Ebert, R. W., Elliott, H. A., Goldstein, B. E., Gosling, J. T., Schwadron, N. A., and Skoug, R. M. (2008). Weaker solar wind from the polar coronal holes and the whole Sun. *Geophysical Research Letters*, 35(18):L18103. 5

McMullin, J. P., Rimmele, T. R., Warner, M., Pillet, V. M., Casini, R., Berukoff, S., Craig, S. C., Elmore, D., Ferayorni, A., Goodrich, B. D., Hubbard, R. P., Harrington, D., Hegwer, S., Jeffers, P., Johansson, E. M., Kuhn, J., Lin, H., Marshall, H., Mathioudakis, M., McBride, W. R., McVeigh, W., Phelps, L., Schmidt, W., Shimko, S., Sueoka, S., Tritschler, A., Williams, T. R., and Wöger, F. (2016). Construction status of the Daniel K. Inouye solar telescope. In Hall, H. J., Gilmozzi, R., and Marshall, H. K., editors, *Ground-based and Airborne Telescopes VI*, number July, page 99061B. SPIE. 35

Meyer, J. P. (1991). Diagnostic methods for coronal abundances. *Advances in Space Research*, 11(1):269–280. 32

Meyer, J. P. (1993). Elemental abundances in active regions, flares and interplanetary medium. *Advances in Space Research*, 13(9):377–390. 32

Miyamoto, S. (1949). Ionization Theory of Solar Corona. *Publications of the Astronomical Society of Japan*, 1. 1

Montgomery, M. D., Gary, S. P., Feldman, W. C., and Forslund, D. W. (1976). Electromagnetic instabilities driven by unequal proton beams in the solar wind. *Journal of Geophysical Research*, 81(16):2743–2749. 19, 21, 37, 54, 56, 90

Montgomery, M. D., Gary, S. P., Forslund, D. W., and Feldman, W. C. (1975). Electromagnetic Ion-Beam Instabilities in the Solar Wind. *Physical Review Letters*, 35(10):667–670. 19, 21

Müller, D., Marsden, R. G., St. Cyr, O. C., and Gilbert, H. R. (2013). Solar Orbiter: Exploring the Sun-Heliosphere Connection. *Solar Physics*, 285(1-2):25–70. 35, 87

Neugebauer, M. (1976). The role of Coulomb collisions in limiting differential flow and temperature differences in the solar wind. *Journal of Geophysical Research*, 81(1):78–82. 12, 37, 67, 88, 114, 137

Neugebauer, M. (2003). In-situ Measurements of the Solar Wind. *AIP Conference Proceedings*, 679(September):8–13. 118

Neugebauer, M., Goldstein, B. E., Winterhalter, D., Smith, E. J., MacDowall, R. J., and Gary, S. P. (2001). Ion distributions in large magnetic holes in the fast solar wind. *Journal of Geophysical Research: Space Physics*, 106(A4):5635–5648. 38

Neugebauer, M. and Snyder, C. W. (1962). Solar Plasma Experiment. *Science*, 138(3545):1095–1097. 2, 118

Numata, R., Howes, G. G., Tatsuno, T., Barnes, M., and Dorland, W. (2010). AstroGK: Astrophysical gyrokinetics code. *Journal of Computational Physics*, 229(24):9347–9372. 17

Nyquist, H. (1932). Regeneration Theory. *Bell System Technical Journal*, 11(1):126–147. 125, 131, 139

Ogilvie, K. W., Chornay, D. J., Fritzenreiter, R. J., Hunsaker, F., Keller, J., Lobell, J., Miller, G., Scudder, J. D., Sittler, E. C., Torbert, R. B., Bodet, D., Needell, G., Lazarus, A. J., Steinberg, J. T., Tappan, J. H., Mavretic, A., and Gergin, E. (1995). SWE, a comprehensive plasma instrument for the WIND spacecraft. *Space Science Reviews*, 71(1-4):55–77. 26, 38, 39, 57, 69, 94, 118, 119

Özgüç, A. and Ataç, T. (2001). Observations of Hysteresis Between Flare Index and Some Solar Indices. In Brekke, P., Fleck, B., and Gurman, J., editors, *Recent Insights into the Physics of the Sun and Heliosphere: Highlights from SOHO and Other Space Missions*, volume 203 of *IAU Symposium*, page 125. 29

Pagel, A. C., Crooker, N. U., Zurbuchen, T. H., and Gosling, J. T. (2004). Correlation of solar wind entropy and oxygen ion charge state ratio. *Journal of Geophysical Research: Space Physics*, 109(A1):1–11. 44, 96, 113

Parker, E. N. (1958). Dynamics of the Interplanetary Gas and Magnetic Fields. *The Astrophysical Journal*, 128:664. 2, 67

Parker, E. N. (1960). The Hydrodynamic Treatment of the Expanding Solar Corona. *The Astrophysical Journal*, 132:175. 2

Parker, E. N. (1964a). Dynamical Properties of Stellar Coronas and Stellar Winds. I. Integration of the Momentum Equation. *The Astrophysical Journal*, 139(Parker 1960):72. 2, 137, 140, 141, 147

Parker, E. N. (1964b). Dynamical Properties of Stellar Coronas and Stellar Winds. II. Integration of the Heat-Flow Equation. *The Astrophysical Journal*, 139:93. 2, 137, 140, 141, 147

Parker, E. N. (1964c). Dynamical Properties of Stellar Coronas and Stellar Winds. III. The Dynamics of Coronal Streamers. *The Astrophysical Journal*, 139:690. 2, 141

Parker, E. N. (1965a). Dynamical Properties of Stellar Coronas and Stellar Winds, IV. The Separate Existence of Subsonic and Supersonic Solutions. *The Astrophysical Journal*, 141:1463. 2, 141

Parker, E. N. (1965b). Dynamical Properties of Stellar Coronas and Stellar Winds. V. Stability and Wave Propagation. *The Astrophysical Journal*, 143:32. 2, 137, 140, 141, 147

Parker, E. N. (1997). Reflections on macrophysics and the sun (Special Historical Review). *Solar Physics*, 176(2):219–247. 1

Perrone, D., Stansby, D., Horbury, T. S., and Matteini, L. (2019). Radial evolution of the solar wind in pure high-speed streams: HELIOS revised observations. *Monthly Notices of the Royal Astronomical Society*, 483(3):3730–3737. 96

Pezzi, O., Valentini, F., and Veltri, P. (2016). Collisional Relaxation of Fine Velocity Structures in Plasmas. *Physical Review Letters*, 116(14):1–5. 54, 85, 87, 137, 142

Planck, M. (1967a). On an Improvement of Wien's Equation for the Spectrum. In *The Old Quantum Theory*, pages 79–81. Elsevier. 1

Planck, M. (1967b). On the Theory of the Energy Distribution Law of the Normal Spectrum. *The Old Quantum Theory*, 237(1900):82–90. 1

Rakowski, C. E. and Laming, J. M. (2012). on the Origin of the Slow Speed Solar Wind: Helium Abundance Variations. *The Astrophysical Journal*, 754(2011):65. 33

Ramesh, K. B. and Vasantharaju, N. (2014). Temporal offsets among solar activity indicators. *Astrophysics and Space Science*, 350(2):479–487. 25, 31, 34

Reisenfeld, D. B., Gary, S. P., Gosling, J. T., Steinberg, J. T., McComas, D. J., Goldstein, B. E., and Neugebauer, M. (2001). Helium energetics in the high-latitude solar wind: Ulysses observations. *Journal of Geophysical Research*, 106(A4):5693. 72

Rempel, M. and Schlichenmaier, R. (2011). Sunspot Modeling: From Simplified Models to Radiative MHD Simulations. *Living Reviews in Solar Physics*, 8. 5

Richardson, I. G. and Cane, H. V. (2010). Near-earth interplanetary coronal mass ejections during solar cycle 23 (1996 - 2009): Catalog and summary of properties. *Solar Physics*, 264(1):189–237. 44

Sakurai, T. (2017). Heating mechanisms of the solar corona. *Proceedings of the Japan Academy Series B: Physical and Biological Sciences*, 93(2):87–97. 1

Savitzky, A. and Golay, M. J. E. (1964). Smoothing and Differentiation of Data by Simplified Least Squares Procedures. *Analytical Chemistry*, 36(8):1627–1639. 51

Schekochihin, A. A., Cowley, S. C., Dorland, W., Hammett, G. W., Howes, G. G., Quataert, E., and Tatsuno, T. (2009). ASTROPHYSICAL GYROKINETICS: KINETIC AND FLUID TURBULENT CASCADES IN MAGNETIZED WEAKLY COLLISIONAL PLASMAS. *The Astrophysical Journal Supplement Series*, 182(1):310–377. 17

Schulz, M. (1973). Interplanetary sector structure and the helliomagnetic equator. *Astrophysics and Space Science*, 24(2):371–383. 6

Schwabe, H. (1844). Sonnen — Beobachtungen im Jahre 1843. *Astronomische Nachrichten*, 21(15):234–235. 5

Schwadron, N. A., Fisk, L. A., and Zurbuchen, T. H. (1999). Elemental Fractionation in the Slow Solar Wind. *The Astrophysical Journal*, 521:859–867. 33

Schwartz, S. J. (1980). Plasma instabilities in the solar wind: A theoretical review. *Reviews of Geophysics*, 18(9):313. 17, 19, 21, 36, 37

Schwartz, S. J., Feldman, W. C., and Gary, S. P. (1981). The source of proton anisotropy in the high-speed solar wind. *Journal of Geophysical Research*, 86(A2):541. 37

Schwenn, R. (2006a). Solar wind sources and their variations over the solar cycle. *Space Science Reviews*, 124(1-4):51–76. 5, 6, 35

Schwenn, R. (2006b). Space Weather: The Solar Perspective. *Living Reviews in Solar Physics*, 3(2006). 6

Schwenn, R., Rosenbauer, H., and Mühlhäuser, K.-H. (1980). Singly-ionized helium in the driver gas of an interplanetary shock wave. *Geophysical Research Letters*, 7(3):201–204. 38

SILSO World Data Center (2018). The International Sunspot Number. 27, 44

Siscoe, G. and Intriligator, D. (1993). Three views of two giant streams: Aligned observations at 1 AU, 4.6 AU, and 5.9 AU. *Geophysical Research Letters*, 20(20):2267–2270. 44, 96

Siscoe, G. L. (1983). Solar System Magnetohydrodynamics. In Carovillano, R. L. and Forbes, J. M., editors, *Solar-Terrestrial Physics: Principles and Theoretical Foundations*, pages 11–100. Astrophysics and Space Science Library. 44

Southwood, D. J. and Kivelson, M. G. (1993). Mirror instability: 1. Physical mechanism of linear instability. *Journal of Geophysical Research*, 98(A6):9181. 19

Spitzer, L. (1962). *Physics of fully ionized gases*. Dover Publications, 2 edition. 10, 14, 73

Stakhiv, M., Lepri, S. T., Landi, E., Tracy, P. J., and Zurbuchen, T. H. (2016). on Solar Wind Origin and Acceleration: Measurements From Ace. *The Astrophysical Journal*, 829(2):117. 32

Stansby, D., Horbury, T. S., and Matteini, L. (2019). Diagnosing solar wind origins using in situ measurements in the inner heliosphere. *Monthly Notices of the Royal Astronomical Society*, 482(2):1706–1714. 8, 38

Stein, R. F. (2012). Solar surface magneto-convection. *Living Reviews in Solar Physics*, 9. 3

Steinberg, J. T., Lazarus, A. J., Ogilvie, K. W., Lepping, R. P., and Byrnes, J. (1996). Differential flow between solar wind protons and alpha particles: First WIND observations. *Geophysical Research Letters*, 23(10):1183. 3, 67

Steinier, J., Termonia, Y., and Deltour, J. (1972). Smoothing and differentiation of data by simplified least square procedure. *Analytical Chemistry*, 44(11):1906–1909. 51

Stevens, M. L. and Alterman, B. L. (2019). 21 Years of Solar Wind Proton Beam at 1 AU. *in prep*. 95, 119

Stevens, M. L. and Kasper, J. C. (2018). Center for Astrophysics Shock Database. 44

Stix, T. H. (1992). *Waves in Plasma*. American Institute of Physics. 117

Stone, J. M., Gardiner, T. A., Teuben, P., Hawley, J. F., and Simon, J. B. (2008). Athena: A New Code for Astrophysical MHD. *The Astrophysical Journal Supplement Series*, 178(1):137–177. 17

Temmer, M., Veronig, A., and Hanslmeier, A. (2003). Does solar flare activity lag behind sunspot activity? *Solar Physics*, 215(1):111–126. 25, 32

Thomas, J. H. and Weiss, N. O. (2008). Overall structure of a sunspot. In *Sunspots and Starspots*, Cambridge Astrophysics, chapter 3, pages 38–67. Cambridge University Press, Cambridge. 5

Tracy, P. J., Kasper, J. C., Raines, J. M., Shearer, P., Gilbert, J. A., and Zurbuchen, T. H. (2016). Constraining Solar Wind Heating Processes by Kinetic Properties of Heavy Ions. *Physical Review Letters*, 255101(June):255101. 14, 37, 73, 76, 88

Tracy, P. J., Kasper, J. C., Zurbuchen, T. H., Raines, J. M., Shearer, P., and Gilbert, J. (2015). Thermalization of Heavy Ions in the Solar Wind. *The Astrophysical Journal*, 812(2):170. 14

Tu, C. Y., Marsch, E., and Qin, Z. R. (2004). Dependence of the proton beam drift velocity on the proton core plasma beta in the solar wind. *Journal of Geophysical Research: Space Physics*, 109:1–6. xi, 21, 73, 117, 118, 123, 124, 125, 130, 131, 133, 139

Tu, C. Y., Marsch, E., and Wang, L. H. (2003). Cyclotron-resonant diffusion regulating the core and beam of solar wind proton distributions. *AIP Conference Proceedings*, 679:389–392. 115

Tu, C. Y., Wang, L. H., and Marsch, E. (2002). Formation of the proton beam distribution in high-speed solar wind. *Journal of Geophysical Research: Space Physics*, 107(A10):1–8. 37, 115, 138

van Driel-Gesztelyi, L. and Green, L. M. (2015). Evolution of Active Regions. *Living Reviews in Solar Physics*, 12(1):1. 5, 7, 32

Vanlommel, P., Cugnon, P., Van Der Linden, R. A. M., Berghmans, D., and Clette, F. (2005). The sidc: World data center for the sunspot index. *Solar Physics*, 224(1-2):113–120. 27

Vauclair, S. and Charbonnel, C. (1991). Helium gravitational settling below the solar convection zone. In *Challenges to Theories of the Structure of Moderate-Mass Stars*, pages 37–41. Springer Berlin Heidelberg, Berlin, Heidelberg. 33

Verscharen, D. (2019). HolmMHD: A Versatile Magnetohydrodynamics Code. *Research Notes of the AAS*, 3(7):96. 17

Verscharen, D., Bourouaine, S., and Chandran, B. D. G. (2013a). Instabilities Driven By the Drift and Temperature Anisotropy of Alpha Particles in the Solar Wind. *The Astrophysical Journal*, 773:163. 19, 85

Verscharen, D., Bourouaine, S., Chandran, B. D. G., and Maruca, B. A. (2013b). A PARALLEL-PROPAGATING ALFVÉNIC ION-BEAM INSTABILITY IN THE HIGH-BETA SOLAR WIND. *The Astrophysical Journal*, 773:8. 50, 85

Verscharen, D. and Chandran, B. D. G. (2013). The dispersion relations and instability thresholds of oblique plasma modes in the presence of an ion beam. *Astrophysical Journal*, 764(1):88. 85

Verscharen, D. and Chandran, B. D. G. (2018). NHDS: The New Hampshire Dispersion Relation Solver. *Research Notes of the AAS*, 2(2):13. 17

Verscharen, D., Chandran, B. D. G., Klein, K. G., and Quataert, E. (2016). Collisionless Isotropization of the Solar-Wind Protons By Compressive Fluctuations and Plasma Instabilities. *The Astrophysical Journal*, 831(2):128. vi, xi, xiv, 18, 19, 20, 39, 51, 117, 120, 121, 122, 126, 127, 128, 129, 130, 131, 133, 139

Verscharen, D., Klein, K. G., Chandran, B. D. G., Stevens, M. L., Salem, C. S., and Bale, S. D. (2018). ALPS: the Arbitrary Linear Plasma Solver. *Journal of Plasma Physics*, 84(4):905840403. 17

Verscharen, D., Klein, K. G., and Maruca, B. A. (2019). The multi-scale nature of the solar wind. *Living Reviews in Solar Physics*. 4, 6, 10, 11, 12, 16, 17, 18, 19, 37, 50, 54, 57, 89, 90, 117, 130, 133, 135, 139, 142

Voitenko, Y. and Pierrard, V. (2015). Generation of Proton Beams by Non-uniform Solar Wind Turbulence. *Solar Physics*, pages 1231–1241. 87, 88, 138 von Steiger, R., Schwadron, N. A., Fisk, L. A., Geiss, J., Gloeckler, G., Hefti, S., Wilken, B., Wimmer-Schweingruber, R. R., and Zurbuchen, T. H. (2000). Composition of quasi-stationary solar wind flows from Ulysses/Solar Wind Ion Composition Spectrometer. *Journal of Geophysical Research*, 105(A12):27217. 6

Waldmeier, M. (1955). Ergenbnisse der Zurcher Sonnenfinsternisexpedition 1954. I. Vorlaufige Photometrie der Korona. Mit 7 Textabbildungen. *Zeitschrift für Astrophysik*, 36:275. 6

Waldmeier, M. (1956). Synoptische Karten der Sonnenkorona. Mit 16 Textabbildungen. *Zeitschrift für Astrophysikür Astrophysik*, 38:219. 5

Waldmeier, M. (1975). The coronal hole at the 7 March 1970 solar eclipse. *Solar Physics*, 40(2):351–358. 5

Whittlesey, P. and SWEAP (2019). The Solar Probe Electron Analyzer on Parker Solar Probe. *in prep.* 92

Winske, D., Yin, L., Omidi, N., Karimabadi, H., and Quest, K. (1985). Hybrid Simulation Codes: Past, Present and Future—A Tutorial. In *Space Plasma Simulation*, pages 136–165. Springer Berlin Heidelberg, Berlin, Heidelberg. 17

Woodham, L. D., Wicks, R. T., Verscharen, D., and Owen, C. J. (2018). The Role of Proton-Cyclotron Resonance as a Dissipation Mechanism in Solar Wind Turbulence: A Statistical Study at Ion-Kinetic Scales. *The Astrophysical Journal*, 856(1):49. 95

Woodham, L. D., Wicks, R. T., Verscharen, D., Owen, C. J., Alterman, B. L., and Maruca, B. A. (2019). Parallel-propagating Fluctuations at Proton-kinetic Scales in the Solar Wind Are Dominated By Kinetic Instabilities. *The Astrophysical Journal Letters*, 884(2):L53. 117

Wüest, M., Evans, D. S., and von Steiger, R., editors (2007). *Calibration of Particle Instruments in Space Physics*. ESA Publications Division. 42

Xu, F. and Borovsky, J. (2015). A new four-plasma categorization scheme for the solar wind. *Journal of Geophysical Research: Space Physics*, 120(1):70–100. 6

Zhao, L., Landi, E., Lepri, S. T., Gilbert, J. A., Zurbuchen, T. H., Fisk, L. A., and Raines, J. M. (2017). On the Relation between the In Situ Properties and the Coronal Sources of the Solar Wind. *The Astrophysical Journal*, 846(2):135. 6

Zurbuchen, T. H. (2007). A New View of the Coupling of the Sun and the Heliosphere. *Annual Review of Astronomy and Astrophysics*, 45(1):297–338. 6

Zurbuchen, T. H., Fisk, L. A., Gloeckler, G., and von Steiger, R. (2002). The solar wind composition throughout the solar cycle: A continuum of dynamic states. *Geophysical Research Letters*, 29(9):66–1–66–4. 96

Zurbuchen, T. H., Steiger, R., Gruesbeck, J., Landi, E., Lepri, S. T., Zhao, L., and Hansteen, V. (2012). Sources of Solar Wind at Solar Minimum: Constraints from Composition Data. *Space Science Reviews*, pages 41–55. 6

Ďurovcová, T., Šafránková, J., and Němeček, Z. (2019). Evolution of Relative Drifts in the Expanding Solar Wind: Helios Observations. *Solar Physics*, 294(7):97. xiii, 37, 38, 58, 59, 90, 113, 114